

DisC@V@r

2022

May 17-20 • Villars-sur-Ollon • Switzerland

EPFL

FNSNF
FONDS NATIONAL SUISSE
SCHWEIZERISCHER NATIONALFONDS
FONDO NAZIONALE SVIZZERO
SWISS NATIONAL SCIENCE FOUNDATION



UNSTEADY FLOW
DIAGNOSTICS LAB
UNF@LD

This event was made
possible thanks
to our sponsors:

EPFL



FONDS NATIONAL SUISSE
SCHWEIZERISCHER NATIONALFONDS
FONDO NAZIONALE SVIZZERO
SWISS NATIONAL SCIENCE FOUNDATION



GMP

Your Swiss distributor for














Contents

Programme	5
Overview	5
Monday May 16	6
Tuesday May 17	7
Wednesday May 18	9
Thursday May 19	13
Friday May 20	15
Abstracts	15
Session A: Aero-acoustics and aero-elastics	16
W. Wolf	16
K. Menon	19
M. Lauber	21
R. Mittal	23
K. Shoele	25
Session B: Stall	27
A. Goza	27
C.E. Brunner	30
C. Toppings	32
D. Gloutak	34
I. Gursul	36
Poster session 1	38
M. Dave	38
P. Gehlert	41
I. Gursul	43
T. Han	45
T. Jardin	48
S. Le Fouest	50
J. Massey	52
K. Menon	54
P. Ormonde	56
N. Yaghoobian	59
Session C: Flapping and swimming	61
D. Quinn	61
A. Mivehchi	64
J. King	66
R. Vilumbrales-Garcia	68






A. Gehrke	70
V. Stin	72
Session D: Prediction and theory	74
K. Ramesh	74
A. Gopalarathnam	77
K. Manohar	78
J. Eldredge	80
S. Otomo	82
Session E: Vortex formation	84
J. Franck	84
B. Ashok	87
K. Breuer	89
A. Goyal	91
J. Reijtenbagh	93
E. Gregorio	95
Session F: Gust encounters	97
T. Jardin	97
A. Jones	100
I. Andreu Angulo	102
F. Kaiser	104
L. Thomas	106
Poster session 2	108
C. Bose	108
L. Chatellier	111
R. Fuzaro Miotto	113
J. Leetch	115
A. Martínez	117
B.L. Rocha Ribeiro	119
W. Rolansky	121
A. Shahriar	123
K. Shoele	125
I.M. Viola	127
Session G: Wakes	129
T. Saxton-Fox	129
G. Winckelmans	132
A. Abraham	134
P. Chatelain	136
T. Leweke	138
A. Castillo-Castellanos	140
Invited speakers	142
Organising and advisory committee	144
List of participants	145

Programme

Programme overview

	TUE May 17	WED May 18	THU May 19	FRI May 20
8:45-9:15	Invited talk 1	Invited talk 3	Invited talk 5	Invited talk 7
9:15-10:30	Session A: Aeroacoustics and aeroelastics	Session C: Swimming and flying	Session E: Vortex formation	Session G: Wakes
10:30-11:00	 Break	 Break	 Break	Closing
11:00-11:30	Invited talk 2	Invited talk 4	Invited talk 6	
11:30-12:30	Session B: Stall	Session D: Prediction and theory	Session F: Gust encounters	
12:30-14:00	 Lunch	 Lunch bag  transfer to EPFL	 Lunch	
14:00-17:45	Afternoon activity: hike around Villars-sur-Ollon OR visit of chateau d'Aigle	Afternoon activity: visit of EPFL	Afternoon activity: hike around Col de Bretaye OR wine tasting at Domaine Trécord	
17:45-19:00	Poster session P1	 Transfer back to Villars-sur-Ollon	Poster session P2	
19:00-21:00	 Dinner (not included)	 Collo- quium dinner: Swiss fondue in restaurant Le Sporting	 Dinner (not included)	

Monday May 16

17:30-19:00	 REGISTRATION AND WELCOME DRINK in the bar of hotel VIU
19:00-21:00	 DINNER (not included) <i>Restaurants in Villars-sur-Ollon:</i>  Le Sporting  Le Francis  Les Ecovets

Tuesday May 17

08:45-09:00	Opening (Karen Mulleners & Rajat Mittal)
09:00-09:30	William Wolf - University of Campinas The role of suction and pressure sides on airfoil tonal noise generation mechanisms at transitional Reynolds numbers
09:30-09:45	Karthik Menon - Stanford University Application of force partitioning to vortex-induced vibration and flutter
09:45-10:00	Marin Lauber - University of Southampton Development and application of an immersed boundary fluid-membrane interaction solver
10:00-10:15	Rajat Mittal - Johns Hopkins University Source Analysis for the Far-Field Acoustics from the Slat of Multi-Element High-Lift Airfoil
10:15-10:30	Kourosh Shoele - Florida State University Geometrically Weighted Modal Decomposition of Morphing Bodies
10:30-11:00	 COFFEE BREAK
11:00-11:30	Andres Goza - UIUC Effects of flap-vortex interactions on the lift of an airfoil mounted with a passively deployable flap
11:30-11:45	Claudia Brunner - Princeton University Dynamic stall at high Reynolds numbers
11:45-12:00	Connor Toppings - University of Waterloo Dynamics of Laminar Separation Bubbles in an Unsteady Freestream
12:00-12:15	Dasha Gloutak - University of Colorado Boulder Vortex Dynamics of a Separated Wing in Streamwise Gusts
12:15-12:30	Ismet Gursul - University of Bath Harnessing of Leading-Edge Vortices
12:30-14:00	 LUNCH
14:00-17:45	Optional afternoon activities: <ul style="list-style-type: none"> • hike around Villars-sur-Ollon • visit of Chateau d'Aigle
17:45-19:00	Poster session P1
19:00-21:00	 DINNER (not included)

Optional afternoon activities Tuesday

Hike around Villars-sur-Ollon



This hike lets us see the immediate surroundings of Villars-sur-Ollon. We will traverse La Gryone and discover the calm woods and charming alpine pastures of this Swiss canton. The hike takes approximately two and a half hours and is suited for people of all physical fitness levels. Join us!

Duration: 2h30

Meeting time: 2:00 pm

Meeting location: Hotel Viu, in the lobby

Difficulty: all fitness levels welcome!

Price: free

Visit of chateau d'Aigle (Aigle's Castle)

The former residence of knights, nobles, and later Bernese governors opens its doors and hosts today the museum of vine and wine. In a setting dating from the 12th century, you will discover a unique piece of Swiss heritage. The museum's exhibition inside tells the history of winemaking and deals with the themes of landscapes, biodiversity, and taste education.

We will leave from Hotel Viu at 2:30pm to take the bus at Villars-sur-Ollon Gare up to Aigle Gare and then walk 15 minutes to the castle. The return bus will leave from Aigle Gare at 4:49 pm and is back in Villars-sur-Ollon at 5:37 pm right in time for the poster session.

Topic of the visit: Castle and wine museum

Meeting time: 2:30 pm

Meeting location: Hotel Viu, in the lobby

Transport: Bus 144 from Villars Gare to Aigle Gare


Price: 30CHF (20CHF if more than 10 participants)



We request you to register for the afternoon activities by the end of the coffee break the same day such that we have an idea of the group sizes and to organise the purchase of entrance and transportation tickets. Sign up sheets will be provided the morning of the activity. For activities with an additional cost, we will purchase group tickets for the entrance fee and transportation. You can pay with credit card by scanning the QR-code corresponding to the activity. Please wait to proceed with the payment until after the activity, as the final price of the activity depends on the number of participants and will be adjusted accordingly.



Wednesday May 18

08:45-09:15	Dan Quinn - University of Virginia On the permanence of deflected vortex wakes behind pitching foils
09:15-09:30	Amin Mivehchi - Lehigh University Non-Uniform Flexibility and Schooling Interactions Lead to High Efficiency Swimming
09:30-09:45	Justin King - University of Minnesota Wake topologies and vortex patterns in bio-inspired propulsion
09:45-10:00	Rodrigo Vilumbrales-Garcia - University of Southampton Different routes to optimal flapping in unsteady conditions
10:00-10:15	Alexander Gehrke - EPFL Aerodynamic performance of a bio-inspired membrane wing
10:15-10:30	Vincent Stin - Sorbonne Université Hairpin-like vortices produced by swimming snakes
10:30-11:00	 COFFEE BREAK
11:00-11:30	Kiran Ramesh - University of Glasgow Physics-Based Low-Order Modelling of Unsteady External Flows
11:30-11:45	Ashok Gopalarathnam - North Carolina State University Prediction of Leading-Edge Vortex Initiation Using Criticality of the Boundary Layer
11:45-12:00	Kevin Manohar - University of Calgary Sensor Fusion for Temporal Super-Resolution of Turbulent Separated Flows
12:00-12:15	Jeff Eldredge - UCLA The inference of vortical flows from pressure measurements
12:15-12:30	Shuji Otomo - University of Edinburgh Low-order modelling of lift on pitching aerofoils
12:30-14:30	 LUNCH package and  transfer to EPFL
14:30-17:30	Optional afternoon activity: visit to EPFL
17:30-19:00	 transfer from EPFL to Villars-sur-Ollon
19:30-21:30	 Colloquium DINNER Swiss fondue in restaurant Le Sporting

Visit of EPFL

The École polytechnique fédérale de Lausanne (EPFL) is one of the most dynamic university campuses in Europe and ranks among the top 20 universities worldwide. The EPFL employs 6000 people supporting the three main missions of the institutions: education, research and innovation. The EPFL campus offers an exceptional working environment at the heart of a community of 16 000 people, including over 10 000 students and 3500 researchers from 120 different countries.

photo: Alain Herzog

EPFL is organised into five schools and two colleges:

- School of Basic Sciences (SB)
- School of Engineering (STI)
- School of Architecture, Civil and Environmental Engineering (ENAC)
- School of Computer and Communication Sciences (IC)
- School of Life Sciences (SV)
- College of Management of Technology (CDM)
- College of Humanities (CDH)

We plan to visit three labs from the School of Engineering (UNFoLD, CREATE, LIS) and one from the School of Architecture, Civil and Environmental Engineering (WIRE). There will also be presentations from our two silver sponsors: ILA5150 and WindShape.

Unsteady flow diagnostics laboratory (UNFoLD)

head of laboratory: Prof. Karen Mulleners

The unsteady flow diagnostics laboratory (UNFoLD) focuses on the investigation of unsteady vortex dominated flow phenomena by combining high spatially and temporally resolved flow field measurements with – what we refer to as – a fluid dynamical differential diagnosis. We develop methodologies to help bridge the gap between our observations and understanding of the development and interaction of characteristic flow structures (e.g. vortices) and technically relevant quantities, such as aerodynamic forces or power output, with applications in biological and bio-inspired propulsion, wind turbine rotor blade aerodynamics, etc.

Computational robot design & fabrication lab (CREATE)

head of laboratory: Prof. Josie Hughes

The CREATE Lab (Computational Robot Design & Fabrication Lab) aims to develop new fabrication and computational design tools for the development of robots with new and exciting capabilities, and to better understand the physical world. Our research objective is to change how we design and use robots. Firstly, to develop new fabrication methods for improved capabilities for robots – looking at how we make increasing complex, multi-material sensorized structures that allow for human-like intelligent environmental interactions. The second goal is to use robots for large scale physical experimentation to understand complex phenomena or physical occurrences, and to allow for data-driven design methods to be applied. For example, to explore and understand the complexities of taste in cooking, or to optimize complex agricultural and biological systems.

Laboratory of intelligent systems (LIS)

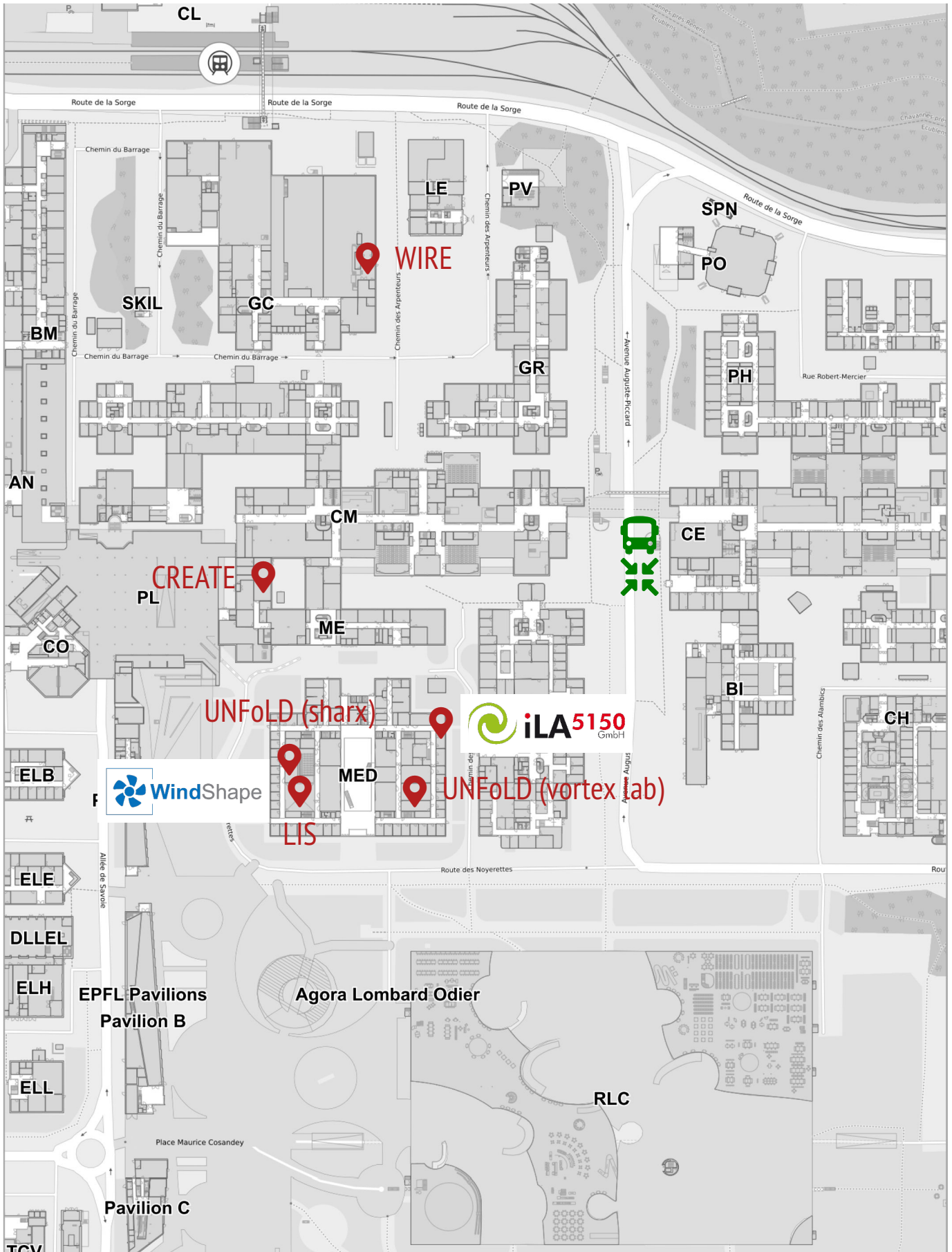
head of laboratory: Prof. Dario Floreano

The Laboratory of Intelligent Systems directed by Prof. Dario Floreano explores future avenues of artificial intelligence and robotics at the convergence of biology and engineering, humans and machines under three sections: aerial, wearable and soft robotics. We take inspiration from nature for the design, learning and control of agile drones that can fly in cluttered environments and in swarms (Aerial Robotics). We investigate and develop novel soft wearable robots for natural interactions between humans and robots (Wearable Robotics). We investigate smart materials, mechanical design, learning and control of soft robots that capture the resilience and adaptability of living organisms (Soft Robotics).

Wind engineering and renewable energy laboratory (WIRE)

head of laboratory: Prof. Fernando Porté-Agel

The main goal of our research is to improve our understanding and ability to predict turbulent transport of momentum and scalars (e.g., heat, water vapor, pollutants) in environmental flows, with emphasis on the atmospheric boundary layer and wind energy systems. Improved descriptions of those processes are developed and used in engineering, environmental and wind energy applications (e.g., weather, air quality and wind resource assessment models). Our research involves a synergistic combination of experimental (field and wind tunnel) work, numerical modelling (large-eddy simulation) and theoretical development. Specific areas of research include: Wind energy, flow over complex terrain, flow in urban canopies, large-eddy simulation, thermally stratified flows, boundary-layer turbulence.



Thursday May 19

08:45-09:15	Jen Franck - University of Wisconsin-Madison Connecting wavelength and vortex topology in undulated seal whisker geometries
09:15-09:30	B Ashok - Indian Institute of Science Effects of passive flexibility at the exit on the formation of an axisymmetric starting jet
09:30-09:45	Kenny Breuer - Brown University Vortex dynamics associated with a pitching wing in quiescent water
09:45-10:00	Anushka Goyal - McGill University Formation of vortex pairs using a single surging plate
10:00-10:15	Jesse Reijtenbagh - Delft University of Technology Scaling of drag forces of an accelerated flat plate
10:15-10:30	Elizabeth Gregorio - The George Washington University Rip Entry Investigation: Divers Manipulate The Air Cavity
10:30-11:00	 COFFEE BREAK
11:00-11:30	Thierry Jardin - ISAE-Supaero Effect of large amplitude streamwise gust on laminar separation bubbles
11:30-11:45	Anya Jones - University of Maryland Mitigation of transverse gusts using open- and closed-loop pitch maneuvers
11:45-12:00	Ignacio Andreu Angulo - University of Cambridge Unsteady Flow and Force Response - A General Overview
12:00-12:15	Frieder Kaiser - Queen's University Data-driven aerodynamic load estimation in gusty environments from sparse pressure data
12:15-12:30	Lionel Thomas - Institut Pprime, France Detection of coherent structures in a surge propagating in a channel
12:30-14:00	 LUNCH
14:00-17:45	Optional afternoon activities: <ul style="list-style-type: none"> • hike around Col de Bretaye • wine tasting at the domaine Trécord
17:45-19:00	Poster session P2
19:00-21:00	 DINNER (not included)

Optional afternoon activities Thursday

Hike at Col de Bretaye



This hike gives us the unique opportunity to ride the local rack and pinion railway that voyages up this steep alpine terrain. We start the hike at Col de Bretaye and venture towards Chavonnes lake, which supports rich wildlife. We may even be surprised by an alpine ibex or a bearded vulture. The hike takes approximately two hours. The last train back leaves at 4:45 pm. We will leave from Villars-sur-Ollon gare at 2:20pm heading to Col de Bretaye.

Duration: 2h

Meeting time: 2:00 pm

Meeting location: Hotel Viu, in the lobby

Difficulty: base fitness level required

Price for rack railway: 25CHF (18CHF if more than 10 participants)

Wine tasting at Domaine Trécord

Domaine de Trécord is a small family-owned vineyard in Ollon. Harald and Daniela founded the Domaine in 2007 and since then have been crafting exquisite Vaudois wines. The family welcomes you to discover and taste the wines of Domaine de Trécord.

We will leave from Hotel Viu at 2:30 pm and take the bus from Villars-sur-Ollon to Ollon and walk 10 minutes to the domaine. The bus to return to Villars leaves at 5:02 pm at the Ollon bus stop.



Location: Domaine Trécord, Ollon

Meeting time: 2:30 pm

Meeting location: Hotel Viu, in the lobby

Transport: Bus 144 from Villars-sur-Ollon to Ollon

Price: 21CHF (15CHF if more than 15 participants)



Please register for the activity by the end of the coffee break to organise the purchase of entrance and transportation tickets. Sign up sheets will be provided the morning of the activity. We will purchase group tickets for the entrance fee and transportation. You can pay with credit card by scanning the QR-code corresponding to the activity. Please wait to proceed with the payment until after the activity, as the final price of the activity depends on the number of participants and will be adjusted accordingly.

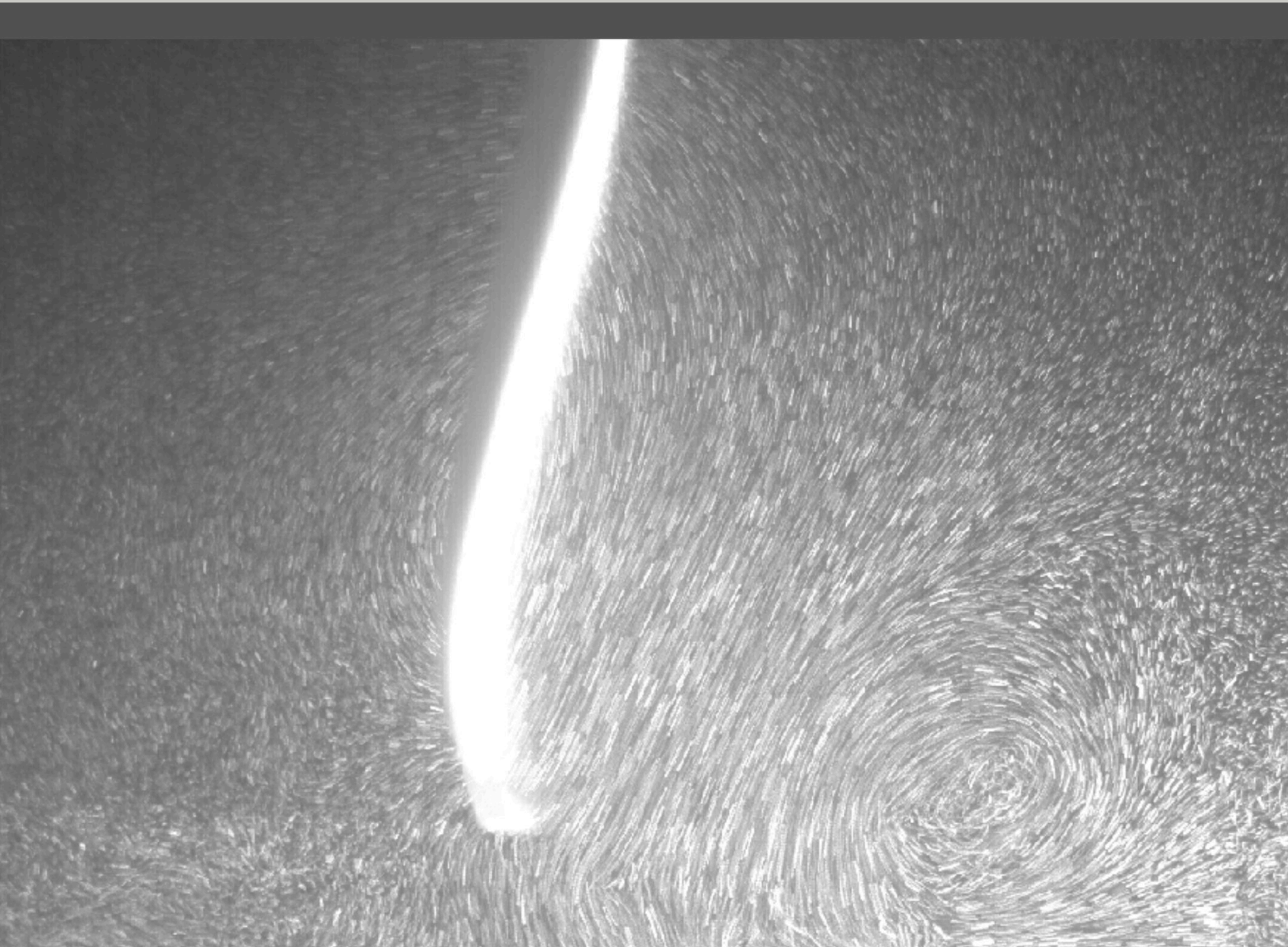


Friday May 20

08:45-09:15	Theresa Saxton-Fox - UIUC Interaction of a cylinder wake with a turbulent boundary layer
09:15-09:30	Grégoire Winckelmans - UCLouvain When turbulence matters in vortex dominated flows
09:30-09:45	Aliza Abraham - Aix-Marseille Université Simplified model for capturing helical vortex interactions with applications to asymmetric rotor wakes
09:45-10:00	Philippe Chatelain - UCLouvain Vortex sensing and uncertainty propagation for aircraft formation flight
10:00-10:15	Thomas Leweke - CNRS-IRPHE Vortex pairs in the wake of fixed and rotating split-tip wings
10:15-10:30	Andrés Castillo-Castellanos - Aix Marseille Université Numerical analysis of helical vortex pairs
10:30-11:00	Closing

Session A

Aero-acoustics and aero-elastics



The role of suction and pressure sides on airfoil tonal noise generation mechanisms at transitional Reynolds numbers

Tulio Rodarte Ricciardi* and William Roberto Wolf

School of Mechanical Engineering, University of Campinas, Campinas, SP, 13083-860, Brazil¹

*Correspondence: wolf@fem.unicamp.br

1 Introduction

At moderate Reynolds numbers, noise generation by airfoils is characterized by multiple discrete tones in the acoustic spectra, which are often characterized by a main tonal peak and multiple equidistant secondary tones. This pattern is attributed to spanwise coherent instabilities shed from laminar separation bubbles (LSBs) which lead to acoustic scattering on the trailing edge. The acoustic waves would then propagate upstream and excite new hydrodynamic disturbances, sustaining a self-excited acoustic feedback loop [1].

Based on the high spanwise flow coherence observed in early experiments, the first numerical simulations of airfoil flows with focus on secondary tones and acoustic feedback loop only considered two-dimensional solutions at moderate Reynolds numbers $50k < Re < 200k$ [1, 2]. However, these simulations lack intrinsic three-dimensional mechanisms, such as vortex stretching and transition to turbulence, and the flow stays laminar. To overcome this limitation, only recently that 3D simulations were employed where the effects of transition to turbulence have been shown in the context of airfoil secondary tones [3]. Another important observation is that, in opposition to the early experimental studies, the aforementioned numerical simulations, either 2D or 3D, report flow recirculation on the airfoil suction side. The separation bubbles, either on pressure or suction sides, are responsible for triggering flow instabilities and vortex shedding which are responsible for noise generation [4, 5]. Thus, the vortex dynamics downstream the separation bubble plays an important role in the overall dynamics.

Motivated by the work of Pröbsting et al. [6], where different regimes of noise emission are discussed, large eddy simulations (LES) are employed to study the Reynolds number dependence on the noise spectrum, with particular attention to the behavior of secondary tones. The assessment is performed for a NACA0012 airfoil considering the following Reynolds numbers: $Re = 0.5, 1, 2$ and 4×10^5 . The freestream Mach number is set as $M_\infty = 0.3$ and the angle of attack is fixed at 3 deg. The boundary layers are allowed to develop naturally to understand the role of coherent structures on both sides of the airfoil in the noise generation process.

¹This work was supported by Fundação de Amparo à Pesquisa do Estado de São Paulo, FAPESP, under grants No. 2013/08293-7 and 2021/06448-0.

2 Results

As an initial assessment of the flow dynamics, the visualization of solution snapshots in terms of iso-surfaces of Q-criterion ($Q = 2.5$) colored by streamwise velocity component u is presented in Fig. 1 for the configurations analyzed. In the plots, a magenta shaded region indicates instantaneous reversed flow with negative values of u in order to highlight the LSB. For the lowest Reynolds number, $Re = 0.5 \times 10^5$, the overall dynamics is dictated by vortex pairing on the suction side [3]. The flow instabilities that originate near mid-chord are purely two dimensional but, as they are advected, interaction among vortices may introduce three-dimensionality to the structures that eventually leads to vortex breakdown. This process results in flow intermittency at the trailing edge and it is possible to see in Figs. 1(a) and (b), respectively, a spanwise coherent structure or small-scale turbulent eddies.

With an increase in the Reynolds number to 1×10^5 , the different patterns are still observed. For instance, coherent structures at the trailing edge are illustrated in Fig. 1(c) while Fig. 1(d) shows turbulent packets with small-scale eddies. One important difference from the previous setup is the presence of non-zero spanwise wavenumbers near the mid-chord region, during the onset of flow instabilities, as illustrated in Fig. 1(c). This has a direct influence on the vortex pairing because it is more likely that this process results in breakdown rather than merging. The only coherent structures reaching the trailing edge are those that originated from flow instabilities with zero spanwise wavenumber, similarly to those observed in upstream positions in Fig. 1(d). For higher Reynolds numbers, the flows always transition to turbulence along the suction side and no laminar-like coherent structures have been observed to reach the trailing edge, as illustrated in Figs. 1(e) and (f) for $Re = 2$ and 4×10^5 , respectively. As presented in Fig. 1(e), non-zero wavenumbers can be observed in the vortices for $Re = 2 \times 10^5$. For $Re = 4 \times 10^5$, the flow instabilities still exhibit non-zero wavenumbers and always transition to turbulence despite the shorter spanwise length.

The trailing-edge noise generation by airfoils depends on the spanwise coherence of flow structures and their subsequent acoustic scattering. Proper orthogonal decomposition (POD) is applied to the spanwise averaged pressure field to

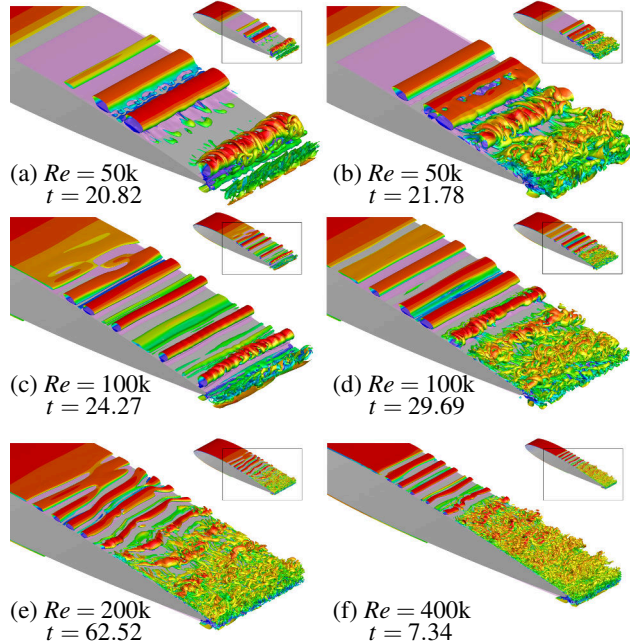


Figure 1: Iso-surface of Q-criterion colored by streamwise velocity component. The magenta shaded surfaces indicate instantaneous negative velocities to highlight the LSB.

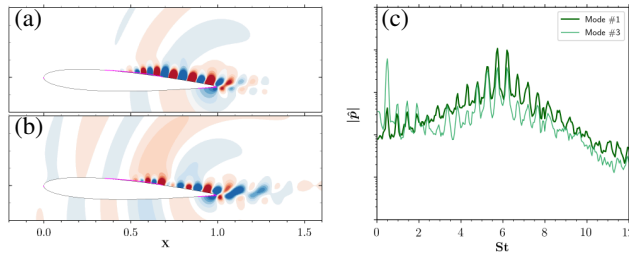


Figure 2: POD analysis for $Re = 1 \times 10^5$ in terms of pressure spatial modes (a) #1 and (b) #3, and (c) Fourier-transformed temporal modes.

identify coherent structures. The present methodology allows the identification of dominant flow features, presented as spatial modes, and their respective frequency spectra, presented as Fourier transforms of the POD temporal modes. Results for $Re = 1.0 \times 10^5$ are presented in Figs. 2(a,b) as the spatial modes #1 and #3. It is possible to see that the dominant flow structures appear downstream the separation bubble, indicated by the magenta line, along the suction side. Acoustic waves can be seen radiating from the trailing edge in the same figures. The Fourier-transformed temporal modes are presented in Fig. 2(c), where multiple tonal peaks are observed. For the highest Reynolds number, $Re = 4 \times 10^5$, the spatial modes depicted in Figs. 3(a,b) show that the flow patterns from the suction side lose their coherence downstream the tiny separation bubble. These spatial modes also highlight the importance of the pressure side and aerodynamic wake in the trailing-edge noise generation.

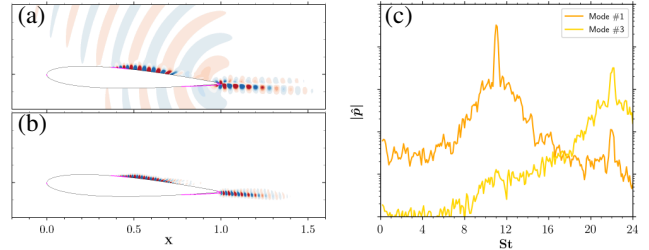


Figure 3: POD analysis for $Re = 4 \times 10^5$ in terms of pressure spatial modes (a) #1 and (b) #3, and (c) Fourier-transformed temporal modes.

ration. The temporal modes presented in Fig. 3 depict a dominant tonal frequency at $St = 11.0$ and its harmonic at $St = 22.0$.

3 Conclusions

Large eddy simulations are performed at moderate Reynolds numbers to investigate the mechanisms of noise generation and the switch from suction to pressure side dominated dynamics. Laminar separation bubbles are responsible for shedding of coherent structures which, in turn, generate trailing-edge noise efficiently. The lower Reynolds number flows present more pronounced recirculation bubbles on the suction side. On the other hand, increasing the Reynolds number not only reduces the suction side recirculation but also results in a more prominent bubble on the pressure side. As a consequence, the coherent structures shed from the bubbles are identified by the proper orthogonal decomposition using spanwise averaged data in regions where flow patterns are more important for the noise generation. For the lower Reynolds numbers, $Re = 0.5$ and 1×10^5 , the coherent structures are observed on the suction side, including the vicinity of the trailing edge. When increasing the Reynolds numbers to $Re = 2$ and 4×10^5 , the turbulent transition on the suction side greatly reduces the coherence of flow structures towards the trailing edge. Thus, coherent structures along the wake become the main source of sound.

References

- [1] G. Desquesnes, M. Terracol, and P. Sagaut. Numerical investigation of the tone noise mechanism over laminar airfoils. *J. Fluid Mech.*, 591:155–182, 11 2007.
- [2] M. Fosas de Pando, P. J. Schmid, and D. Sipp. A global analysis of tonal noise in flows around aerofoils. *J. Fluid Mech.*, 754:5–38, 2014.
- [3] T. R. Ricciardi, W. R. Wolf, and K. Taira. The role of transition, intermittency and phase interference in airfoil secondary tones, 2021.
- [4] T. Michelis, S. Yarusevych, and M. Kotsonis. On the origin of spanwise vortex deformations in laminar separation bubbles. *J. Fluid Mech.*, 841:81–108, 2018.
- [5] J. W. Kurelek, A. R. Lambert, and S. Yarusevych. Coherent structures in the transition process of a laminar separation bubble. *AIAA J.*, 54(8):2295–2309, 2016.
- [6] S. Pröbsting, F. Scarano, and S. C. Morris. Regimes of tonal noise on an airfoil at moderate Reynolds number. *J. Fluid Mech.*, 780:407–438, 2015.

Application of force partitioning to vortex-induced vibration and flutter

Karthik Menon ^{a,b} and Rajat Mittal ^{a*}

^a Johns Hopkins University, Baltimore, MD, USA ¹

^b Stanford University, Stanford, CA, USA

*Correspondence: mittal@jhu.edu

1 Introduction

The characterization of the forces and moments induced on surfaces by fluid flows has been a subject of interest since the earliest studies of fluid mechanics. Of particular interest in the domains of aerodynamics and fluid-structure interaction is the influence of vortices and vortex-induced loads on immersed surfaces. These vortex structures can drive the motion of immersed bodies, which in turn leads to the generation of additional vortices, and gives rise to complex nonlinearities in the response of fluid-structure interaction systems. Therefore, the ability to disentangle the roles of individual vortices, as well as other physical mechanisms, in the production of loads on immersed surfaces is important for understanding the physics of a problems in a number of arenas including bluff-body oscillation, wing flutter, biological propulsion, and physiological flows [1–5].

In this work, we present results from our recent papers [6–8] on applying a novel force partitioning method (FPM) to dissect the mechanisms behind fluid dynamic force production in some canonical “vortex-dominated” flows. The FPM allows us to express the force/moment on an immersed body in terms of contributions from different physical mechanisms, namely the kinematics of the immersed body (i.e. acceleration-associated effects), viscous contributions, and vortex-induced loads. Of particular interest in this research is the vortex-induced loading component, which quantifies the loads induced on surfaces within a fluid flow by vortical regions in the flow-field. Furthermore, the mathematical form of this vortex-induced component also allows us to isolate its contribution in distinct vortical regions of the flow, i.e. the loads induced on an immersed surface by distinct vortices in the flow-field. However, the task of isolating and tracking regions corresponding to individual vortices in flows involving multiple interacting and evolving vortices is itself a significant challenge. Therefore, we combine the FPM with a data-driven framework to individually identify, isolate and track the volume occupied by each vortex throughout the spatio-temporal evolution of the flow – thereby allowing us to dissect the production of aerodynamic loads at the level of individual vortices.

We present applications of this combined force partitioning and vortex tracking framework to the analysis of two fundamental problems in aerodynamics and flow-induced oscillations – the aerodynamics of pitching wings and the vortex-induced vibration of bluff bodies. We show that this framework has allowed us to investigate fundamental physics as well as highlight important gaps in our understanding of flows around oscillating cylinders and unsteady wings; both canonical problems that have long been the basis of many other research questions in this domain.

2 Results

We first briefly discuss findings from the application of FPM to the analysis vortex-induced vibration of cylinders. Previous studies have *qualitatively* attributed these vibrations, and changes in vibration characteristics, to patterns of vortex shedding in the wake of the cylinder. With the FPM framework, we have been able to *quantify* the vortex-induced effect of the cylinder wake in driving bluff-body oscillations, as well as distinguish wake effects from the other dominant forcing mechanisms in this flow – the shear layer on the surface of the cylinder. By computing the work done by vortex-induced loads due to each of these regions, we have been able to show that the flow-induced oscillations are actually not driven by the wake, but by the shear layer. In fact, we also show that although the wake contributes to the initiation of oscillations, it acts against the oscillations at larger amplitudes.

In figure 1 we show results for one sample case of an oscillating circular cylinder. Figure 1(a) shows the distinct regions corresponding to the shear layer and wake within which vortex-induced loads are estimated, and figure 1 shows the heave amplitude of the cylinder. Figures 1(b) and 1(c) show the work done by the vortex-induced lift within the shear layer and wake regions respectively. We see that as the oscillation amplitude grows, the shear layer does increasingly positive work, whereas the wake does negative work on the oscillation.

A second application that we will discuss is the analysis of lift production and dynamic stall of pitching wings. Dynamic stall is generally considered to be driven by the generation and shedding of the leading-edge vortex (LEV) [?],

¹This work was supported by AFOSR under grant number FA9550-16-1-0404.

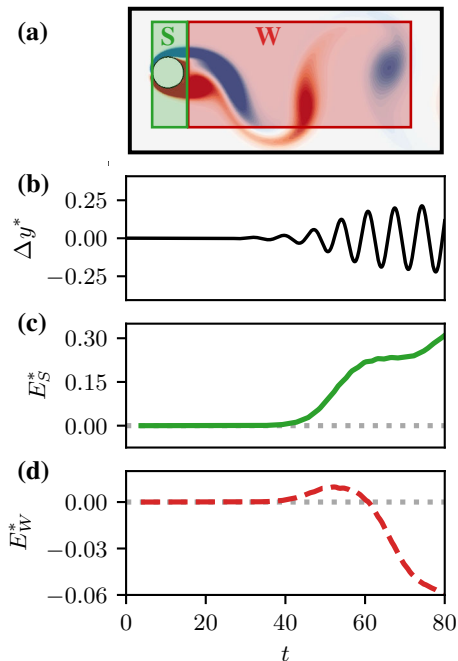


Figure 1: Sample results for application of FPM to analyze flow-induced vibration of cylinders. See discussion for details.

and the LEV is also known to play a role in other unsteady aerodynamics phenomena such as insect flight. Here, by using the combined FPM and vortex tracking framework to quantify loads induced by individual vortices, we show that although most studies of vortex-induced effects primarily focus on the influence of the rotation-dominated cores of vortices, vortices in viscous flows are in fact surrounded by strain-dominated regions that are dynamically important and can sometimes even dictate the induced aerodynamic loads.

In figure 2 we see this illustrated for one case of a pitching airfoil. Figure 2(a) and 2(b) show the spatial distribution of vortex-induced lift at two instantaneous snapshots ($t = t_1, t_2$), with some important vortices highlighted. The total lift on the airfoil is shown in figure 2(c) and the contributions of individual vortices are shown in figure 2(d). We see in figure 2(d) that the LEV (—) dominates the vortex-induced lift (—), but is in fact out-of-phase with the total lift in figure 2(c). By comparing the vortex-induced lift (—) with lift-induced by the strain associated with vortices (—) in figure 2(e), we see that the negative strain-induced lift peaks at $t = t_2$, which corresponds to the drop in total lift.

3 Conclusion

The physics of fluid-structure interactions and aerodynamic force production in vortex-dominated flows is driven by several different mechanisms and complex vortex interactions. By developing a physics-based and data driven framework that includes a method to partition the contributions of different physical mechanisms as well as individual vortices to

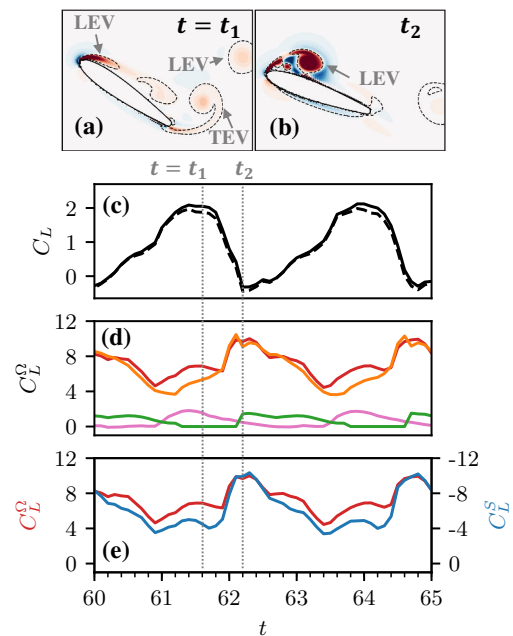


Figure 2: Sample results for application of FPM to analyze dynamic stall of pitching wings. See discussion for details.

force production, we have been able to provide new insight into the physics of fundamental problems in the domain of vortex-dominated flows.

References

- [1] C. H.K. Williamson. Vortex dynamics in the cylinder wake. *Annual Review of Fluid Mechanics*, 28:477–539, 1996.
- [2] M. S. Triantafyllou, G. S. Triantafyllou, and D. K. P. Yue. Hydrodynamics of Fishlike Swimming. *Annual Review of Fluid Mechanics*, 32(1):33–53, 2000.
- [3] Z. Jane Wang. Dissecting Insect Flight. *Annual Review of Fluid Mechanics*, 37(1):183–210, 2005.
- [4] Rajat Mittal. Matters of the heart. *Journal of Fluid Mechanics*, 844:1–4, 2018.
- [5] Jeff D. Eldredge and Anya R. Jones. Leading-edge vortices: Mechanics and modeling. *Annual Review of Fluid Mechanics*, 51:75–104, 2019.
- [6] Karthik Menon and Rajat Mittal. On the initiation and sustenance of flow-induced vibration of cylinders: insights from force partitioning. *Journal of Fluid Mechanics*, 907:A37, 2020.
- [7] Karthik Menon and Rajat Mittal. Quantitative analysis of the kinematics and induced aerodynamic loading of individual vortices in vortex-dominated flows: a computation and data-driven approach. *Journal of Computational Physics*, 443:110515, 2021.
- [8] Karthik Menon and Rajat Mittal. Significance of the strain-dominated region around a vortex on induced aerodynamic loads. *Journal of Fluid Mechanics*, 918(R3):1–10, 2021.

Development and application of an immersed boundary fluid-membrane interaction solver

Marin Lauber^{a*}, Gabriel D. Weymouth^{a,b} and Georges Limbert^{a,c}

^a University of Southampton, Faculty of Engineering and Physical Sciences, Southampton, UK¹

^b Alan Turing Institute, Data-Centric Engineering Programme, London, UK

^c University of Cape town, Faculty of Health Science, Cape Town, South Africa

*Correspondence: *M.Lauber@soton.ac.uk*

1 Introduction

Fluid-structure interaction of flexible membranes/shells with an unsteady flow is ubiquitous in nature, from leaves reconfiguration to bat wing flapping. Correct modelling of those systems is of interest both from a numerical and physical point of view.

However, this is challenging; the structures can accommodate extremely large displacements, complex dynamical deformations and orthotropic material properties. The usual small mass of the structure itself also imposes restrictions to the coupling methods that can be used for stability, this is known as the added-mass instability problem.

We present a partitioned fluid-structure interaction solver for problem involving shells/membranes in an unsteady flow. We couple a finite-volume flow solver that uses BDIM- σ , presented in [1], to a finite-element structural solver (CalculiX, [2]). This immersed boundary method ensures proper treatment of the pressure boundary condition on the immersed object for thin moving interface. This is especially important as these light structures can be subject to large acceleration and an erroneous treatment of the pressure boundary condition would result in fluid leakage across the interface. The coupling interface uses the *preCICE* library for coupled multi-physics simulation. The library provides data-mapping methods for non-matching meshes and various weakly and strongly coupled algorithm (i.e. Aitken under-relaxation, Quasi-Newton schemes).

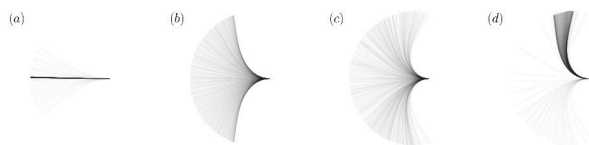


Figure 1: Schematic of the different dynamic modes of an inverted flag for small mass ratio ($M_\rho < 1$); (a) small deflection flapping, (b) large amplitude limit-cycle flapping, (c) chaotic flapping and (d) deflected mode flapping.

2 Numerical Method

The BDIM- σ formulation builds on the excellent results obtained by the BDIM method and extends them to membrane-like structure. The general thin structure is parametrized in the fluid solver by a mid-plane surface σ and a local thickness d . The points on the body surface are defined as

$$\vec{x} \in \partial\Omega_b = \vec{\sigma}(\vec{\xi}) \pm \frac{1}{2}d(\vec{\xi})\hat{n}(\vec{\xi}) \quad (1)$$

where $\vec{\xi}$ are the curvilinear coordinates of the mid-surface and \hat{n} is the unit normal. To ensure correct treatment of the pressure boundary condition (in addition to the no-slip condition) BDIM- σ uses a variable coefficient Poisson equation. Proper construction of these coefficients on the background mesh via a modified distance function

$$s(\vec{x}, t) = s_\sigma(\vec{x}, t) - \max\left(\frac{1}{2}d(\vec{x}, t), C_1\Delta x\right), \quad (2)$$

where C_1 is related to the dimension of the problem, allows correct treatment of low dimension immersed membranes, \mathbb{R}^2 , in a \mathbb{R}^3 fluid domain.

To model the dynamic response of the structure, we use a continuum shell model that doesn't make any assumptions for the through-thickness behaviour of the structure. This allows thick and thin shells to be treated accurately. The generalized- α method is used to implicitly integrate the equation of motion in time. Constant and linear triangular elements are implemented and can be used.

An *interface quasi-Newton schemes* is used to strongly couple the fluid and the solid sub-problems, with *radial basis function mapping* to map face-center data to vertices.

3 Results

An inverted flapping flag is used to validate our coupled solver. The system is governed by three non-dimensional parameters

$$Re = \frac{UL}{\nu_f}, \quad K_B = \frac{Eh^3}{12\rho_f U^2 L^3}, \quad M_\rho = \frac{\rho_s h}{\rho_f L}, \quad (3)$$

where ν_f , ρ_f and U are the fluid's viscosity, density and velocity. The density, length and thickness of the flag are ρ_s , L and h respectively.

¹This work was supported by UKRI under grant number EP/L015382/1

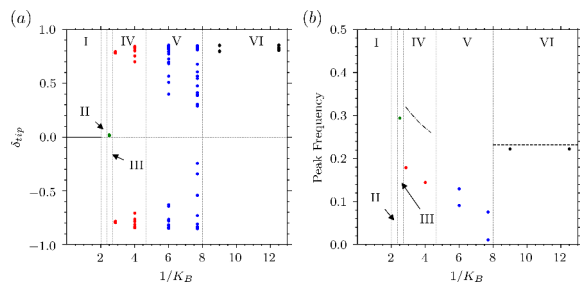


Figure 2: (a) Bifurcation diagram of an inverted flag at $Re = 200$ and $M_p = 0.5$, (b) peak frequency response of the limit-cycle flapping.

For small mass ratio ($M_p < 1$) reduction of the non-dimensional stiffness (K_B) of the system results a transition between the different flapping regimes, see Figure 1. To investigate the ability of the partitioned solver to deal with small mass ratios and dynamic cases, we focus on the flow at a Reynolds number $Re = 200$ and a mass ratio $M_p = 0.5$ for a range of non-dimensional stiffness such that all the different flapping modes are investigate. We perform 2D simulations of the previous system using the in-house coupled code described above.

The low mass-ratio allows us to observe all the flapping modes described above, whereas larger mass ratio have been shown to prevent chaotic flapping [4]. Figure 2a shows the Hopf bifurcation diagram for the vertical leading-edge displacement.

The dominant frequencies of flapping are shown Figure 2b. We observe that for high stiffness flag (low K_B) the oscillating frequency is high, it reduces with reduced stiffness until it reaches a lower limit during chaotic flapping. In the small-amplitude large displacement flapping range the frequency equivalent to the vortex shedding frequency of the bluff body wake ($\sim 0.2L_p$). We also note that the high frequency small amplitude flapping follows the scaling presented in [3], shown on Figure 2b as a dash-dotted line. The results with varying mesh density are shown in Table 1, showing an excellent agreement with the reference data.

We also observe the asymptotic behaviour of the flapping dynamic with respect to mass ratio, where a ten-fold reduction in the mass of the flag results in a nearly identical vortex shedding and flapping synchronisation, see Figure 3.

4 Future Application

Finally, we perform 2D simulation of a tandem airfoil configuration, where the first airfoil is pitching following standard kinematics. The trailing foil is mounted on a rod, such that is is free to rotate round the pitching point of the leading airfoil, see Figure 4. Interaction of the flexible airfoil with the *Karman vortex street* in the wake of the leading airfoil can result in a positive trust on the tethered swimmer. The findings are confirmed with experimental measurements.

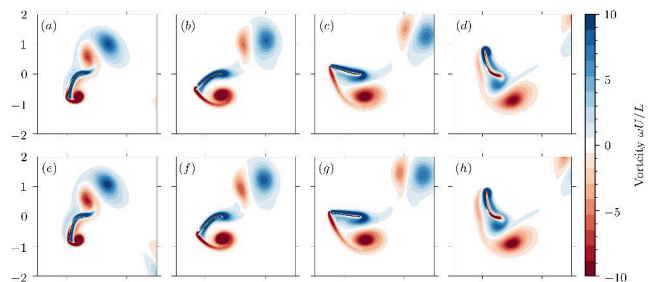


Figure 3: Inverted flag dynamic for half a period of motion (spaced uniformly distributed in time $t/T \in (0, 1/2]$) for $Re = 200$ and $K_B = 0.35$. Top row ((a–d)) is and $M_p = 0.5$ and bottom row ((e–f)) is with $M_p = 0.05$.

Table 1: Convergence study for the inverted flag with $Re = 200$, $K_B = 0.35$ and $M_p = 0.5$

Resolution Δx	Deflection (δ_{tip}/L)	Frequency (Hz)
$L/32$	± 0.743	0.128
$L/64$	± 0.796	0.179
$L/128$	± 0.797	0.180
Reference [4]	± 0.810	0.180

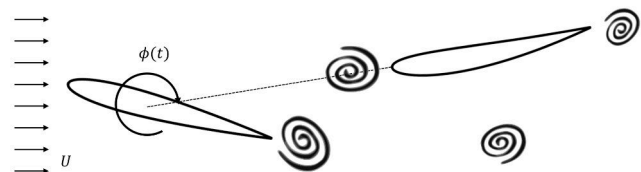


Figure 4: Schematic of the tandem foil arrangement with flexible trailing foil.

5 Conclusion

We presented a coupled fluid-structure interaction flow solver to study fluid-structure interaction in vortex-dominated flows. We validate it on the problem of an inverted flag. We show that our solver is able to accurately simulated complex inverted flag motion, with large structural displacements and capture accurately flapping amplitude and peak frequencies even at very low mass ratios. This opens a range of possible fluid-structure interaction investigation that are covered by thin shells/membranes within an unsteady flow.

References

- [1] Lauber M., Weymouth G. D., and Limbert G. Immersed Boundary Simulations of Flows Driven by Moving Thin Membranes. *arXiv - physics.flu-dyn* 2110.06535, 2021.
- [2] Dhondt G., The Finite Element Method for Three-Dimensional Thermo-mechanical Applications *John Wiley & Sons Ltd* Chichester, UK, 2004.
- [3] Shen N., Chakraborty D., and Safer J. E. Resonant frequencies of cantilevered sheets under various clamping configurations immersed in fluid. *Journal of Applied Physic* 120, 144504, 2016.
- [4] Goza A., Colonius T. A strongly-coupled immersed-boundary formulation for thin elastic structures *Journal of Computational Physics* 33672, 401–411, 2017.

Source Analysis for the Far-Field Acoustics from the Slat of Multi-Element High-Lift Airfoil

Yang Zhang^a, Louis Cattafesta^{a*}, Jung-Hee Seo^b, and Rajat Mittal^b

^a Department of Mechanical Engineering, Florida State University, Tallahassee, USA¹

^b Department of Mechanical Engineering, Johns Hopkins University, Baltimore, USA

*Correspondence: lcattafesta@fsu.edu

1 Introduction

The leading edge slat of a high-lift system is known to be a large contributor to the overall radiated acoustic field from an aircraft during the approach phase of the flight path. Slat noise often consists of both narrowband peaks and broadband noise, which are due to the vortices shed from the leading edge slat and subsequent interactions in the slat-cove and near the leading edge of the main element. Slat noise has been extensively studied for many years, using both experimental and computational approaches [1, 2].

Generally, there are several basic flow mechanisms associated with the slat-noise (see Figure 1). The flow separation at the slat cusp forms a free shear layer that impinges on the cove surface and generates a acoustic feedback loop, which is analogous to the classic cavity flow [3]. This interaction introduces multiple narrowband peaks (usually observed at low to moderate Reynolds numbers). The flapping motion of the slat-cove shear layer also results in a breathing/pumping effect through the gap between the slat and main element. This also leads to the slow oscillatory motion of enclosed large circulation bubble in the cove region [4, 5]. The third noise generation mechanism is the shedding peak induced by the flow separation at the slat trailing edge, which is characterized by the thickness of the blunt slat trailing edge and flow speed [6]. The final mechanism is the broadband noise associated with impingement, recirculation, and scattering of flow structures in the turbulent shear layer.

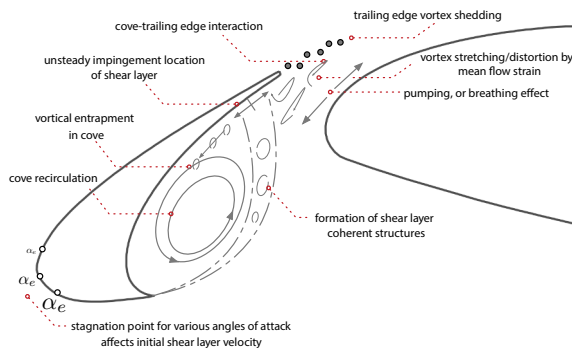


Figure 1: Slat noise generation mechanism [4]

Conventional measurement techniques include near field surface pressure measurements, far-field phased microphone measurements, and laser based velocity field measurements. The pressure field can be obtained by solving the pressure Poisson equation using the turbulent velocity field as input. If the time-resolved velocity field is available, then the resulting pressure field is also time-resolved. Furthermore, Curle's analogy can project the time-resolved pressure forces on the airfoil surface to the acoustic far field [7]. Using this approach, the far-field acoustic signature can be linked to the local velocity/vorticity field. An example of this approach is given in Figure 2, which shows good agreement between the estimated and measured acoustic spectra.

Due to the nature of this vortical flow field, we were motivated to explore a new method to study the link between the local flow field and far-field acoustics. Recently, Seo et al. [8] demonstrated that the various noise sources associated with vortex-surface interactions can be decomposed from the loading noise using an aeroacoustic partitioning method (APM). Unlike microphone arrays, the APM can decompose the source contributions to the far-field noise. In the current case of slat-noise, the vortices in the slat-cove shear layer impinge on the cove surface and radiate acoustic waves. In an effort to understand how these interactions affect the far-field acoustics, temporally-resolved two-component velocity vector fields are obtained using time-resolved planar PIV measurements in the slat cove region of a two-dimensional multi-element 30P30N airfoil. Spectral Orthogonal Decomposition [9] is used to obtain the vorticity fields associated with the dominant modes (i.e., the narrowband peak induced by the slat-cove shear layer in this case). Our next step is to use the APM to estimate the contributions of various modes to the far-field acoustic spectrum. The results will establish the connection between the dominant unsteady flow structures most responsible for the radiated noise and provide insight for future noise reduction efforts.

2 Methodologies

The details of the experimental setup can be found in [5]. In brief, the effective free field angle-of-attack is 5.5° , and the stowed-chord based Reynolds number is $Re_c = 1.71 \times 10^6$. The sampling rate of the time-resolved PIV measurements

¹This work was supported by NASA under contract 80NSSC18P3447

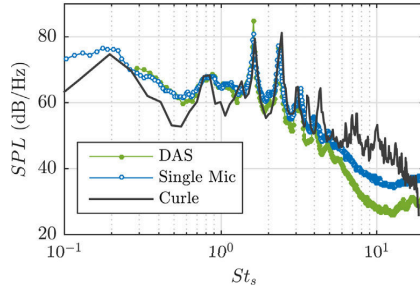


Figure 2: Acoustic spectra from Curle's projection [7]

is 11 kHz; note that this sampling rate can only temporally resolve the slat-cove shear layer but not the slat trailing edge shedding peak. Based on the force partitioning method (FPM) [10, 11], the APM can quantify the far-field dipole sounds generated by the local flow structures in the form of volume integrals [8]. Furthermore, the APM allows us to find which part of the aerodynamic body is more responsible for the generation of the far-field dipole sound by using the uni-potential functions. The APM will be applied to the time-resolved PIV data and the velocity fields obtained from the SPOD modes decomposition to identify the dominant flow structure generating the far-field dipole sound.

3 Results

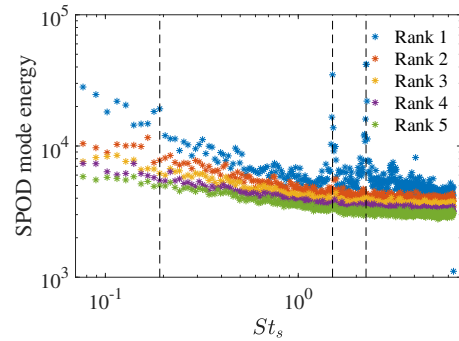
The SPOD results derived from the time-resolved PIV measurements are shown in Figure 3 [5]. Portion (a) shows the rank-1 mode is dominant, and part (b) shows the SPOD modes corresponding to the dominant peaks in the SPOD spectra. The contribution of these modes and their nonlinear interaction will be assessed using the APM.

4 Conclusion

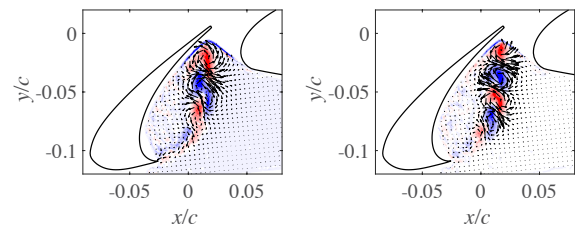
In a previous study, the aggregate far-field acoustics were estimated using linear stochastic estimation and then by solving the pressure Poisson's equation and using Curle's analogy [7]. In the full paper, we utilize the measured time-resolved velocity field combined with the APM to determine the source contributions to the far-field acoustics. The full paper will provide additional details of the proposed approach, results, and discussion. The current study will help us understand the generation of the narrowband noise due to the vortices in the slat-cove shear layer.

References

- [1] W. Dobrzynski. Almost 40 years of airframe noise research: What did we achieve? *Journal of Aircraft*, 47:353–367, 2010.
- [2] Meelan M Choudhari and David P Lockard. Assessment of Slat Noise Predictions for 30P30N High-Lift Configuration from BANC-III Workshop. In *21st AIAA/CEAS Aeroacoustics Conference*, Reston, Virginia, June 2015. American Institute of Aeronautics and Astronautics. AIAA Paper 2015-2844.
- [3] M. Roger and S. Perennes. Low-frequency noise sources in two-dimensional high-lift devices. In *6th Aeroacoustics Conference and*



(a) SPOD spectra



(b) SPOD modes. Left: $St_s = 1.51$; Right: $St_s = 2.25$

Figure 3: SPOD of vorticity field [5]

Exhibit. American Institute of Aeronautics and Astronautics, jun 2000. AIAA Paper 2000-1972.

- [4] K. Pascioni. *An Aeroacoustic Characterization of a Multi-Element High-Lift Airfoil*. PhD thesis, Florida State University, Tallahassee, FL, 2017.
- [5] Yang Zhang, Louis N. Cattafesta, Kyle A. Pascioni, Meelan M. Choudhari, David P. Lockard, Mehdi R. Khorrami, and Travis Turner. Slat noise control using a slat gap filler. In *AIAA AVIATION 2020 FORUM*, jun 2020. AIAA Paper 2020-2553.
- [6] Mehdi R Khorrami, Mert E Berkman, and Meelan Choudhari. Unsteady Flow Computations of a Slat with a Blunt Trailing Edge. *AIAA Journal*, 38(11):2050–2058, 2000.
- [7] Kyle A Pascioni and Louis N. Cattafesta. An aeroacoustic study of a leading-edge slat: Beamforming and far field estimation using near field quantities. *Journal of Sound and Vibration*, 429:224–244, September 2018.
- [8] Jung-Hee Seo, Karthik Menon, and Rajat Mittal. A method for partitioning the sources of aerodynamic loading noise in vortex dominated flows. *AIAA Journal*, in review, 2022.
- [9] Aaron Towne, Oliver T. Schmidt, and Tim Colonius. Spectral proper orthogonal decomposition and its relationship to dynamic mode decomposition and resolvent analysis. *Journal of Fluid Mechanics*, 847:821–867, may 2018.
- [10] Karthik Menon and Rajat Mittal. On the initiation and sustenance of flow-induced vibration of cylinders: insights from force partitioning. *Journal of Fluid Mechanics*, 907, 2021. Publisher: Cambridge University Press.
- [11] Karthik Menon and Rajat Mittal. Significance of the strain-dominated region around a vortex on induced aerodynamic loads. *Journal of Fluid Mechanics*, 918, 2021. Publisher: Cambridge University Press.

Geometrically Weighted Modal Decomposition of Morphing Bodies

Tso-Kang Wang^a and Kouros Shoele^{a*}

^a Department of Mechanical Engineering,

FAMU-FSU College of Engineering, Mechanical Engineering, Tallahassee, Florida 32310, USA¹

*Correspondence: *kshoele@eng.famu.fsu.edu*

1 Introduction

Modal analysis methods are tools used for highlighting energetically or dynamically important features of data. Different variants of modal analysis methods have been proposed in the fluid community to achieve different purposes, including but not limited to identifying underlying mechanisms of complex fluidic phenomena or constructing reduced-order models with linear representation. However, most of these methods are not geared toward dealing with submerged moving or deformable bodies, even though these situations are ubiquitous in fluid-structure interaction systems. Different approaches have been proposed to incorporate geometrical description into the formulation to instigate these systems. For example, Goza and Colonius [1] defined the combined energy of the fluid and a flapping flag based on their respective properties to construct POD modes for understanding how they interact. Liberge and Hamdouni [2] computed the POD modes of an oscillating cylinder by interpolating the time-variant grid to a fixed uniform grid to form a global velocity field. Tadmor et al. [3] leveraged the known periodicity of the system to partition the data and extract the physical harmonic modes. However, when the system involves deforming volumetric bodies, these methods face certain challenges. The representation of moving interfaces at the High Reynolds number requires an infinite number of modes. Moreover, the non-periodic dynamics of the system prevents the use of any prior knowledge.

To address the shortcomings of the existing modal decomposition methods, we proposed a novel method to introduce a conformal mapping technique into classic methods [4]. Conformal mapping techniques provide a systematic way of mapping moving interfaces to a fixed reference frame and extracting the geometric effect in the form of Jacobian. The temporally evolving Jacobian is used to weight the data, and with the angle-preserving nature of the conformal mapping, this weighting is proved to be energy-conserving when combined with the proper orthogonal decomposition (POD). Classic modal analysis methods, POD and dynamic mode decomposition (DMD), are performed in the transformed domain with a time-invariant grid. The acquired modes are now hybrid spatio-temporal modes that contain the information of the structural deformation-induced flow features. In this paper, we show how effective the so called

geometrically-weighted modal decomposition (GW-MD) is able to instigate the complex dynamics of the FSI systems with a submerged morphing body.

2 Results

To demonstrate the efficacy of GW-MD, we model a flapping EET high-lift airfoil [5] as an airfoil with an active trailing-edge flap attached. Figure 1(a) shows the physical model of the plunging EET airfoil, where a set of linear spring-damper systems models the aeroelastic oscillating effect. The active flap is given a sinusoidal oscillation at different frequencies and amplitudes to examine how the flap motion affects the foil's aeroelastic motion. The foil is fixed at an angle of attack $\text{AoA} = 10^\circ$ and the flap length is $l = 0.12L$. The sinusoidally oscillating flap angle relative to the mean chord is $\theta = \theta_0 + A \sin(\Omega t)$, where θ_0 and A are the mean angle and amplitude, respectively. Frequency of the flap oscillation is defined as $f = \Omega/2\pi$. Reynolds number ($Re = U_\infty L/\nu$) based on the chord length of the foil L is chosen to be 1000.

Figure 1(b) demonstrates the computational grid of the model in both physical domain and the transformed domain. DMD is performed in the transformed domain and mapped back to the physical domain. The computational grid is stretched logarithmically in the radial direction to capture fine details of flow close to the deforming/moving body where most of the diverse dynamics happen. The GW-DMD modes of two cases with small flap amplitude of $A = 1.5^\circ$ and $f = 0.1$ and $f = 0.9$ are shown in Fig. 1(c) and (d), respectively. It is noted that although not shown here, the two cases with different flap frequencies have a very similar heaving response. In both cases, the foil features a high-frequency small amplitude oscillation on top of a low frequency, large amplitude heaving behavior. Both flows have very similar wake distributions. The question naturally arises: what role does the flap play in the plunging motion? The GW-DMD modes gave an affirmative response. We can see these two cases share exactly the same modes 1, 2 and 4 and their corresponding frequencies. These modes all have the frequencies of the mean mode or the superharmonics of the natural frequency ($St = 0.96$ from the uncontrolled, freely heaving case). The only difference lies in mode 3, which has the frequency of the flap motion in the respective case. In the $f = 0.1$ case, we that the flow fluctuation is confined near the body, and the non-convective flow

¹This work was supported by Defense Advanced Research Projects Agency under Grant number D19AP00035.

pattern indicates that the role of this mode is not inducing any flow transportation. Instead, the low frequency movement of the flap changes the apparent AoA of the airfoil and generate varied lift force at different posture. This is why we see the low-frequency, large-amplitude plunging motion. On the other hand, in the $f = 0.9$ case, we see that the mode 3 now has an extended wake with the same frequency as the flap oscillation. When the flap moves much faster, the larger pressure gradient induces a vortex every time the flap goes through the down sweep motion. This wake interferes with the vortices shedding from the leading edge due to the positive AoA ($St = 0.96$) and creates the low frequency plunging motion at the frequency of the two mechanisms' difference ($f = 0.06$). Although these cases have very similar flow and heaving responses, they are, in fact, driven by very different mechanisms. The GW-DMD can extract this important information for future controller design.

3 Conclusion

This research provides a technique for identification of the most critical flow features in a reconfigurable system. We showcase how the proposed geometrically weighted process combined with the classic modal analysis method can pinpoint the key dynamics from the two examples. It should be emphasized that without proper geometrical description, the moving interfaces would be difficult to represent. Conformal and Pseudo-conformal mappings with properly encoded properties provide an optimal way to ensure energy conservation and conveniently a template for easy implementation. We are now working on expanding this idea to more complex 3-D conditions and employing more flexible geometrical descriptions such as discrete conformal mapping that preserves the angle of the mesh while remaining Laplacian conservative [6]. Another direction to this project is extending the idea to multiply-connected domains, common in nature (e.g. bird or fish school) and engineering solutions (e.g. wind farm or plane formation). The ultimate goal is to create a robust and adaptable modal analysis framework for all FSI systems with submerged deforming or moving bodies. As demonstrated with a simple case, the acquired modes could be essential for understanding the underlying physics in these complex systems. The modes can also construct reduced-order models crucial to flow control implementations in these conditions.

References

- [1] Goza, Andres and Colonius, Tim Modal decomposition of fluid-structure interaction with application to flag flapping. *Journal of Fluids and Structures*, 81 (2018): 728-737.
- [2] Liberge, Erwan and Hamdouni, Aziz. Reduced order modelling method via proper orthogonal decomposition (POD) for flow around an oscillating cylinder. *Journal of Fluids and Structures*, 26.2 (2010): 292-311.
- [3] Tadmor, Gilead and Bissex, Daniel and Noack, Bernd and Morzynski, Marek and Colonius, Tim and Taira, Kunihiko Temporal-harmonic specific POD mode extraction *4th Flow Control Conference*, p. 4190 (2008).
- [4] Wang, Tso-Kang and Shoele, Kourosh Geometrically weighted modal decomposition techniques *Journal of Fluid Mechanics*, 911 (2011).

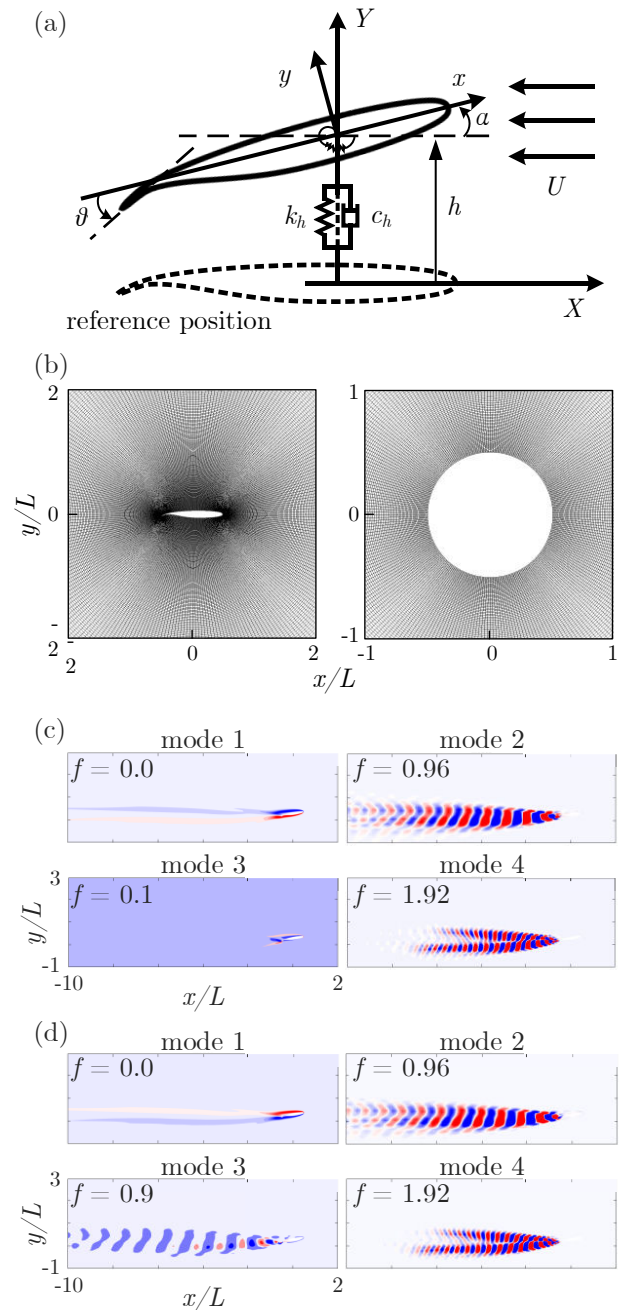


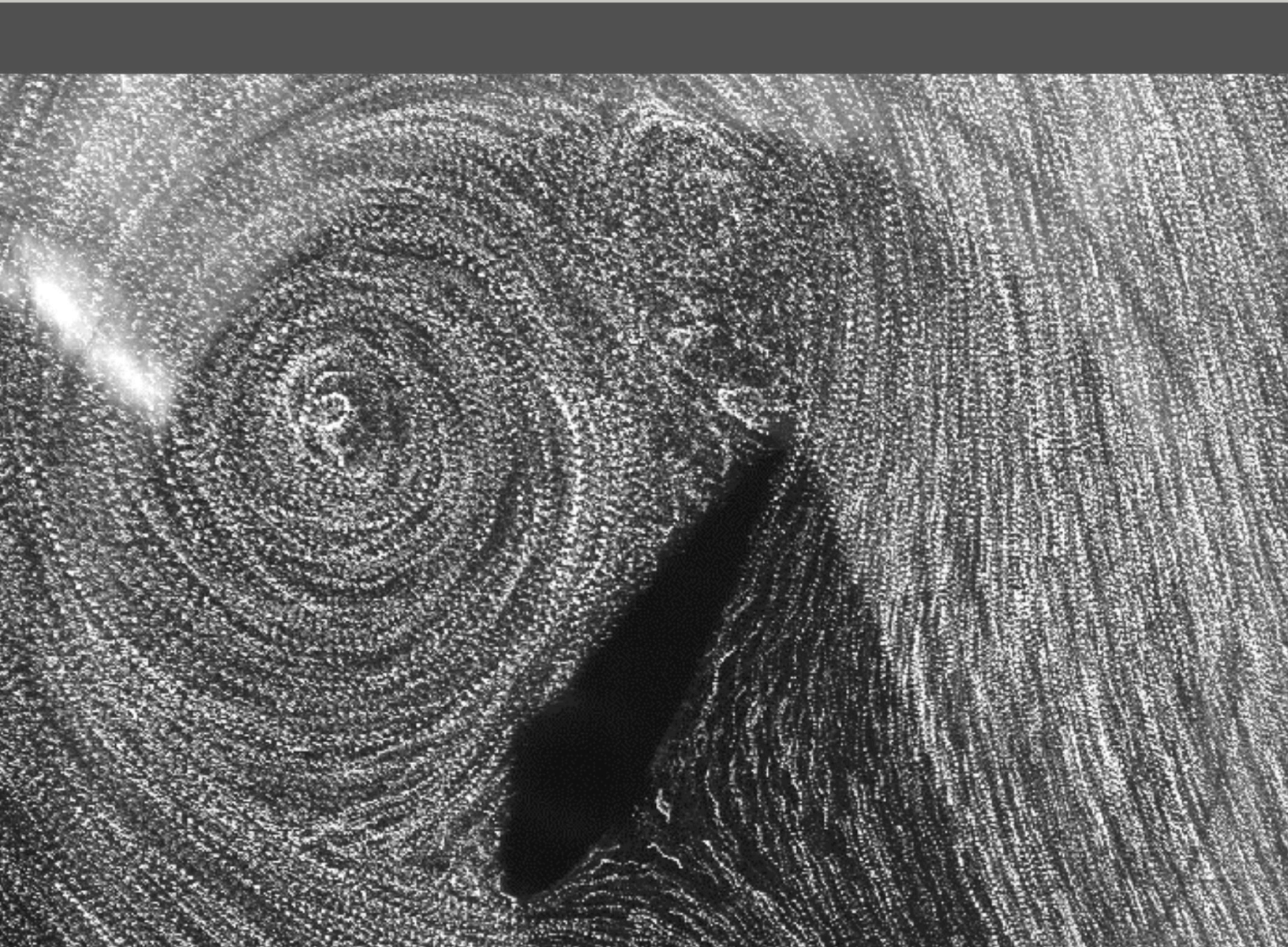
Figure 1: The (a) EET high-lift foil model, (b) physical and transformed grid of it and the leading GW-DMD modes for flap frequency (c) $f = 0.1$ and (d) $f = 0.9$.

- [5] Morgan Jr, Harry L Experimental test results of energy efficient transport (EET) high-lift airfoil in langley low-turbulence pressure tunnel NASA (2002).

- [6] Li, Hongdong and Hartley, Richard Conformal spherical representation of 3D genus-zero meshes *Pattern recognition*, 40.10 (2007): 2742-2753.

Session B

Stall



Effects of flap-vortex interactions on the lift of an airfoil mounted with a passively deployable flap

Nirmal J. Nair^a and Andres Goza^{a*}

^a University of Illinois at Urbana-Champaign, Aerospace Engineering, Urbana, USA¹

*Correspondence: agoza@illinois.edu

1 Introduction

Birds have a remarkable ability to perform complex maneuvers at post-stall angles of attack such as landing, take-off, hovering and perching. The passive deployment of self-actuating covert feathers in response to unsteady flow separation while performing such maneuvers provides a passive, adaptive flow control paradigm for these aerodynamic capabilities. Most studies involving covert-feathers-inspired passive flow control have modeled the feathers as a rigidly attached or freely moving flap on a wing. A flap mounted via a torsional spring as shown in Fig. 1 enables a configuration more emblematic of the finite stiffness associated with the covert-feather dynamics [1, 2, 3]. In this work, we numerically investigate this airfoil-flap system at a low Reynolds number of $Re = 1,000$ and angle of attack of 20° by performing high-fidelity nonlinear simulations. A wide range of non-dimensional mass ratio of the flap and stiffness of the spring varying over several orders of magnitude as well as multiple flap locations are considered.

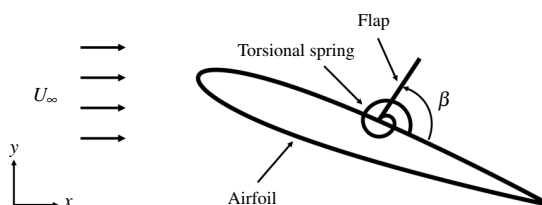


Figure 1: Schematic of the airfoil-flap system.

2 Results

In this section, we briefly describe some of the important results of the numerical study. More details on the problem setup and on related results can be found in Nair and Goza [2] (the authors are also planning a manuscript submission on this topic, and the DisCoVor presentation will be a synthesis and expansion of these related efforts).

A parametric study is performed by varying the stiffness of the hinge, mass of the flap and location of the hinge. The results of this study are presented in Fig. 2 only for

¹This work was supported by the National Science Foundation under grant number CBET 20-29028

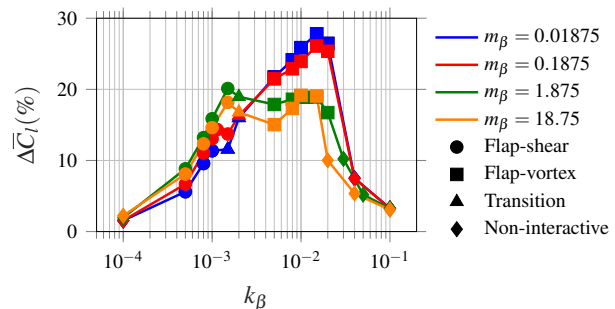


Figure 2: Performance plots showing percentage change in mean lift for the flap at 60% location. The marker symbols denote the identified flow regimes.

the flap located at 60% chord from the leading edge for brevity. Here, improvements in mean lift of the airfoil with a torsionally mounted flap compared to the flap-less airfoil case in percentage, $\Delta \bar{C}_l$, are plotted against stiffness for various mass ratios. Lift improvements as high as 27% are attained using a passively deployable flap. Two performance peaks are observed at $k_\beta \approx 0.0015$ and $k_\beta \approx 0.015$.

Firstly, we discuss the effect of stiffness on performance. One of the dominant effects of stiffness is to set the mean deflection angle in a manner largely agnostic to the mass ratio. This mean deflection angle is the primary parameter in setting the qualitative flow regimes. These flow regimes are identified by using a k-means clustering algorithm which utilizes two meaningfully chosen length scales representative of the shear layer separating the bulk and near-body flow dynamics and the proximity of the flap to shedding of the leading edge vortex. The results of this flow classification procedure are indicated by the markers in Fig. 2. It can be observed from Fig. 2 that the cases with stiffness in the vicinity of $k_\beta = 0.0015$ belong to the what we term the *flap-shear interaction regime*. To visualize the associated flap configuration, a vorticity contour for $m_\beta = 1.875$ and $k_\beta = 0.0015$ is plotted in Fig. 3a. It can be seen that the relatively large flap deflection is such that the flap tip lies in close vicinity of the high momentum shear layer. All parameters classified within this regime share the prominently (but not overly) deployed flap that has a mean deployment near the shear layer separating the bulk and near-body flow, which underscores the chosen terminology. On the other hand, the

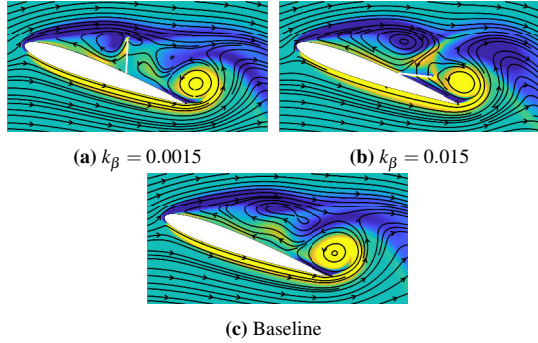


Figure 3: Vorticity contours demonstrating flap configurations and TEV induced reverse flow in the (a) flap-shear and (b) flap-vortex interaction regimes for $m_\beta = 1.875$ and 60% location and compared with the (c) baseline case.

cases around $k_\beta = 0.015$, which correspond to the second peak, are assigned by the k-means algorithm to the *flap-vortex interaction regime*. The associated vorticity contour for $m_\beta = 1.875$ and $k_\beta = 0.015$ is plotted in Fig. 3b. The relatively low flap deflection is such that the flap strongly interacts with the vortex-shedding process.

The significant performance gains in these regimes are attributed to the “pressure dam” effect, where a low pressure zone is maintained upstream of the flap due to the blockade of trailing edge vortex (TEV) induced reverse flow. For visualization, a vorticity contour for the flap-less baseline case is plotted in Fig. 3c, where multiple upstream moving streamlines from the trailing to the leading edge can be observed in the presence of the TEV. On the other hand, the flap-shear and flap-vortex cases in Fig. 3a and 3b, respectively, have significantly reduced upstream propagating streamlines. In the flap-shear regime, this blockade is achieved solely by the significantly extended flap towards the shear layer, while in the flap-vortex regime, the flap and the leading edge vortex work in conjunction to block the reverse flow.

Finally, we discuss the effect of inertia or mass ratio on performance. One of the dominant effects of mass ratio is to set the amplitude and phase of flap oscillations. For demonstration, flap deflections in one time period of vortex shedding cycle for $k_\beta = 0.015$ and various mass ratios are plotted in Fig. 4. It can be observed that the lowest mass flaps oscillate with largest amplitude which decreases monotonically with increasing mass. For a very large mass ratio of $m_\beta = 18.75$, the flap response is quasi-static. The effect of the time-dependent flap dynamics encoded in mass ratio is not uniformly beneficial or detrimental for performance. For example from Fig. 2, for the cases in the flap-shear interaction regime near $k_\beta = 0.0015$, the lighter flaps perform more poorly than the heavier ones, with optimal performance provided by $m_\beta = 1.875$ flap. In contrast, for the cases in the flap-vortex interaction regime near $k_\beta = 0.015$, the lighter flaps provide larger mean lift improvements.

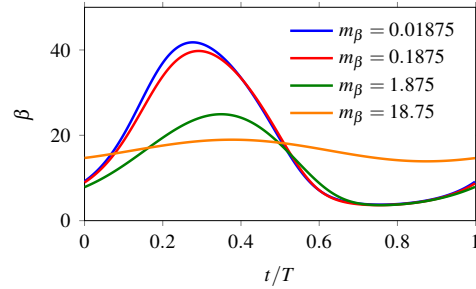


Figure 4: Flap deflection in one time period of the vortex shedding cycle for 60% location and $k_\beta = 0.015$.

3 Conclusions and future work for the presentation

In this manuscript, we numerically modeled covert feathers as a passively deployable torsional flap mounted on the suction surface of a stationary airfoil and investigated the flow physics of this airfoil-flap-flow system via high-fidelity 2D simulations. The primary role of stiffness was to set a mean flap deflection angle which in turn dictated the aerodynamic performance trends while flap inertia had a secondary role in modifying these trends by means of inducing time-dependent dynamics. Two flow regimes that provided enhanced performance, identified using a k-means flow classification algorithm, were the flap-shear and flap-vortex interaction regimes. To be discussed in further detail at the Colloquium, the stiffness-dependent mean flap deflection and inertia-dependent amplitude and phase of flap oscillations altered the dominant flow characteristics in both the regimes. Of special interest for performance benefits are the flap parameters that enhance the lift-conductive leading-edge vortex while weakening the trailing-edge vortex and associated detrimental effect of upstream propagation of reverse flow. These parameters also yielded a temporal synchronization of flap oscillations with the vortex shedding process in both regimes.

References

- [1] Marco E Rosti, Mohammad Omidyeganeh, and Alfredo Pinelli. Passive control of the flow around unsteady aerofoils using a self-activated deployable flap. *Journal of Turbulence*, 19(3):204–228, 2018.
- [2] Nirmal J. Nair and Andres Goza. Effects of torsional stiffness and inertia on a passively deployable flap for aerodynamic lift enhancement. In *AIAA SCITECH 2022 Forum*, page 1968, 2022.
- [3] Nirmal J. Nair, Zoey Flynn, and Andres Goza. Numerical study of multiple bio-inspired torsionally hinged flaps for passive flow control. *Fluids*, 7(2):44, 2022.

Dynamic stall at high Reynolds numbers

Claudia E. Brunner^{a*}, Janik Kiefer^b, Martin O. L. Hansen^b and Marcus Hultmark^a

^a Department of Mechanical and Aerospace Engineering, Princeton University, Princeton, NJ, USA¹

^b Department of Wind Energy, Technical University of Denmark, Kgs. Lyngby, Denmark

*Correspondence: cbrunner@princeton.edu

1 Introduction

Dynamic stall occurs in a variety of applications that span a wide range of Reynolds numbers, from biological locomotion to wind turbines and helicopters. Here, we present insights into dynamic stall at high Reynolds numbers gained from a series of experiments conducted in the High Reynolds number Test Facility at Princeton University. This facility uses pressurized air to achieve high Reynolds numbers at low velocities and therefore without compressibility effects. Furthermore, at low velocities the time scales can be kept relatively large, allowing for investigations of highly dynamic events at high Reynolds numbers, which are extremely challenging to conduct in conventional facilities. Aside from the Reynolds number Re_c , dynamic stall is governed by the reduced frequency k and the kinematics of the motion. The pressurized facility was used to cover a wide parameter space including a Reynolds number range of $0.5 \times 10^6 \leq Re_c \leq 5.5 \times 10^6$ and a reduced frequency range of $0.01 \leq k \leq 0.40$. The effects of reduced frequency, Reynolds number and the kinematics of the motion on the dynamic stall process were investigated.

2 Experimental setup

The experiments were conducted in the High Reynolds number Test Facility (HRTF), a closed-loop high-pressure wind tunnel located at the Gas Dynamics Laboratory at Princeton University. The flow facility uses dry air as a working fluid, compressed to static pressures of up to 24 MPa. A NACA0021 airfoil profile with a chord length of $c = 0.17$ m and an aspect ratio of $AR = 1.5$ was employed in the experiments. The time-resolved data were derived from surface pressure measurements acquired by 32 temperature-compensated differential pressure sensors. In all test cases, the dynamic stall process was repeated at least 150 times and then phase averaged to yield the results that will be presented.

3 Results

The results that will be presented are largely based on [1]. The overall development of dynamic stall on a moderately

¹This work was supported by the National Science Foundation of the United States under grant number CBET 1652583 and by the United States Department of Defense through an National Defense Science and Engineering Graduate Fellowship.

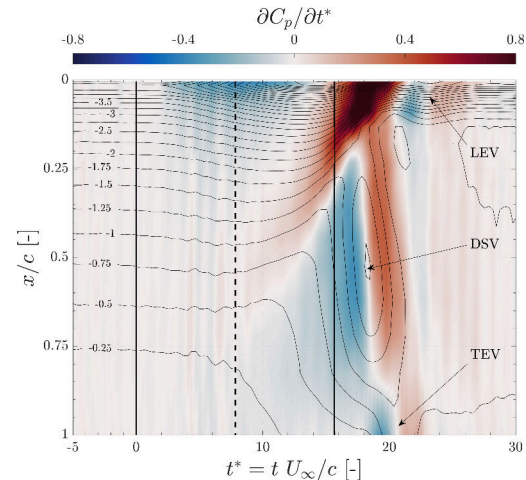


Figure 1: Temporal development of the suction side pressure distribution during an upward pitch motion with $k = 0.10$, $\bar{\alpha} = 24^\circ$, $\hat{\alpha} = 5^\circ$ and $Re_c = 3.0 \times 10^6$. The time span of $0 \leq t^* \leq 15.7$ indicates when the airfoil is in motion. Isolines indicate constant C_p -levels.

thick airfoil at high Reynolds numbers will be discussed, as well as the effects of reduced frequency, Reynolds number and pitching kinematics. The temporal scaling of the earlier and later stages of the dynamic stall process will be elucidated.

All test cases exhibited gradual trailing-edge stall, in which the dynamic stall vortex forms approximately at mid-chord. The temporal development of the suction-side pressure distribution of a baseline test case is shown in figure 1. Here, C_p -levels are indicated by black isolines while the vertical black solid lines mark the start and finish of the pitching maneuver and the black dashed line indicates the passing of the static stall angle. The plot is additionally colored to illustrate the temporal change of the pressure distribution $\partial C_p / \partial t^*$. Blue colors reveal an increase in suction and red colors a loss of suction over time. The time histories of surface pressure as well as lift, drag and moment histories will be presented to provide insight into the parameters and time scales governing dynamic stall.

The angles over which the airfoil is pitched with respect to the Reynolds-number dependent static stall angle are found to define the temporal development of the stall process. The

time until stall onset is characterized by a power law, where a final angle just above the static stall angle results in a drastically prolonged stall delay. Furthermore, the results indicate that vortex-induced loads scale linearly with the angle of attack at which the leading-edge suction peak collapses. In test cases where the final angle of attack is reached before the dynamic stall vortex detaches from the airfoil, the reduced frequency does not sufficiently characterize the dynamic stall process. Beyond a critical reduced frequency both the forces on the airfoil and the vortex evolution become reduced frequency independent and instead depend on the geometry of the motion and the convective time scale, respectively. Overall, the characteristics of vortex evolution induced by dynamic stall show remarkable similarities to the framework of optimal vortex formation reported in [2].

References

- [1] Kiefer, J., Brunner, C. E., Hansen, M. O. L. and Hultmark, M. Dynamic stall at high Reynolds numbers induced by ramp-type pitching motions. *J. Fluid Mech.* In press.
- [2] Gharib, M. and Rambod, E. and Shariff, K. A universal time scale for vortex ring formation. *J. Fluid Mech.* 360:121–140, 1998.

Dynamics of Laminar Separation Bubbles in an Unsteady Freestream

Connor Toppings^a and Serhiy Yarusevych^{a*}

^a University of Waterloo, Department of Mechanical and Mechatronics Engineering, Waterloo, Canada¹

*Correspondence: *syarus@uwaterloo.ca*

1 Introduction

Laminar boundary layers may persist over a substantial portion of a lifting surface at low chord Reynolds numbers ($Re_c < 5 \times 10^5$) [1] and are prone to separation. As a consequence of boundary layer separation and the subsequent increase in drag, airfoil performance degrades significantly at low Reynolds numbers [2]. When a laminar boundary layer separates, transition from laminar to turbulent flow usually occurs in the highly unstable separated laminar shear layer. Transition substantially increases the rate of wall-normal momentum transfer, which may lead to reattachment in a time-average sense if the Reynolds number is sufficiently large and the adverse pressure gradient is not too severe [3]. Reattachment notably improves lifting surface performance relative to the case of entirely separated flow. The thin region of recirculating flow between the locations of laminar separation and turbulent reattachment is known as a laminar separation bubble (LSB) [4]. Transition in LSBs is characterised by the amplification of disturbances in the separated laminar shear layer through the Kelvin-Helmholtz instability mechanism, which leads to quasi-periodic vortex shedding [5]. Deformations of the shear layer roll-up vortices eventually lead to vortex breakup and the development of a turbulent boundary layer downstream of the mean reattachment location. LSBs are extremely sensitive to disturbances, and small variations in Reynolds number or angle of attack may lead to substantial changes in LSB structure, transition dynamics, and associated aerodynamic loads [6, 3]. Bubble bursting occurs when a decrease in Reynolds number or increase in adverse pressure gradient causes the separated flow to fail to reattach, leading to a sudden loss of lift and increase in drag [3].

Although the dynamics of LSB transition has been studied extensively in steady flows [4, 3, 6, 5], unsteady effects play a major role in many practical situations where LSBs occur, such as on the wings and control surfaces of small unmanned aircraft. Prior studies have observed that the locations of separation, transition, and reattachment occur farther downstream during freestream acceleration than in a steady freestream of equal velocity. Conversely, these locations occur farther upstream during freestream deceleration [7]. However, the LSB dynamics responsible for

these changes has received little attention. The objective of this study is to elucidate the role of coherent structures in transient LSB dynamics during a controlled change in freestream velocity between two steady states.

2 Experimental Methods

An experimental investigation is conducted using a NACA 0018 airfoil model in the recirculating wind tunnel at the University of Waterloo. The airfoil has a chord length of 200 mm, and spans the entire 0.61 m width of the square test section. The motor that drives the wind tunnel fan is powered by a variable frequency drive circuit that enables controlled variations of the freestream velocity in the test section. Within the chord Reynolds number range of $0.4 \times 10^5 < Re_c < 2.5 \times 10^5$, the turbulence intensity measured in the centre of the empty test section using a hotwire anemometer is less than 0.1%. Measurements at a steady freestream velocity are used as a baseline for comparing LSB behaviour under time varying freestream velocities. Mean surface pressure measurements are obtained using an array of 65 surface pressure taps distributed over the suction and pressure surfaces of the airfoil model. Fluctuating surface pressure measurements are obtained using an array of Panasonic WM-62C condenser microphones located within the airfoil model. The flowfield of the LSB on the suction surface of the airfoil is quantitatively measured using two-component planar particle image velocimetry (PIV). The flow is seeded with water-glycol fog particles, which are illuminated with a Photonics DM20-527 Nd:YLF pulsed laser. Image acquisition and processing are performed using the LaVision DaVis 10 software, with which velocity fields are calculated from the particle images using iterative multi-pass cross-correlation.

3 Results

3.1 Steady-State Flow Development

Vortex shedding in the LSB forming on the airfoil model in steady freestream conditions at an angle of attack of $\alpha = 4^\circ$ and a chord Reynolds number of $Re_c = 1.25 \times 10^5$ is illustrated by the time-resolved snapshots of spanwise vorticity presented in fig. 1. Vortex roll-up occurs in the separated laminar shear layer near $x/c = 0.52$, downstream of which the vortices begin to break up in the reattaching turbulent boundary layer.

¹The authors gratefully acknowledge the Natural Sciences and Engineering Research Council of Canada for funding this work.

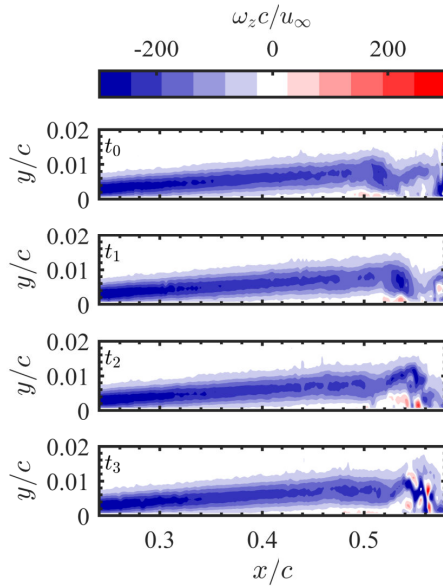


Figure 1: Vortex shedding from steady state LSB at $Re_c = 1.25 \times 10^5$ and $\alpha = 4^\circ$. Frame separation is 0.26 ms

The dependence of mean surface pressure on chord Reynolds number is illustrated in fig. 2, which presents measurements for three different Reynolds numbers in steady freestream conditions. The presence of a pressure plateau in the region of adverse pressure gradient indicates the presence of a laminar separation bubble on the suction surface. The rapid pressure recovery at the downstream end of the pressure plateau denotes the location of transition in the separated shear layer. The transition location occurs farther upstream for higher chord Reynolds numbers in quasi-steady conditions. Also, the pressure plateau becomes less pronounced at higher chord Reynolds numbers, implying reduced LSB thickness.

3.2 Unsteady Flow Development (To be Included in full Presentation)

The observed differences in LSB mean surface pressure distributions between steady flows at different chord Reynolds numbers highlight the changes in mean LSB size and location that occur as airfoil operating conditions change. Concurrently, the vortex shedding wavenumber and frequency also change [8]. Unsteady LSB dynamics will be investigated during freestream velocity changes between the steady state conditions presented in fig. 2. Additionally, the dynamics of bubble bursting and formation processes will be studied by considering decelerations and accelerations to and from Reynolds numbers below the bubble bursting Reynolds number. The transient effects of freestream accelerations and decelerations on shear layer vortex shedding frequencies and wavenumbers will be investigated for various acceleration rates, up to the wind tunnel's maximum acceleration of 4.0 m/s^2 . PIV measurements will be used to ob-

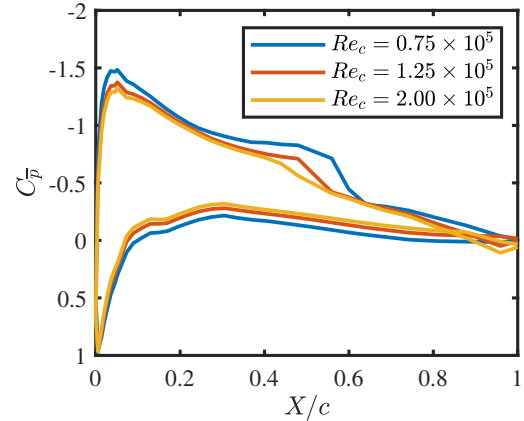


Figure 2: Reynolds number dependence of surface pressure distribution on NACA 0018 airfoil at steady state for an angle of attack of $\alpha = 4^\circ$.

serve structural changes to the LSB flowfield, and phase averaging will be employed to describe the evolution of the mean and fluctuating velocity fields during freestream velocity changes. Fluctuating surface pressure measurements will enable a time-resolved characterisation of the most unstable disturbance frequencies in the separated shear layer. The results will provide new insight into LSB dynamics under conditions relevant to the unsteady flows found in real-world applications of low Reynolds number lifting surfaces.

References

- [1] B H Carmichael. *Low Reynolds Number Airfoil Survey*. Tech. rep. NASA CR-165803. Capistrano Beach, CA: Low Energy Transportation Systems, Oct. 1981.
- [2] P B S Lissaman. "Low-Reynolds-Number Airfoils". In: *Annual Review of Fluid Mechanics* 15.1 (Jan. 1983), pp. 223–239. DOI: 10.1146/annurev.fl.15.010183.001255.
- [3] M Gaster. *The Structure and Behaviour of Laminar Separation Bubbles*. Tech. rep. Aeronautical Research Council Reports and Memoranda 3595. London, 1967, pp. 1–33.
- [4] Itiro Tani. "Low-speed flows involving bubble separations". In: *Progress in Aerospace Sciences* 5 (Jan. 1964), pp. 70–103. DOI: 10.1016/0376-0421(64)90004-1.
- [5] Sourabh S. Diwan and O. N. Ramesh. "On the origin of the inflectional instability of a laminar separation bubble". In: *Journal of Fluid Mechanics* 629 (June 2009), pp. 263–298. DOI: 10.1017/S002211200900634X.
- [6] Michael Ol et al. "Comparison of Laminar Separation Bubble Measurements on a Low Reynolds Number Airfoil in Three Facilities". In: *35th AIAA Fluid Dynamics Conference and Exhibit*. Reston, Virginia: American Institute of Aeronautics and Astronautics, June 2005. DOI: 10.2514/6.2005-5149.
- [7] R. H. Ellsworth and Thomas J. Mueller. "Airfoil Boundary Layer Measurements at Low Re in an Accelerating Flow from a Nonzero Velocity". In: *Experiments in Fluids* 11.6 (Oct. 1991), pp. 368–374. DOI: 10.1007/BF00211791.
- [8] Andrew R. Lambert and Serhiy Yarusyevych. "Characterization of vortex dynamics in a laminar separation bubble". In: *AIAA Journal* 55.8 (2017), pp. 2664–2675. DOI: 10.2514/1.J055501.

Vortex Dynamics of a Separated Wing in Streamwise Gusts

D. Gloutak, K. Jansen, and J. Farnsworth*

University of Colorado Boulder, Aerospace Engineering, Boulder, Colorado, USA¹

*Correspondence: *John.Farnsworth@colorado.edu*

1 Introduction

Streamwise gusts potentially threaten the efficiency and stability of aerodynamic systems operating within the atmospheric boundary layer. Existing literature primarily examines two-dimensional airfoil performance in high frequency, large amplitude gusts frequently encountered in rotorcraft environments [1–3]. The current study investigates the effect of streamwise gusts on a finite-span wing at reduced frequencies and amplitudes more similar to gusts encountered within the atmospheric boundary layer.

Experiments were conducted within the unsteady open-return, blow-down wind tunnel facility at the University of Colorado Boulder [4]. Louvers dynamically changed the wind tunnel inlet area to generate time-varying streamwise velocities $u(t)$ within the test section that generally followed a sinusoidal profile: $u(t) = \bar{u}(1 + \sigma \sin(2\pi ft))$. Streamwise gusts generated within the test section were spatially uniform and therefore global, or purely unsteady, gusts.

A NACA 0015 wing with a semi-span aspect ratio of $sAR = 3$ and a chord length of $c = 0.1524\text{m}$ was placed within the test section at a post-stall angle of attack of $\alpha = 13^\circ$. Streamwise gusts were generated with a time-averaged chord-based Reynolds Number of $Re_c = 1.0 \times 10^5$ at a reduced frequency of $k = 0.12$. Synchronized high speed particle image velocimetry (PIV) and surface pressure measurements were recorded at the wing midspan.

2 Results

The following examines the aerodynamic response of a separated wing during the decelerating and accelerating portions of a streamwise gusting cycle. The phase-averaged velocity of the imposed streamwise gust is plotted in Fig. 1. The phase-averaged (solid line) sectional lift coefficient, $c_l = 2L'/\rho u^2 c$, and its standard deviation (dashed line) are plotted in Fig. 2, where sectional lift, L' , is integrated from the surface pressure measurements.

As seen in Fig. 2, the phase-averaged c_l is rather constant throughout the entire cycle. However, the standard deviation

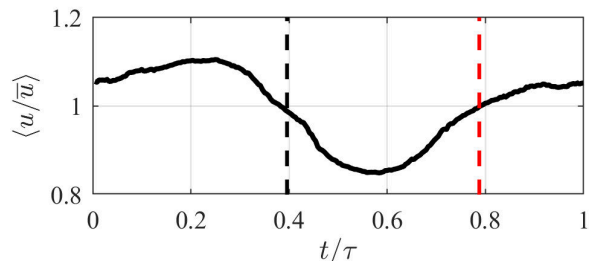


Figure 1: Phase-averaged velocity versus normalized time.

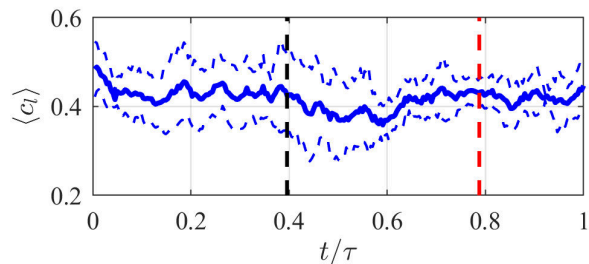


Figure 2: Phase-averaged lift coefficient versus normalized time, with plus/minus one standard deviation denoted.

of c_l indicates larger variations occur during the velocity deceleration, near the black dashed line, than during the velocity acceleration, near the red dashed line. The cycle-to-cycle variations of instantaneous c_l can be attributed to the vortex dynamics at play over the separated wing.

Velocity vector fields captured during deceleration and acceleration are shown in Fig. 3 and Fig. 4, respectively. Note that these are instantaneous snapshots of the velocity field extracted from a single cycle at the points indicated in Fig. 1. Surface plots are colored with the velocity magnitude, $|u|$, and overlaid with velocity vectors. Isolated vortices were identified using Q-criterion and are indicated with a circle, centred at the peak in the Q-field, that scales in size with vortex circulation, Γ_i . Vortices with positive (counter-clockwise) circulation, $\Gamma_i > 0$, are indicated by a white circle, and those with a negative (clockwise) circulation, $\Gamma_i < 0$, are indicated by a black circle.

For an airfoil in steady flow, lift is proportional to both the velocity and the bound circulation, Γ_w , over the wing by the Kutta-Joukowski theorem: $L' = -\rho u \Gamma_w$, where $\Gamma_w < 0$. Rearranging this equation and substituting in lift coefficient

¹This material is based upon work supported by the Air Force Office of Scientific Research under award number FA9550-18-1-0311. Support for the construction and testing of the dynamic louver system is acknowledged from the 2017 Innovative Seed Grant Program from the Research & Innovation Office at the University of Colorado Boulder.

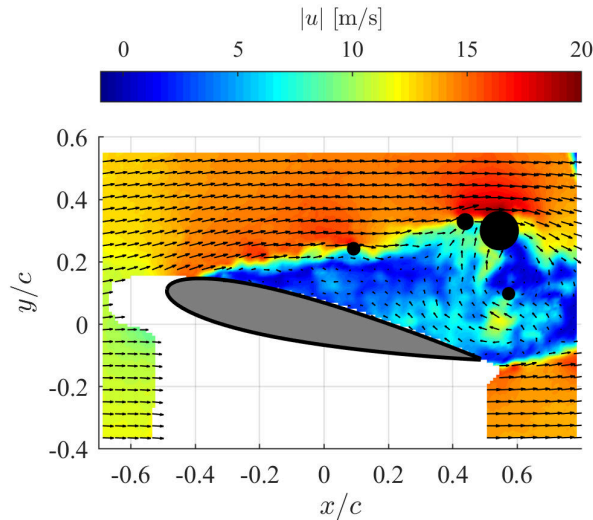


Figure 3: Instantaneous velocity during decelerating flow.

it is found that: $\Gamma_w = -1/2c_luc$. For the conditions considered in this study, Γ_w is dependent only on velocity since the average c_l remains constant throughout the streamwise gust cycle as demonstrated in Fig. 2. Therefore, $|\Gamma_w|$ is directly proportional to the instantaneous free-stream velocity.

However, the total circulation within the fluid domain must be conserved over time via Kelvin's circulation theorem: $\partial\Gamma/\partial t = 0$. As the bound circulation changes with velocity, excess circulation must be shed from the wing. For the decelerating flow, $|\Gamma_w|$ decreases and excess circulation is shed from the wing through vortical structure with $\Gamma_i < 0$. For the accelerating flow, $|\Gamma_w|$ increases and a vortex with $\Gamma_i > 0$ is shed from the trailing edge as indicated in Fig. 4.

The behavior of the vortices formed near the wing leading edge are governed by their interactions with 1) the wing surface, 2) neighbouring vortices, and 3) the bound circulation within the wing. Specifically, the surface impacts can be explained and modelled through the method of images. Additionally, vortical structures, including shed vortices and the bound circulation, with larger circulation will influence their surroundings to a greater degree than those with lesser circulation.

During deceleration, a vortical structure with $\Gamma_i < 0$ is generated in the separating shear layer near the leading edge to counteract the decrease in $|\Gamma_w|$. As the vortex advects over the wing surface, its motion is slowed, relative to the local free-stream velocity, due to the action of its image pair. Subsequent vortices generated near the leading edge pair and induce additional clockwise oriented rotation on each other, pushing the upstream vortices away from the surface and the downstream vortices closer to it. Subsequent vortices coalesce and form stronger vortices with an enlarged area. As these strong vortical structures advect over the surface and shed from the wing, the lift first increases and then

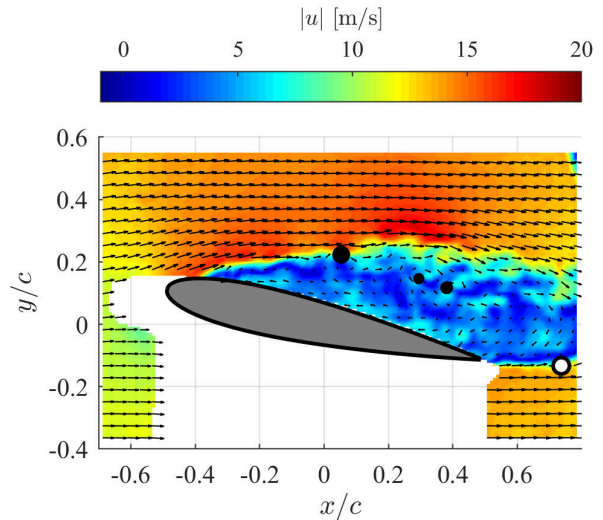


Figure 4: Instantaneous velocity during accelerating flow.

decreases dramatically resulting in the large fluctuations in c_l seen during deceleration phase in Fig. 2.

During acceleration, a vortical structure with $\Gamma_i > 0$ is generated near the trailing edge to counteract the increase in $|\Gamma_w|$. The vortices generated near the leading edge with $\Gamma_i < 0$ are comparatively weak in strength, and thus their behaviour is largely unaffected by interactions with the surface and each other. Their advective velocity is primarily influenced by the trailing edge vortices and by the increasing $|\Gamma_w|$, both of which induce flow vertically downward towards the trailing edge. Furthermore, the vortices formed near the leading edge are less likely to coalesce and therefore produce relatively smaller fluctuations in the lift, as indicated by the smaller standard deviations in c_l , during the accelerating flow as shown in Fig. 2.

3 Conclusion

Spatially uniform streamwise gusts influence the aerodynamic performance of a separated, finite-span wing. Freestream acceleration dictates the behavior of vortical structures generated near the leading edge including their circulation strength, degree of interaction, and trajectory. Fluctuations in the integrated lift coefficient are observed to grow during flow deceleration as larger, stronger vortices formed near the leading edge advect over the wing and shed into the wake.

References

- [1] R. Fernie and H. Babinsky. NACA 0012 aerofoil in an oscillating transonic free-stream. *40th AIAA Aerospace Sciences Meeting*, 2002-115.
- [2] C. Jensen, et al. Unsteady Compressible Flow on a NACA 0021 Airfoil. *49th AIAA Aerospace Sciences Meeting*, 2011-670.
- [3] K. Granlund, et al. Streamwise Oscillation of Airfoils into Reverse Flow. *AIAA Journal*, 54:1-9, 2016.
- [4] J Farnsworth, et al. Design and qualification of an unsteady low-speed wind tunnel with an upstream louver system. *Experiments In Fluids*, 61(8):0723–4864, 2020.

Harnessing of Leading-Edge Vortices

I. Gursul, Z. Zhang, J. Tan, Z. Wang
 University of Bath, United Kingdom
 Correspondence: i.a.gursul@bath.ac.uk

1 Motivation

It is well known that Leading-Edge Vortices (LEVs) increase the mean lift on flying insects [1]. LEVs are also responsible for increasing the mean lift for unsteady freestream [2] and periodic plunging motion [3]. In both cases the mean lift enhancement is strongly frequency dependent in the post-stall regime, revealing similar optimal frequency range. Active flow control studies also show similar optimal frequency range for the post-stall flow [5,6]. Wu *et al.* [6] were the first to explain that the optimal range corresponds to the natural vortex shedding frequency and its harmonics of the baseline flow at the post-stall angles of attack.

In this research, we explore potential methods to harness the LEVs to enhance the mean lift at the post-stall angles of attack. The most obvious case is to exploit unsteady external flows such as free shear layers (wakes, jets, and mixing layers). Examples of the shear flows in aerodynamics include the tandem wing configurations, novel formation flight configurations, separated flows from other objects such as buildings, and engine jets. We chose unsteady wakes as generic shear flows, and explored whether the wakes could be exploited to delay the stall and increase the lift of airfoils and wings. In the second step, in the absence of external wakes to exploit, we investigated whether the unsteady wakes could be produced closer to the airfoil separation point by using flexible flags (which could be easily stored and deployed in practical applications). In this case, flags were positioned closer to the airfoil surface, but in the freestream where there was no shear. For the final step, we explored the self-excited flag oscillations when the fixed end of the flags was attached to the airfoil surface. If the flags interact with the unsteady separated flow, self-excited flag oscillations are possible, which in turn cause the roll up of LEVs periodically.

2 Results

We recently reported [7] that wings in the wakes of upstream bodies as shown schematically in Figure 1 can exhibit spectacular lift increase and delay of the stall. It is remarkable that the maximum lift is even larger when the wing is placed at an optimal offset distance from the wake centerline, where the velocity fluctuations are smaller. The stall angle can be delayed up to $\alpha = 20$ to 25 deg. This achievement is comparable to what might be expected (or hoped) from active flow control methods (such as blowing, suction, etc.) applied at post-stall angles of attack. We suggested that the lift enhancement is due to the formation of leading-edge vortices, when the wing is submerged into the unsteady wake as also shown in Figure 1. In *DisCoVor 2022*, we plan to present our ongoing research to understand why there is an optimal location at a nonzero offset distance, the effects of scale, circulation, frequency of the vortices in the incident wake, wing streamwise location, the degree of two-dimensionality of the wake, and the spanwise length scale of the vortices with respect to the wing-span (wing aspect ratio).

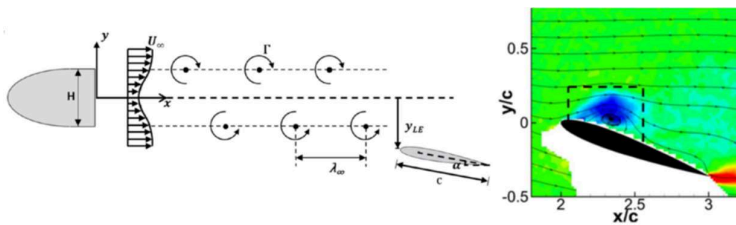


Figure 1: Schematic of wing in a wake (left); LEV formation when the wing is located at the centerline. $Re=100,000$.

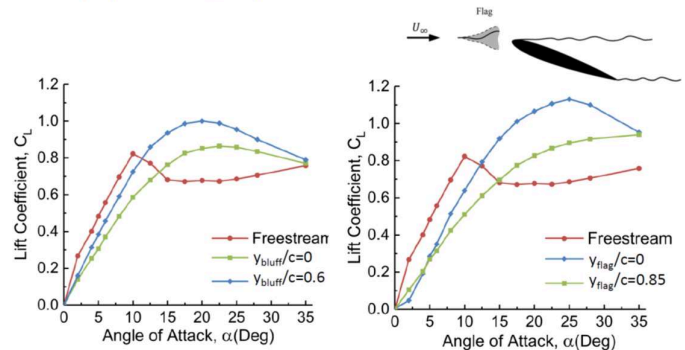


Figure 2: Mean lift coefficient as a function of angle of attack in freestream and in the wake of an upstream bluff body (left) and in the wake of an upstream flag (right).

Figure 2 compares the mean lift coefficient in freestream, at the wake centerline and the optimal offset distance, for a wake generated by an upstream bluff body (left). On the right hand side we show the mean lift coefficient for a wake produced by an upstream flapping flag. With the PIV measurements, we investigate similar aspects as above, in particular: the effects of circulation and frequency of the vortices in the incident wake, and the degree of two-dimensionality of the vortices in the wake.

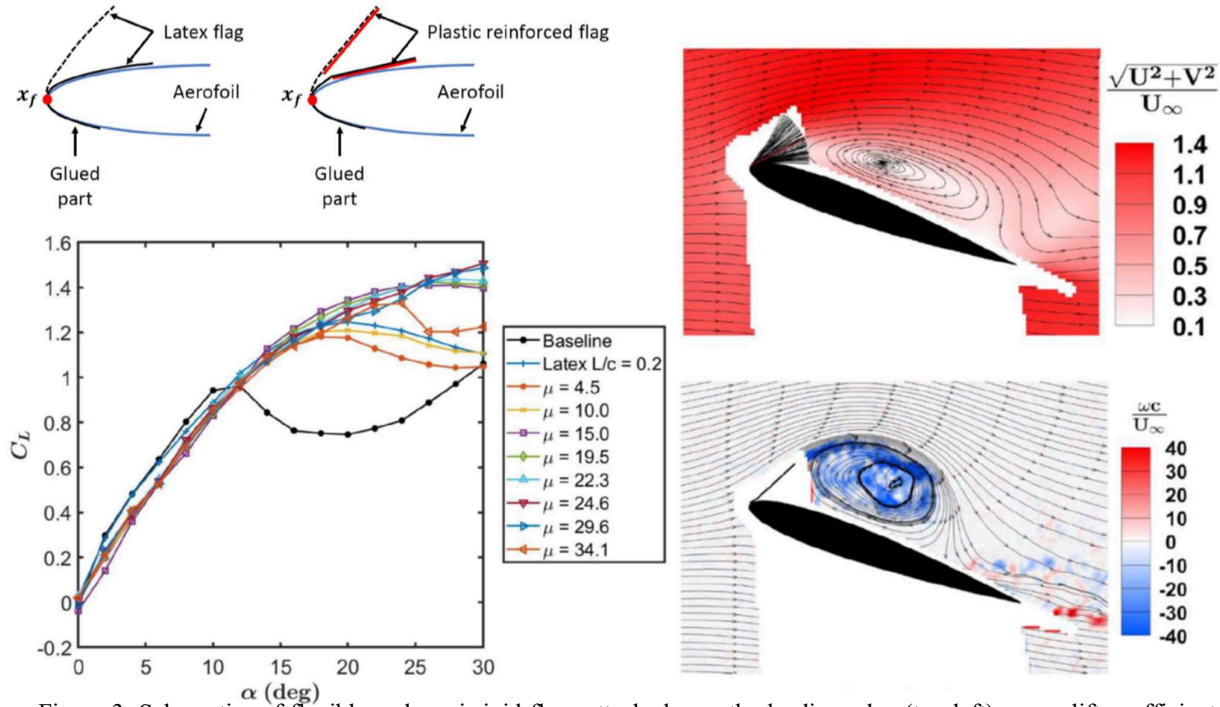


Figure 3: Schematics of flexible and semi-rigid flags attached near the leading-edge (top left); mean lift coefficient versus angle of attack (bottom left); time-averaged velocity (top right); and instantaneous vorticity (bottom right).

Recently we presented experiments demonstrating that a small flag attached to the surface of an airfoil near the leading edge may exhibit self-excited oscillations when the airfoil is set at a post-stall angle of attack [8]. In the ongoing research, we manufactured flags from flexible latex sheets as well as thin-plastic reinforced (semi-rigid) flags as sketched in Figure 3. We were able to vary the mass ratio and the bending stiffness over a wide range. The variation of the lift coefficient as a function of angle of attack in Figure 3 shows that, for some mass ratios, remarkable increases in the maximum lift coefficient and stall angle (approaching 30 degrees) can be achieved. The time-averaged flow on the right hand side in Figure 3 reveals that the limit cycle oscillations of the flag between the airfoil surface and the freestream produces a recirculation region above the airfoil. LEV shedding and formation of a separation bubble are observed when the flag tip approaches the maximum displacement.

The instantaneous flow and the range of oscillation frequency have strong similarities to those of the active flow control methods for separation, yet this is a passive flow control method that relies on unsteady effects. The flag oscillations occur mostly in the first structural mode, while the higher modes reveal the three-dimensionality of the flag deformation field. We have found that, for semi-rigid flags, the flag behaviour is essentially two-dimensional.

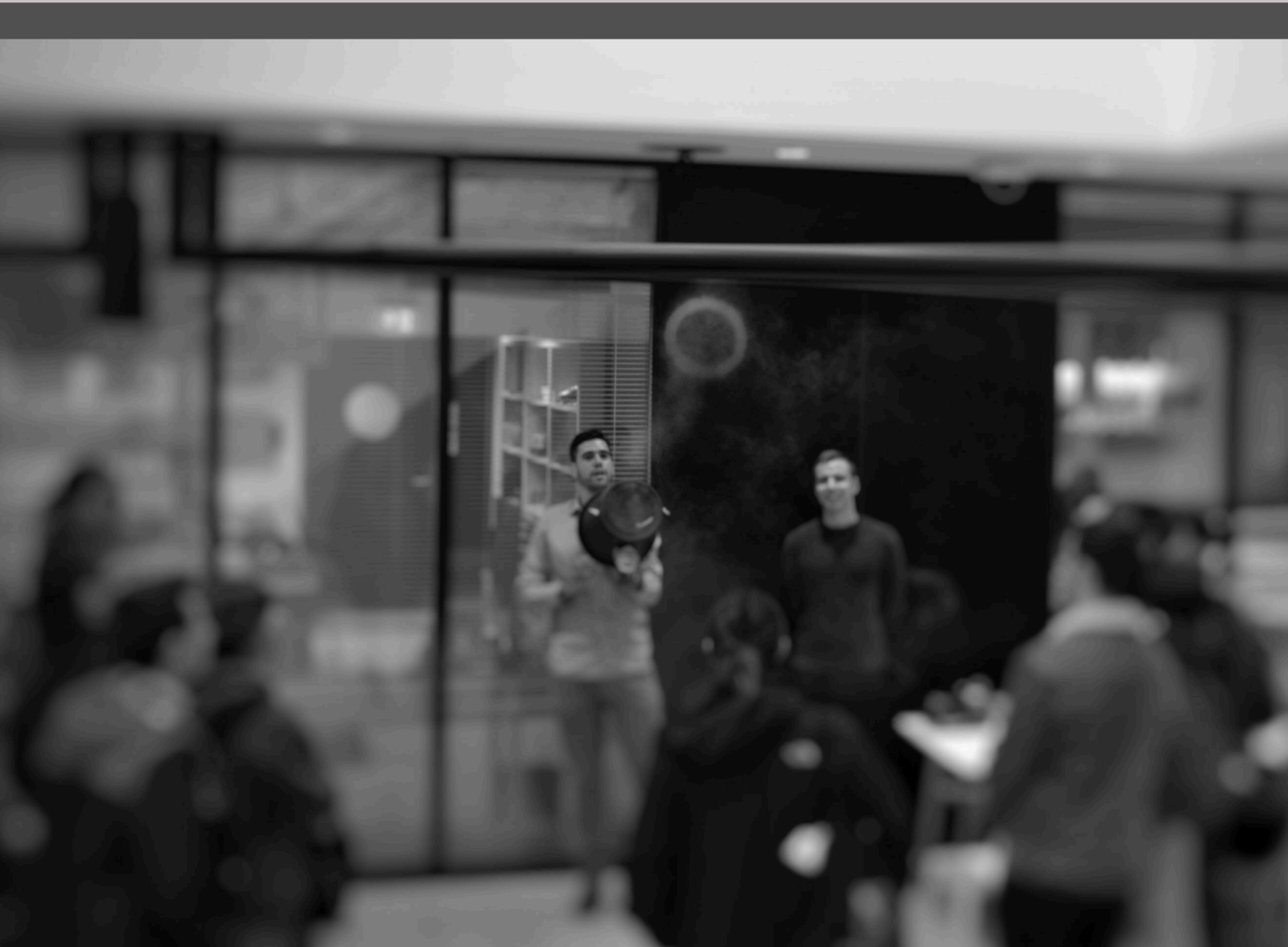
The oscillation frequencies of the flag are in the same range of vortex shedding frequency of the baseline airfoil, suggesting that the wake resonance mechanism may be behind the observations of the enhanced lift at the post-stall angles of attack. Ongoing research focusses on the coupling of the flag with wake instabilities, how the flag can be tuned by proper design, whether the three-dimensionality of the flag oscillations can be controlled, and how this concept can be applied to three-dimensional swept wings.

This work was supported by EPSRC Grants No. EP/F026099/1 and EP/K040391/1.

References

- [1] C. P. Ellington, C. van den Berg, A. P. Willmott, and A. L. R. Thomas, Leading-edge vortices in insect flight, *Nature*, 384, 626 (1996).
- [2] I. Gursul, & C.M. Ho, High aerodynamic loads on an airfoil submerged in an unsteady stream, *AIAA Journal*, 30(4), 1117-1119 (1992).
- [3] D. J. Cleaver, Z.Wang, I. Gursul, and M. R. Visbal, Lift enhancement by means of small-amplitude airfoil oscillations at low Reynolds numbers, *AIAA J.* 49, 2018 (2011).
- [5] D. Greenblatt and I. J. Wygnanski, The control of flow separation by periodic excitation, *Prog. Aerosp. Sci.* 36, 487 (2000).
- [6] J. Z. Wu, X. Y. Lu, A. G. Denny, M. Fan, and J. M. Wu, Post-stall flow control on an airfoil by local unsteady forcing, *J. Fluid Mech.* 371, 21 (1998).
- [7] Z. Zhang, Z. Wang, and I. Gursul, Lift enhancement of a stationary wing in a wake, *AIAA J.* 58, 4613 (2020).
- [8] J. Tan, Z. Wang, and I. Gursul, Self-excited flag vibrations produce post-stall flow control, *Physical Review Fluids* 6, L102701 (2021).

Poster session 1



Dominant flow features on a cross-flow turbine blade with constant and intracycle angular velocity

Mukul Dave and Jennifer A. Franck

University of Wisconsin-Madison, Department of Engineering Physics, USA.

*Correspondence: *mhdave@wisc.edu*

1 Introduction

Modal analysis of unsteady flow is used to identify dominant features and to create a low-dimensional basis of the system for applications [1] such as to inform control strategies [2] or to compare the system trajectories across a parameter space [3]. Techniques that project the flow field onto a linear subspace are particularly popular due their simplicity of implementation and ability to isolate distinct flow features through spatial modes.

Flow over cross-flow turbines (CFT) that rotate on an axis perpendicular to oncoming flow, is an active area of research due to their potential in harvesting hydrokinetic energy and the complex dynamic stall cycle experienced during their rotational motion. Modal analysis has previously been employed to deconstruct dynamic stall in experiments involving a pitching foil [4] or a pitching-surfing foil experiencing relative motion similar to a CFT blade [5]. However they focus on a single kinematics and include only a part of the flow region around the blade due to limitations of particle image velocimetry. Moreover as demonstrated through computations, Coriolis forces on the flow due to rotational motion of the blades play a crucial role in determining the flow field, particularly the position of the stall vortex, which is not adequately modeled by a pitching-surfing blade [6].

In this research, a low-dimensional basis is constructed for the full circumferential flow field around rotating CFT blades through proper orthogonal decomposition (POD) implemented on flow data from large-eddy simulation (LES). First, a constant angular velocity rotation that represents the optimal constant tip-speed ratio is presented. The dominant spatial modes and their time development coefficients are analyzed in reference to the relative velocity experienced and the torque generated. Next, a sinusoidal variation of angular velocity that potentially improves turbine performance [7, 8] will be processed. In the second step, a common basis will be determined to directly compare the different CFT kinematics, and to inform active control strategies for enhancing power generation.

2 Methods

2.1 Turbine geometry and kinematics

As shown in Fig. 1, the CFT blade rotates in the freestream with an angular velocity, ω , the instantaneous velocity of the

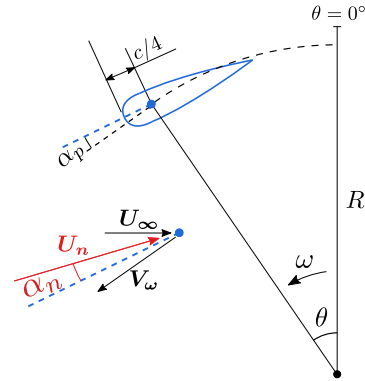


Figure 1: Geometric and kinematic parameters for the foil.

blade is shown as \mathbf{V}_ω . Lift is generated through the apparent angle of attack, α_n , which is the angle the blade encounters with respect to the relative flow velocity, \mathbf{U}_n . The component of this lift force that is tangential to the blade motion drives the turbine. Turbine performance is characterized as a function of tip speed ratio, defined as the ratio of turbine tip speed to the flow freestream velocity, $\lambda(\theta) = \omega(\theta)R/U_\infty$. The turbine has two NACA0018 foils with $c/R = 0.47$ and $\alpha_p = 6^\circ$. The Reynolds number is $Re = cU_\infty/\nu = 4.5 \times 10^4$ and the blockage ratio, ratio of the turbine cross-section to that of the flow, is 10.6%. A constant angular velocity rotation with $\lambda = 1.9$ is explored, which represents the optimal tip speed ratio for this turbine configuration [9].

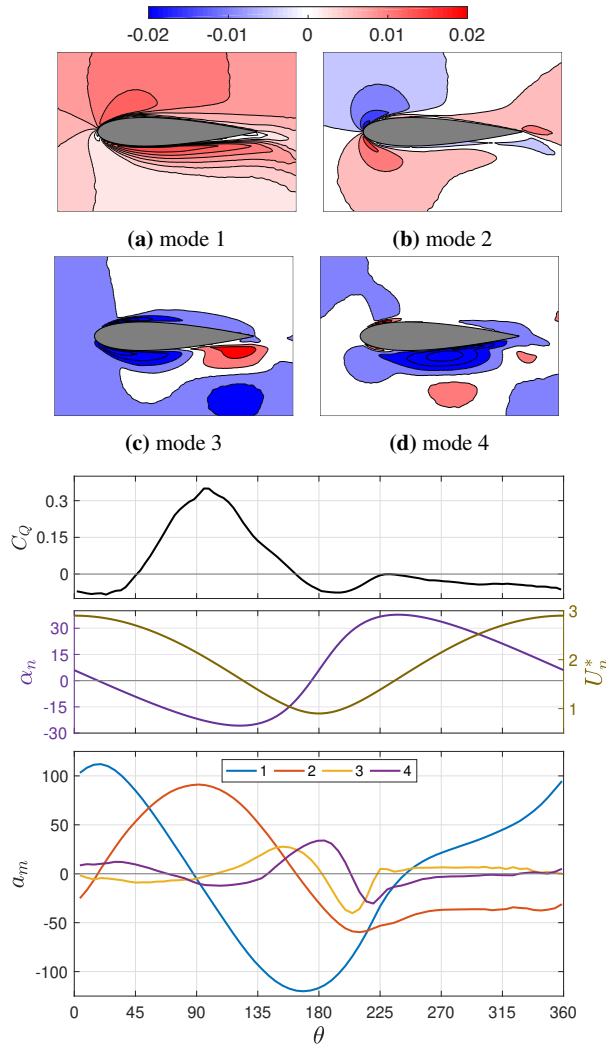
2.2 Proper orthogonal decomposition

The local dynamic k -equation model is implemented in a wall-resolved LES with cyclic boundary conditions along the blade span. Ten rotations of the turbine are simulated and the last six are considered for modal analysis as the power generation curve and flow physics stop changing significantly from one rotation to another. A total of 840 temporal data frames are obtained, resulting in an equivalent number of modes computed.

Span-averaged velocity, normalized by the freestream velocity, is extracted on a grid of resolution $0.01c$ from a region of size $1.5c \times 1c$ centered at the blade. To provide a uniform reference frame across time, a velocity field relative to the blade, \mathbf{u} , is calculated with the blade position fixed horizontally. Next, the time-averaged mean velocity field is

subtracted from all frames, $\mathbf{u}' = \mathbf{u} - \bar{\mathbf{u}}$. Velocities along x (along the blade) and y (lateral to the blade) directions on the two-dimensional grid from each frame are then stacked as a one-dimensional column vector, with time advancement along rows of the matrix. Finally a singular value decomposition of this matrix provides the spatial modes, $\psi_m(x, y)$, and their time development coefficients, $a_m(t_n)$, in decreasing order of their singular values or significance, such that $\mathbf{u}'(x, y, t_n) = \sum_{m=1}^N a_m(t_n) \psi_m(x, y)$.

3 Results



(e) Time development coefficients (bottom), nominal relative flow (middle), and torque generation (top) through a blade rotation.

Figure 2: Modes as x -velocity fields (a-d) along with their time development coefficients (e), for $\lambda = 1.9$.

Figures 2a-2d present the x -velocities for the first four modes, which account for 94% of the energy in terms of squares of their singular values. Figure 2e includes their time development coefficients in the bottom frame for a specific instance of rotation along with the nominal relative flow

variation in the middle frame and the phase-averaged normalized torque generation, C_Q , in the top frame.

Mode 1 represents uniform flow along the turbine blade and has its maximum and minimum when the angle of attack is low, representing attached flow at the start of the blade's upstream motion and deep stall condition at the end of its upstream motion respectively. Mode 2 shows the flow swirling around the leading edge and its peak is associated with light stall and high torque generation. Modes 3 and 4 prominently include regions of rotational flow and represent the roll-up and pinching off of the stall vortex at the leading edge and its subsequent convection along the blade.

Preliminary analysis is performed (not presented here) for a sinusoidal variation of angular velocity, $\omega(\theta) = \bar{\omega} + A_\omega \sin(2\theta + \phi_\omega)$, for which the blade experiences a distinct relative velocity profile and results in large flow separation. The spatial modes are similar to that for the constant rotation rate, with the dominant modes representing uniform flow, light stall, and regions of rotational flow.

Hence, a detailed analysis for two or more distinct kinematics will be presented using common spatial modes, comparing the trajectories of flow dynamics to inform control strategies.

References

- [1] Kunihiko Taira, Maziar S. Hemati, Steven L. Brunton, Yiyang Sun, Karthik Duraisamy, Shervin Bagheri, Scott T.M. Dawson, and Chi An Yeh. Modal analysis of fluid flows: Applications and outlook. *AIAA J.*, 58(3):998–1022, oct 2020.
- [2] Chi An Yeh and Kunihiko Taira. Resolvent-analysis-based design of airfoil separation control. *J. Fluid Mech.*, 867:572–610, may 2019.
- [3] Dustin G. Coleman, Flint O. Thomas, Stanislav Gordeyev, and Thomas C. Corke. Parametric Modal Decomposition of Dynamic Stall. <https://doi.org/10.2514/1.J057077>, 57(1):176–190, nov 2018.
- [4] Karen Mulleners and Markus Raffel. The onset of dynamic stall revisited. *Exp. Fluids*, 52(3):779–793, mar 2012.
- [5] Reeve Dunne and Beverley J. McKeon. Dynamic stall on a pitching and surging airfoil. *Exp. Fluids*, 56(8):157, aug 2015.
- [6] Hsieh-Chen Tsai and Tim Colonius. Coriolis Effect on Dynamic Stall in a Vertical Axis Wind Turbine. *AIAA J.*, 54(1):216–226, jan 2016.
- [7] Benjamin Strom, Steven L. Brunton, and Brian Polagye. Intracycle angular velocity control of cross-flow turbines. *Nat. Energy*, 2(8):1–9, 2017.
- [8] Mukul Dave, Benjamin Strom, Abigale Snortland, Owen Williams, Brian Polagye, and Jennifer A. Franck. Simulations of Intracycle Angular Velocity Control for a Crossflow Turbine. *AIAA J.*, 59(3):812–824, mar 2021.
- [9] Abigale Snortland, Brian Polagye, and Owen Williams. Influence of Near-blade hydrodynamics on Cross-flow Turbine performance. In *Proc. 13th Eur. Wave Tidal Energy Conf.*, pages 1–9, 2019.

Gust Mitigation using Unsteady Flow Control

Pascal Gehlert^a and Holger Babinsky^a

^a University of Cambridge, Engineering, Cambridge, U.K.¹

*Correspondence: pg469@cam.ac.uk

1 Introduction

Rapidly changing flow fields are a common feature of the atmospheric boundary layer or the tidal flow in the ocean [1]. The time varying nature can lead to large transient forces that significantly extend beyond the static-state equivalent affecting immersed bodies [2]. Wind or water turbines that are subjected to such transient conditions can consequently suffer from catastrophic failure when the peak load during a gust event exceeds the failure strength. Alternatively, blade oscillations resulting from the time varying flow field may reduce the lifespan and increase the number of servicing intervals of the turbines.

To prevent premature failure, the force acting on the blades is ideally kept constant, regardless of the surrounding flow field. Attempts to achieve this utilise small deployable gurney tabs, short trailing edge flaps or pitch the entire wing. Especially the latter shows significant success in mitigating the large load spike due to a transverse gust [3]. Unfortunately however, it may not always be possible to pitch the entire wing, either due to the complexity of the construction or because the inertia of the blade prevents the required pitch rates to be attainable. Therefore, an alternative that does not rely on pitching the blade could be beneficial, either to be used in isolation or in conjunction with other force mitigating mechanisms.

Here, we therefore want to modify and manipulate the unsteady flow field through flow control by relying on our understanding of unsteady flow and the related force development, to determine the most appropriate implementation. The poster presentation focuses on first identifying the dominant force contributions during a transverse gust wing encounter and subsequently shows how the transient force can be modified through forced boundary layer separation.

2 Results

2.1 Wing and Towing Tank

The wing-transverse gust encounter is performed in the University of Cambridge Towing Tank facilities. The tank is 9 m long, 1 m wide and filled to a height of 0.8 m and a servo-motor controlled carriage moves the length of the tank. A force balance measuring the lift and drag response with a resolution of ± 0.01 N is situated on the carriage to

¹This work was supported by funding from the Engineering and Physical Sciences Research Council.

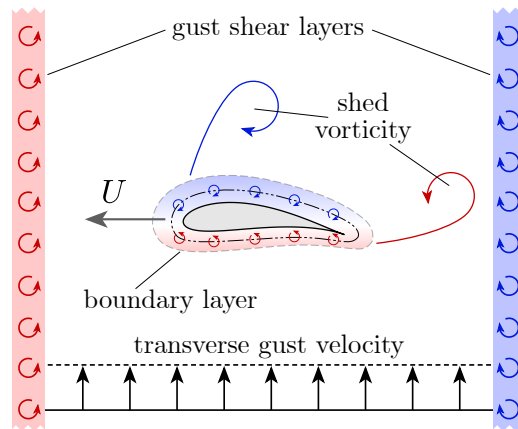


Figure 1: Schematic illustration of a wing immersed in a gust. The boundary layer (the layer of fluid closest to the wing surface) as well as the shed vortices and the gust shear layers are shown.

which a rapid prototyped wing is vertically mounted. The Reynolds number based on surge velocity is of the order of 10000. Internal piping within the wing allows for water to be pumped out along the leading edge, to enforce separation at the desired moment in time. A gust rig [4] is situated in the tank and creates a top-hat shaped sharp edged transverse velocity profile through which the wing is towed, thereby re-creating a transverse gust encounter. The flow response is obtained using planar particle image velocimetry by illuminating a horizontal plane at the midspan using an Nd:YLF laser. Two high-speed Phantom M310 cameras are positioned below the tank and are located upstream and downstream of the wing to allow for complete optical access without any blockage.

2.2 Topics of Discussion

The main topics of discussion that the poster presentation aims to comment on are:

- During the gust encounter, schematically illustrated in figure 1, the force acting on the wing can be grouped into a *non-circulatory* as well as a *circulatory* contribution. The former is created when the wing enters (and exits) the gust. It can be linked to a change in wing boundary layer vortex sheet strength as a result of vorticity residing within the gust shear layers

and for a given shape of the wing, translation velocity and gust profile is fixed. The circulatory force component on the other hand is a function of the position and motion of free vorticity and can therefore readily be affected by changing how vorticity sheds from the wing. Since both force contributions are, to a first order, independent of each other, one first way to reduce the force spike is to ensure that the maximum force of both does not occur at the same time but that the load peaks are offset. This may for example be achieved by manipulating when and how the leading edge vortex (LEV) forms.

- Since free vorticity has a significant force contribution, we will discuss the effect that a LEV has on the force. The analysis shows that when shed vorticity contained within the LEV is very close to the wing, a positive lift force is established. However, as soon as this vorticity resides further away, a net negative force is created. It therefore appears beneficial to *move* the LEV away from the wing as quickly as possible. In the present scenario we attempt to do this through intermittent surface normal blowing which aims to initiate separation and to cause shed vorticity to advect away from the wing.
- Regardless of how we manipulate flow separation, any changes to the force will always require a finite amount of time before they act on the wing. Since the non-circulatory force due to entering the gust, however, instantaneously acts on the wing, complete force mitigation cannot be achieved through flow control alone. Instead, a counteracting non-circulatory force is required to offset the loading during initial gust entry. As such, a pitching trailing edge flap could be used.
- Having theoretically explored how to mitigate a transverse gust force by modifying the flow field through controlled separation, as schematically illustrated in figure 2, we aim to discuss the initial experimental results of the wing gust encounter. The focus will be on how surface normal blowing affects the flow field, leads to flow separation and what its effect on the position of vorticity shed from the leading edge of the wing is. Force balance measurements will further be used to assess changes to the transient loading throughout the gust encounter to better understand how to control the force response.

3 Conclusion

The force during a transverse gust wing encounter is governed by a non-circulatory force during gust entry (and exit) as well as a circulatory component due to vorticity shedding from the wing's leading and trailing edges. With the aim in mind to mitigate the transient force spike during the gust encounter as much as possible, our understanding of unsteady

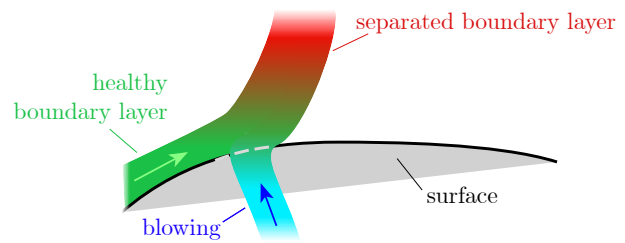


Figure 2: Schematic illustration of induced separation through surface normal blowing.

flow and force development is used to create an idealised flow response that minimizes the gust force. This relies on initiating flow separation at the leading edge at a desired moment in time and moving the leading edge vortex as far and as quickly away from the wings surface as possible, in order to reduce its positive lift contribution. These ideas are subsequently tested in an experimental top-hat shaped transverse wing gust encounter.

References

- [1] Mohamed, A., Abdulrahim, M., Watkins, S., Clothier, R., Development and Flight Testing of a Turbulence Mitigation System for Micro Air Vehicles. *Journal of Field Robotics*, 649–660, 2016.
- [2] Eldredge, J. D., Jones, A. R., Leading-Edge Vortices: Mechanics and Modeling. *Annual Review of Fluid Mechanics*, 75–104, 2019.
- [3] Andreu Angulo, I., Babinsky, H., Lift Control on Pitching Wings Experiencing Gusts. *AIAA 2022 Scitech Forum*, 2022.
- [4] Corkery, S. J., Babinsky, H., Harvey, J. K., On the Development and Early Observations from a Towing Tank-Based Transverse WingGust Encounter Test Rig. *Experiments in Fluids*, 2018.

Three-Dimensionality of Vortices

I. Gursul, O. Son, B. Turhan, Z. Zhang, Z. Wang
 University of Bath, United Kingdom
 Correspondence: i.a.gursul@bath.ac.uk

1 Motivation

Leading-edge vortices (LEVs) and trailing-edge vortices (TEVs) found in aerodynamics are never two-dimensional, even for two dimensional airfoils and bodies. Transition in the shear layers, increasing small-scale turbulence with streamwise distance, and spanwise vortex instabilities may be responsible for the three-dimensionality. It is not known how fast the three-dimensionality develops after the separation from the leading-edges and trailing-edges, and how much this affects the aerodynamic forces.

In previous research for the turbulent near wake of a stationary bluff body, the spanwise length scale of vortices was found to be on the order of the wake thickness [1]. There is no knowledge on how the airfoil oscillations may affect the wake coherence. The degree of coherence in the spanwise direction may be important for the wake-wing interactions [2], experimental simulation of vortex-wing interactions [3], and gust generators [4]. Recent evidence suggests that vortex interactions during the formation and convection of the vortices may be behind the spanwise instabilities on airfoils and wings [5,6].

2 Results

In this research, we investigate the degree of two-dimensionality of the TEVs and wakes by using the two-point cross-correlations of the PIV measurements in a crossflow plane. This method was applied to turbulent wakes of stationary bluff bodies (wake Reynolds number in the range of 10,000 to 50,000) and oscillating wakes of a periodically plunging airfoil (chord Reynolds number of 20,000) as sketched in Figure 1. In addition, we investigated the unsteady LEV filaments on airfoils and wings by using three-dimensional volumetric velocity measurements. These measurements and analysis offer an insight to the degree of three-dimensionality and flow physics, which we wish to present in *DisCoVor 2022*.

Figure 1 shows an example map of two-point cross-correlations in the turbulent wake of a bluff-body (top right). From these measurements we estimate the integral length scale in the spanwise direction. We use the same methodology to investigate the wakes of oscillating airfoils. The cross-correlations increase with

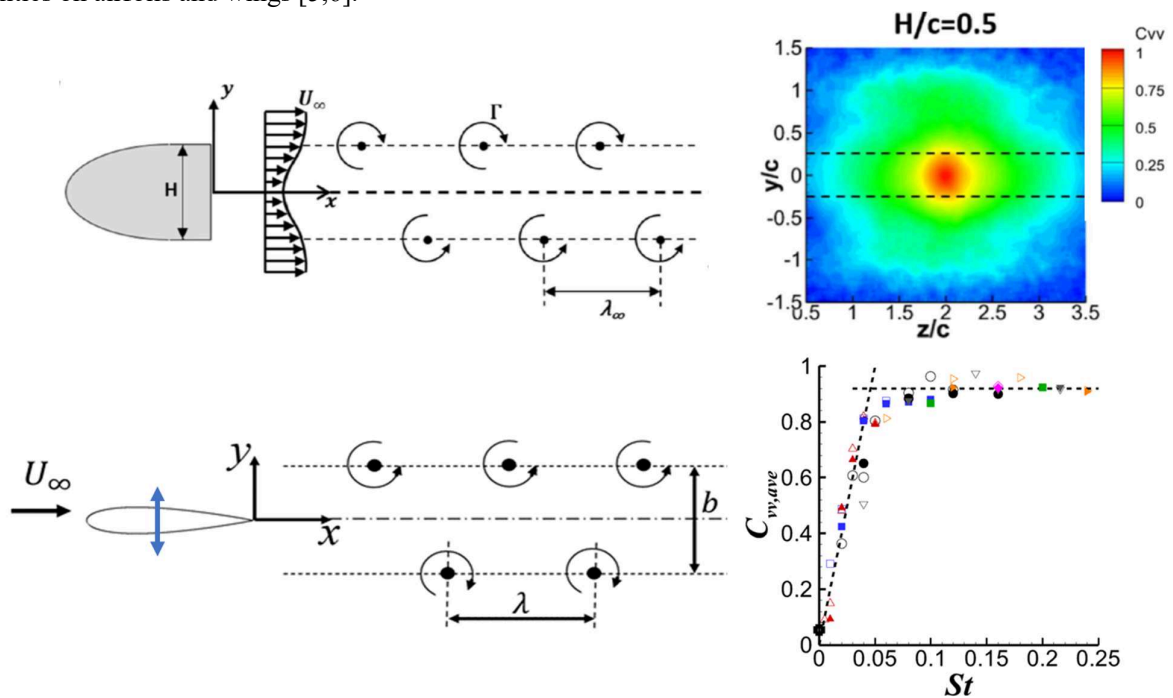


Figure 1: Schematic of bluff-body wake (top left); two-point cross-correlation coefficient in cross-flow plane (top right); schematic of plunging airfoil (bottom left); spanwise-averaged cross-correlation coefficient versus Strouhal number.

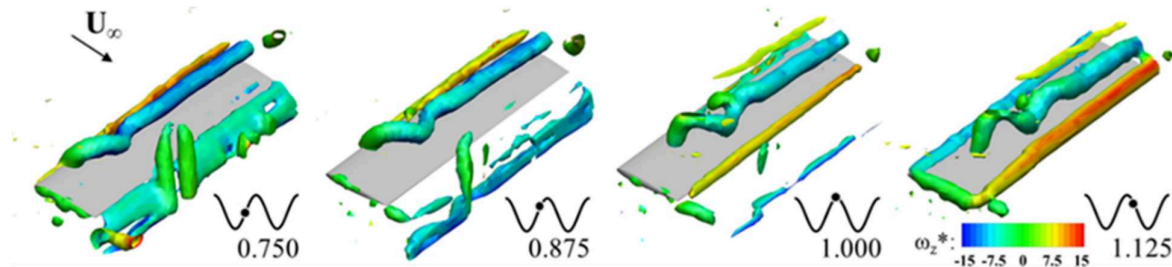


Figure 2: Vortical flow over a high-aspect-ratio wing at different phases of plunging motion.

airfoil oscillations. The spanwise-averaged cross-correlation is shown as a function of Strouhal number based on the peak-to-peak amplitude in Figure 1 (bottom left). These measurements taken at $x/c=4$ suggest that the vortices are essentially two-dimensional for $St \geq 0.05$, but poorly correlated for lower Strouhal numbers.

The vortex dynamics of the leading-edge vortices on plunging high-aspect-ratio ($AR = 10$) wings are illustrated in Figure 2. The LEV filaments on the wing exhibit spanwise waves. The motion of the vortex leg emerges as a main factor for the LEV filament deformation. The presence of a wing tip causes the leg of the vortex to remain attached to the wing's upper surface, while the initial deformation of the filament near the wing-tip resembles a helical vortex. We will present the characteristics of the helical wave that originates from the leg as a function of kinematic parameters.

Figure 3 shows the LEV filaments for an airfoil (with end-plates). Interactions with secondary vortices and trailing-edge vortices appear to cause the observed spanwise instabilities, which arise near the trailing-edge and convect into the wake. The characteristics of the vortex pair interactions will be presented as a function of the reduced frequency. Both for wings and airfoils, we found reasonable agreement with the theoretical predictions for isolated vortices. It is likely that the presence of the wing flow as well as other vortices

result in the strain and disturbances that excite the vortex cores.

In order to introduce spanwise instabilities and excite the leading-edge vortex filament, various control methods are tested. These include vortex generators, spoilers, and wing-tip geometry modifications. The results show that these methods could be effective in controlling the leading-edge vortex structure and accelerating the three-dimensionality of the vortex filaments on plunging wings. These will be illustrated in the presentation.

This work was supported by EPSRC Grants No. EP/S028994/1 and EP/K040391/1.

References

- [1] Hayakawa, M. & Hussain, F. 1989 Three-dimensionality of organized structures in a plane turbulent wake, *J. Fluid Mechanics*, 206, pp. 375-404.
- [2] Zhang, Z., Wang, Z. & Gursul, I. Lift enhancement of a stationary wing in a wake, *AIAA J.* 58, 4613 (2020).
- [3] Wilder, M. C. & Telionis, D. P. 1998 Parallel blade-vortex interaction, *J. Fluids Struct.*, 12, pp. 801-838.
- [4] Wei, *et al.* 2019 Insights into the periodic gust response of airfoils, *J. Fluid Mechanics*, 876, pp. 237-263.
- [5] Son, O., Wnag, Z. & Gursul, I. 2021, Three-dimensional instabilities of vortices on a periodically plunging wing, AIAA 2021-1211, *AIAA SciTech 2021*.
- [6] Son, O., Wnag, Z. & Gursul, I. 2022, Leading-edge vortex dynamics on plunging 2D and 3D wings, AIAA 2022-2014, *AIAA SciTech 2022*.

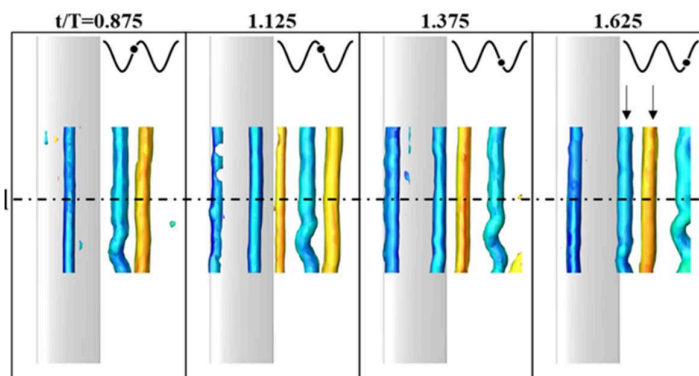


Figure 3: Vortical flow over a plunging airfoil at different phases.

Revealing the fundamental forces behind the stable equilibrium altitudes of pitching foils in ground effect

Tianjun Han^{a*}, Qiang Zhong^b, Daniel B. Quinn^b and Keith W. Moored^a

^a Lehigh University, Department of Mechanical Engineering, Bethlehem, USA

^b University of Virginia, Department of Mechanical and Aerospace Engineering, Charlottesville, USA

*Correspondence: tih216@lehigh.edu

1 Introduction

In nature, many animals are known to swim or glide near the seafloor or lake surfaces to improve their energetic cost of transport and increase their gliding distance [1–3]. Blake conducted experiments on mandarin fish to calculate minimum induced thrust and power required to hover above the ground, and concluded that reductions in the total power needed to hover can be up to 30–60% compared to hovering out of ground effect [4]. In addition, dark-edged-wing flying fish models were made to find that the flying fish achieves a reduction of drag and increase of lift-to-drag ratio by using ground effect [5]. Inspired by the known advantages of near-ground propulsion in biology, engineers have conducted research on this phenomenon, which will benefit the design of underwater robots.

For steady ground effect, it has been found that a higher lift coefficient and lift-to-drag ratio can be obtained when the foil is close to a solid boundary [6–14]. Unsteady ground effect is experienced by swimmers when they oscillate near a solid boundary. There are a lot of interesting hydrodynamic phenomena happening in unsteady ground effect like thrust or cruising speed enhancement with no penalty on propulsive efficiency [15–19], wake deflection [20–22], as well as the existence of stable equilibrium altitudes where the time-averaged lift force is zero and altitude perturbations generate forces that return a swimmer to its equilibrium.

It's essential to determine the fundamental competing forces that lead to equilibrium altitudes in order to better predict and manipulate them. Here, we will follow the work of Sears [23] and McCune [24] to decompose the lift force into the added mass force, wake-induced force and quasi-steady force to address the following questions: (1) What are the fundamental competing forces behind stable and unstable equilibria in unsteady ground effect? (2) How does the behavior of the fundamental forces make equilibrium altitudes increase with St and decrease with k ? (3) How does the behavior of the fundamental forces make the unstable equilibrium altitude appear at high St ?

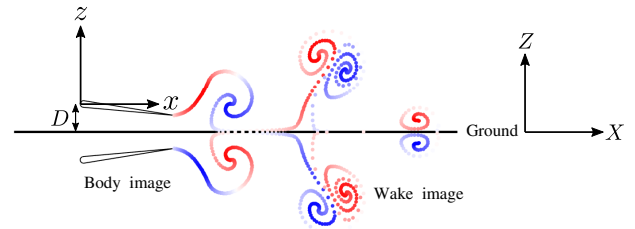


Figure 1: Illustration of a hydrofoil propelling under unsteady ground effect.

2 Results

To model the presence of the ground, a system based on the method of images will be created in potential flow simulation where the flow is assumed to be irrotational, incompressible and inviscid. In Figure 1, a 7% thick tear-drop hydrofoil is swimming at height D above the ground while the image hydrofoil is swimming 180° out-of-phase at height $-D$ below the ground, which automatically satisfies the no-flux boundary condition at $Z = 0$. By following previous studies [25–30], an unsteady boundary element method will be employed.

By using the decomposition method of Sears [23] and McCune [24] with the unsteady boundary element method simulations, the contributions of the added mass, wake-induced, and quasi-steady lift are determined that act on a pitching foil in ground effect. Fig. 2 reveals that the added mass lift, C_{L_a} , is zero, the wake-induced lift, C_{L_w} , is positive, and the quasi-steady lift, C_{L_q} , is negative across all ground proximities. In this manner, the added mass lift does not play a role in generating the equilibrium altitude and the equilibrium altitude is generated by the balance between the positive wake-induced lift and negative quasi-steady lift. Moreover, the magnitude of C_{L_w} and C_{L_q} both increase with decreasing D^* . Fig. 2(c) and (d) (high St cases) show that there is an unstable equilibria and negative C_L when the foil is close to the ground. This occurs since the magnitude of the quasi-steady lift force grows faster than and overtakes (in magnitude) the wake induced lift force as the ground proximity decreases. Since the quasi-steady lift force is negative (pulls a swimmer towards the ground) then the total lift switches

¹This work was supported by the National Science Foundation under Program Director Dr. R. Joslin in Fluid Dynamics, award number 1921809 ...

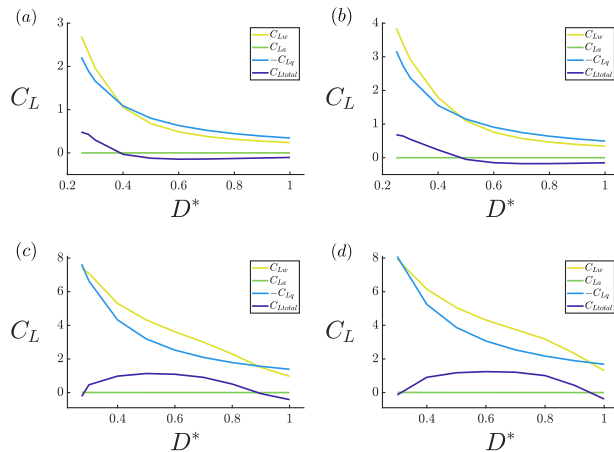


Figure 2: The quasi-steady lift is more enhanced than the wake-induced lift when St gets larger at a really low D^* . Force decomposition with k fixed at 1. (a) $St = 0.25$. (b) $St = 0.3$. (c) $St = 0.5$. (d) $St = 0.55$.

sign and becomes negative close to the ground thus generating an unstable equilibrium altitude.

3 Conclusion

We decomposed the lift force under unsteady ground effect into the added mass force, wake-induced force and quasi-steady force based on the unsteady Bernoulli equation. The wake-induced lift coefficient is found to be positive and the quasi-steady lift coefficient is found to be negative across all ground proximities while the added mass lift coefficient is maintained at zero. So the conclusion is made that both the stable and unstable equilibrium altitude where the total lift coefficient is zero is generated by the balancing between the positive wake-induced lift and negative quasi-steady lift while the added mass lift does not make any contribution.

References

[1] Paul W Webb. the Effect of Solid and Porous Channel Walls on Steady Swimming of Steelhead Trout *Oncorhynchus Mykiss*. *Journal of Experimental Biology*, 178(1):97–108, 1993.

[2] F. Hainsworth. Induced drag savings from ground effect and formation flight in brown pelicans. *Journal of experimental biology*, 135:431–444, 1988.

[3] R.V. Baudinette and K. Schmidt-Nielsen. Spatial Heterogeneity and Population Stability Evidence Against a Genetical Component to Performance on IQ Tests. *Nature*, 248:83–84, 1974.

[4] B Y R W Blake. The Energetics of Hovering in the Mandarin Fish (*Synchropus Picturatus*). *Journal of Experimental Biology*, 82(1):25–33, 1979.

[5] Hyungmin Park and Haecheon Choi. Aerodynamic characteristics of flying fish in gliding flight. *Journal of Experimental Biology*, 213(19):3269–3279, 2010.

[6] V Tremblay Dionne and T Lee. Ground effect on the aerodynamics of a naca 0015 airfoil with a plain trailing-edge flap. *Fluid Mechanics research International Journal*, 2(1):1–7, 2018.

[7] Yilei He, Qiulin Qu, and Ramesh K. Agarwal. Shape optimization of an airfoil in ground effect for application to WIG craft. *53rd AIAA Aerospace Sciences Meeting*, 2014, 2015.

[8] Sang Hwan Lee and Juhee Lee. Optimization of three-dimensional wings in ground effect using multiobjective genetic algorithm. *Journal of Aircraft*, 48(5):1633–1645, 2011.

[9] Qiulin Qu, Zhe Lu, Hao Guo, Peiqing Liu, and Ramesh K. Agarwal. Numerical investigation of the aerodynamics of a delta wing in ground effect. *Journal of Aircraft*, 52(1):329–340, 2015.

[10] Wei Yang, Feng Lin, and Zhigang Yang. Three-dimensional Ground Viscous Effect on Study of Wing-in- ground Effect. *Proceedings of Third International Conference on Modelling and Simulation (ICMS2010)*, 5(January 2010):8–11, 2010.

[11] Zhigang Yang, Wei Yang, and Yulong Li. Analysis of two configurations for a commercial WIG craft based on CFD. *Collection of Technical Papers - AIAA Applied Aerodynamics Conference*, (May), 2009.

[12] Pedro J. Boschetti, Elsa M. Cárdenas, Andrea Amerio, and Ángela Arévalo. Stability and performance of a light unmanned airplane in ground effect. *48th AIAA Aerospace Sciences Meeting Including the New Horizons Forum and Aerospace Exposition*, (January), 2010.

[13] Sheila E. Widnall and Timothy M. Barrows. An analytic solution for two- and three-dimensional wings in ground effect. *Journal of Fluid Mechanics*, 41(4):769–792, 1970.

[14] Peter J. Baddoo, Melike Kurt, Lorna J. Ayton, and Keith W. Moored. Exact solutions for ground effect. *Journal of Fluid Mechanics*, pages 1–13, 2020.

[15] Jie Wu, Chang Shu, Ning Zhao, and Weiwei Yan. Fluid dynamics of flapping insect wing in ground effect. *Journal of Bionic Engineering*, 11(1):52–60, 2014.

[16] Sung Goon Park, Boyoung Kim, and Hyung Jin Sunga. Hydrodynamics of a self-propelled flexible fin near the ground. *Physics of Fluids*, 29(5), 2017.

[17] Longzhen Dai, Guowei He, and Xing Zhang. Self-propelled swimming of a flexible plunging foil near a solid wall. *Bioinspiration and Biomimetics*, 11(4), 2016.

[18] Rafael Fernández-Prats, Veronica Raspa, Benjamin Thiria, Francisco Huera-Huarte, and Ramiro Godoy-Diana. Large-amplitude undulatory swimming near a wall. *Bioinspiration and Biomimetics*, 10(1), 2015.

[19] Daniel B. Quinn, George V. Lauder, and Alexander J. Smits. Flexible propulsors in ground effect. *Bioinspiration and Biomimetics*, 9(3), 2014.

[20] Daniel B. Quinn, Keith W. Moored, Peter A. Dewey, and Alexander J. Smits. Unsteady propulsion near a solid boundary. *Journal of Fluid Mechanics*, 742:152–170, 2014.

[21] Melike Kurt, Jackson Cochran-Carney, Qiang Zhong, Amin Mivehchi, Daniel B. Quinn, and Keith W. Moored. Swimming freely near the ground leads to flow-mediated equilibrium altitudes. *Journal of Fluid Mechanics*, 875:R1, 2019.

[22] Qiang Zhong, Tianjun Han, Keith W Moored, and Daniel B Quinn. Aspect ratio affects the equilibrium altitude of near-ground swimmers. *Journal of Fluid Mechanics*, 2019.

[23] Theodore Von Kármán and William R Sears. Airfoil Theory for Non-Uniform Motion. *Journal of the aeronautical sciences*, 5:379–390, 1938.

[24] J E Mccune and T S Tavares. Perspective : Unsteady Wing Theory — The Karman / Sears. 115(December 1993), 1993.

[25] Fatma Ayancik, Qiang Zhong, Daniel B. Quinn, Aaron Brandes, Hilary Bart-Smith, and Keith W. Moored. Scaling Laws for the Propulsive Performance of Three-Dimensional Pitching Propulsors. pages 1117–1138, 2018.

[26] K. W. Moored. Unsteady three-dimensional boundary element method for self-propelled bio-inspired locomotion. *Computers and Fluids*, 167:324–340, 2018.

[27] J. Katz. Calculation of the Aerodynamic Forces on Automotive Lifting Surfaces. *Journal of Fluids Engineering, Transactions of the ASME*, 107(4):438–443, 1985.

[28] Emre Akoz and Keith W. Moored. Unsteady Propulsion by an Intermittent Swimming Gait. pages 149–172, 2017.

[29] Emre Akoz, Pan Han, Geng Liu, Haibo Dong, and Keith W. Moored. Large-Amplitude Intermittent Swimming in Viscous and Inviscid Flows. *AIAA Journal*, pages 1–8, 2019.

[30] Amin Mivehchi, Qiang Zhong, Melike Kurt, Daniel B. Quinn, and Keith W. Moored. Scaling laws for the propulsive performance of a purely pitching foil in ground effect. *Journal of Fluid Mechanics*, 919:1–13, 2021.

Experiments and simulations on deformable flapping wings

D. Diaz-Arriba^a, T. Jardin^{a*}, N. Gourdain^a, F. Pons^b and L. David^b

^a ISAE-Supaero, Université de Toulouse, France

^b Institut Pprime, UPR 3346, CNRS-Université de Poitiers-ENSMA, Poitiers, France

*Correspondence: t.jardin@isae.fr

1 Introduction

Flapping wings have been extensively studied for almost five decades now, with pioneering works by [1], for example. Nevertheless, the optimization of flapping wing kinematics for application to extremely small scale ($\approx 1\text{cm}$) and lightweight ($\approx 100\text{mg}$) flying vehicles has remained somewhat untractable due to the complex three-dimensional unsteady, non-linear flow dynamics (which makes cheap, low order models inaccurate in some situations) and to the large parameter space that needs to be explored. This is particularly true for hovering flight configurations where unsteady effects are usually predominant. Attempts to optimize flapping kinematics under hovering flight conditions using high-fidelity approaches (i.e. 3D experiments and direct or large eddy numerical simulations) based on a reduced number of parameters through systematic exploration of the parameter space or using dedicated algorithm [2–4], for example, have been reported recently but the latter are generally restricted to rigid wings. In this presentation, we investigate the influence of flapping wing parameters on aerodynamic performance. We first explore a relatively large portion of the parameter space using a rigid wing and then analyze the influence of wing deformation. Results are obtained using both experimental and numerical approaches.

2 Methodology

2.1 Problem setup

We consider a wing with aspect ratio 4 revolving about its root and pitching about a spanwise axis located one quarter chord downstream the leading edge. The wing has a NACA0012 profile extruded in the spanwise direction without twist. The characteristic Reynolds number based on the wing chord and the maximum revolving speed at a radial distance of $0.72R$, where R is the wing radius, is set to 1000.

2.2 Experiments

Experiments are performed in a water tank with dimensions $1 \times 1 \times 1.5\text{ m}^3$ as shown in figure 1. Time-resolved scanning tomography PIV measurements are conducted, together with digital image correlations for deformation measurements of flexible wings. For some specific cases, forces are derived from control volume approaches based on PIV measurements.

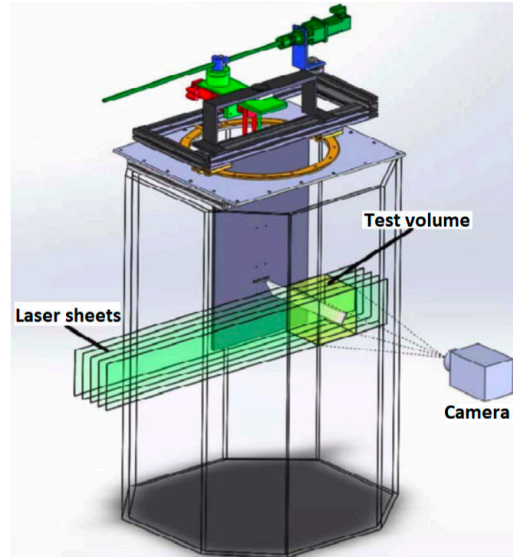


Figure 1: Sketch of the experimental setup.

2.3 Numerical simulations

The flow around the flapping wing is computed using the flow solver StarCCM+. The latter directly solves the three-dimensional Navier–Stokes equations using a cell-centered finite volume method. An overset mesh approach is employed where the wing is embedded in a small cylindrical domain which moves in a larger background cylindrical domain. Systematic exploration of the parameter space is performed using a relatively coarse spatial and temporal resolution where the wing surface and the wake are discretized using 50 and 25 cells per chord length, respectively, and 250 time steps per flapping period are used. Higher resolutions with 200 and 100 cells per chord length, respectively, and 1000 time steps per period are then used to analyze optimal configurations.

3 Results

We first fix the flapping amplitude to 120° and vary the upstroke and downstroke angles of attack. Figure 3 displays the time-average vertical force coefficient \bar{C}_V as a function of the time-average vertical force to power coefficients ratio \bar{C}_V/\bar{C}_P for different pairs of angles of attack. It is shown that maximum efficiency is obtained for lower angles of at-

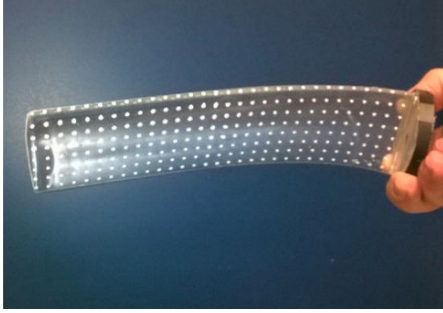


Figure 2: Photography of a flexible wing with markers for deformation measurements.

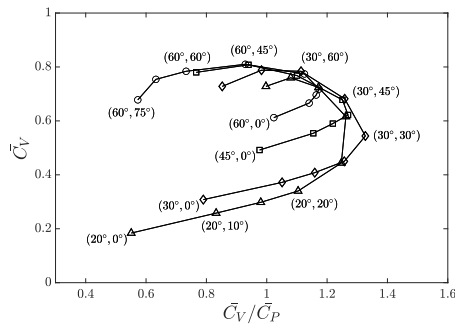


Figure 3: \bar{C}_V vs. \bar{C}_V/\bar{C}_P obtained for a rigid flapping wing with different upstroke and downstroke angles of attack.

tack than those yielding maximum vertical force. Plotting these quantities as a function of the mean angle of attack shows that the data somewhat collapse onto a single curve, as shown for \bar{C}_V in figure 4. Maximum \bar{C}_V and maximum \bar{C}_V/\bar{C}_P are found to be obtained for $\bar{\alpha} = 57^\circ$ and $\bar{\alpha} = 38^\circ$, respectively. We then analyze the role of pitch rate and show that to leading order, the latter influences aerodynamic performance through direct modification of the mean angle of attack $\bar{\alpha}$. Again, this is put into evidence by the data collapsing onto the single curve shown in figure 4. We further extend our analysis to additional flapping amplitudes and demonstrate that the above results hold for amplitudes ranging from 75° to 180° , encompassing amplitudes found in nature. In addition, it is shown that larger amplitudes can enhance efficiency while shorter amplitudes can enhance vertical force. For constrained amplitudes, imposed by mechanical constraints at the wing root, it is possible to indirectly increase the effective amplitude through wing flexibility. We thus investigate the influence of flexibility on aerodynamic performance. We first compare numerical and experimental data obtained for a reference case located on the Pareto front of figure 3 and show that reasonable agreement is obtained for wing deformation, as indicated in figure 5 which plots the position of markers at a given instant during the flapping cycle. We then introduce flexibility to this case and demonstrate that aerodynamic performance can significantly be enhanced.

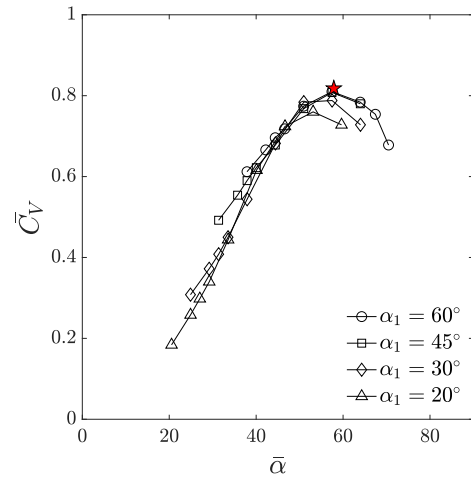


Figure 4: \bar{C}_V vs. $\bar{\alpha}$ obtained for a rigid flapping wing with different upstroke and downstroke angles of attack.

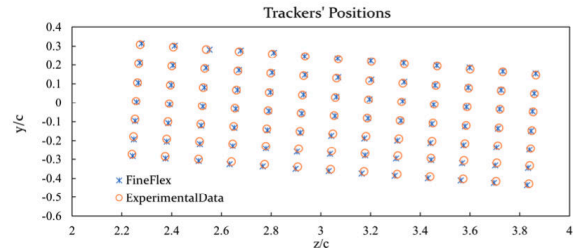


Figure 5: Positions of markers placed on the wing. Comparison between experiments and simulations at a given instant during the flapping period.

4 Conclusion

We use experiments and high-fidelity numerical simulations to investigate the influence of angle of attack, pitch rate, flapping amplitudes and wing flexibility on the aerodynamic of flapping wings under hovering flight conditions. We show that the mean angle of attack drives both efficiency and vertical force, to leading order, despite the increase contribution of drag to vertical force in asymmetric configurations. We also show that flexibility can help further increase aerodynamic performance, partly due to the indirect increase in effective flapping amplitude.

References

- [1] Ellington, C. P. The aerodynamics of hovering insect flight. *Transactions of the Royal Society of London. B, Biological Sciences*, 305(1122): 1-181, 1984.
- [2] Lee, Y. J. & Lua, K. B. Optimization of simple and complex pitching motions for flapping wings in hover. *AIAA Journal*, 56(6): 2466-2470, 2018.
- [3] Gehrke, A. & Mulleners, K. Phenomenology and scaling of optimal flapping wing kinematics. *Bioinspiration & Biomimetics*, 16(2): 026016, 2021.
- [4] Diaz-Arriba, D., Jardin, T., Gourdain, N., Pons, F. & David, L. Numerical investigation of three-dimensional asymmetric hovering flapping flight. *Physics of Fluids*, 33(11), 111907, 2021.

Optimal blade pitching to solve the VAWT dynamic stall dilemma

Sébastien Le Fouest, Alexander Gehrke and Karen Mulleners*

UNFoLD, Institute of Mechanical Engineering, École Polytechnique Fédérale de Lausanne,
CH-1015 Lausanne, Switzerland.¹

*Correspondence: karen.mulleners@epfl.ch

Vertical-axis wind turbines feature many advantages to complement traditional wind turbines in power production including omni-directionality, low noise production, and scalability. The inherent aerodynamic complexity of vertical-axis wind turbines has challenged their development for large-scale power production. The effective flow conditions acting on the turbine blade vary periodically as they result from a vectorial combination of the free-stream velocity and the blade velocity, assuming the induced velocity from blade-vortex interactions is small. The amplitude of the effective flow variation is governed by the ratio between the blade velocity and free-stream velocity, also known as the tip-speed ratio $\lambda = \frac{R\omega}{U_\infty}$. The theoretical angle of attack variation derived from the trigonometric relationship between the blade velocity and the incoming flow velocity can be expressed as: $\alpha_{\text{trig}} = \tan^{-1}(\sin(\theta)/(\lambda + \cos(\theta)))$, where θ is the blade's azimuthal position, assuming it begins its rotation facing the wind. For a turbine operating at low tip-speed ratios typically below 3, the blade exceeds its static stall angle, leading to dynamic stall [1]. This phenomenon is characterised by the formation, growth and shedding of large-scale dynamic stall vortices [2]. Vortex formation is responsible for a significant spike in power production, while vortex shedding causes highly transient and heavy loads that vary cycle-to-cycle and jeopardise the turbine's structural integrity [3]. Wind turbines face a dilemma: producing torque while avoiding failure.

We experimentally evaluate the potential of active blade pitching to alter the occurrence of dynamic stall on low tip-speed ratio turbines. We use a genetic algorithm to find the optimal individual blade kinematics based on two performance objectives: maximising the blade torque production and minimising the load transients related to flow separation. To distinguish load fluctuation related to the blade kinematics from load transients caused by flow separation, we use a diagnostic tool that compares experimental loads to an adapted Greenberg model for wind turbine blade kinematics [5]. The unsteady loads acting on the blade that executes optimal pitching kinematics will be compared to the baseline loads experienced by the non-pitching blade. Further analysis will characterise how active blade pitching affects the spatio-temporal evolution of timescales, flow structures, and loads on a turbine blade undergoing dynamic stall.

¹This work was supported by the Swiss national science foundation under grant number PYAPP2.173652.

Preliminary measurements were performed in the recirculating free surface water channel at EPFL which has a test section of dimensions $0.6 \text{ m} \times 0.6 \text{ m} \times 3 \text{ m}$ and a maximum flow velocity of 1 m/s. A scaled-down model of a single-bladed H-type Darrieus wind turbine was mounted in the centre of the test section. The turbine blade has a NACA0018 profile, with a 6 cm chord and 15 cm span. The turbine diameter was kept constant at 30 cm yielding a chord-to-diameter ratio of 0.2. The turbine model is motor driven and its rotational frequency was kept constant at 0.89 Hz, yielding a constant chord-based Reynolds number of $Re_c = (\omega R c)/\nu = 50000$, with ωR the rotational velocity of the blade and ν the kinematic viscosity. The incoming flow speed was set to $U_\infty = 0.56 \text{ m/s}$, yielding a constant tip-speed ratio of $\lambda = 1.5$. This tip-speed ratio was selected to ensure the wind turbine is within the deep-stall regime, where there is the highest potential for power production, as well as the highest risk for load transients related to flow separation. The blade is pitched about its quarter-chord axis with a position accuracy of 0.075° using a stepper motor and gearbox. The temporal evolution of the pitching motion can be completely arbitrary and independent of the main rotation. The blade shaft was equipped with twenty strain gages forming five full Wheatstone bridge channels. The strain gages are powered and their output signal is amplified using an instrumentation amplifier with precision voltage reference placed on a printed circuit board that is mounted directly on the rotor arm. This on-board load cell is used to measure unsteady loads acting on the blade at 1000 Hz for three relevant components: the shear forces acting orthogonally and tangentially to the circular path of the blade, referred to as the radial and azimuthal force, and the axial moment. All three components achieve an experimental uncertainty below 3 % on the full measurement range.

A genetic algorithm-based experimental optimisation of the pitching kinematics is implemented using the MATLAB global optimization toolbox [6]. The algorithm has two objectives: maximising the blade's torque production and minimising the power required for blade pitching. Future work will implement a third objective to minimize load transients related to flow separation using the diagnostic tool from [5]. The pitching kinematics were parametrised using a sum of 3 sine waves with frequencies that are multiples of the main rotational frequency ω : $\alpha_{\text{pitch}}(t) = \sum_{n=1}^3 A_n \sin(n\omega t + \theta_n)$, with A_n the amplitude and θ_n the

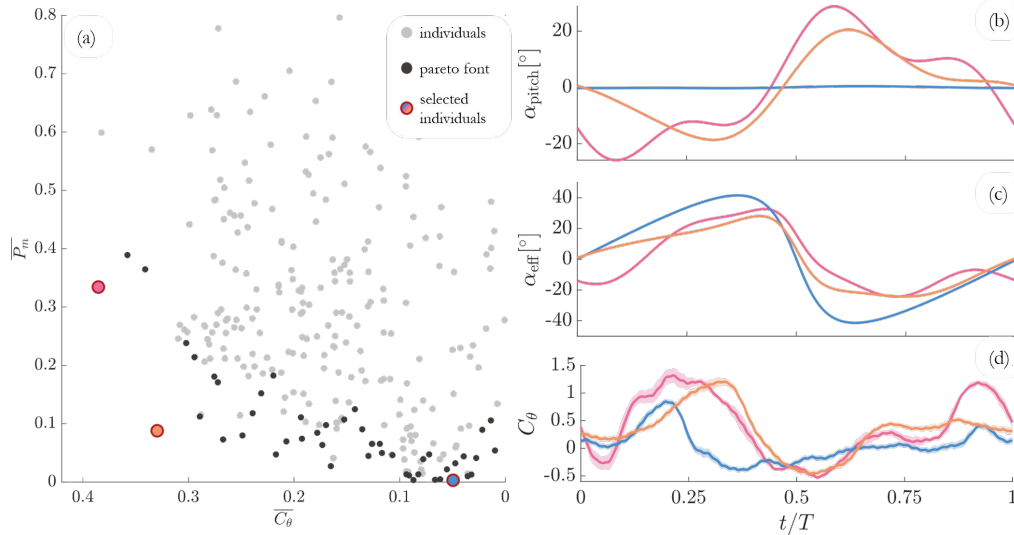


Figure 1: Preliminary results from the optimisation of the pitching kinematics of the turbine blade.

phase shift of the n^{th} sine wave. The values of the amplitude coefficients were bounded: $A_1 \in [-31^\circ, 0^\circ]$, $A_2 \in [0^\circ, 21^\circ]$, and $A_3 \in [-10.5^\circ, 0^\circ]$. These boundaries were chosen to allow the blade to pitch by an angle comparable to the maximum expected angle of attack for a wind turbine blade operating at tip-speed ratio of $\lambda = 1.5$. Additional variation was given to the pitching kinematics by allowing phase shifts $\theta_n \in [-45^\circ, 45^\circ]$ on all sine waves. Initial results were gathered as a proof of concept for this extended abstract. The genetic algorithm ran for 10 generations, each of which had a population of 30 individuals, resulting in 300 kinematics tested. The 300 experiments are not enough to yield fully converged optimisation results, but should suffice to validate the methodology and give an idea of the type of results we hope to present at DisCoVor.

Preliminary results of the experimental optimisation of the pitching kinematics of a turbine blade are summarised in fig. 1. The mean phase-averaged pitching power versus azimuthal force coefficient is presented in fig. 1a for all tested individuals. The darker symbols indicate Pareto-optimal individuals. The horizontal axis is inverted following standard conventions. Individual blade pitching can increase the mean phase-averaged azimuthal force coefficient up to 0.38 based on these preliminary results. The temporal evolution of the prescribed pitching profile, the effective angle of attack, and the azimuthal force coefficient for three selected Pareto-optimal individuals are presented in fig. 1b-d. The individual that required minimum pitching power has zero pitching amplitude and represents a base-case for comparison. The individual that yielded highest torque production had a higher pitching amplitude than the other two selected individuals (fig. 1c). The effective angle of attack is defined as the sum of the theoretical angle of attack variation experienced by a non-pitching turbine blade α_{trig} and the pitching profile executed by the turbine blade α_{pitch} . The intermediate individual achieved a slower rise and lower ampli-

tude in effective angle of attack compared to the base case, resulting in a significant peak in azimuthal force around $t/T = 0.35$. This peak is comparable to the peak achieved by the strongest individual around the same time. The pitching kinematics of the intermediate individual resulted in a 380% increase in mean azimuthal force compared to the base case, while only requiring a third of the pitching power demand compared to the strongest individual. Final results will include fully converged solutions to the pitching kinematics optimisation, which will feature a more densely populated Pareto front. Time-resolved particle image velocimetry will be acquired to determine the impact of active flow control on the timescales, strength and size of coherent flow structures, specifically leading-edge dynamic stall vortices. A detailed discussion about the interplay between the spatio-temporal evolution of the flow field and unsteady loads will be presented for selected Pareto-optimal individuals.

References

- [1] Abel John Buchner, Julio Soria, Damon Honnery, and Alexander J. Smits. Dynamic stall in vertical axis wind turbines: Scaling and topological considerations. *Journal of Fluid Mechanics*, 841:746–766, 2018.
- [2] Karen Mulleners and Markus Raffel. The onset of dynamic stall revisited. *Experiments in Fluids*, 52(3):779–793, 2012.
- [3] Pablo Ouro, Thorsten Stoesser, and Luis Ramirez. Effect of blade cambering on dynamic stall in view of designing vertical axis turbines. *Journal of Fluids Engineering*, 140:1–12, 2018.
- [4] J.M.R. Gorle, L. Chatellier, F. Pons, and M. Ba. Modulated circulation control around the blades of a vertical axis hydrokinetic turbine for flow control and improved performance. *Renewable and Sustainable Energy Reviews*, 105:363–377, 2019.
- [5] David Bensason, Sébastien Le Fouest, Anna Young, and Karen Mulleners. Greenberg’s force prediction for vertical-axis wind turbine blades. *AIAA journal (accepted for publication)*, nov 2021.
- [6] A.J. Chipperfield. The MATLAB Genetic Algorithm Toolbox. In *IEE Colloquium on Applied Control Techniques Using MATLAB*, volume 1995. IEE, 1995.

The effect of roughness on the locomotive properties of an swimming flat plate

Jonathan Massey^{a,*}, Gabriel Weymouth^{a,b}, Bharathram Ganapathisubramani^a

^a Engineering and Physical Sciences, University of Southampton, Southampton, UK ¹

^b Data-Centric Engineering, Alan Turing Institute, London, UK

*Correspondence: jmom1n15@soton.ac.uk

1 Introduction

Underwater propulsion is an area of research that brings together engineers and biologists alike; it has fostered a deeper understanding of aquatic locomotion and inspired innovation in underwater systems. The kinematics have the most significant effect on the locomotive properties of aquatic animals; however, the inconspicuous intricacies of animal evolution, like Sharks' skin, have sparked research into the hydrodynamic benefits of aquatic surface textures.

During steady aquatic locomotion, animals exert force on the surrounding water, analogous to a travelling wave with increasing amplitude. Mathematically the excursion of the body from the centre-line can be defined as

$$y(x) = A(x) \sin(\omega t - kx) \quad (1)$$

where all the lengths are scaled by the chord length c , and all times by c/u_∞ . x denotes the position along the body, $A(x)$ is the function to define the amplitude envelope, k is the wavenumber, and $\omega/2\pi = St u_\infty / (2A(c))$ is the specific frequency of the oscillation defined by Strouhal number (St). [1] tested the kinematics of 53 different types of fish based on Lighthill's elongated body theory and found that for high aspect-ratio tails, the optimal Strouhal number range was $St = 0.2 - 0.4$, they also showed the tail beat amplitude to be in the range $A(c) = 0.05 - 0.15$.

The denticles or placoid scales found on sharks have been a prevalent flow control research topic since the 80s, but despite its intricate design, there is not any agreement as to whether shark skin is an effective drag reduction mechanism ([2]). To understand the potential hydrodynamic benefit of shark skin, we must look at them under their natural swim cycle. Whilst swimming, the skin uses passive control in the flank region to bristle the skin, increasing boundary layer mixing and helping to keep the flow attached at areas of flow reversal. Experiments have shown that the bristling can increase the swimming efficiency of a flat plate covered in biomimetic shark skin [3]. However, using biomimetic denticles vs traditional vortex generators is not significant. The mechanisms attributed to shark skin for drag reduction

bear a distinct resemblance to those found on more simple roughness topologies, and it does not seem as though the intricate shape of the denticle is particularly important.

In this work, we will study how a low parameter roughness topology [4] affects the locomotive characteristics of a flat plate. The amplitude envelope ($A(x)$) we use is the generalised Body Caudal Fin (BCF) [5] which has $A(c) = 0.1c$ as per [1]. We will use an infinite span flat plate of thickness $0.03c$ and $Re = 12,000$. In this abstract, we present the first part of this work to determine the best kinematics for Self Propelled Swimming (SPS) for a smooth plate.

First, we perform a grid search to populate the parameter space of our optimisation. Next, we will use Brent's method to find k that results in SPS for $St = 0.2 - 0.4$. Then, we will determine the power required to maintain SPS with the range of SPS kinematics. Finally, minimising the power for SPS will result in the single fully defined kinematic, which we will compare against the optimal kinematic determined in the same way for the rough topology.

2 Results

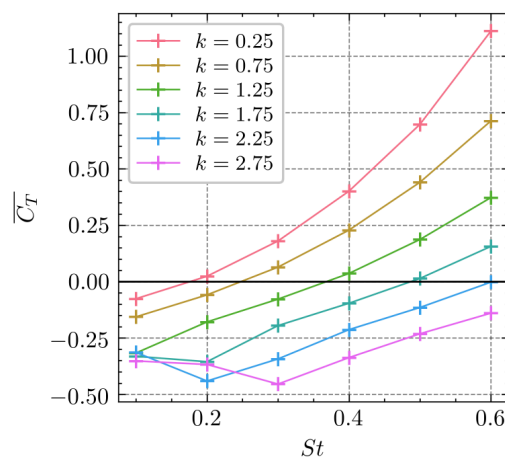


Figure 1: Grid search to find SPS at a range of wavenumbers.

In Fig. 1 we calculate C_D at a range of $St(0.1, 0.6)$ for samples of k . The grid-search gives us a map of the effect k has

¹This work was supported by the Office of Naval Research under grant number N62909-18-1-2091

on C_T given St , and the black line represents SPS. To get the kinematics of SPS, we use Brent's method to determine the exact k for a given St that give us zero net force in the system. The relationship of k and St for SPS gives us a range of possible kinematics to analyse.

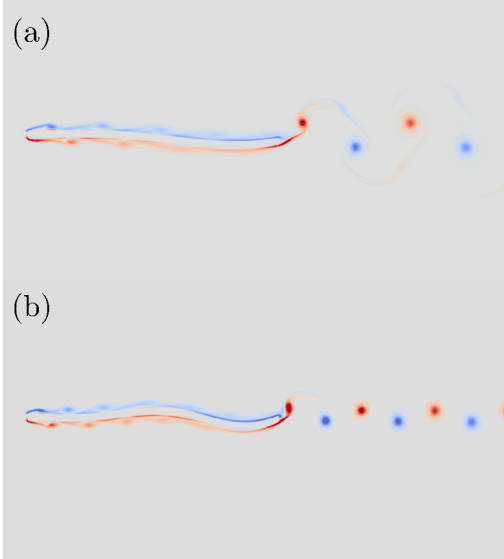


Figure 2: A vorticity plot of a thin flat plate undergoing SPS at (a) $St = 0.25$ (b) $St = 0.4$

Fig. 2 and shows SPS for $St = 0.25, 0.4$. We can see just how different the flow structures for each of these cases are. $St = 0.25$ gives us the characteristic vortex pairs we traditionally associate with SPS, and $St = 0.4$ exhibits a much more tightly packed structure but with more instability in the boundary layer due to the higher frequency shedding coming off the leading edge. To find the optimum kinematics in the SPS range, we determine the power required to maintain the state. We use C_P and define it as

$$C_P = \frac{F_n \cdot \vec{v} ds}{0.5 \rho U_\infty^3 A_s} \quad (2)$$

where F_n is the force normal to the body, and \vec{v} is the body velocity, ρ is the density, U_∞ the free-stream velocity, and A_s the surface area.

Fig. 3 shows that, for the smooth plate kinematics where $St = 0.29, k = 0.9$ require the minimum power to maintain SPS at $Re = 12,000$. There is a sweet spot in the range $St = 0.25 - 0.3$ where C_P is not significantly affected. We estimate that this sweet spot will exist for the rough surface through a larger span of St as the turbulent mixing will reduce the growth of the instabilities. However, the optimum kinematics for the rough surface will likely require more power to maintain SPS due to the increased viscous forces.

3 Conclusion

We have optimised the kinematics for a flat plate undergoing SPS at $Re = 12,000$. At *Discover 2022* we will show the

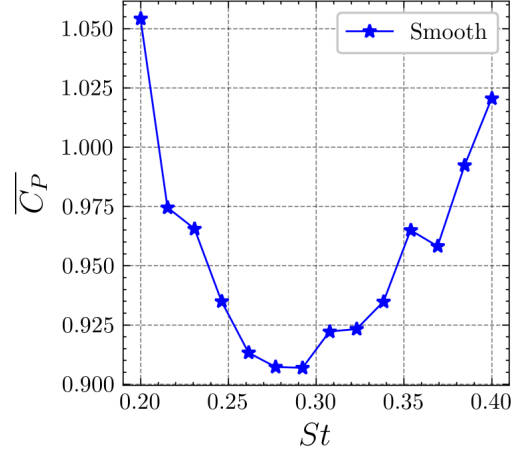


Figure 3: Power required to maintain SPS at a given St .

effect that roughness has on the locomotive properties of a flat plate. To define the upper and lower surface of the plate, we will use a low parameter roughness distribution set out in [4]. The procedure to determine the optimum kinematics will be the same laid out in this abstract. We will finally compare the smooth and the rough plate focusing on how Fig. 3 is affected and why.

References

- [1] M. Saadat, F. E. Fish, A. G. Domel, V. Di Santo, G. V. Lauder, and H. Haj-Hariri. On the rules for aquatic locomotion. *Physical Review Fluids*, 2(8):083102, 8 2017.
- [2] Brian Dean and Bharat Bhushan. Shark-skin surfaces for fluid-drag reduction in turbulent flow: a review. *Philosophical Transactions of the Royal Society A: Mathematical, Physical and Engineering Sciences*, 368(1929):4775–4806, 2010.
- [3] Li Wen, James C. Weaver, and George V. Lauder. Biomimetic shark skin: design, fabrication and hydrodynamic function. *Journal of Experimental Biology*, 217(10):1656–1666, 5 2014.
- [4] L Chan, M Macdonald, D Chung, N Hutchins, and A Ooi. A systematic investigation of roughness height and wavelength in turbulent pipe flow in the transitionally rough regime. *J. Fluid Mech*, 771:743–777, 2015.
- [5] Valentina Di Santo, Elsa Goerig, Dylan K Wainwright, Otar Akanyeti, James C Liao, Theodore Castro-Santos, and George V Lauder. Convergence of undulatory swimming kinematics across a diversity of fishes. *Proceedings of the National Academy of Sciences of the United States of America*, 118(49), 12 2021.

Contribution of spanwise and streamwise vortex structures to the force on a lifting surface: Insights from force partitioning

Karthik Menon ^{a,b} and Rajat Mittal ^{a*}

^a Johns Hopkins University, Baltimore, MD, USA ¹

^b Stanford University, Stanford, CA, USA

*Correspondence: mittal@jhu.edu

1 Introduction

This study reports on the vortex-induced lift production mechanisms in low Reynolds number flows over rectangular low aspect-ratio wings. In flows over finite-span wings (or finite wings), three-dimensional vortex structures have been shown to exhibit highly non-linear evolution and their influence on aerodynamic loads has been shown to depend on a variety of factors. For instance, while the tip-vortex is generally considered detrimental to lift on static wings, it can be beneficial in flapping flight [1, 2]. Similarly, interactions between the LEV and tip-vortices in flows over finite wings effect their influence on the production of aerodynamic forces on such wings [3, 4]. These complexities have motivated numerous studies of the effect of wing shape, kinematics and other factors on the three-dimensional vortex dynamics over such wings as well as their associated aerodynamic load generation.

However, although past studies have highlighted the important vortex structures in flows over finite wings, as well as their contribution to aerodynamic loads, they have generally *qualitatively* correlated the spatio-temporal evolution of particular vortices to observed aerodynamic loads on the wing. Furthermore, in recent work [5] we showed that although the majority of past work has focused on the role of vortices, i.e. *rotation-dominated* regions of the flow, in aerodynamic force generation, these vortices are in fact surrounded by regions of *strain-dominated* flow which can have a significant impact and whose physics are often overlooked. The aim of this work is therefore to demonstrate the use of a force partitioning method (FPM) [6] to *quantitatively* evaluate the distinct contributions of important types of vortex structures on aerodynamic load generation on finite wings. In addition, this method allows us to separate the influence of rotation-dominated regions from strain-dominated regions of the flow in the generation of aerodynamic loads.

The specific focus of this study is on the roles that vortex structures corresponding to spanwise oriented and cross-span oriented vorticity play in lift production. The motivation for distinguishing spanwise from cross-span vorticity contributions is to quantify the importance of 3D vortices

¹This work was supported by AFOSR under grant number FA9550-16-1-0404.

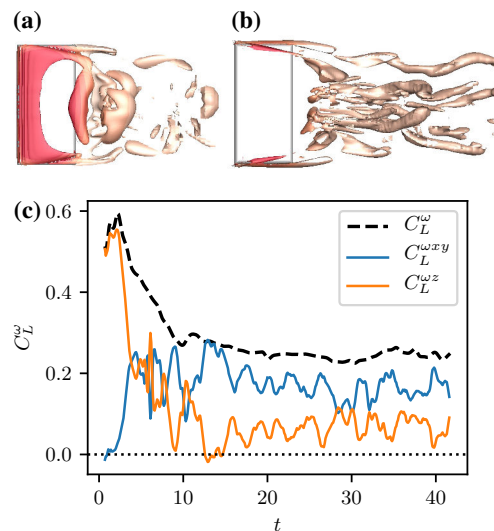


Figure 1: Visualizations of spanwise and cross-span vortex structures are shown in (a) and (b). Total vortex-induced lift (C_L^ω) compared with cross-span ($C_L^{\omega xy}$) and spanwise ($C_L^{\omega z}$) contributions are shown in (c).

such as the leading-edge vortex (LEV), which is predominantly spanwise-oriented. Furthermore, we also analyze the influence of the rotation-dominant and strain-dominant regions associated with these flow structures over the wing as well as in its wake. As we will show, the analyses highlight interesting aspects of the spatio-temporal evolution of these flow structures and their influence on lift generation over finite wings.

2 Results

The results are briefly discussed for a 2:1 aspect ratio rectangular wing, placed in a uniform incoming flow-field at $Re = 1000$. The separation of flow-field regions corresponding to spanwise and cross-span vortices is performed using a simple method based on the the direction of the vorticity unit vector at every point in the flow-field. We identify “spanwise oriented” vorticity very simply as regions where the angle between the local vorticity vector and the Z-direction is less than 45° . Figures 1(a) and 1(b) show snapshots of vor-

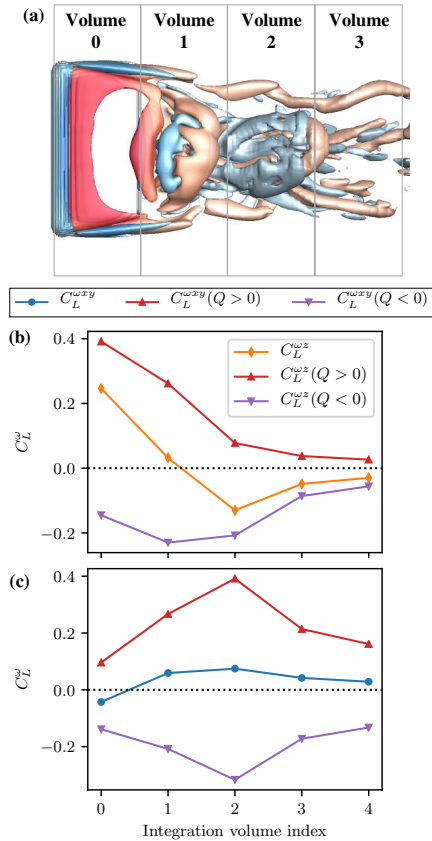


Figure 2: Lorem ipsum dolor sit amet, consectetur adipiscing elit.

tex structures (visualized using Q -criterion) corresponding to spanwise and cross-span vorticity-containing regions respectively. The regions isolated as spanwise and cross-span vortices are then used in the FPM formulation to estimate their corresponding vortex-induced lift contributions. In figure 1(c) we show a comparison of total vortex-induced lift (C_L^{ω}) with the contributions from regions containing spanwise ($C_L^{\omega_z}$) and cross-span ($C_L^{\omega_{xy}}$) vorticity. Due to the presumed dominance of the LEV, we expect spanwise vorticity to be the major contributor to lift, however figure 1(a)(c) shows that cross-span vorticity is in fact the larger contributor to the lift on the wing.

The counter-intuitive dominance of non-spanwise vortices in lift production is investigated by isolating the lift produced in different regions of the flow around the wing, as well as by quantifying the lift induced by rotational cores and the associated strain regions of these vortices. Figure 2(a) shows the different regions of the flow-field analyzed. Figure 2(b) shows that although the lift due to spanwise vortices ($C_L^{\omega_z}$) is indeed dominant over the wing, it rapidly drops in the wake and, surprisingly, produces negative lift in the near-wake. On the other hand, the lift due to non-spanwise vortices ($C_L^{\omega_{xy}}$), shown in figure 2(c), increases in the wake of the wing, thus producing an overall larger lift contribution. This can be explained by analyzing the contributions

of vortex cores ($Q > 0$) and their associated regions of strain ($Q < 0$) for each of these two kinds of vortex structures. Figure 2(b) indicates that the lift contributed by the spanwise vortex cores quickly dissipates in the near wake, whereas the negative lift due to the straining regions does not. This has the effect of a net lift loss in the near wake. Conversely, figure 2(c) shows that the cross-span structures exhibit the opposite behaviour, resulting in a net lift enhancement in the wake. This behaviour can be attributed to the non-linear effect of vortex stretching and tilting.

3 Conclusion

We use a force partitioning method which allows the estimation of the roles that vortex structures corresponding to spanwise oriented and cross-span oriented vorticity play in lift production. We quantify the lift induced on the wing by these different kinds of vortices, and also estimate their influence within different regions of the flow-field around the wing and in the wake. We show that although the spanwise oriented leading-edge vortex is generally thought to be the dominant mechanism for force production at low Reynolds numbers, the spanwise vorticity in fact does not dominate the overall lift production on the rectangular wing. Furthermore, the spanwise vorticity is capable of producing net negative lift in the wake of the wing. We explain this by separating and quantifying the influence of vortex cores and regions of strain in the wake. Due to non-linearities associated with vortex stretching and tilting, rotational and strain regions of vorticity exhibit different spatio-temporal evolution over the wing and have important effects on the lift production due to spanwise and non-spanwise vorticity.

References

- [1] Wei Shyy, Pat Trizila, Chang Kwon Kang, and Hikaru Aono. Can tip vortices enhance lift of a flapping wing? *AIAA Journal*, 47(2):289–293, 2009.
- [2] Pat Trizila, Chang Kwon Kang, Hikaru Aono, Wei Shyy, and Miguel Visbal. Low-reynolds-number aerodynamics of a flapping rigid flat plate. *AIAA Journal*, 49(4):806–823, 2011.
- [3] Kunihiko Taira and Tim Colonius. Three-dimensional flows around low-aspect-ratio flat-plate wings at low Reynolds numbers. *Journal of Fluid Mechanics*, 623:187–207, 2009.
- [4] Ryan T. Jantzen, Kunihiko Taira, Kenneth O. Granlund, and Michael V. Ol. Vortex dynamics around pitching plates. *Physics of Fluids*, 26(5), 2014.
- [5] Karthik Menon and Rajat Mittal. Significance of the strain-dominated region around a vortex on induced aerodynamic loads. *Journal of Fluid Mechanics*, 918(R3):1–10, 2021.
- [6] Karthik Menon and Rajat Mittal. Quantitative analysis of the kinematics and induced aerodynamic loading of individual vortices in vortex-dominated flows: a computation and data-driven approach. *Journal of Computational Physics*, 443:110515, 2021.

Two-dimensional stability of two unconstrained swimmers: Effects of phase synchrony and Lighthill number

Pedro Ormonde^{*}, Amin Mivehchi and Keith Moored
Lehigh University, Mech. Eng. & Mechanics Dept, Bethlehem, PA USA¹
^{*}Correspondence: pc0218@lehigh.edu

1 Introduction

Collectives of swimming and flying animals are commonly found in nature. Several aspects of this phenomenon have been studied in light of biological motivations such as the social aspects of schooling [1–4], food search efficiency [5] and protection from predation [6, 7]. Several models [4, 8–13] propose simple sets of interaction rules to describe the collective behavior of schools based on conditions proposed *a priori*, disregarding the hydrodynamic forces acting upon the swimmers.

Studies [14–18] have shown that flying and swimming in formations can improve their performance and reduce their energetic cost of locomotion, but little is known about the stability of these arrangements [19–22].

A recent study [23] from our research group showed, *for the first time*, that a minimal school of two swimmers can be two-dimensionally stable for a side-by-side configuration with anti-phase synchrony, $\phi = \pi$. Figure 1 presents the final equilibrium configuration achieved by the system.

The objective of the present study is to expand the current set of parameters investigated in this previous study and search for stable equilibrium configurations for swimmers with other phase synchronies ϕ , not just in anti-phase, as well as stable configurations for swimmers of different Lighthill numbers. The methodology is described in the next section.

2 Methods

The water channel apparatus used in [23] simulates a minimal school of two swimmers: One hydrofoil is fixed relative to the water channel (the leader) and the second is connected to a platform supported by air bearings (the follower), and is free to move both in the streamwise (x) and cross-stream (y) direction (see Figure 2). One limitation of this setup is the determination of the free-swimming speed, and consequently the Strouhal number and reduced frequency. For anti-phase kinematics it is possible to tune the freestream velocity in order to minimize the equilibrium position X_{eq}^* given the symmetry of the problem, in accordance with our 2D potential flow simulations. This method is not valid,

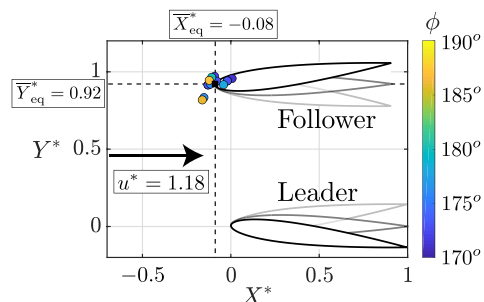


Figure 1: Equilibrium position of the side-by-side arrangement for an unconstrained follower free to move in the X^*-Y^* plane. The equilibrium position markers represent the final positions of individual experiments and their color is mapped to the synchrony of the follower in the range of $170^\circ \leq \phi \leq 190^\circ$. An average equilibrium position is found at $(\bar{X}_{eq}^*, \bar{Y}_{eq}^*) = (-0.08, 0.92)$. The resulting formation achieves a normalized swimming speed of $u^* = 1.18$, which is 18% higher than that of an isolated swimmer.

however, for other phase synchronies given that the kinematics of one swimmer is not the mirror image of the other.

The present study proposes modifying the current experimental setup in order to explore whether stable organizations also emerge naturally for different phase synchronies ϕ and for two swimmers of different Lighthill numbers. The Lighthill number essentially represents the effect of drag acting on a swimmer’s body and is defined as $Li = C_D S_{wp}$ where C_D is the drag coefficient of the body of the swimmer and S_{wp} is a ratio of the total wetted area of body of the swimmer and propulsor to the planform area of the propulsor.

In free swimming the Lighthill number and prescribed kinematics dictate the swimming speed U , Strouhal number $St = fA/U$, reduced frequency $k = fc/U$ and chord-based Reynolds number $Re_c = Uc/\nu$, where c is the chord length of a foil, ν is the kinematic viscosity, f is the frequency of oscillation, and A is the peak-to-peak trailing edge amplitude. The Lighthill number will be varied by attaching drag generating bodies to the streamwise carriage of the supporting platform. The drag producing bodies are positioned sufficiently far from the leader and the follower to prevent them from disturbing the flow around the propulsor foils.

¹This work was supported by funding_agency under grant number ...

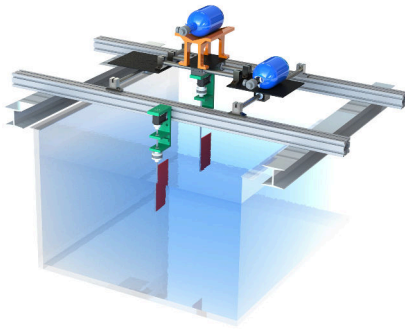


Figure 2: Schematics of the experimental apparatus. The leader foil is fixed to the water channel, and the follower foil is controlled via a wireless connection. Dual-axis air bearings support the follower and the embedded electronics, allowing for free-swimming of the follower in the streamwise and cross-stream directions.

3 Expected Results

As the experimental setup is enhanced to allow for both wings to swim freely in the horizontal plane, it is expected that new equilibrium configurations will be found. Having both swimmers unconstrained allows for studying how the phase synchrony ϕ and Lighthill number Li affect the side-by-side stable configuration. It is expected that both of these variables will modify the spatial arrangement of the pair, changing both the streamwise and cross-stream equilibrium position of the follower (relative to the leader), creating a stable staggered formation.

Large enough deviations from the stable side-by-side formation obtained for $\phi = \pi$ may also cause the system to lose its stability altogether, especially if the interactions between the two vortex wakes shed by the swimmers are changed substantially. Understanding what are the conditions in which stability breaks down will help us further understand the hydrodynamic forces involved in the spontaneous formation of stable arrangements like the ones discussed here.

It is also expected that the final swimming speed U will be different than that found for the anti-phase, side-by-side configuration. Since the surrounding flow field affects the performance of each swimmer (see Figure 3), changes in the phase synchrony and Lighthill number will likely alter the final efficiency of the pair, which in turn will modify the final swimming speed.

References

[1] James E Morrow Jr. Schooling behavior in fishes. *The Quarterly review of biology*, 23(1):27–38, 1948.
 [2] Charlotte K Hemelrijk and Hanno Hildenbrandt. Self-organized shape and frontal density of fish schools. *Ethology*, 114(3):245–254, 2008.
 [3] Ugo Lopez, Jacques Gautrais, Iain D Couzin, and Guy Theraulaz. From behavioural analyses to models of collective motion in fish schools. *Interface focus*, 2(6):693–707, 2012.

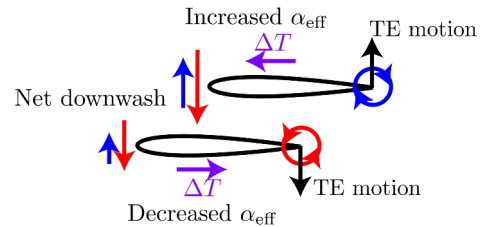


Figure 3: Schematic of proposed trailing-edge vortex mechanism responsible for a restorative force back to the stable side-by-side arrangement. Image extracted from [23].

[4] Michele Ballerini, Nicola Cabibbo, Raphael Candelier, Andrea Cavagna, Evaristo Cisbani, Irene Giardina, Vivien Lecomte, Alberto Orlandi, Giorgio Parisi, Andrea Procaccini, et al. Interaction ruling animal collective behavior depends on topological rather than metric distance: Evidence from a field study. *Proceedings of the national academy of sciences*, 105(4):1232–1237, 2008.
 [5] Hauke Reuter, Maren Kruse, Alberto Rovellini, and Broder Breckling. Evolutionary trends in fish schools in heterogeneous environments. *Ecological modelling*, 326:23–35, 2016.
 [6] Anne E Magurran and Anthony Higham. Information transfer across fish shoals under predator threat. *Ethology*, 78(2):153–158, 1988.
 [7] Brian L Partridge. The structure and function of fish schools. *Scientific american*, 246(6):114–123, 1982.
 [8] Craig W Reynolds. Flocks, herds and schools: A distributed behavioral model. In *Proceedings of the 14th annual conference on Computer graphics and interactive techniques*, pages 25–34, 1987.
 [9] Ichiro Aoki. A simulation study on the schooling mechanism in fish. *Bulletin of the Japanese Society of Scientific Fisheries*, 48(8):1081–1088, 1982.
 [10] Andreas Huth and Christian Wissel. The simulation of the movement of fish schools. *Journal of theoretical biology*, 156(3):365–385, 1992.
 [11] Yoshinobu Inada and Keiji Kawachi. Order and flexibility in the motion of fish schools. *Journal of theoretical Biology*, 214(3):371–387, 2002.
 [12] Guillaume Grégoire, Hugues Chaté, and Yuhai Tu. Moving and staying together without a leader. *Physica D: Nonlinear Phenomena*, 181(3-4):157–170, 2003.
 [13] Audrey Filella, François Nadal, Clément Sire, Eva Kanso, and Christophe Eloy. Model of collective fish behavior with hydrodynamic interactions. *Physical review letters*, 120(19):198101, 2018.
 [14] Steven J Portugal, Tatjana Y Hubel, Johannes Fritz, Stefanie Heese, Daniela Trobe, Bernhard Voelkl, Stephen Hailes, Alan M Wilson, and James R Usherwood. Upwash exploitation and downwash avoidance by flap phasing in ibis formation flight. *Nature*, 505(7483):399, 2014.
 [15] J Herskin and JF Steffensen. Energy savings in sea bass swimming in a school: measurements of tail beat frequency and oxygen consumption at different swimming speeds. *Journal of Fish Biology*, 53(2):366–376, 1998.
 [16] Erik Burgerhout, Christian Tudorache, Sebastiaan A Brittrijn, Arjan P Palstra, Ron P Dirks, and Guido EEJM van den Thillart. Schooling reduces energy consumption in swimming male european eels, *anguilla anguilla* l. *Journal of experimental marine biology and ecology*, 448:66–71, 2013.
 [17] Faust R Parker Jr. Reduced metabolic rates in fishes as a result of induced schooling. *Transactions of the American Fisheries Society*, 102(1):125–131, 1973.
 [18] Stefano Marras, Shaun S Killen, Jan Lindström, David J McKenzie, John F Steffensen, and Paolo Domenici. Fish swimming in schools save energy regardless of their spatial position. *Behavioral ecology and sociobiology*, 69(2):219–226, 2015.
 [19] Sophie Ramanarivo, Fang Fang, Anand Oza, Jun Zhang, and Leif Ristroph. Flow interactions lead to orderly formations of flapping wings in forward flight. *Physical Review Fluids*, 1(7):071201, 2016.

- [20] Longzhen Dai, Guowei He, Xiang Zhang, and Xing Zhang. Stable formations of self-propelled fish-like swimmers induced by hydrodynamic interactions. *Journal of The Royal Society Interface*, 15(147):20180490, 2018.
- [21] Joel W Newbolt, Jun Zhang, and Leif Ristroph. Flow interactions between uncoordinated flapping swimmers give rise to group cohesion. *Proceedings of the National Academy of Sciences*, 116(7):2419–2424, 2019.
- [22] Ze-Rui Peng, Haibo Huang, and Xi-Yun Lu. Collective locomotion of two closely spaced self-propelled flapping plates. *Journal of Fluid Mechanics*, 849:1068–1095, 2018.
- [23] Melike Kurt, Pedro Ormonde, Amin Mivehchi, and Keith Moored. Two-dimensionally stable self-organization arises in simple schooling swimmers through hydrodynamic interactions. *arXiv preprint arXiv:2102.03571*, 0(0):1–11, 2021.

Flight Behavior of a Smoldering Spherical Particle

Bikash Mahato, Saurabh Saxena and Neda Yaghoobian*

Florida State University, Department of Mechanical Engineering, Tallahassee, FL, USA¹

*Correspondence: nyaghoobian@eng.famu.fsu.edu

1 Introduction

Spotting is an erratic fire propagation mechanism associated with the transport of burning or smoldering debris by the wind and their subsequent landing. The debris is created from local fuel at the vicinity of the main fire and is lofted to the atmosphere by updraft currents. Once airborne, this debris is carried away by the wind and, on landing, can ignite local fuel far downwind the main fire front, generating secondary fires known as spot fires. Due to its intermittent nature, the spotting process makes the overall behavior of wildfires and their propagation even more difficult to predict. Spotting is also known to be the major mechanism of fire propagation to communities in the wildland-urban interface (WUI) fires [1–4], and its erratic nature can pose serious threats to human lives and properties in WUI communities. [5–7]

The transport of firebrands is characterized by the forces exerted by the local wind on smoldering particles. As a result, the study of firebrand flight behavior, their landing distribution, and thus, spot fire risks are critically dependent on understanding the interaction of the evolving firebrands with the immediate wind field and the characteristics of the particles in terms of their shape, size, material, surface temperature, and smoldering condition. Despite a large body of research on firebrand transport, detailed investigations of the flight behavior of a single smoldering particle is missing in the literature. A comprehensive analysis of the interaction between smoldering particles and their immediate flow field can lead to a better understanding of the firebrand transport phenomena and the possible risk of spot fire. In this study, we develop a computational model to investigate the flight dynamics of a single firebrand particle under the influence of realistic evolving smoldering heat over its surface. The aerodynamic forces on the firebrand particle are obtained using direct numerical simulation (DNS) under the effect of spatiotemporally varying thermal forces from the firebrand surface. The temperature evolution over the surface of the firebrand particle is obtained from a novel detailed surface energy balance model, which is capable of simulating the energy budget over objects of any complex-shape geometries and material properties, under any environmental conditions.

¹This work was supported by funding from the Department of Defence under grant SERDP RC20-1298

2 Results

The non-dimensional incompressible Navier-Stokes equations with Boussinesq approximation are solved to capture the time-evolving flow dynamics over the smoldering sphere. [8]

Figure 1(a)-(c) shows different views of flow structures (q -criterion) at an instantaneous time (Time = 200) of the continuously evolving flow field. The formation of two tunnel-shaped vortices in the wake region is being observed for surface temperature greater than 80°C. The unusual vortex structure is due to the buoyancy-driven flow taking place near the sphere surface. The buoyancy-driven upward moving flow disturbs the regular vortex dynamics and creates two opposite rotating tunnel-shaped vortices, as shown in the schematics in Fig. 1(d). We have observed that, the position and strength of the vortices depends on the temperature of the surface of the sphere.

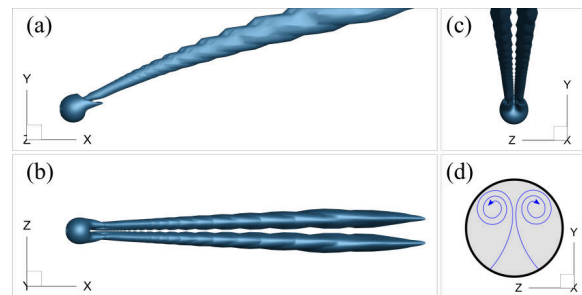


Figure 1: (a) Side view, (b) top view, and (c) view from downstream direction. (d) Schematic of the streamlines generated behind the sphere.

The variation of drag and lift coefficient over time is calculated and shown in Fig. 2. The drag coefficient on the sphere shows a similar trend as the average external surface temperature. An increase in surface temperature causes a thicker thermal boundary layer, leading to an increase in drag. The lift coefficient is always negative for the present smoldering sphere problem, and the value depends on the surface temperature. Although the buoyancy force creates a positive lift on the sphere, the pressure force generated due to velocity difference at the top and bottom halves of the sphere creates a large negative lift force; hence the resultant lift force is always negative on the sphere for the present problem.

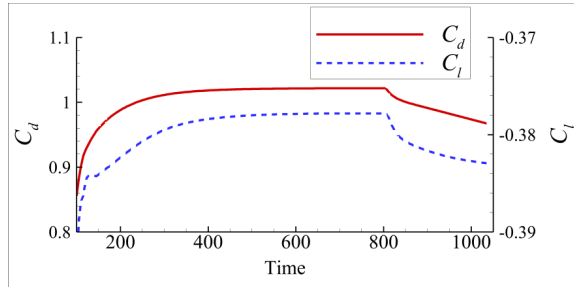


Figure 2: Drag (C_d) and lift (C_l) coefficient variation with time.

3 Conclusion

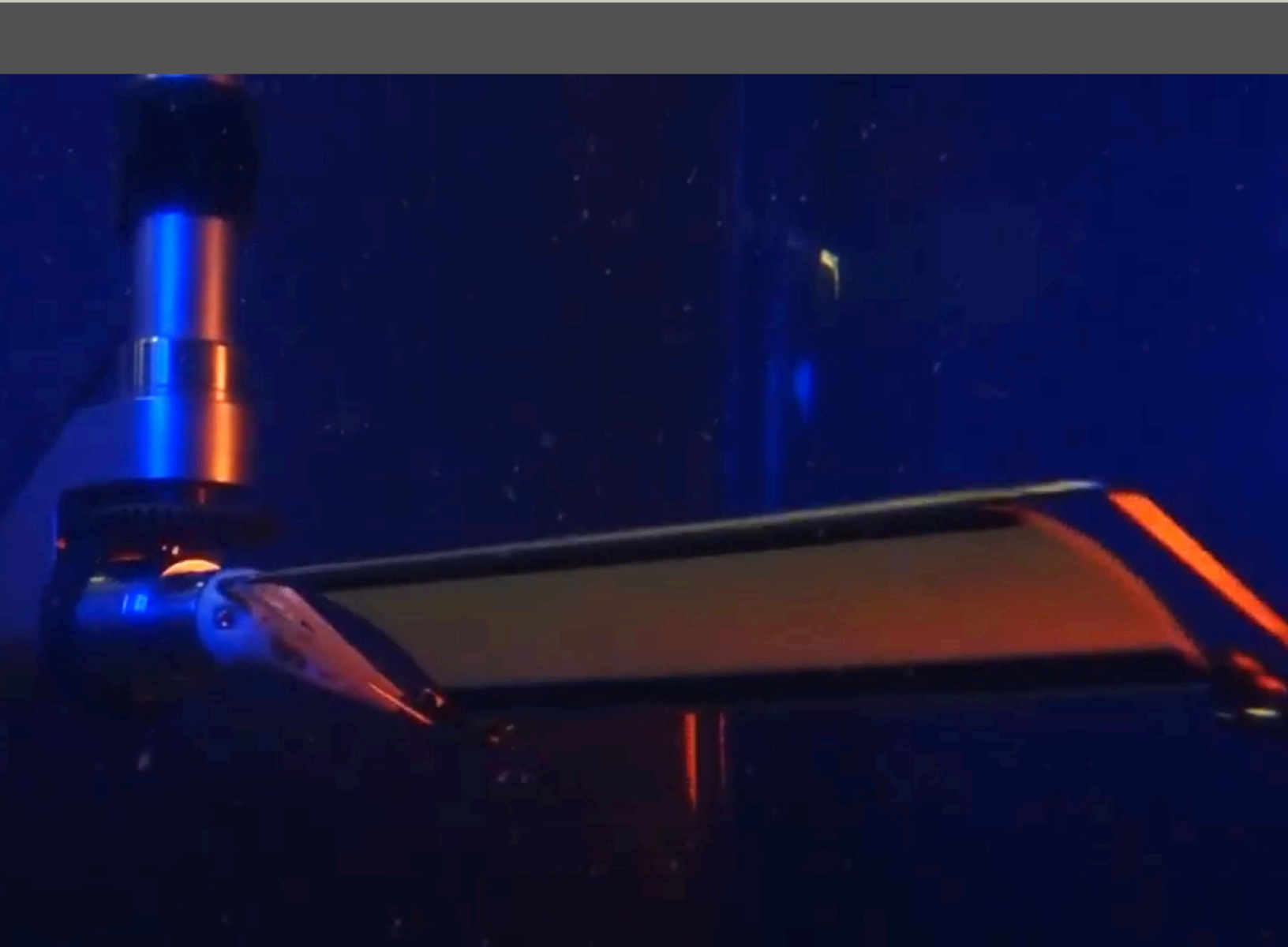
Using highly resolved simulations, the aerodynamic forces are calculated on the surface of a smoldering spherical shaped pine wood sample. Two tunnel-shaped vortex structures are observed behind the sphere for surface temperatures beyond 80°C . In this case, the buoyancy force assists surface adjacent fluid particles to move upward, disturbs the regular vortex shedding pattern, and generates two dominant oppositely rotating vortices behind the sphere. The results show an increase in drag coefficients with increased temperature, whereas the lift coefficient is always negative throughout the smoldering process. Therefore, the smoldering spherical particle drops faster and travels less distance compare to non-smoldering particle.

References

- [1] Alexander Maranghides and William Mell. A case study of a community affected by the Witch and Guejito wildland fires. *Fire Technology*, 47(2):379–420, 2011.
- [2] Samuel L Manzello and Ethan ID Foote. Characterizing firebrand exposure from wildland–urban interface (WUI) fires: results from the 2007 Angora Fire. *Fire Technology*, 50(1):105–124, 2014.
- [3] Jan C Thomas, Eric V Mueller, Simon Santamaria, Michael Gallagher, Mohamad El Houssami, Alexander Filkov, Kenneth Clark, Nicholas Skowronski, Rory M Hadden, William Mell, et al. Investigation of firebrand generation from an experimental fire: Development of a reliable data collection methodology. *Fire Safety Journal*, 91:864–871, 2017.
- [4] James L Urban, Jiayun Song, Simon Santamaria, and Carlos Fernandez-Pello. Ignition of a spot smolder in a moist fuel bed by a firebrand. *Fire Safety Journal*, 108:102833, 2019.
- [5] Samuel L Manzello, Thomas G Cleary, John R Shields, Alexander Maranghides, William Mell, and Jiann C Yang. Experimental investigation of firebrands: generation and ignition of fuel beds. *Fire Safety Journal*, 43(3):226–233, 2008.
- [6] Alexander Maranghides, William Mell, et al. Framework for addressing the national wildland urban interface fire problem—Determining fire and ember exposure zones using a WUI hazard scale (NISTTN 1748), 2013.
- [7] Jonathan Martin and Thomas Hillen. The spotting distribution of wildfires. *Applied Sciences*, 6(6):177, 2016.
- [8] Rajat Mittal, Haibo Dong, Meliha Bozkurtas, FM Najjar, Abel Vargas, and Alfred Von Loebbecke. A versatile sharp interface immersed boundary method for incompressible flows with complex boundaries. *Journal of Computational Physics*, 227(10):4825–4852, 2008.

Session C

Flapping and swimming



On the permanence of deflected vortex wakes behind pitching foils

Q. Zhong^a and D.B. Quinn^{a*}

^a University of Virginia, Charlottesville, VA, USA¹

*Correspondence: danquinn@virginia.edu

1 Introduction

A foil undergoing *symmetric* pitch oscillations can generate an *asymmetric* wake. As a result, the foil can feel a net lateral force despite having laterally-symmetric kinematics. This phenomenon, which tends to appear at high frequency-amplitude combinations, has been reproduced in a variety of experimental and numerical studies [1–5]. The asymmetry is caused by vortex dipoles that deflect the foil’s wake; the mechanism is primarily inviscid: it appears in both finite Reynolds number experiments [6] and infinite Reynolds number vortex models [1, 7].

When a foil’s wake is deflected, it tends to deflect in a direction opposite to the initial pitch direction [1, 8, 9]. However, in some cases, the deflection angle can drift or even switch sign. The dynamics of this drift are remarkably slow: a flip in the jet angle can take upwards of 100 pitching cycles [3, 10]. Work is ongoing to understand the mechanisms that govern this “very low-frequency instability” [11]. Here we present force and wake measurements on pitching hydrofoils over long times (100+ cycles). We show that the wake’s deflection is sometimes permanent and sometimes transient, and a discrete vortex model can help to explain the transition between these two states.

2 Results

To test how wake asymmetry depends on a foil’s kinematics, we measured the lateral forces on a teardrop-shaped hydrofoil in a recirculating water channel (chord = 95 mm; $Re = 6840$). We installed end plates on the foil’s top and bottom edges to keep the wake as two-dimensional as possible. The foil underwent harmonic pitch oscillations over a range of Strouhal numbers St (0.35 to 0.8 by 0.05) and amplitude-to-chord ratios A (0.2 to 0.4 by 0.05). At a subset of these conditions, we used particle image velocimetry to quantify the wake’s deflection angle.

As in previous work, we found that beyond certain St - A combinations, wakes became asymmetric (Fig. 1). Like others, we observed vortex dipoles that skewed the momentum jet away from the horizontal in a direction opposite to the initial pitch angle. However, we found that not all of the asymmetries were permanent. At an intermediate range of St - A combinations, wake asymmetries decayed over time,

¹This work was supported by the National Science Foundation under grant numbers 1921809 and 2040351. ...

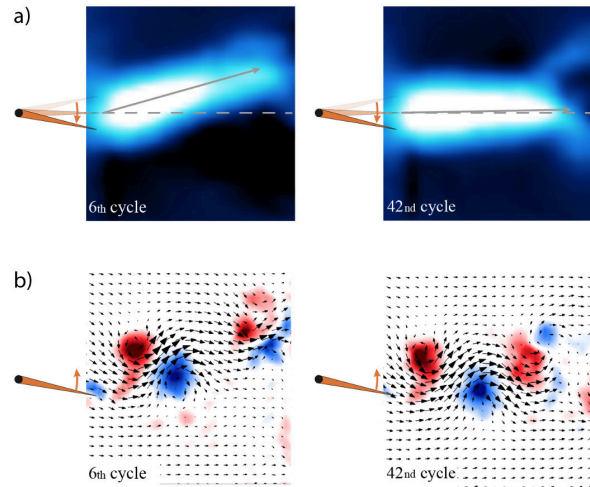


Figure 1: Particle image velocimetry reveals how wake asymmetries can decay over time. a) Time-averaged velocity fields. After 6 pitching cycles (left), the momentum jet is angled upward, opposite from the initial downward pitch direction. By the 42nd pitching cycle (right), the momentum jet no longer exhibits noticeable asymmetry. b) Instantaneous vorticity fields. During the 6th pitching cycle (left), strong vortex dipoles advect upward, leading to a deflected momentum jet. By the 42nd pitching cycle (right), the vortices are equally spaced.

and the deflection angle eventually returned to zero (Figs. 1, 2).

To explore the source of the asymmetry’s permanence/transience, we used a discrete vortex model as an approximation of the wake. In the model, irrotational vortices with alternating sign are released from the origin into an otherwise uniform horizontal flow. The vortices are then left to advect freely according to the Biot-Savart law [12]. This approach has been used by others to explore wake deflections [7]; here we applied it to a study of the deflection angle’s evolution in time.

Our discrete vortex model captured all three of the regimes we observed experimentally: symmetric wakes at low St - A combinations, asymmetric wakes that slowly decayed into symmetric wakes at intermediate St - A combinations, and permanently asymmetric wakes at high St - A combinations. The model suggests that the decay rate of the asymmetry (or

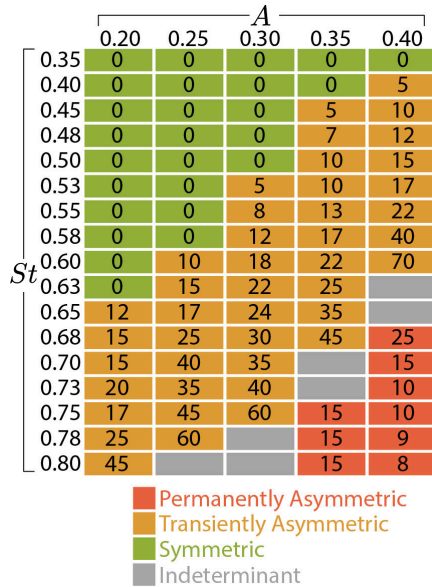


Figure 2: Whether the wake is permanently asymmetric, transiently asymmetric, or symmetric depends on the Strouhal number (St) and the amplitude-to-chord ratio (A). The number in each box indicates the number of pitching cycles before the wake converged (to a permanent asymmetric state or a symmetric state) based on lateral force data. Gray rectangles indicate conditions where the wake state had not converged after 100 pitching cycles.

lack thereof) is a function of the spacing and strength of the vortices. It also shows how the asymmetry's decay is decoupled from the mechanisms responsible for vortex formation. This decoupling helps to explain why the asymmetry's decay is so slow compared to the time scales of pitching.

3 Conclusion

Because wake asymmetries lead to net lateral forces, their permanence/transience is critical for predicting the lateral stability of a pitching foil over time. 3D fins/wings tend to exhibit symmetric wakes [13], so the dynamics governing wake deflection may be less relevant for real bio-inspired vehicles. Nevertheless, the wake deflection behind 2D foils offers a unique fundamental study of vortex wakes that are governed by multiple timescales. Here, the timescales are vastly different: wake asymmetries are created over one or two pitching periods, but they decay over timescales that are about a hundred times longer. This type of multi-scale vortex system could potentially serve as a template model for more complex 3D wakes.

References

- [1] KD Jones, CM Dohring, and MF Platzer. Experimental and computational investigation of the knoller-betz effect. *AIAA journal*, 36(7):1240–1246, 1998.
- [2] Gregory C Lewin and Hossein Haj-Hariri. Modelling

thrust generation of a two-dimensional heaving airfoil in a viscous flow. *Journal of Fluid Mechanics*, 492:339–362, 2003.

- [3] S Heathcote and I Gursul. Jet switching phenomenon for a periodically plunging airfoil. *Physics of Fluids*, 19(2):027104, 2007.
- [4] Ramiro Godoy-Diana, Jean-Luc Aider, and José Eduardo Wesfreid. Transitions in the wake of a flapping foil. *Physical Review E*, 77(1):016308, 2008.
- [5] Karl D von Ellenrieder and Stamatios Pothos. Piv measurements of the asymmetric wake of a two dimensional heaving hydrofoil. *Experiments in fluids*, 44(5):733–745, 2008.
- [6] Ramiro Godoy-Diana, Catherine Marais, Jean-Luc Aider, and José Eduardo Wesfreid. A model for the symmetry breaking of the reverse Bénard–von Kármán vortex street produced by a flapping foil. *Journal of Fluid Mechanics*, 622:23–32, 2009.
- [7] Xuzhao He and Ismet Gursul. Point vortex model of deflected wakes of oscillating airfoils. *AIAA Journal*, 54(11):3647–3651, 2016.
- [8] Zhongquan Charlie Zheng and Z Wei. Study of mechanisms and factors that influence the formation of vortical wake of a heaving airfoil. *Physics of Fluids*, 24(10):103601, 2012.
- [9] David James Cleaver, Z Wang, and I Gursul. Bifurcating flows of plunging aerofoils at high strouhal numbers. *Journal of Fluid Mechanics*, 708:349–376, 2012.
- [10] DJ Cleaver, Zhijin Wang, and Ismet Gursul. Investigation of high-lift mechanisms for a flat-plate airfoil undergoing small-amplitude plunging oscillations. *AIAA journal*, 51(4):968–980, 2013.
- [11] Ismet Gursul and David Cleaver. Plunging oscillations of airfoils and wings: Progress, opportunities, and challenges. *AIAA Journal*, 57(9):3648–3665, 2019.
- [12] Joseph Katz and Allen Plotkin. *Low-speed aerodynamics*, volume 13. Cambridge university press, 2001.
- [13] DE Calderon, DJ Cleaver, I Gursul, and Z Wang. On the absence of asymmetric wakes for periodically plunging finite wings. *Physics of Fluids*, 26(7):349–376, 2014.

Non-Uniform Flexibility and Schooling Interactions Lead to High Efficiency Swimming

Amin Mivehchi^{a*}, Tianjun Han^a, Melike Kurt^b, and Keith W. Moored^a

^aDepartment of Mechanical Engineering and Mechanics, Lehigh University, Bethlehem, USA

^bAerodynamics and Flight Mechanics Group, University of Southampton, Southampton, UK

*Correspondence: mivehchi@lehigh.edu

1 Introduction

In nature, animals propel themselves with flexible fins or wings [1–3]. Uniform flexibility has been implicated in enhancing the thrust, speed and efficiency of propulsive surfaces [4–10]. However, animals propulsive surfaces are known to be non-uniformly flexible where their flexibility increases from the leading edge to the trailing edge or from the center to the edge [11–14]. Yet, few studies have examined the effects of non-uniform flexibility on the propulsive performance of foils [15–18].

The prominent difference between non-uniformly flexible foils and their uniform counterparts is the bending pattern. While the resonance of flexible foils has been well understood to have a strong relation with improved propulsive performance [9, 10, 19, 20], few studies have isolated the impact of tailoring the bending pattern from the impact of altering the resonant condition. Yeh *et al.* [21] has probed the independent effect of the bending pattern which leads to a larger trailing edge displacement, and found that fin thickness tapering drastically increases the range of flexibility at which fins can maintain high thrust and swimming velocity while fins with uniform thickness show high performance at a narrow range near resonant condition. But the bending point of their fins doesn't change, and remains at the leading edge throughout their study. Zeyghami and Moored [22] adopted a non-uniformly flexible fin model in two-dimensional numerical simulations by placing a torsional spring with varying flexibility at different locations along the chord to vary the bending pattern and resonance condition independently. They determined that both the flexibility and the bending pattern played a large role in maximizing the performance of pitching foils.

Motivated by these studies, we advance the work of Zeyghami and Moored [22] by developing a three-dimensional non-uniformly flexible foil that is comprised of a continuous flexible sheet and a rigid plate where the bending pattern and the resonant frequency can be altered independently by changing the flexion ratio, that is the length of the rigid material compared to the total chord length, and the

¹This work was supported by the National Science Foundation under Program Director Dr. R. Joslin in Fluid Dynamics, award number 1921809 ...

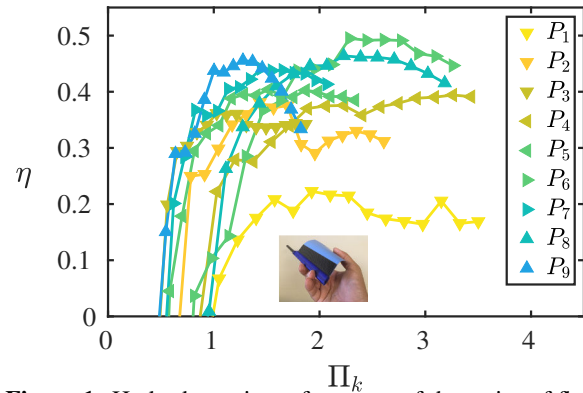


Figure 1: Hydrodynamic performance of the series of flexible foil with nonuniform flexibility.

flexibility of the flexible sheet.

2 Results

To identify the effect of bending patterns on the propulsive performance of flapping foils, a series of force measurements were conducted for various foils with different flexion ratios and effective flexibilities. The Reynolds number of 10000 was maintained across the experiments. The thrust, power and efficiency performance of the foils (Figure 1) were measured as well as the amplitude of motion and the bending pattern. Some of the foils exhibited clear resonance conditions where the trailing-edge amplitude was maximized at a resonant frequency while other showed no clear resonance. Using physical insight a new dimensionless effective flexibility Π_k is proposed and shown to collapse the resonant frequencies of the resonating foil cases. The thrust-to-drag transition occurs over a narrow range of effective flexibility from $0.5 \leq \Pi_k \leq 1$ for the resonating cases and from $0.5 \leq \Pi_k \leq 1.5$ for the non-resonating cases. Peaks in efficiency for all of the cases occur in the range of $1 \leq \Pi_k \leq 4$. By extracting the peak efficiency of each tested foil it is clear that a flexion ratio of $0.4 \leq \lambda \leq 0.7$ maximizes the efficiency with the global peak efficiency for the data set of $\eta = 51\%$ occurring at $\lambda = 0.6$.

We further examine how interacting two of these optimized non-uniformly flexible foils can lead to further enhancement

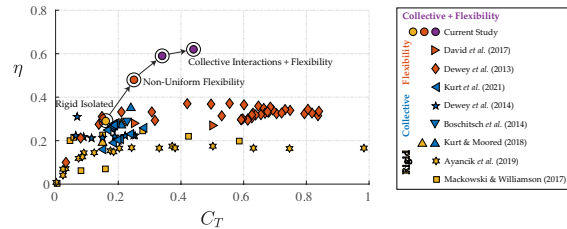


Figure 2: The current study charts a path to exceeding 60% collective efficiency while pitching foil studies typically never break 40% efficiency. The markers are colored yellow for single rigid foil studies, blue for studies of a pair of interacting rigid foils, red for single flexible foil studies, and purple for our current study where we examine a pair of interacting flexible foils. Not all data was extracted from each study. The highest efficiency cases were chosen for two-dimensional foils and three-dimensional foils with $AR \approx 2$.

of the efficiency and thrust of the collective. We probe the relative spacing, synchronization, and amplitude ratio between the two foils to chart a path to high efficiency where we measure a collective efficiency of $\eta_C = 62\%$ (Figure 2).

Lastly, we examine non-uniformly flexible combined heaving and pitching foils. By applying guidance from previously developed scaling laws we are able to hone in on high efficiency cases of $72\% \leq \eta \leq 76\%$ for a single foil. We expect to extend this data by examining the interaction of two non-uniformly flexible combined heaving and pitching foils.

3 Conclusions

Through this study, effective flexibility was proposed and proved to scale with the ratio between the driving frequency and resonant frequency of the fluid-structure interaction system, enabling us to investigate the independent effect of tailoring the bending pattern on the propulsive performance of the flapping foil. We further enhanced the propulsive efficiency and collective thrust generation by collective interaction of the most efficient isolated flipper. We will demonstrate a pathway to improve the performance from a low-efficiency and low-thrust pitching system to a high-efficiency and high-thrust system with a collective efficiency $\eta = 62\%$ and collective thrust of $C_{T,C} = 0.44$. Furthermore, by the guidance of the scaling laws on the propulsive performance of a combined pitching and heaving foil, we demonstrate that the efficiency of the non-uniform flexible foil is further enhanced for an isolated swimmer to the high efficiency of 71% with the thrust of $C_{T,C} = 0.41$, reducing the gap of performance of flapping foil systems in comparison to the standard fixed-pitch propellers such as Wageningen B-series, which range in peak efficiencies from 60-85%.

References

[1] Thomas L. Daniel. Forward flapping flight from flexible fins. *Canadian Journal of Zoology*, 66(3):630–638, 1988.

[2] S. A. Combes and T. L. Daniel. Shape, flapping and flexion: Wing and fin design for forward flight. *Journal of Experimental Biology*, 204(12):2073–2085, 2001.

[3] G. V. Lauder, P. G.A. Madden, J. L. Tangorra, E. Anderson, and T. V. Baker. Bioinspiration from fish for smart material design and function. *Smart Materials and Structures*, 20(9), 2011.

[4] Mariel Luisa N. Rosic, Patrick J.M. Thornycroft, Kara L. Feilich, Kelsey N. Lucas, and George V. Lauder. Performance variation due to stiffness in a tuna-inspired flexible foil model. *Bioinspiration and Biomimetics*, 12(1):aa5113, 2017.

[5] P. Prempraneerach, F. S. Hover, and Michael S. Triantafyllou. The effect of chordwise flexibility on the thrust and efficiency of a flapping foil. In *International Symposium on Unmanned Untethered Submersible Technology*, 2003.

[6] Sophie Ramanarivo, Ramiro Godoy-Diana, and Benjamin Thiria. Rather than resonance, flapping wing flyers may play on aerodynamics to improve performance. *Proceedings of the National Academy of Sciences of the United States of America*, 108(15):5964–5969, 2011.

[7] Hu Dai, Haoxiang Luo, Paulo J.S.A. Ferreira de Sousa, and James F. Doyle. Thrust performance of a flexible low-aspect-ratio pitching plate. *Physics of Fluids*, 24(10), 2012.

[8] Ru Nan Hua, Luoding Zhu, and Xi Yun Lu. Locomotion of a flapping flexible plate. *Physics of Fluids*, 25(12), 2013.

[9] Peter A. Dewey, Birgitt M. Boschitsch, Keith W. Moored, Howard A. Stone, and Alexander J. Smits. Scaling laws for the thrust production of flexible pitching panels. *Journal of Fluid Mechanics*, 732:29–46, 2013.

[10] Daniel B. Quinn, George V. Lauder, and Alexander J. Smits. Scaling the propulsive performance of heaving flexible panels. *Journal of Fluid Mechanics*, 738:250–267, 2014.

[11] A. K. Kancharala and M. K. Philen. Optimal chordwise stiffness profiles of self-propelled flapping fins. *Bioinspiration and Biomimetics*, 11(5), 2016.

[12] F.E. Fish and G.V. Lauder. Passive and Active Flow Control By Swimming Fishes and Mammals. *Annual Review of Fluid Mechanics*, 38(1):193–224, 2006.

[13] N. Bose, J. Lien, and J. Ahia. Measurements of the bodies and flukes of several cetacean species. *Proceedings of the Royal Society B: Biological Sciences*, 242(1305):163–173, 1990.

[14] Mark C. DeBlois and Ryosuke Motani. Flipper bone distribution reveals flexible trailing edge in underwater flying marine tetrapods. *Journal of Morphology*, 280(6):908–924, 2019.

[15] Kelsey N. Lucas, Patrick J.M. Thornycroft, Brad J. Gemmill, Sean P. Colin, John H. Costello, and George V. Lauder. Effects of non-uniform stiffness on the swimming performance of a passively-flexing, fish-like foil model. *Bioinspiration and Biomimetics*, 10(5), 2015.

[16] M. Nicholas J. Moore. Torsional spring is the optimal flexibility arrangement for thrust production of a flapping wing. *Physics of Fluids*, 27(9), 2015.

[17] M. Jimreeves David, R. N. Govardhan, and J. H. Arakeri. Thrust generation from pitching foils with flexible trailing edge flaps. *Journal of Fluid Mechanics*, 828:70–103, 2017.

[18] Li Ming Chao, Guang Pan, Yong Hui Cao, Dong Zhang, and Guo Xin Yan. On the propulsive performance of a pitching foil with chordwise flexibility at the high Strouhal number. *Journal of Fluids and Structures*, 82:610–618, 2018.

[19] Hassan Masoud and Alexander Alexeev. Resonance of flexible flapping wings at low Reynolds number. *Physical Review E - Statistical, Nonlinear, and Soft Matter Physics*, 81(5):1–5, 2010.

[20] C. K. Kang, H. Aono, C. E.S. Cesnik, and W. Shyy. Effects of flexibility on the aerodynamic performance of flapping wings. *Journal of Fluid Mechanics*, 689:32–74, 2011.

[21] Peter D. Yeh, Yuanda Li, and Alexander Alexeev. Efficient swimming using flexible fins with tapered thickness. *Physical Review Fluids*, 2(10):1–9, 2017.

[22] Samane Zeyghami and Keith W. Moored. Effect of Nonuniform Flexibility on Hydrodynamic Performance of Pitching Propulsors. *Journal of Fluids Engineering*, 141(4):041108, 2019.

Wake topologies and vortex patterns in bio-inspired propulsion

Justin T. King^{a*} and Melissa A. Green^a

^a University of Minnesota, Aerospace Engineering and Mechanics, Minneapolis, MN, USA¹

*Correspondence: king1526@umn.edu

1 Introduction

Recently, engineers working on swimming and flying vehicles have looked to nature for motivation and have incorporated their findings into man-made vehicles [1, 2]. Bio-inspired vehicles have the potential to be valuable in applications like surveillance, oceanic sampling, and reconnaissance [3, 4]. Crucial to the design of such vehicles and the understanding of biological propulsion, is comprehension of unsteady fluid flows and their time-varying forces.

For some swimming animals, thrust is generated primarily by a caudal fin, which may display a range of planforms, including those of different trailing edge shape [5]. Geometric abstractions of some caudal fins are shown in Fig. 1, which illustrates the diversity in leading and trailing edge shapes. The top row of Fig. 1 displays high AR fins that are typically associated with improved performance [6], and fins of low AR and reduced performance are in the bottom row. Increases in AR are due to reductions in area, increases in span, or both. Area can be reduced through inward inflection of the trailing edge or increased through outward trailing edge inflection. Experiments in the current work focus on three shapes from Fig. 1: forked, truncate, and pointed. This work explores the influence of propulsor planform on vortex dynamics and performance of bio-inspired swimmers.

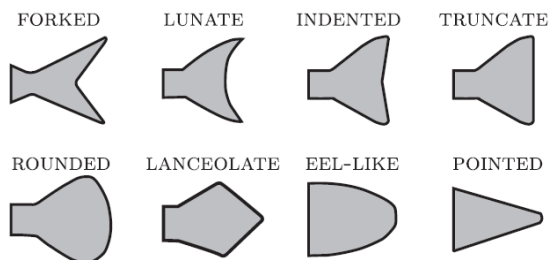


Figure 1: Geometric abstractions of caudal fins from a variety of fish species. *Adapted from Van Buren et al. [7].*

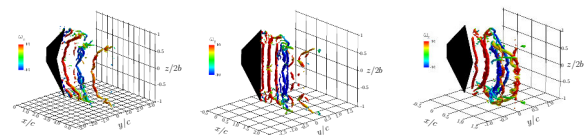
2 Results

Results obtained from stereoscopic particle image velocimetry (SPIV) on five trapezoidal panels of different trailing edge shape show that the wake is strongly influenced by

¹This work was supported by ONR Award No. N00014-17-1-2759 and an award from NYS Department of Economic Development through the Syracuse Center of Excellence.

planform and kinematics. The St , which is dictated by kinematics in the current work, plays a more significant role than shape on wake topology. Regardless of geometry or St , the wake can be broadly described as a series of linked vortex rings of alternating sign formed from spanwise and streamwise vortices. This general structure is a well known feature of oscillating propulsors [8, 9]. However, changes to planform and St often result in additional, secondary spanwise vortices and less frequently secondary streamwise vortices.

Even though St is the dominant influence on wake topology, minor variations at similar St may arise when geometry changes. This is most pronounced when St is small, and differences among three panel wakes at low St are shown in Figure 2. At $St = 0.09$, the rings of Panel 1 (forked) are formed when a single spanwise vortex sheds during each half of a pitching cycle, leading to a 2S wake. However, Panel 3 (truncate) and Panel 5 (pointed) generate two additional like-signed spanwise vortices during each half of the cycle, resulting in a 6S pattern. Even when initial topologies are similar, panel shape may influence the temporal evolution. The three like-signed vortices of Panel 5 at $St = 0.14$ merge, causing changes to wake structure downstream, a behavior that occurs for all panels across different St .

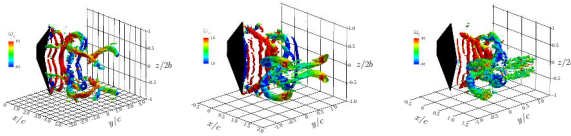


(a) Panel 1, $St = 0.09$ (b) Panel 3, $St = 0.11$ (c) Panel 5, $St = 0.14$

Figure 2: Q isosurfaces at $Q = 20$ for Panel 1, Panel 3, and Panel 5 at their lowest St . Isosurfaces are coloured by ω_z .

All panels generate four or more like-signed spanwise vortices per half cycle at intermediate St as shown in Figure 3. Panel 1 and Panel 2 (forked) produce an 8S wake with four spanwise vortices of each sign. The wakes of Panel 4 (pointed) and Panel 5 experience different changes and their wakes are dominated by a large number of Kelvin-Helmholtz-like instabilities. These instability vortices form a series of discrete secondary vortices trailing the primary von Kármán vortex associated with a reverse von Kármán vortex street. The instability vortices tend to be smaller in cross-section than a primary spanwise vortex, but can cover almost the entire spanwise extent of the wake.

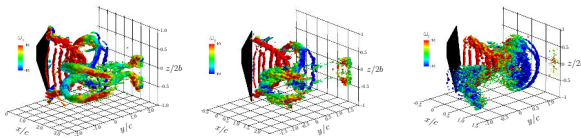
Kelvin-Helmholtz-like instabilities have been observed elsewhere in the wakes produced by pitching panels [10].



(a) Panel 1, $St = 0.25$ (b) Panel 4, $St = 0.36$ (c) Panel 5, $St = 0.40$

Figure 3: Q isosurfaces at $Q = 20$ for Panel 1, Panel 3, and Panel 5 at intermediate St . Isosurfaces are coloured by ω_z .

Instability vortices arise for all geometries at large St except for Panel 1, which experiences a reduction in the number of vortices when $St \geq 0.33$. Once instability vortices become prominent, further increases in the St do little to change topology, although minor variations in the number of instability vortices may result. The dominant presence of Kelvin-Helmholtz-like instabilities in the wakes of Panels 2-5 is evident in Figure 4. Also evident through wake comparisons in Figure 4 are temporal behaviours influenced by changes to planform and St . Wake structures distort and breakdown as they convect downstream as they experience transverse expansion and spanwise compression. These behaviours are correlated to vortex-induced flows, which facilitate the deformation and bending of rings.



(a) Panel 2, $St = 0.47$ (b) Panel 3, $St = 0.53$ (c) Panel 5, $St = 0.66$

Figure 4: Q isosurfaces at $Q = 20$ for Panel 2, Panel 3, and Panel 5 at their highest St . Isosurfaces are coloured ω_z .

A comparison of performance with wake patterns shows it is not reasonable to correlate specific vortical arrangements to performance characteristics. Forked panels fail to produce thrust under any scenario, while truncate and pointed panels always generate positive thrust or experience self-propelled swimming. Efficiency is largest for Panel 5 at $St = 0.27$, while thrust is largest for Panel 5 at $St = 0.66$. The vortex patterns of Panel 5 at these St also occur for other panels at similar St , even when thrust and efficiency are negative. These results further corroborate recent work suggesting that caution be taken when drawing conclusions about performance directly from wake patterns [11].

3 Conclusion

Results obtained from SPIV are used to investigate the influence of trailing edge shape and St on the wake structures and performance of bio-inspired pitching panels. Wake topology, especially with respect to the number of spanwise vor-

tices, is sensitive to changes in St and planform. St plays a dominant role with respect the vortex topology, even though changes to shape at similar St can result in different wake structures. Uniquely identifiable wake patterns tend to develop within a specific St range, even when the patterns occur for multiple panels. At low St , the number of spanwise vortices is reduced, and anywhere from one to three like-signed vortices are generated during a half of a pitching cycle. More forked geometries usually generate fewer spanwise structures at low St . When St increases, the number of spanwise vortices increases until the wake becomes dominated by Kelvin-Helmholtz-like instability vortices.

Simplistic wake descriptions can be difficult to develop and may prove rather inaccurate. The wake can form a complex series of vortex rings that preclude some simplistic descriptions commonly applied to the wakes of bio-inspired swimming. Results illustrate that biologically inspired planforms can generate complex wakes that can be categorized as 2S, 8S, and even 14S. Although not observed here, additional wake complexity may arise in other scenarios from pairs of counter-rotating vortices, such as those in a 2P wake pattern [11]. As future work becomes more focused on planforms and kinematics that better mimic biology, more detailed wake characterizations may be necessary to capture the intricacies of vortex patterns. Simple descriptions like 2S or 2P may be useful for two-dimensional or quasi-two-dimensional propulsors, but they may fail to depict the wakes of finite AR , bio-inspired propulsors.

References

- [1] D.T. Roper, S. Sharma, R. Sutton, and P. Culverhouse. A review of developments towards biologically inspired propulsion systems for autonomous underwater vehicles. *Proc. IMechE*, 225:77–96, 2010.
- [2] R. Siddall and M. Kovac. Launching the aquamav: bioinspired design for aerial-aquatic robotic platforms. *Bioinspiration & Biomimetics*, 9, 2014.
- [3] Edwin F. S. Danson. *Technology and Applications of Autonomous Underwater Vehicles*, chapter AUV tasks in the offshore industry, pages 127–138. Taylor and Francis, London, 2003.
- [4] Simon Corfield and Christopher Hillenbrand. *Technology and Applications of Underwater Autonomous Vehicles*, chapter Defence applications for unmanned underwater vehicles, pages 161–178. Taylor and Francis, London, 2003.
- [5] M. J. Lighthill. Hydromechanics of aquatic animal propulsion. *Annual Review of Fluid Mechanics*, 1:413–446, 1969.
- [6] Michael Sfakiotakis, David M. Lane, and J. Bruce C. Davies. Review of fish swimming modes for aquatic locomotion. *IEEE Journal of oceanic engineering*, 24(2):237–252, 1999.
- [7] Tyler Van Buren, D. Floryan, D. Brunner, U. Senturk, and Alexander J. Smits. Impact of trailing edge shape on the wake and propulsive performance of pitching panels. *Physical Review Fluids*, 2(1):014702, Jan 2017.
- [8] James H.J. Buchholz and Alexander J. Smits. On the evolution of wake structure produced by a low-aspect-ratio pitching panel. *J. Fluid Mech.*, 546:433–443, 2006.
- [9] K.D. von Ellenrieder, K. Parker, and J. Soria. Flow structures behind a heaving and pitching finite-span wing. *J. Fluid Mech.*, 490:129–138, 2003.
- [10] Zakery R. Carr, Adam C. DeVoria, and Matthew J. Ringuette. Aspect-ratio effects on rotating wings: circulation and forces. *J. Fluid Mech.*, 767:497–525, 2015.
- [11] Alexander J Smits. Undulatory and oscillatory swimming. *Journal of Fluid Mechanics*, 874, 2019.

Different routes to optimal flapping in unsteady conditions

R. Vilumbrales-Garcia ^{a*}, G.D. Weymouth ^{a,b} and B. Ganapathisubramani ^a

^a University of Southampton, Faculty of Engineering and Physical Science, Southampton, UK¹

^b Alan Turing Institute, Data-Centric Engineering Group, London, UK

*Correspondence: *r.vilumbrales-garcia@soton.ac.uk*

1 Introduction

Coordinated controlled maneuvering through upstream wakes is important for a wide range of applications; from surface ships to autonomous underwater vehicles. A proper understanding of the unsteadiness of the surrounding flow is essential, and it is a requirement to develop operations involving several autonomous vehicles. Also, previous work has shown that animals can greatly improve their performance in terms of thrust production or efficiency if their kinematics and paths are properly adapted to the incoming flow [2].

Flapping foils, commonly used to replicate the motion of fish, are a powerful tool to analyse the mechanisms responsible for the performance augmentation that occurs in fish-schooling. To do so, a set of two flippers in 'tandem' arrangement, one in the front - fore - and another in the back - hind - can be defined. By doing so, the fore object can be used as an 'unsteadiness generator' that will impose a set of flow conditions on the hind one. If the hind foil is properly tuned with the incoming wake, it can obtain a surplus on its propulsive performance. [1]

Several studies have covered the parameters required to achieve a surplus in tandem flapping foils. However, very little work has been done on the maneuvering methods that are required to transition from one point to another to achieve this surplus. If we start at a given spacing/phase difference between the foils, the hind needs to maneuver in order to locate itself at the optimum place to increase its propulsive performance. And to do so, it needs to understand its surrounding flow conditions, and to, by the use of a predictive/control model, make a decision in real time of where to go next.

Here, we try to develop a predictive/control model able to analyse several candidate paths for a flapping foil immersed in unsteady incoming flow, and to decide which of those routes is the optimal to maximise its performance. We also aim to do that by using physically relevant parameters in our model, in order to reduce the amount of data required, and to improve generalisation [5].

¹This research was supported financially by the Office of Naval Research award N62909-18-1-2091.

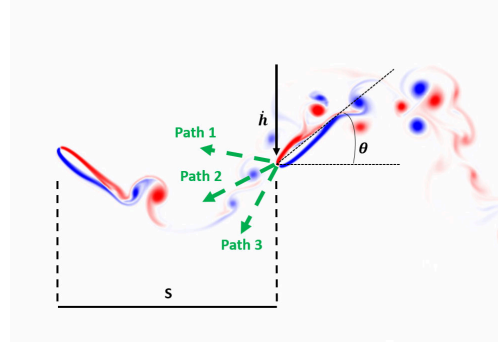


Figure 1: Sketch of the study

2 Methodology

In this study, we use a tandem flapping foil arrangement, as presented in Fig. 1, where the upstream foil is used as an unsteadiness generator to impose vorticity on the downstream foil. Both foils follow sinusoidal kinematics, with identical frequency, pitching, and heaving amplitude (more details about the kinematics at [6]). The longitudinal distance S is set to 3 chords, and the Strouhal value ($St = 2Af/u$) to 0.36, similar to [6]. As demonstrated by [1], for a set of tandem flapping foils at a given longitudinal distance, the performance of the back foil relies only on the phase delay ϕ between the fore and hind foils.

However, unlike in previous work where ϕ is treated as a constant, we define the motion of the hind using an open loop approach, allowing it to transition from a given ϕ_0 , to a new ϕ_1 using a sigmoid evolution, as presented in Fig. 2. Using 8 values of $\phi = 0, \pi/4, \dots, 7\pi/4$ and all possible ϕ_0 and ϕ_1 combinations, we develop a data set of 64 transition cases.

3 Preliminary results

Figure 3 presents the phase averages thrust force $\overline{C_X}$ on the downstream foil for each of the training cases at the ϕ_1 cycle. The color scale indicates the absolute change between ϕ_0 and ϕ_1 , and the dashed black line is the base case ($\phi_0 = \phi_1$). Although all the data points of Fig. 3 at a certain ϕ_1 represent a hind foil waving through the same incoming wake, and following the same kinematics, the $\overline{C_X}$ differs - see $\phi_1 = \pi$ at Fig 3 -. That proves that the transition phase is having

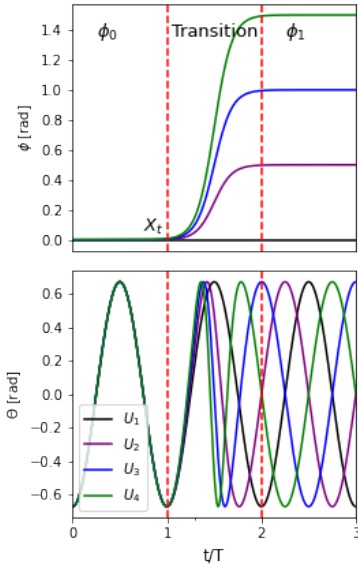


Figure 2: Top: sigmoid function to transition from ϕ_0 to ϕ_1 , for several kinematics candidates. Vertical dashed red line denote the start and end of the transition. Bottom: example of the kinematics candidates (pitch) after adding the sigmoid increment.

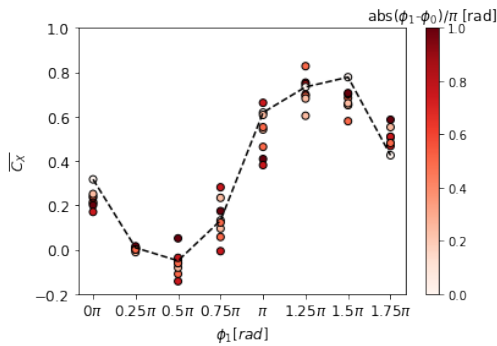


Figure 3: \overline{C}_X of each of the training cases. The color scale indicates the transition change [rad]. Black dashed line presents the base-case, where the increment is zero.

an influence in the thrust production at the ϕ_1 stage, what is nor surprising considering that it is happening in a highly-unsteady flow, full of vorticity structures. It also opens the path to smarter ways to transit, such as intermediate steps before arriving at the final ϕ_1 . That aspect will be studied further.

4 Future work

After analysing the importance of the transition cycle in our open-loop approach, the next step will be to develop a control approach to improve the downstream's foils performance, given any starting position. To do this, we first must build a model to predict the fluid loading on the downstream foil. Then this model can be used to determine an optimal path through the upstream wake.

Koopman Operator based systems are gaining relevance for predictive and control applications [3, 4]. Those methods are highly relevant to develop our predictive/control model as those they are suitable to evolve a state vector through nonlinear dynamics, as defined in Equations 1-2:

$$X_{t+1} = f(X_t, U_t) \quad (1)$$

$$k_* y(X_t, U_t) = y(f(X_t, u_t), *) = y(X_{t+1}, *) \quad (2)$$

where t is the time, k is the Koopman Operator, and X_t , the state vector, will be the information of the state of the foil just before the transition phase - see Fig. 2 - . The information contained in X_t will be made of physically-relevant parameters, in an effort to reduce the amount training data, and to improve the generalization of the method. The f is the predictive function that advances X_t to X_{t+1} , and will be obtained using the training data and the SINDYc algorithm [4]. We will also prescribe a set of new possible paths, U_{t+1} , as explained in Fig 2. Finally, we can predict various X_{t+1} - one per possible route - and evaluate them in terms of propulsive performance, with the purpose of selecting the optimum path for the hind foil.

In conclusion, we try to, starting from the well known problem of tandem flapping foils, evolve to a predictive-control model that, by understanding the flow around the foil, can predict the optimum path to follow in order to maximise performance. In order to avoid expensive methods such as reinforcement learning, we try to, by the use of approaches based on the Koopman Operator, obtain a rapid estimation tool capable of being implemented in a real environment, with little training data. The final study will include a deep analysis of the transition phase, and the results regarding the predictions/control and the evaluation of the Koopman-based methods capabilities to predict the optimum path for a flapping foil under unsteady upstream flow.

References

- [1] Muscutt, LE and Weymouth, GD and Ganapathisubramani, Bharathram Performance augmentation mechanism of in-line tandem flapping foils. *Journal of Fluid Mechanics*, 827:484–505, 2017.
- [2] Weihs, D Hydromechanics of fish schooling *Nature*, 5387:290–291, 1973.
- [3] Brunton, Steven L and Budišić, Marko and Kaiser, Eurika and Kutz, J Nathan Modern Koopman theory for dynamical systems *arXiv preprint*, arXiv:2102.12086, 2021.
- [4] Brunton, Steven L and Proctor, Joshua L and Kutz, J Nathan Sparse identification of nonlinear dynamics with control (SINDYc) *IFAC-PapersOnLine*, 49.18:710–715, 2021.
- [5] Weymouth, GD and Yue, D. K. P. Physics-Based Learning Models for Ship Hydrodynamics *Journal of Ship Research*, 57.1:1-12, 2013.
- [6] Muscutt, Luke E and Dyke, Gareth and Weymouth, Gabriel D and Naish, Darren and Palmer, Colin and Ganapathisubramani, Bharathram he four-flipper swimming method of plesiosaurs enabled efficient and effective locomotion *Proceedings of the Royal Society B: Biological Sciences*, 284.1861:20170951, 2017.

Aerodynamic performance of a bio-inspired membrane wing

Alexander Gehrke, Jules Richeux and Karen Mulleners*

École polytechnique fédérale de Lausanne, Institute of Mechanical Engineering,
Unsteady flow diagnostics laboratory, 1015 Lausanne, Switzerland¹

*Correspondence: karen.mulleners@epfl.ch

Many animals, like insects, birds and bats, amaze us with their agile and versatile flight performances and they have served as inspiration for the design of human-made flying devices for centuries. Nature's fliers use flexible wings which adapt to different flight conditions through active and passive shape deformations. Bats, squirrels, lemurs and other flying mammals use membrane wings to fly. Membranes allow for large shape deformations compared to the size of the wing, yet they are very thin and lightweight. Bats for example, use complex bone and muscle structures in their wings to control the deformation which leads to strong augmentations in their aerodynamic performance [1, 2].

In this study, we introduce a novel bio-inspired membrane wing design. The leading and trailing edges of the wing are rigid and can rotate around their span-wise axes. The trailing edge has an additional degree of freedom which allows it to translate in the chord-wise direction. Depending on the aerodynamic pressure difference between the pressure and suction side of the membrane, the wing passively cambers as the distance between leading and trailing edge shortens. We experimentally characterize the flow and force response of membrane wings over a large range of flapping kinematics and wing material properties using load measurements and particle image velocimetry. Additional deformation measurements are conducted to capture the membrane shape throughout the flapping wing cycle.

The aerodynamic performance of different membrane wings is evaluated experimentally with a robotic flapping wing device [3]. The mechanism is controlled by two servo motors which guide the stroke and pitch axis of the system. The aerodynamic loads are recorded with a force and torque transducer mounted at the wing root. Two cameras in stereoscopic configuration are used to track markers on the membrane wings.

Rectangular membranes (150 mm × 55 mm) are cut from silicon sheets with thicknesses varying between $h = 0.3$ and 1.4 mm (fig. 1a). The wings are mounted on the adaptive wing holder which is connected to the load cell and the flapping wing mechanism. The trailing edge of the wing holder is designed such that it can translate along the chord-wise direction of the wing (fig. 1b). By moving the trailing edge towards the leading edge, the effective chord length c' decreases and the maximum camber \hat{z}_{\max} increases. The

adaptive wing is designed to enhance the aerodynamic performance of the wing in two ways: 1) the camber \hat{z}_{\max} of the wing grows with increasing aerodynamic pressure, and 2) the leading and trailing edges of the wing rotate and align favourable with the flow. The combined effects of these two mechanisms are higher lift versus angle of attack slopes, higher maximum values of the lift coefficient, and delayed stall to higher angles of attack due to a reduction in the effective angle of attack [1].

The wing kinematics in hovering flight are described in terms of their stroke angle ϕ and pitch angle β , which determines the angle of attack ($\alpha = 90^\circ - \beta$) throughout the flapping wing cycle T . The stroke angle profile varies sinusoidal from $\phi = -45^\circ$ to 45° and changes with the flapping frequency between $f = 0.125$ and 0.4 Hz. The angle of attack has a trapezoidal profile and reaches amplitudes of $\hat{\alpha} = 15^\circ$ to $\hat{\alpha} = 75^\circ$.

In this study, we are especially interested in characterising how the membrane deformation affects the stroke-average lift coefficient \bar{C}_L , which determines how much weight is supported or how fast altitude can be gained, and the hovering efficiency of the flapping wing system η , which is the ratio between lift production and power expenditure in eq. (1) and limits the flight time [3]. The stroke average lift coefficient and the hovering efficiency are defined by:

$$C_L = \frac{L}{\frac{1}{2}\rho R c \bar{U}^2}, \quad C_P = \frac{P}{\frac{1}{2}\rho R c \bar{U}^3}, \quad \eta = \frac{\bar{C}_L}{\bar{C}_P}, \quad (1)$$

where L is the aerodynamic lift generated and P the power required by the wing. The dynamic pressure is computed with the wing's initial chord length c , span R , stroke-average velocity \bar{U} and the fluid density $\rho = 1181 \text{ kg/m}^3$.

The aeroelastic number Ae is the ratio between the membrane compliance and the dynamic pressure [2]:

$$Ae = \frac{Eh}{\frac{1}{2}\rho c \bar{U}^2 c}, \quad (2)$$

where $E = 1.22 \times 10^3 \text{ Pa}$ is the Young's modulus of the membrane material. The aeroelastic number ranges from $Ae = 0.24$ to 8900 and allows use to scale the flapping frequency f and the membrane thickness h of all our experiments with one non-dimensional parameter. The stroke-average lift coefficient \bar{C}_L over the aeroelastic number Ae is shown for different angle of attack amplitudes $\hat{\alpha}$ in fig. 1c.

¹This work was supported by the Swiss National Science Foundation under grant number 200021_175792

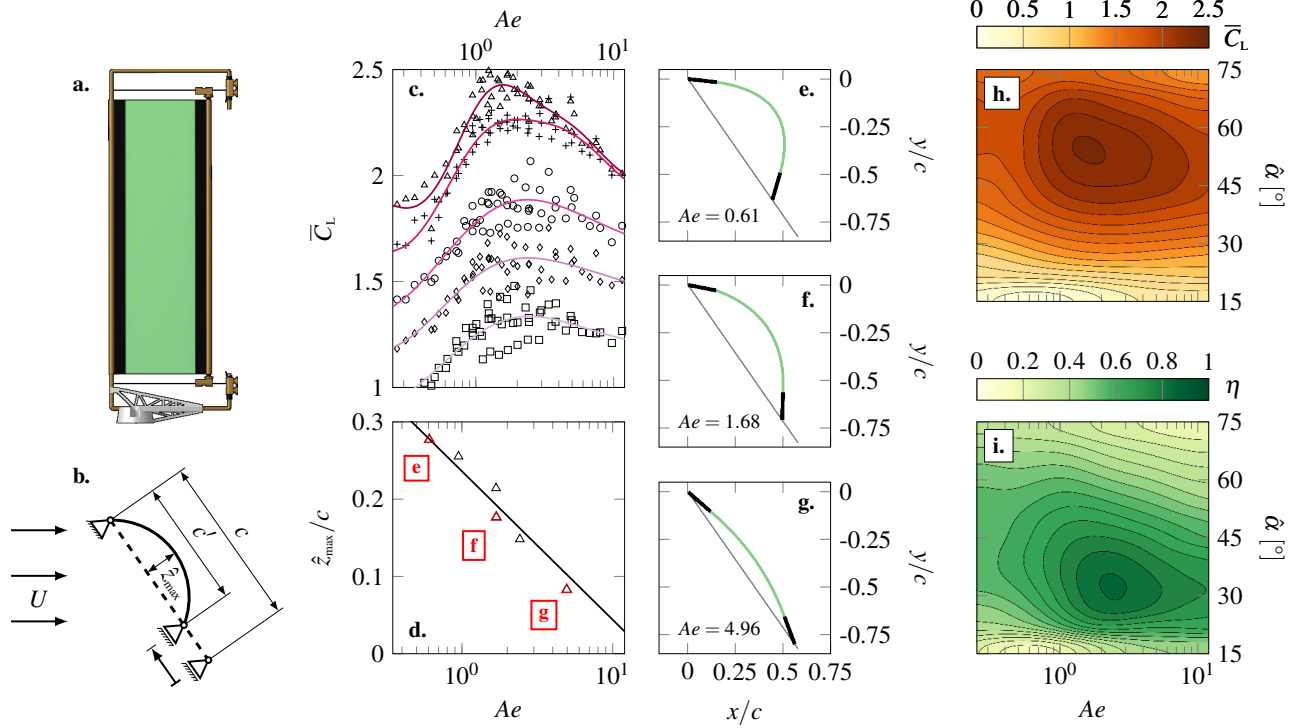


Figure 1: a. Adaptive membrane wing, b. Cambering mechanism, c. \bar{C}_L vs Ae - the marker symbols indicate different angles $\hat{\alpha}$ ($\square = 25^\circ$, $\diamond = 30^\circ$, $\circ = 35^\circ$, $+$ = 45° , $\triangle = 55^\circ$), d. \hat{z}_{max}/c vs Ae at $\hat{\alpha} = 55^\circ$, e.-g. Camber lines at $t/T = 0.25$ for $\hat{\alpha} = 55^\circ$, h. \bar{C}_L vs Ae and $\hat{\alpha}$, i. η vs Ae and $\hat{\alpha}$

The lift increases with increasing Ae until a maximum of $\bar{C}_L = 2.43$ is reached at $Ae = 1.68$. After the maximum, \bar{C}_L drops when Ae is further increased for all pitching amplitudes $\hat{\alpha}$. The highest overall \bar{C}_L is reached at $\hat{\alpha} = 55^\circ$.

The maximum camber \hat{z}_{max} determined from the deformation measurements is presented in fig. 1d for $\hat{\alpha} = 55^\circ$. The red markers correspond to the snapshots highlighted in fig. 1e to fig. 1g., which indicate the wing's camber line at mid-stroke ($t/T = 0.25$) for $Ae = 0.61$, 1.68 , and 4.96 . The maximum camber in fig. 1d decreases linearly on the logarithmic scale with increasing aerodynamic number. The general decrease of \hat{z}_{max} with increasing Ae is due to a decrease in the dynamic pressure with respect to the membrane stiffness expressed in eq. (2). An increase in camber due to a lower Ae coincides first with an increase in \bar{C}_L until the maximum camber of $\hat{z}_{max} = 0.2c$ at $Ae = 1.68$ is reached. The leading edge of the highest lift producing membrane aligns with the incoming flow and the trailing edge is oriented perpendicular to the stroke-plane (fig. 1f). This high \bar{C}_L camber line profile promotes the deflection of incoming flow downwards and orients the resulting force in the lift direction. A further increase in camber leads to a decrease in lift for the same angle of attack $\hat{\alpha}$. The camber line in fig. 1e exhibits a higher curvature than the membrane in fig. 1f and as a result the trailing edge rotates too far and points into the direction of motion. This leads to a loss in \bar{C}_L . We summarise the effect of Ae and $\hat{\alpha}$ on the aerodynamic force production for

the entire experimental parameter range in fig. 1h and i. The maximum \bar{C}_L in fig. 1h is found at $Ae = 1.68$ and $\hat{\alpha} = 55^\circ$ as seen in fig. 1c. The most efficient hovering $\eta = 0.858$ occurs at $Ae = 2.44$ and $\hat{\alpha} = 33^\circ$ in fig. 1i. Lower angles of attack are more efficient for rigid flapping wings, where they allow for a stable growth of the leading edge vortex and a lift favouring orientation of the normal force vector [3].

The flexible membrane wing system displays significant aerodynamic advantages over rigid wings and its passive adaptation make it a promising design for the construction of micro air vehicles. The ability to modulate the angle of attack and the rigidity of the wing in flight or as a design parameter has the potential to extend and improve the performance envelope of such vehicles.

References

- [1] A. Song, et al. Aeromechanics of Membrane Wings with Implications for Animal Flight. *AIAA Journal*, 46(8):2096–2106, 2008.
- [2] Gali Alon Tzezana and Kenneth S. Breuer. Thrust, drag and wake structure in flapping compliant membrane wings. *Journal of Fluid Mechanics*, 862:871–888, March 2019.
- [3] A. Gehrke and K. Mulleners. Phenomenology and Scaling of Optimal Flapping Wing Kinematics. *Bioinspiration & Biomimetics*, 16(2):026016, 2021.

Hairpin-like vortices produced by swimming snakes

V. Stin^{a,b}, R. Godoy-Diana^a, A. Herrel^b and X. Bonnet^c

^a PMMH, CNRS, ESPCI Paris-PSL, Sorbonne Université, Université de Paris, Paris, France ¹

^b MECADEV, Département Adaptation du Vivant, MNHN, CNRS, Paris, France

^c Centre d'Étude Biologique de Chizé, CNRS, Villiers-en-Bois, France

1 Introduction

Snakes are represented by more than 3000 species with different lifestyles such as terrestrial, amphibious and marine snakes. Their elongated and limbless morphology has been conserved during more than 100 million years of evolution. While being relatively simple, this morphology is associated to more than 10 different gaits to move in different environments (Jayne 2020). Snakes are anguilliform swimmers, which is characterized by an undulation with an increasing amplitude along all the body.

The hydrodynamics of anguilliform swimming have been experimentally studied on eels (Müller et al. 2001, Tytell 2004) and lampreys (Gemmell et al. 2016, Du Clos et al. 2019) using 2D Particle Image Velocimetry (PIV). To our knowledge there are neither studies of the hydrodynamics of swimming snakes, nor experimental results on the 3D characteristics of the wake of an anguilliform swimmer. Numerical investigations have been conducted (Kern and Koumoutsakos 2006, Borazjani and Sotiropoulos 2009, Ogunka et al. 2020, Khalid et al. 2021) in order to model the flow created by idealized anguilliform swimmers. These studies highlight the hairpin-like structure of the vortices shed in the wake during anguilliform swimming.

The goal of this experimental study is to provide a first insight into the 3D wake structure of the water snake *Natrix tessellata* using a 3D Particle Image Velocimetry setup (Figure 1.a). The vortices shed in the wake of the swimmer are characterized in order to compare to existing numerical simulations and 2D experimental studies.

2 Results

The wake structures were obtained for 3 captive water snakes (*Natrix tessellata*) housed in the laboratory (MNHN lab, Paris) using a volumetric 3-component PIV setup (V3V-9000-CS system, TSI). A total of 109 free swimming trials were recorded with at least one tail beat in the measuring volume. The body length (L) of the 3 studied animals is 83.4cm, 82.4cm and 64.7cm. The Reynolds number $Re = \frac{LU}{\nu}$ based on the average swimming speeds are in the range of 100000 to 400000.

¹This work was supported by the Paris Sorbonne IPV doctorate program and the ANR DRAGON2 (ANR-20-CE02-0010)

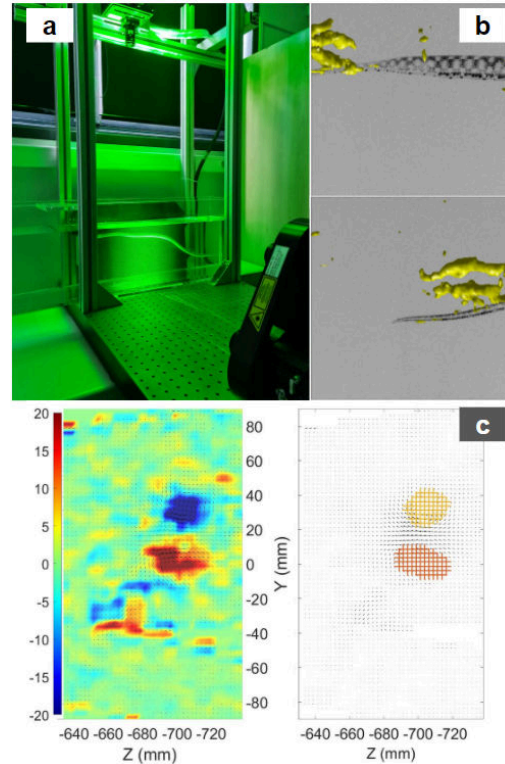


Figure 1: (a) Volumetric PIV setup. (b) Projection of two consecutive hairpin vortices in the XY plane highlighted with Q-criterion isosurfaces. (c) X-vorticity slice of a vortex (left) with identified vortex cores (right).

The main vortical structures are identified in time by computing the temporal evolution of the maximal Q-criterion in the measurement volume. The wake contains lateral jets of fluid, alternating in direction. The jets are characterized by their angle relative to the swimming direction and their magnitude. The mean maximum velocity of the jets is 29cm/s. The vortices surrounding the jet are identified with Q-criterion isosurfaces and have a hairpin-like structure as predicted by the numerical investigations of anguilliform swimming (Figure 1.b). In a full tail beat cycle, the snake creates two hairpin vortices of opposite directions.

The vortex core locations are identified using a proper orthogonal decomposition (POD) algorithm (Grafietaux et al.

2001) as seen in Figure 1.c. The hairpin vortex height scales with the snake size and widens linearly through time. The computed circulation of the vortex cores increases rapidly just after the tail beat and then decreases over time as the vortex is shed in the wake.

3 Conclusion

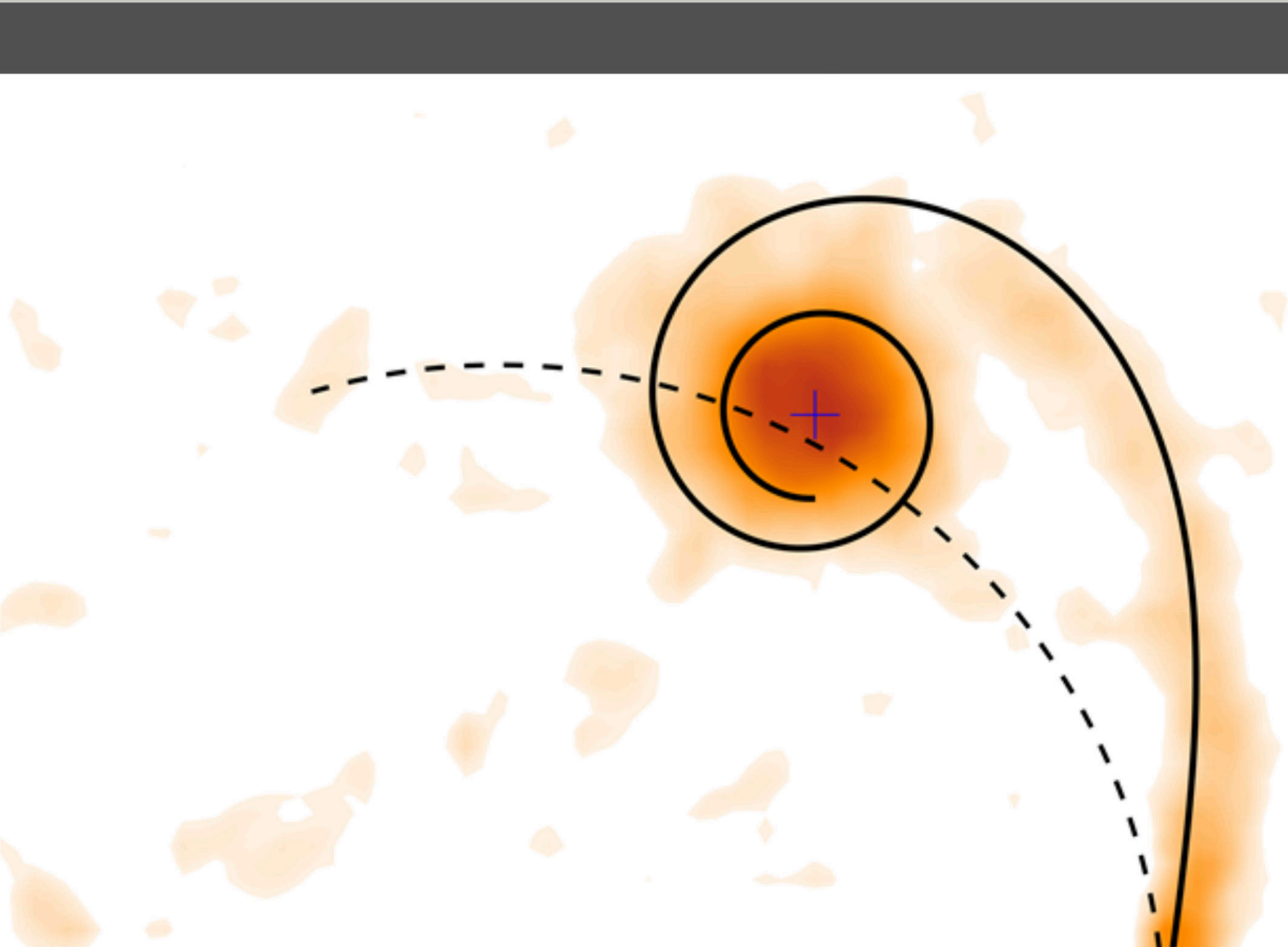
These results are a first step towards the understanding of the efficiency of anguilliform swimming and will be compared to results for other species of snakes that have independently evolved an aquatic life-style. This may help future developments of bio-inspired aquatic systems.

References

- [1] B. C. Jayne. What Defines Different Modes of Snake Locomotion? *Integrative and Comparative Biology*, Volume 60, Issue 1, 2020.
- [2] U. K. Müller, et al. How the body contributes to the wake in undulatory fish swimming: Flow fields of a swimming eel (*Anguilla anguilla*). *Journal of Experimental Biology*, 204(16), 2751-2762, (2001).
- [3] E. D. Tytell & G. V. Lauder The hydrodynamics of eel swimming: I. Wake structure. *J Exp Biol.*, 207(Pt 11):1825-41, 2004.
- [4] B. J. Gemmell, et al. How the bending kinematics of swimming lampreys build negative pressure fields for suction thrust. *J Exp Biol.*, 219(Pt 24):3884-3895, 2016.
- [5] K. T. Du Clos, et al. Thrust generation during steady swimming and acceleration from rest in anguilliform swimmers. *J Exp Biol.*, 22, (2019).
- [6] S. Kern & P. Koumoutsakos. Simulations of optimized anguilliform swimming. *The Journal of experimental biology*. 209. 4841-57, (2007).
- [7] I. Borazjani & F. Sotiropoulos. Numerical investigation of the hydrodynamics of anguilliform swimming in the transitional and inertial flow regimes. *J Exp Biol.*; 212(Pt 4):576-92, 2009.
- [8] U. E. Ogunka, et al. The Ground Effect in Anguilliform Swimming. *Biomimetics*; 5(1):9, 2020.
- [9] M. Khalid, et al. Why do anguilliform swimmers perform undulation with wavelengths shorter than their bodylengths? *Physics of Fluids* 33, 031911 (2021).
- [10] L. Graftieaux, et al. Combining PIV, POD and vortex identification algorithms for the study of unsteady turbulent swirling flows *Meas. Sci. Technol.*; 12 1422, (2001).

Session D

Prediction and theory



Physics-Based Low-Order Modelling of Unsteady External Flows

Kiran Ramesh^a

^a University of Glasgow, School of Engineering, Glasgow, UK

*Correspondence: kiran.ramesh@glasgow.ac.uk

1 Introduction

Unsteady external flows are prevalent in modern aerospace applications across a large range of scales. The flow physics include significant nonlinearities such as flow separation and vortex shedding. Theoretical solutions in unsteady aerodynamics are quick and cheap to use, and provide useful insight into the flow physics, but are based on simplifying assumptions which render them invalid for these problems. Semi-empirical tools are commonly used instead. These are another class of methods that use curve-fits and empirical relations derived from computational and experimental data to make predictions. These are computationally fast but do not provide insight into the flow phenomena and are only valid in regimes where they have been previously validated.

In this presentation, we will discuss and present the latest results from an approach which integrates analytical and numerical methods, while also being strongly informed by experimental data. The analytical solutions are based on the unsteady potential flow equations in which the farfield boundary conditions are naturally enforced. Numerical methods using discrete-vortex elements are used to model physics and phenomena that are not accounted for in the analytical solution, resulting from viscosity. This approach allows the external flow system to be described by a relatively small number of time-varying states, to which machine learning approach to improve predictions may be easily applied.

2 Results

Early results for a low-order criterion to determine arbitrary flow separation from any location on an airfoil are shown in this section. This is a generalization of the LESP [1] criterion which is only applicable for separation from the leading edge of the airfoil. The method is based on solving the integral boundary-layer equations in tandem with the potential flow solution using a viscous-inviscid interaction scheme. We note that this approach is similar to that used in XFOIL with two significant differences; (i) XFOIL solves for steady flow, while in the current approach both potential flow and BL equations are time dependent, (ii) XFOIL can model reversed flow and BL thickening but not BL separation which is necessarily unsteady. We aim to also model BL detachment and subsequent emanation of free shear layers by shedding discrete vortices from the separation location. Figure 1 shows results for a cylinder impulsively started from rest.

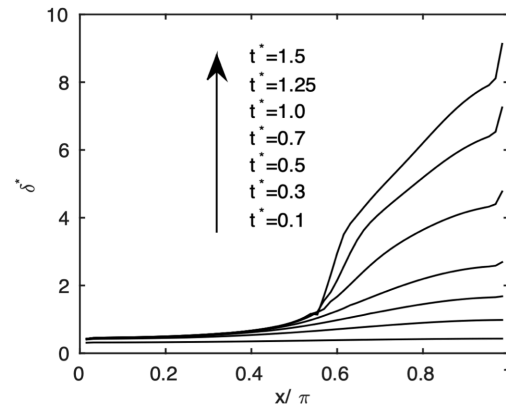


Figure 1: Evolution of boundary layer displacement thickness on a cylinder.

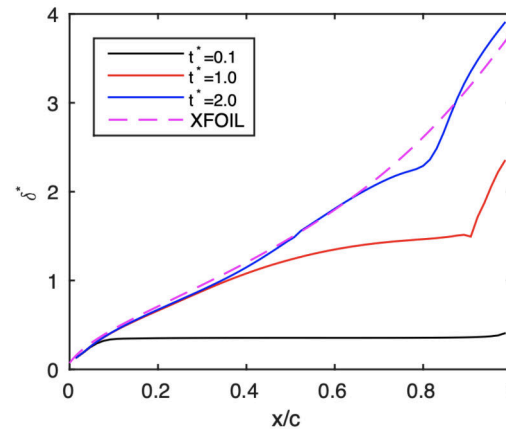


Figure 2: Evolution of boundary layer displacement thickness on a NACA0012 airfoil.

BL detachment occurs in this scenario and both time and location of separation are predicted well by the low-order method. Figures 2 and 3 shows results for a NACA0012 airfoil started from rest. In this case, despite the occurrence of reversed flow and significant viscous-inviscid interaction (BL thickening) near the trailing-edge region, there is no separation. Results from the low-order method are seen to tend towards the steady solution from XFOIL as time increases.



Figure 3: Effective geometry of a NACA0012 with boundary layer displacement.

3 Conclusions

This abstract shows early results from a new approach to predict generalised separation on airfoils. In the presentation, we will demonstrate the shedding of vorticity resulting from arbitrary separation, and extension of this method to 3D wing surfaces.

References

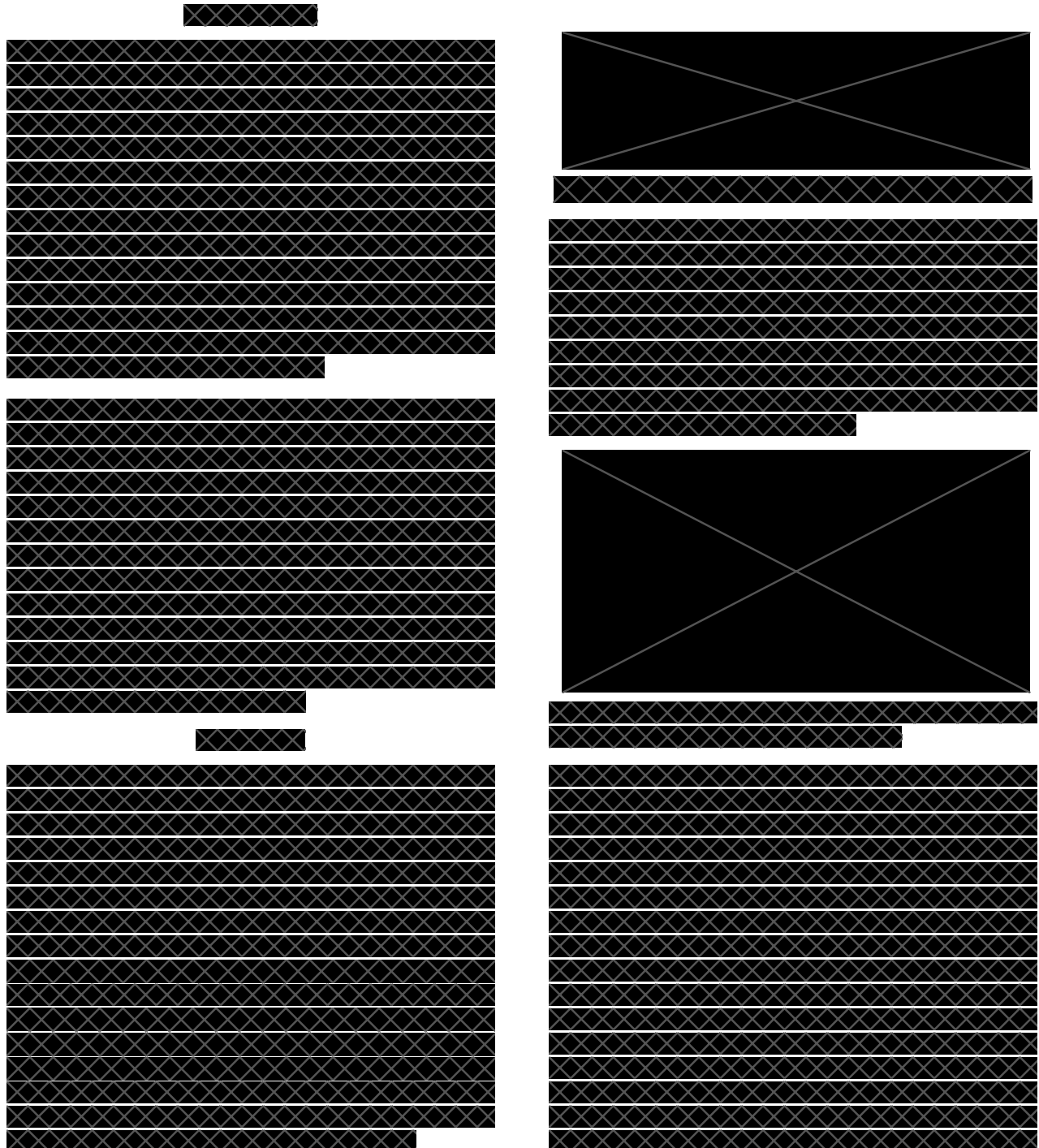
- [1] Ramesh, K. et al. Discrete-vortex method with novel shedding criterion for unsteady airfoil flows with intermittent leading-edge vortex shedding *Journal of Fluid Mechanics*, 751:500-538, 2014.

Prediction of Leading-Edge Vortex Initiation Using Criticality of the Boundary Layer

H. Ramanathan^a and A. Gopalarathnam^{a*}

^a Mechanical and Aerospace Engineering, North Carolina State University, Raleigh, NC, USA

*Correspondence: agopalar@ncsu.edu



Sensor Fusion for Temporal Super-Resolution of Turbulent Separated Flows

Kevin H. Manohar^{a*}, Owen Williams^b, Robert Martinuzzi^a, and Chris Morton^a

^a University of Calgary, Department of Mechanical & Manufacturing Engineering, Calgary, Canada ¹

^b University of Washington, Department of Aeronautics & Astronautics, Seattle, United States of America

*Correspondence: kevin.manohar@ucalgary.ca

1 Introduction

The high Reynolds number turbulent separated flow over a Gaussian speed-bump has presented computational fluid dynamics (CFD) modelling challenges for predicting flow separation, reattachment, turbulent transition, and relaminarization [1]. This has motivated the CFD community to accelerate progress in this area [2]. Unfortunately, the lack of time-resolved (TR) experimental data on the Bump has limited progress on understanding the energy transfer mechanisms between flow scales that lead to flow separation, which would provide substantial insight for the advancement of turbulence models. The above challenges motivate the present work, which attempts to provide TR estimates of the velocity field from experimental Bump data. In particular, we employ novel flow estimation techniques using surface mounted pressure sensors, enabling prediction of time-resolved (TR) transient dynamics that are inherently missing from the (under-sampled) PIV time-series. The recently well-proven efficacy of artificial neural networks in predicting highly non-linear relationships is utilized in place of traditional methods (e.g., stochastic estimators) to enhance the accuracy of sensor-based prediction of unsteady turbulent separation dynamics.

2 Methods

Experiments were conducted in the 3' × 3' low-speed wind tunnel at the University of Washington. Two-dimensional velocity fields were acquired at $f_{\text{PIV}} = 15$ Hz using PIV in a streamwise-vertical plane close to the expected separation points. The wall conditions were measured synchronously and were over-sampled ($f_{\text{sens}} = 31.25$ kHz) at nine pressure taps using differential pressure transducers. The freestream velocity of the present flow case is $U_\infty = 40$ m/s, and the PIV measurement domain Ω captures the unsteady motion of separation along the centre-line/symmetry plane $y/L = 0$ in the range $(x/L, z/L) \in \Omega = [0.008, 0.198] \times [0.025, 0.175]$, where $L = 0.914$ m is the width of the test section (see Figure 1).

The two-dimensional fluctuating velocity field is denoted as $\mathbf{u}'(\mathbf{x}, t_k)$ with components $u'(\mathbf{x}, t_k)$ and $w'(\mathbf{x}, t_k)$ for $t_k =$

¹This work was supported by the Natural Science and Engineering Research Council of Canada under grant number 04079.

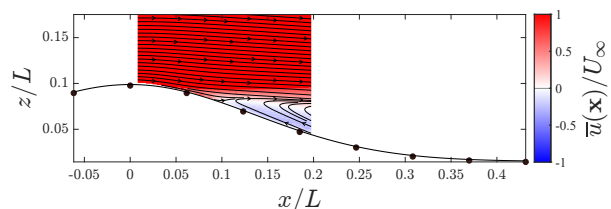


Figure 1: PIV measurement plane Ω , with non-dimensional mean streamwise velocity field $\bar{u}(\mathbf{x})/U_\infty$. Nine pressure taps along Bump surface are marked as black dots.

$k\Delta t_{\text{PIV}}$, where $\Delta t_{\text{PIV}} = 1/15$ s and $\mathbf{x} \in \Omega$. The fluctuating surface pressure data are defined similarly as $p'(\mathbf{x}_s, t_m)$ for $t_m = m\Delta t_{\text{sens}}$, where $\Delta t_{\text{sens}} = 32$ μ s and \mathbf{x}_s denotes pressure tap locations along the Bump surface (see Figure 1).

The TR velocity fields are reconstructed by correlating the PIV measurements with the over-sampled pressure data. As demonstrated in past experimental studies [3], operating within the low-dimensional Proper Orthogonal Decomposition (POD) subspace is effective in improving correlations between pressure sensor and velocity flowfield data. POD is used to decompose the fluctuating time-series $\mathbf{u}'(\mathbf{x}, t_k)$ of N snapshots into a finite sum of basis functions $\Phi_k(\mathbf{x})$ and corresponding coefficients $a(t_k)$:

$$\mathbf{u}'(\mathbf{x}, t) = \sum_{k=1}^N \Phi_k(\mathbf{x}) a(t_k). \quad (1)$$

The energy captured by the first r modes defined as $\sum_{k=1}^r \frac{1}{2} \overline{a(t_k)^2}$ is maximized to yield orthonormal basis functions $\Phi_k(\mathbf{x})$ in \mathcal{L}^2 -Hilbert space. The time-varying coefficients $a(t_k)$ are then obtained by orthogonal projection, and satisfy orthogonality.

We propose a method that leverages available TR sensor history to encode potentially missing correlations between the pressure and velocity field. In particular, we are approximating the map:

$$\mathcal{F} : p'(\mathbf{x}_s, t_{k-S:k-1}) \mapsto a(t_k). \quad (2)$$

Here, the domain of \mathcal{F} includes time-delayed states of the TR pressure signals, $p'(\mathbf{x}, t_{k-S:k-1})$, where S is the sequence length that defines the amount of memory/time history encoded in the input state.

3 Results

A deep feedforward neural network comprised of nine fully-connected hidden layers with 50 neurons each is trained to predict the first $r = 4$ POD modes that resolve 51% of the (planar) turbulent kinetic energy (TKE). The training dataset contains $N = 4\,000$ snapshots with under-sampled velocity data at 15 Hz. The (TR) pressure history of each sensor in the input state spans 0.32 s ($\approx 5\Delta t_{\text{PIV}}$). For super-resolution, the pressure sensor data is used with the trained network to predict the TR evolution of POD coefficients at $f_{\text{PIV}}^+ = 1\,500$ Hz. The TR evolution of mode 1 (containing 34% of TKE) is shown in Figure 2. The results qualitatively show good agreement between the estimated values and true values of a_1 . Similar comparisons have been made with a_{2-4} (not shown here for brevity).

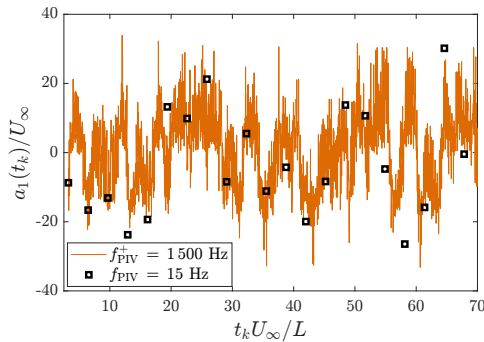


Figure 2: TR evolution of mode 1 coefficient ($f_{\text{PIV}}^+ = 1\,500$ Hz) compared with the original ($f_{\text{PIV}} = 15$ Hz).

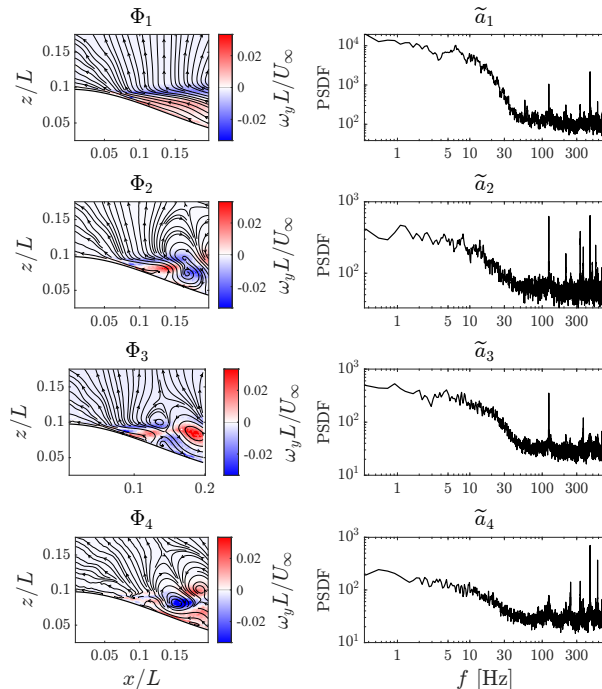


Figure 3: First four POD modes Φ_k (left) and PSDFs of the corresponding TR coefficient estimates \tilde{a}_k (right) for $f_{\text{PIV}}^+ = 1\,500$ Hz. Contours represent non-dimensional vorticity.

To evaluate the super-resolved PIV data further, spectral analysis of the TR POD coefficient estimates \tilde{a}_k was conducted. The results are shown in Figure 3 alongside the first four spatial modes. Several dominant frequencies are observed in the power spectral density functions (PSDFs) of \tilde{a}_k . First, a low-frequency broadband phenomenon centered at ≈ 6 Hz or $St = fL_{\text{sep}}/U_\infty \approx 0.019$ is observed in \tilde{a}_1 , where L_{sep} is the length of the separation bubble in the $y/L = 0$ plane defined as the Euclidean distance between mean separation and reattachment points. Second, a medium-frequency phenomenon at 123 Hz or $St = 0.39$ is observed in all four modes but dominates $\tilde{a}_{2,3}$. These values roughly correspond to Strouhal numbers reported by Taifour & Weiss [4] for a pressure-induced turbulent separation bubble. The low-frequency phenomenon at $St = 0.019$ is speculated to be a breathing mode - describing the contraction and expansion of the separation bubble. On the other hand, the phenomenon at $St = 0.39$ is a flapping mode - describing the formation and dynamics of large-scale vortices in the shear layer. Moreover, the scale and distribution of the structures in Φ_{1-4} are consistent with these behaviors.

Higher frequency peaks at 212, 335 Hz (see $\tilde{a}_{2,4}$) can be expressed as linear combinations of 123 Hz and a secondary frequency at 89 Hz, which is visible in \tilde{a}_4 . i.e., $(89 + 123)$ Hz = 212 Hz and $(89 + 2 \cdot 123)$ Hz = 335 Hz. It is possible that these detectable frequencies in the flow are related to non-linear interactions within the separated shear layer.

4 Conclusions

The present work introduces a novel machine learning method to estimate time-resolved velocity fields from under-sampled PIV and over-sampled surface pressure sensor measurements. The flow case is that of high Reynolds number turbulent separated flow over a Gaussian speed-bump geometry. The proposed technique enables identifying and resolving unsteady dynamics of large-scale structures that are otherwise aliased in the raw PIV measurements. Dominant frequencies are identified in the predicted velocity spectra, and possible connections to unsteady separation mechanisms are briefly discussed. Future work will investigate the effect of training on higher-order modes and the unsteady mechanisms that influence flow separation.

References

- [1] Owen Williams, Madeline Samuel, E Sage Sarwas, Matthew Robbins, and Antonino Ferrante. Experimental study of a cfd validation test case for turbulent separated flows. In *AIAA Scitech 2020 Forum*, page 0092, 2020.
- [2] Riccardo Balin and Kenneth E Jansen. Direct numerical simulation of a turbulent boundary layer over a bump with strong pressure gradients. *Journal of Fluid Mechanics*, 918, 2021.
- [3] Jean P Bonnet, Daniel R Cole, Joël Delville, Mark N Glauser, and Lawrence S Ukeiley. Stochastic estimation and proper orthogonal decomposition: complementary techniques for identifying structure. *Experiments in fluids*, 17(5):307–314, 1994.
- [4] Abdelouahab Mohammed-Taifour and Julien Weiss. Unsteadiness in a large turbulent separation bubble. *Journal of Fluid Mechanics*, 799:383–412, 2016.

The inference of vortical flows from pressure measurements

Jeff D. Eldredge^{*}, Diederik Beckers, and Mathieu Le Provost
University of California, Los Angeles, Mechanical & Aerospace Engineering
Los Angeles, California, United States¹

^{*}Correspondence: jdeldre@ucla.edu

1 Introduction

In fluid dynamics, there are a variety of circumstances in which we would like to expand our knowledge of a vortical flow from a limited set of measurements. For an air vehicle subjected to a gust or other disturbance, we might be better equipped to mitigate the disturbance’s effect if we are armed with more details about the flow. To achieve the fuel-economy benefits of formation flight, we might desire to autonomously detect the wake of a lead aircraft so that a trailing aircraft can position itself optimally. We might also wish to detect flow separation in a short diffuser or serpentine duct. In all of these cases, our sensing is restricted: the IMU and pitot probes on an aircraft or pressure transducers on the surface of a wing or duct. It is generally understood that vortices leave their pressure signature on surfaces. The overarching question that guides this work is: To what extent can this signature be used to infer the state of the vortices?

Our overall approach to this problem is based on the ensemble Kalman filter (EnKF), a data assimilation technique that approximates the state’s probability density function with a finite ensemble of Monte Carlo (i.e., random) realizations of the state [1]. The EnKF provides an attractive practical framework for data assimilation in fluid dynamics problems because one can run a modest ensemble of moderate-dimensional dynamical models (e.g., inviscid vortex models or coarse-grid CFD) and assimilate measurements from the real system to inform our prediction with physics that are missing from the model (e.g., disturbances, physical parameters). In the current approach, the state is composed of the positions and strengths of a small set of singular vortex elements that represents our flow field. In each time step, the set of vortex elements in each ensemble member is first advanced by a step with an inviscid vortex model, providing us with a prediction of the state and its uncertainty—the ‘prior’ probability density of the flow field. This prediction, however, is not entirely trustworthy: it coarsely represents the dynamics of coherent structures and omits viscous diffusion altogether. Thus, in the second part of the time step—the filter step—we compare the true measurements (pressure sensor data from the actual system) with our prediction of these measurements via the *observation function*, obtained here from the solution of the pressure Poisson equation. We

correct the ensemble of states from the measurement discrepancy multiplied by the so-called Kalman gain. This corrected ensemble serves as an approximation of the ‘posterior’ probability density.

For an infinite ensemble and a linear system, the Kalman filter is optimal: it minimizes the uncertainty of our posterior estimate of the state. An actual ensemble is finite, so we only approximately achieve this optimality, but we still reap substantial benefits. In previous work, for example, we have shown that we can estimate the aerodynamic response of a separated flow to strong incident disturbances without any prior knowledge of the disturbance itself [2]. However, in a small ensemble with tens of members—necessary for practical application—we generally see a significant decay (or even instability) in the filter’s performance, due to the deleterious effect of spurious correlations between states and measurements. In such situations, the Kalman gain, which is built from the state–measurement covariance, is fooled into making unphysical corrections to the state. Practitioners of the EnKF have traditionally avoided this performance decay by “localizing” the covariance—essentially, cutting off all covariances between states and measurements that are physically well-separated. Unfortunately, that approach is inappropriate in the current context, because the influence of the state (vortex element properties) on the measurements (pressures) is *fundamentally non-local*, since it is based on the solution of a Poisson equation.

In this talk, we will present a novel low-rank EnKF (LREnKF) that removes the effect of spurious correlations of ensemble Kalman filters, particularly for problems with non-local and non-linear relationships between measurements and states [3]. The key of the new technique is to exploit the Jacobian of the observation function, which quantifies the expected sensitivity of each measurement to each state. We can assess this sensitivity across the ensemble by computing a pair of square matrices, the state-space and the observation-space Gramians. The eigenvectors of these matrices represent, respectively, the fundamental state and observation modes of the problem. Furthermore, the eigenvalues of these matrices generally fall off rapidly, indicating that only a few observation modes are truly informative for correcting a few state modes; the rest can be simply ignored. As we will show, this modal decomposition is crucial for addressing the original guiding question on the connection between vortices and their pressure signature: by pro-

¹This work was supported by AFOSR under grant number FA9550-18-1-0440

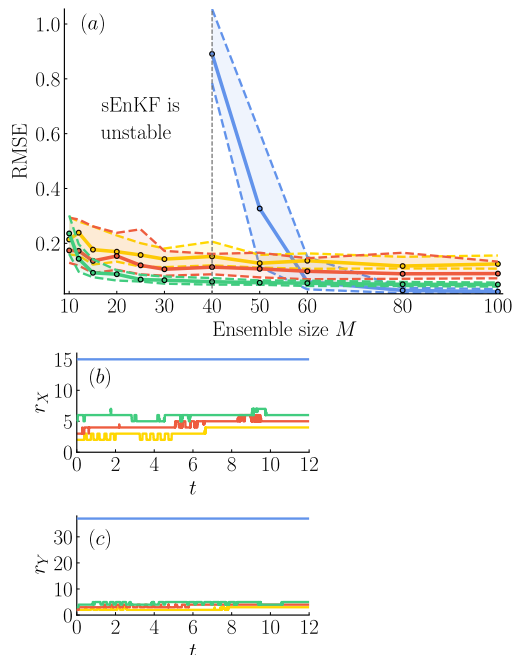


Figure 1: Estimation of a five-vortex system (a) Median root-mean-squared error versus the ensemble size M (computed over 50 realizations) with the traditional EnKF (‘sEnKF’) (blue), and with the low-rank EnKF for different thresholds of the cumulative energy: 85% (yellow), 95% (orange), and 99% (green). The sEnKF is unstable for $M < 40$. Dashed lines depict the 25% and 75% quantiles. Right column [(b)-(c)]: Time histories of the median ranks r_x and r_y of the low-rank EnKF for $M = 30$ (computed over 50 realizations) for different thresholds of the cumulative energy 85% (yellow), 95% (orange), and 99% (green). The dimension of the state and observation spaces, namely n and d , are depicted for comparison in blue.

jecting this signature onto the observation modes, we learn explicitly which modes of the vortex state can be uniquely informed from pressure and which cannot.

2 Results

We will exhibit many of the important features of the LREnKF in the context of vortex estimation. We will first provide intuition for observation and state modes by showing that they are nearly equivalent to the terms of the well-known multipole expansion of the fundamental solutions of a Poisson equation. Then, we will show the application of the LREnKF to several canonical examples for estimating vortex elements from pressure measurements. Figure 1 depicts the results from an example in which we estimated the positions and strengths of five point vortices (i.e., 15 state components) self-advecting along a wall on which 37 pressure sensors are distributed. This is a ‘twin experiment’: truth data was taken from the same inviscid model, but with perfect knowledge of the state; its purpose is to understand the effect of estimating this vortex system with different ensemble sizes. For the LREnKF, the rank of the state and

observation modes was truncated at a pre-chosen threshold of the total energy (the sum of the eigenvalues of each Gramian). These results were compared with the traditional stochastic EnKF (sEnKF), in which no rank reduction was performed.

There are a few important observations to make about these results. First, the sEnKF is actually unstable for ensembles smaller than 40: the spurious correlations overwhelm the state correction and cause the vortex system to deviate from the true trajectories. On the other hand, the LREnKF remains effective for ensembles as small as 10 with little deterioration in the accuracy. The results in (b) and (c) indicate that, although the state dimension is 15 and the observation space dimension is 37, the observation operator is much lower effective rank: for an ensemble of size 30, both the state and the observation can be well approximated with only around 6 modes each. Other examples that we will show exhibit similar characteristics and a low effective rank. Furthermore, we will show that, when the truth measurements are taken from a real (viscous) flow, some of the retained state modes can approximate the effect of viscous diffusion, e.g., the radial spread of a cluster of vortices.

3 Conclusion

Stochastic data assimilation provides fluid mechanics with many interesting opportunities for enhancing our knowledge of a flow. By combining the limited measurements of a real flow with an efficient dynamical model that minimally captures the essential physics, we can obtain detailed predictions of the full flow state. In the approach we present here, an inviscid vortex model efficiently describes the large-scale dynamics of coherent vortex structures, but omits details of these structures’ dynamics, their viscous diffusion, and their disturbance by gusts. We therefore balance our trust of this model with the sensor data taken from the real flow, which contains a perfect knowledge of the flow, albeit limited and noisy.

The ensemble Kalman filter is an enabling approach for data assimilation in fluid mechanics, but requires large ensemble sizes to overcome the effects of spurious correlations. Here, we have presented a low-rank EnKF that identifies the most informative modes in which the flow state can be corrected from sensor data and regularizes the non-informative components so that they cannot corrupt the prediction. The informative modes provide insight on sensor placement and on the vortex model’s economy of vortex elements.

References

- [1] Evensen G. Sequential data assimilation with a nonlinear quasi-geostrophic model using Monte Carlo methods to forecast error statistics. *Journal of Geophysical Research: Oceans* **99**, 10143–10162, 1994.
- [2] Le Provost, M. and Eldredge, J. D. Ensemble Kalman filter for vortex models of disturbed aerodynamic flows. *Physical Review Fluids* **6**, 050506, 2021.
- [3] Le Provost M., Baptista R., Marzouk Y. and Eldredge J. D. A low-rank nonlinear ensemble filter for vortex models of aerodynamic flows. AIAA Scitech 2021 Forum, 2021-1937, 2021.

Low-order modelling of lift on pitching aerofoils

Shūji Ōtomo,^a Karen Mulleners,^b Kiran Ramesh,^c and Ignazio Maria Viola^{a*}

^a School of Engineering, Institute for Energy Systems, University of Edinburgh, Edinburgh, UK¹

^b Unsteady Flow Diagnostics Laboratory, École Polytechnique fédérale de Lausanne (EPFL), Switzerland¹

^c Aerospace Sciences Division, School of Engineering, University of Glasgow, Glasgow, UK

*Correspondence: *i.m.viola@ed.ac.uk*

1 Introduction

Theodorsen's theory [1], which is based on potential flow theory, is widely used to predict unsteady lift for many modern engineering applications. It assumes an attached flow and a planar wake, limiting its applicability to small amplitude oscillations. However, modern engineering application such as micro-air vehicle and flapping-wing energy harvesters often experience massively separated flows characterised by the shedding of coherent leading-edge vortices (LEV) and trailing-edge vortices (TEV). Several investigators [2–4] successfully applied Theodorsen's theory in separated flow conditions, but others [3] questioned their validity when a separated LEV occurs. There is no clear agreement on which are the effective limiting conditions for Theodorsen's theory, nor on which is the physics that causes Theodorsen's theory to fail.

In our previous work [5] we investigated the applicability of Theodorsen's theory in separated flow conditions and we identified a limiting criterion of Theodorsen's theory. In this short paper we summarise these results, and we extend them by developing a low-order model that extends Theodorsen's theory validity to fully separated flow conditions.

2 Methodology

We test an aerofoil undergoing an asymmetric triangular pitching kinematics at a reduced frequency $k = 0.22$, pitching amplitude $\alpha_0 = 64^\circ$, and Reynolds number $Re = 32000$. This kinematics is beyond the applicability of Theodorsen's theory because of the high-amplitude and of the non-sinusoidal nature. Tests are performed in a water tunnel where we measure time-resolved forces. We use particle image velocimetry (PIV) to study the LEV and TEV interaction and we develop a data-driven model and a semi-empirical model with one experimentally fitted parameter. In the following, we compare the measured lift with that predicted by Theodorsen's theory, by the data-driven model, and by the semi-empirical low-order model.

We assume that the force predicted by Theodorsen's the-

ory is chord-normal, because it is derived from the pressure difference between the suction and pressure sides of the aerofoil. The lift L^{TH} is its stream-normal projection. Since the kinematics are non-sinusoidal, we linearly sum the lift computed for the first 20 Fourier terms of the kinematics. In case of flow separation, we hypothesise that the vortex lift associated with the relative velocity of the LEV and the TEV can be linearly added to the lift predicted with Theodorsen's theory. We compute the vortex lift as $L^{\text{V}} = \rho \Gamma_{\text{LEV}} (u_{\text{LEV}} - u_{\text{TEV}})$ [5–8], where ρ is the fluid density, Γ_{LEV} is the circulation of the LEV, u_{LEV} and u_{TEV} are the LEV and TEV streamwise velocities. The total lift is $L = L^{\text{TH}} + L^{\text{V}}$. For the data-drive model, we identify the LEV and the TEV using the swirling strength criterion with a threshold value of 10% of the maximum value, and then we integrate the contained vorticity to estimate Γ_{LEV} and track the centroids to compute u_{LEV} and u_{TEV} . We find that the TEV is often broken down into smaller vortices, however $\Sigma \Gamma_{\text{TEV}} = -\Gamma_{\text{LEV}}$.

For the semi-empirical model, we assume that the LEV advects at half the freestream velocity ($u_{\text{LEV}} = U_\infty/2$), consistently with the PIV result and the observations in literature [6, 9, 10]. The TEV velocity is assumed to be the sum of the trailing-edge shear-layer velocity, $U_\infty \cos^2 \alpha - \dot{\alpha}(1-a)c \sin \alpha$, and the LEV-induced velocity, $\Gamma_{\text{LEV}}/(2\pi c \sin \alpha)$. Here c is the chord and a is the chordwise distance of the pitch axis from the leading-edge. The shear-layer velocity at the leading-edge is estimated as $u_{\text{SL}} = U_\infty \sin \alpha + a\dot{\alpha}$. We assume that the outer shear-layer velocity is $u_{\text{max}} = \kappa u_{\text{SL}}$, with κ constant [11]. The rate of change of LEV circulation is $\dot{\Gamma} = u_{\text{max}}^2/2 = \kappa^2 u_{\text{SL}}^2/2$, whose integral gives the LEV circulation [12]. The proportionality constant κ is found by a global fitting to four different kinematics with the least-square method (hence the semi-empirical nature of the model).

3 Results

Figure 1a compares the lift coefficient $C_L \equiv 2L/(\rho U_\infty^2 c)$ as measured and predicted with Theodorsen's theory, the data-driven model, and the semi-empirical model. The LEV-TEV relative velocity, $u_{\text{LEV}} - u_{\text{TEV}}$, and the LEV circulation, Γ_{LEV} , are plotted in Fig. 1b and 1c respectively. Figure 1d shows the flowfields for the two instants 1 and 2 in-

¹This work was supported by Japan Student Services Organization, Energy Technology Partnership Scotland (No. PECRE059), and Swiss National Science Foundation (SNSF) Assistant Professor energy Grant number PYAPP2_173652.

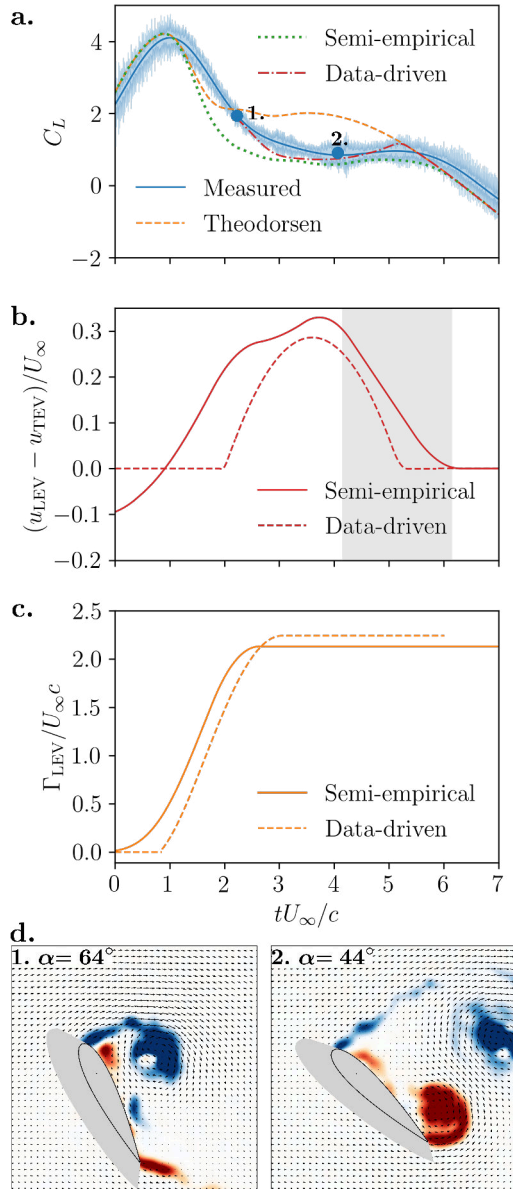


Figure 1: Comparison of **a.** lift coefficient, **b.** relative LEV-TEV velocity, **c.** LEV circulation, and **d.** two flowfields at **1.** $\alpha = 64^\circ$ and **2.** $\alpha = 44^\circ$.

icated in Fig. 1a.

Theodorsen’s theory exhibits a remarkable agreement with the experiment despite the large amplitude and asymmetry of the kinematics. However, at $t \approx 2c/U_\infty$, the discrepancy with Theodorsen’s theory increases. Figure 1b shows that, at that instant, u_{LEV} is faster than u_{TEV} and the LEV-TEV interaction contributes negatively on lift.

By adding the vortex lift coefficient, the data-driven model results are in an excellent agreement with the experiment. We infer that the limiting criterion for Theodorsen’s theory is whether the magnitude of the vortex lift is negligible,

which holds when a coherent TEV is formed and advects downstream at slower velocity than the LEV.

Here, we show that the vortex lift coefficient can be predicted a priori with the proposed semi-empirical model, which shows a good agreement with the experiment (Fig. 1a). The predicted lift deviates from the experiment at $tU_\infty/c < 2$, because the relative velocity $u_{LEV} - u_{TEV}$ cannot be predicted accurately.

4 Conclusion

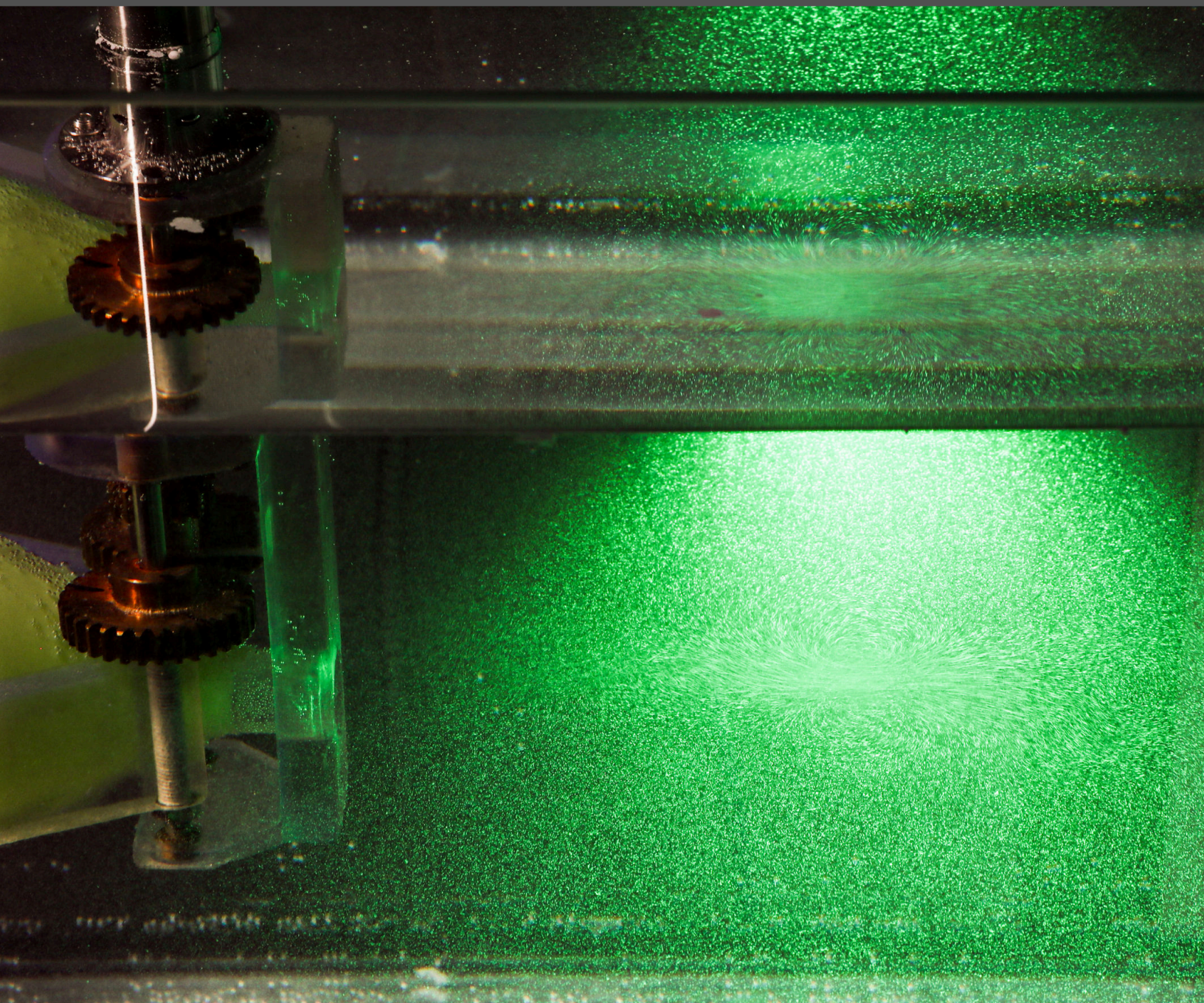
We have shown that Theodorsen’s theory can be adapted for large-amplitude asymmetric kinematics with separated flow. The vortex lift associated with the LEV-TEV interaction accounts for the difference between the measured lift and that predicted by Theodorsen’s theory. This clarifies that the limiting criterion for the validity of Theodorsen’s theory is whether the magnitude of vortex lift is significant compared to the lift predicted with Theodorsen’s theory. Even though we do not propose a fully predictive model yet, a semi-empirical model based on the knowledge of the shear layer velocity is found that provides a reasonable agreement with the experiments. These results provide new insights on the vortex forces and may pave the way to the development of fully predictive low-order models for the unsteady forces in massively separated flow conditions.

References

- [1] Theodorsen, T. General theory of aerodynamic instability and the mechanism of flutter. NACA Report, No. 496, 1935.
- [2] Oi, MV., Bernal, L., Kang, CK., Shyy, W. Shallow and deep dynamic stall for flapping low Reynolds number airfoils. *Exp. Fluids*, 46:883-901, 2009.
- [3] McGowan, MV., Bernal, L., Kang, CK., Shyy, W. Investigations of Lift-Based Pitch-Plunge Equivalence for Airfoils at Low Reynolds Numbers. *AIAA J.*, 49:7, 2011.
- [4] Kang, CK., Baik, YL., Bernal, L., Oi, MV., Shyy, W. Fluid Dynamics of Pitching and Plunging Airfoils of Reynolds Number between 1×10^4 and 6×10^4 . *AIAA Paper*, 2009-536, 2009.
- [5] Ōtomo, S., Henne, S., Mulleners, K., Ramesh, K., Viola, IM. Unsteady lift on a high-amplitude pitching aerofoil. *Exp. Fluids*, 62:6, 2021.
- [6] Babinsky, H., Stevens RJ., Jones, AR., Bernal, LP., Oi, MV. Low-order modelling of lift forces for unsteady pitching and surging wings. *AIAA Paper 2016-0290*, 2016.
- [7] Viola, IM., Arredondo-Galeana, A., Pisetta, G. The force generation mechanism of lifting surfaces with flow separation. *Ocean Eng.*, 239:109749, 2021.
- [8] Kim, D., Gharib, M. Characteristics of vortex formation and thrust performance in drag-based paddling propulsion. *J. Exp. Bio.*, 214:2283-2291, 2011.
- [9] Mancini, P., Medina, A., Jones, AR. Experimental and analytical investigation into lift prediction on large trailing edge flaps. *Phys. Fluids*, 31:013106, 2019.
- [10] Manar, F., Jones, AR. Evaluation of potential flow models for unsteady separated flow with respect to experimental data. *Phys. Rev. Fluids*, 4:034702, 2019.
- [11] Roshko, A. On the drag and shedding frequency of two-dimensional bluff bodies. NACA Report, No. 3169, 1954.
- [12] Fage, A., Johansen, FC. XLII. The structure of vortex sheets *The London, Edinburgh, and Dublin Philosophical Magazine and Journal of Science*, 5:28, 1928.

Session E

Vortex formation



Connecting wavelength and vortex topology in undulated seal whisker geometries

Kathleen M. Lyons^a, Raúl Bayoán Cal^b, Jennifer A. Franck^a

^a University of Wisconsin-Madison, Madison, WI, USA

^b Portland State University, Portland, OR, USA

*Correspondence: jafranck@wisc.edu

1 Introduction

Inspired from the unique geometry of seal whiskers, this research explores the relationship between undulation wavelength of a bluff-body cylinder, and the resulting flow features in the wake. As opposed to the smooth and cylindrical whiskers of most mammals, seal whiskers have opposing sets of undulations along their span. This dual set of undulations contributes to the remarkable sensing and hydrodynamic trail following of seals [1], and also the drag and vortex-induced vibration (VIV) reduction when compared to smooth bodied cylinders.

Similar to helical strakes or ribbon fairings, the spanwise undulations have been shown to break up the strong, coherent vortices from the von Kármán vortex street, forming three-dimensional hairpin vortices within the wake [2]. The exact vortex topology is a function of the intricate seal whisker geometry, but also the flow conditions such as Reynolds number or flow angle. Lyons et al. identified the most important geometric parameters affecting the flow response as the aspect ratio, the two undulation amplitudes, and the undulation wavelength [3]. Some modifications to the geometry and their effects have been investigated, but the underlying flow mechanisms are not fully understood.

Using detailed numerical simulations, this research investigates the wake structure behind six undulated cylinder models with varying wavelength. A turbulence kinetic energy balance will be utilized to uncover underlying flow mechanisms that produce maximum force reduction, and how they are correlated with vortex formation and topology.

2 Methods

The baseline whisker model is constructed using the geometric definition and dimensions presented by Hanke et al. [2]. The geometric parameters are redefined by Lyons et al. [3] to obtain six nondimensional quantities that can be varied independently of one another, including the mean aspect ratio (γ), undulation amplitudes in the chord and thickness (A_C and A_T), the undulation asymmetry (ϕ), the undulation offset (ϵ), and the wavelength (λ). This large parameter space of geometric complexity offers significant variation in potential undulated cylinder models. For this study, the

nominal seal whisker geometry of Hanke et al. is utilized for baseline values of γ , A_C , A_T , ϕ , and ϵ while λ is varied. The baseline model with $\lambda = 3.434$ is simulated, along with two models with lower wavelength, $\lambda = 1$ and $\lambda = 2$, and two models with higher wavelength, $\lambda = 5$ and $\lambda = 6.868$. The top view of each model is shown in Figure 1 with its associated wavelength value. The flow over a smooth ellipse with equal aspect ratio is also performed.

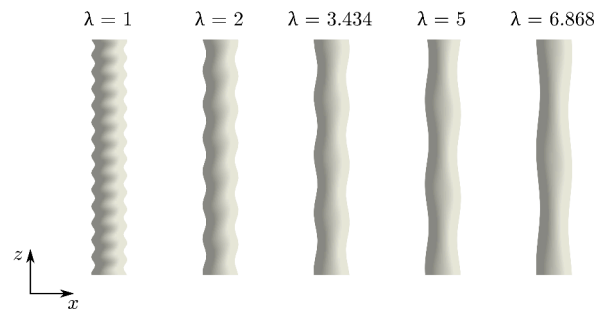


Figure 1: Top view of whisker inspired models at various wavelengths, λ .

Direct numerical simulations (DNS) of the flow over the undulated cylinder models are performed using the open-source software *OpenFOAM*. For each simulation, two periodic wavelengths are simulated. The flow conditions are at zero angle of attack and a Reynolds number of 250, approximating a biologically relevant Reynolds number of seals foraging. For each simulation, the time-resolved forces are computed, as well as the turbulent statistics within the wake of the cylinder. To understand the flow mechanisms responsible for the variations between models, an analysis of the turbulence kinetic energy budget (k) is performed, examining the contributions from convection, turbulent convection, pressure transport, viscous diffusion, production, and viscous dissipation.

3 Results

A comparison of forces over the models demonstrates a nonlinear response with respect to wavelength, and that the nominal biological wavelength of $\lambda = 3.434$ has 10% lower drag and 96% lower RMS lift than the smooth ellipse of equal aspect ratio. The $C_{L,RMS}$ value for the $\lambda = 3.434$ case

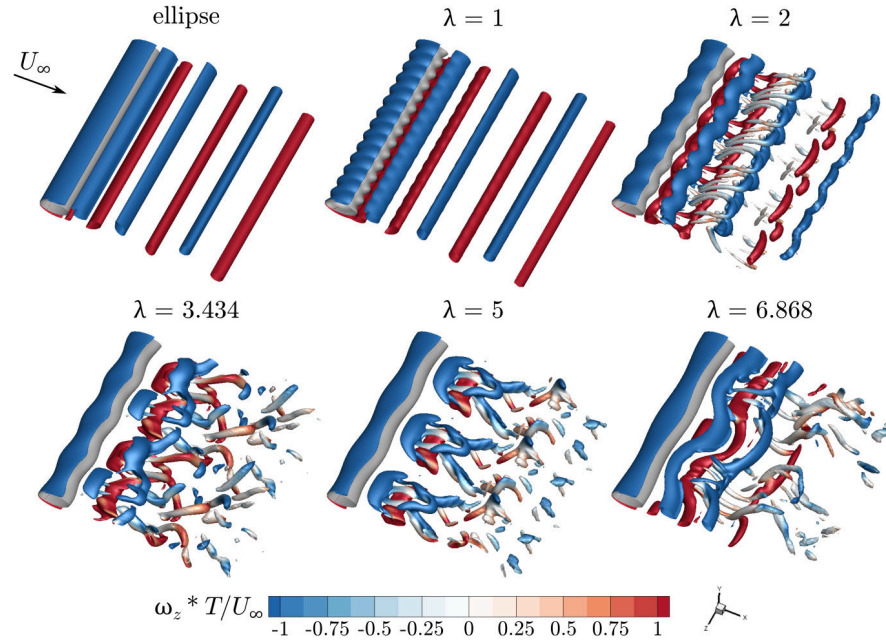


Figure 2: Isosurfaces of nondimensional $Q = 0.3$ colored by z -vorticity illustrate the effect of wavelength modification on flow structure patterns.

is slightly lower than for the $\lambda = 5$ and $\lambda = 6.868$ models, indicating a local minimum around this nominal value.

The force response correlates with changes in the flow patterns within the wake of the cylinders. Isosurfaces of nondimensional Q are plotted in Figure 2 and colored by z -vorticity with red indicating positive and blue indicating negative vorticity. The shed structures behind the $\lambda = 1$ and 2 models are most similar to a typical von Kármán street. The $\lambda = 3.434$ and $\lambda = 5$ models both show development of hairpin vortex structures in the wake. The $\lambda = 3.434$ flow alternates shedding from top and bottom for each wavelength section along the span. In contrast, while the $\lambda = 5$ case develops hairpin vortices, structures are shed in tandem along the span rather than alternating. For both of these cases, the undulations are spaced far enough apart that the spanwise coherent vortex structures are shed without interfering with one another. The $\lambda = 6.868$ case contains a combination of patterns. The undulations are far apart enabling development of hairpin-like structures downstream of peak cross-sections and additional structure formation behind trough cross-sections.

As energy is transferred from the mean flow into turbulence kinetic energy, inspection of k contours and budgets provide a more detailed comparison between models. The production and dissipation of turbulence kinetic energy is examined throughout the wakes of each model in the context of the mean shear and resulting Re stresses. Flow over the $\lambda = 3.434$ model generates both a lower level of k production and a higher amount of k dissipation, allowing for a lower overall level of turbulence kinetic energy compared to the other wavelength models. The spanwise k budget indi-

cate that for the low drag models, the production terms is balanced by the pressure transport term, correlating with the spanwise vortex structures.

4 Conclusion

An investigation into the effect of wavelength on undulated cylinders reveals that the nominal wavelength of $\lambda = 3.434$ demonstrates lower drag and lower lift oscillations than the other wavelengths examined. This is likely a consequence of the unique vortex formation in the near wake, which redistributes and lowers the overall turbulence kinetic energy.

References

- [1] S. Wieskotten, B. Mauck, L. Miersch, G. Dehnardt, and W. Hanke. Hydrodynamic discrimination of wakes caused by objects of different size or shape in a harbour seal (*Phoca vitulina*). *Journal of Experimental Biology*, 214(11):1922–1930, June 2011.
- [2] Wolf Hanke, Matthias Witte, Lars Miersch, Martin Brede, Johannes Oeffner, Mark Michael, Frederike Hanke, Alfred Leder, and Guido Dehnardt. Harbor seal vibrissa morphology suppresses vortex-induced vibrations. *Journal of Experimental Biology*, 213(15):2665–2672, August 2010.
- [3] Kathleen Lyons, Christin T. Murphy, and Jennifer A. Franck. Flow over seal whiskers: Importance of geometric features for force and frequency response. *PLOS ONE*, 15(10):e0241142, October 2020.

Effects of passive flexibility at the exit on the formation of an axisymmetric starting jet

B Ashok ^{a*} and Raghuraman N Govardhan ^a

^a Indian Institute of Science, Mechanical Engineering, Bengaluru, India

*Correspondence: ashokb@iisc.ac.in

1 Introduction

Starting jets are very common in several natural and biological systems, for instance, blood flow in the heart and propulsive systems of aquatic animals like jellyfish and squid. Understanding such flows can help in better designs of prosthetic heart valves and propulsion systems for autonomous underwater vehicles. One of the key characteristics of such starting flows is the formation of a vortex ring, which has been widely studied (for example, Gharib et al. [1]). Most of these studies are focused on starting jets ejected from a rigid exit (figure 1(a)), while most biological systems (like jellyfish) are composed of more flexible materials that can deform due to interactions with the starting flow (figure 1(b)). The study by Das et al. [2] shows that introducing passive flexibility to a two-dimensional jet produces a higher fluid impulse than that of a rigid exit. We are interested here in investigating the role flexibility plays in such starting flows from an axi-symmetric starting jet, such as in the context of jellyfish propulsion, and if there is an optimal flexibility value from a propulsive viewpoint.

In the present work, we study the effects of passive flexibility at the exit on the formation of an axi-symmetric starting jet ejected into quiescent fluid (figure 1(b)). In particular, we investigate the vorticity dynamics of the flow field in the presence of exit with known flexibility and are interested in its implications on propulsive thrust generation.

The experimental setup consists of a piston-cylinder arrangement, which is used to generate the starting jet. The motion of the piston is controlled using a servo motor and a lead-screw mechanism to achieve desired piston velocity profile with time. This piston-cylinder arrangement is placed inside a large open surface water tank. The piston is moved impulsively, i.e., it accelerates quickly (in 0.02s) to reach the desired velocity (U_p) and continues to move at this velocity till it is brought to rest impulsively when the desired piston stroke (L_m) is achieved. As the piston moves, a fluid jet is ejected through a nozzle with circular cross-section of diameter d . For the present study, passive flexibility is introduced at the exit by attaching flexible flaps of known flexural rigidity (EI) around the circumference of the nozzle exit with a certain overlap to prevent leakage during the flow. This flap arrangement was carefully made to allow the flaps to move passively without any hindrance as dictated by the

flow. Figure 1(a) and (b) show the schematic of two nozzle configurations used in the study in an axial plane view, i.e., rigid exit and flexible exit. The Particle Image Velocimetry (PIV) technique was used to quantify and compare the flow fields generated from these two nozzle configurations. The parameters which are varied in the study include flexural rigidity (EI) of the flexible flap arrangement, flap length (L_f), and piston speed (U_p). Some representative results from the experiments are discussed below.

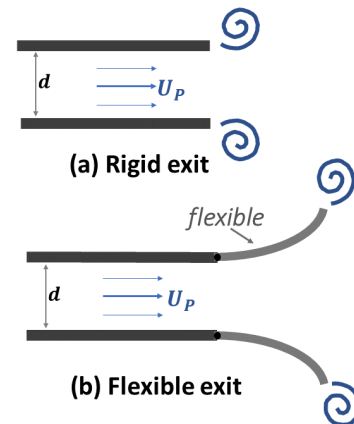


Figure 1: Schematic showing two types of nozzle exit configurations: (a) rigid exit, (b) exit with passive flexibility.

2 Results

In this section, we present the normalized vorticity ($\omega d/U_p$) contours in the axial plane of the nozzle for both the rigid and a sample flexible exit case to highlight the differences caused by passive exit flexibility. The piston motion profile in both cases were kept constant, with a stroke length of $L_m/d = 8$ at a speed of $U_p = 15$ cm/s. For the flexible exit case chosen here, the flexural rigidity (EI) per unit span was 3.2×10^{-6} Nm, and its length was 4 diameters ($L_f/d = 4$). The resulting vorticity field time sequences in the two cases are shown in figure 2 for the rigid case, and in figure 3 for the flexible exit case. In the rigid exit case in figure 2, as the fluid comes out of the rigid exit, it rolls up to form a vortex ring with the ring circulation increasing until it saturates, and the rest of the ejected fluid coming out as a trailing jet, as described in [1]. However, in the flexible exit case shown in figure 3, the vorticity field is drastically different from

the rigid case, as is evident from the distribution of vorticity contours shown. The observed differences in vorticity are due to the large deformations of the flap, which are also marked in the figures. The figures shown correspond to time instances t/τ of 0.20, 0.70, 1.0 and 1.5, where τ is the total piston travel time.

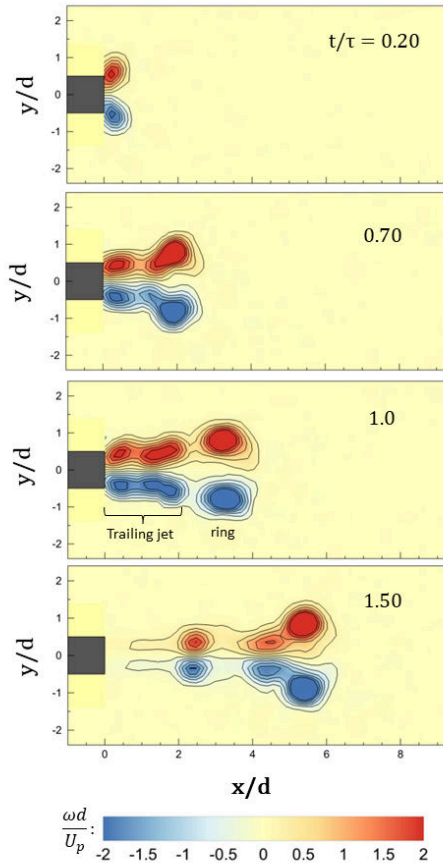


Figure 2: Time sequence of normalized vorticity contours in the axial plane of the flow generated from a **rigid nozzle**.

As the flow initiates, the flaps bulge outward at the centre ($t/\tau=0.20$), and then the tip opens up to a maximum opening ($t/\tau=0.70$). The flaps then gradually return to their initial positions, followed by a sudden inward collapse when the piston stops impulsively ($t/\tau=1.50$). This combination of flap motion and the piston induced flow gives rise to three different pairs of vortices, indicated as A, B, and C vortices in figure 3. The outward motion of the flaps create A vortices, which have opposite sense of rotation to that of vortices formed in case of the rigid exit. The B vortices are formed as the ensuing fluid starts separating at the tip, with these vortices being laterally displaced because of the outward flap motion. The C vortices are primarily formed during the impulsive stopping of the piston and the resulting rapid inward movement of the flaps, which leads to the energetic ejection of this vortex pair relatively close to the jet centerline. The sense of rotation of B and C vortices is

similar to that of vortices ejected from the rigid exit.

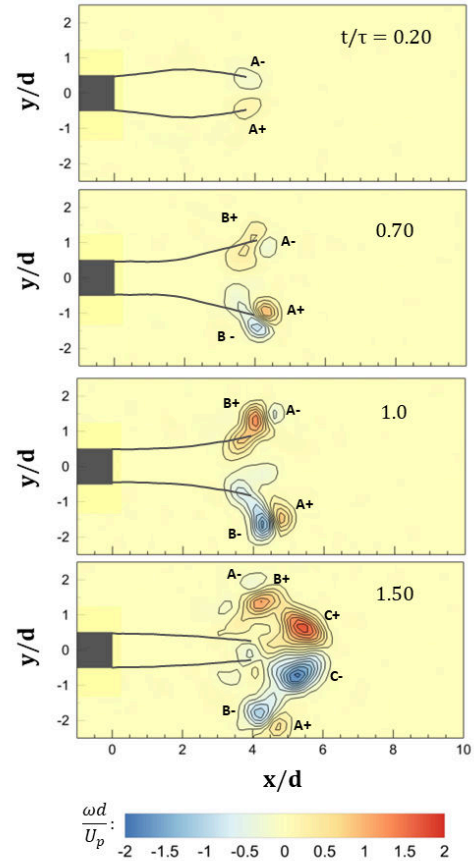


Figure 3: Time sequence of normalized vorticity contours in the axial plane of the flow generated from a nozzle with **passive flexibility**.

3 Conclusion

In the present work, we have experimentally investigated the effects of passive flexibility on the flow field of an axisymmetric starting jet. A drastic difference in vorticity distribution is observed due to the passive flap motion as compared to the rigid exit case. We have identified three types of vortex pairs in the flow field of the passive flexible exit case, referred to as A, B, and C vortices. It is important to note that this vorticity re-arrangement affects the final fluid impulse, which is indicative of the propulsive thrust force generated in such systems. These quantitative results of the fluid impulse along with the flap kinematics for varying flap flexibility will be discussed in detail in the conference.

References

- [1] Gharib, M., et al. A universal time scale for vortex ring formation. *J. Fluid Mech.*, 360, 121-140, 1998.
- [2] Das, P., et al. Unsteady two-dimensional jet with flexible flaps at the channel exit. *J. Fluid Mech.*, 845, 462-498, 2018.

Vortex dynamics associated with a pitching wing in quiescent water

Yuanhang Zhu^{*}, Howon Lee[†] and Kenneth Breuer^{*}

Center for Fluid Mechanics, School of Engineering, Brown University, Providence, RI 02912, USA

^{*}Correspondence: yuanhang_zhu@brown.edu, kenneth_breuer@brown.edu

1 Introduction

When a bluff body moves in a quiescent environment, the shed vortices usually counteract the motion, resulting in fluid drag, or fluid damping in the context of dynamical systems. The dynamics of the shed vortices play a crucial role in shaping the generation of the fluid drag, and to better understand the vortex-induced drag, it is of great importance to study the corresponding vortex dynamics. Francescangeli and Mulleners [1] studied the dynamics of shed vortices from a flat plate pitching at a constant velocity. They proposed to use a modified Kaden spiral to predict the trajectories of the primary and secondary vortices. Zhu, Mathai and Breuer [2] characterized the vortex-induced fluid damping of an elastically mounted pitching wing. Qualitative analysis of the vortex dynamics was used to explain the nonlinear behaviors of the fluid damping. However, direct connections between the vortex dynamics and the resultant fluid damping has yet to be established. The present study aims at addressing this issue by studying the vortex dynamics of a sinusoidally pitching wing in quiescent water.

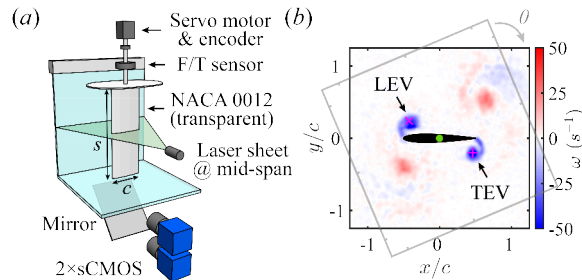


Figure 1: (a) A schematic of the experimental setup. (b) An example of the phase-averaged vorticity field.

2 Experimental setup and results

Fig.1(a) shows a schematic of the experimental setup. A NACA-0012 wing (span, $s = 0.3$ m, chord, $c = 0.1$ m) is mounted vertically in a water tunnel, with the flow speed kept at zero to create a quiescent environment. The wing is driven by a servo motor; a force/torque sensor and an encoder measure the fluid torque and the pitching angle, respectively. The wing pitches sinusoidally, $\theta = A \sin(2\pi f)$, where θ is the pitching angle, A is the pitching amplitude,

and f is the pitching frequency. A 2D PIV system is used to measure the flow field around the transparent wing at the mid-span plane. All the velocity fields are phase-averaged over 20 cycles.

An example of the vorticity field is shown in Fig.1(b). The wing pitches sinusoidally with $A = 60^\circ$ and $f = 0.5$ Hz. This vorticity field is captured when the wing is at mid-downstroke, $\theta = 22.9^\circ$. The green dot marks the pivot axis. Positive vortices are shown in red, negative vortices in blue. Since there is no free-stream flow, we define the rounded edge of the NACA-0012 wing as the leading edge (LE) and the sharp edge as the trailing edge (TE). The magenta cross and plus indicate the locations of the leading-edge vortex (LEV) and the trailing-edge vortex (TEV), identified using the Q -criterion. The positive vortices are the LEV and the TEV from the previous upstroke. The vorticity field is rotated by θ to keep the plotted wing at zero angle of attack (see the gray box).

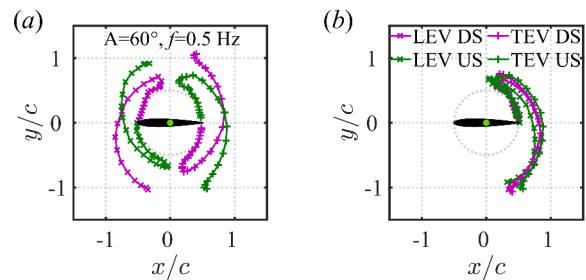


Figure 2: (a) LEV/TEV trajectories during the downstroke/upstroke at $A = 60^\circ$, $f = 0.5$ Hz. Magenta: Downstroke (DS). Green: Upstroke (US). (b) Comparison of vortex trajectories.

2.1 LEV/TEV trajectories during downstroke/upstroke

In the experiments, the LEV is generated at the rounded leading edge and the TEV is generated at the sharp trailing edge. To compare the vortex trajectories of these two vortices, we plot the vortex tracking results for $A = 60^\circ$, $f = 0.5$ Hz in Fig.2. Fig.2(a) shows that the shed LEV/TEV initially follow a circular trajectory closely (i.e. the LE/TE trajectory), similar to the results observed by Francescangeli and Mulleners [1]. Close to the pitch reversal, the vortices deviate from their circular trajectory, presumably due to interactions with opposite-signed residual vortices from the previous stroke. After the pitch reversal, the LEV/TEV reverse their trajectory and move toward the LE/TE due to

This work is supported by AFOSR.

[†]Current Address: Georgia Institute of Technology.

the pitch-induced rotational flow. In Fig.2(b), we mirror the trajectories of the LEV downstroke, the LEV upstroke, and the TEV downstroke about the y -axis, the origin, and the x -axis respectively to compare their differences. It is seen that all the trajectories overlap relatively well, indicating that the vortex trajectories are insensitive to the specific shape of the leading/trailing edge. The upstroke and downstroke trajectories are symmetric about the x -axis because the wing pitches sinusoidally around zero angle of attack. In the following sections, we will only focus on the downstroke motion.

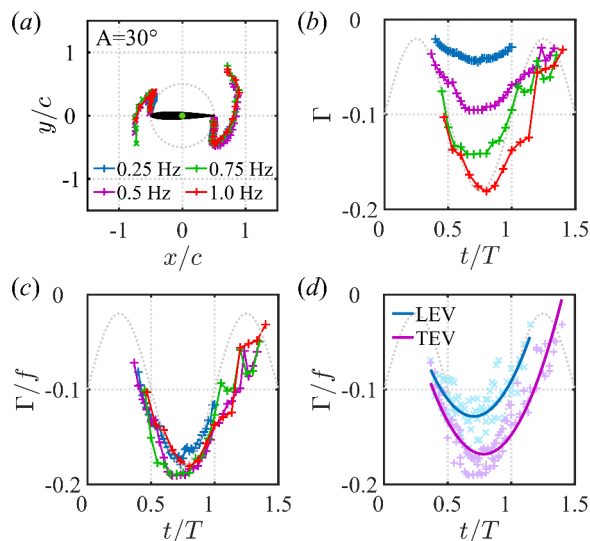


Figure 3: (a) LEV/TEV trajectories for $A = 30^\circ$, $f = 0.25, 0.5, 0.75$ and 1.0 Hz. (b) The corresponding TEV circulation. (c) Frequency scaling of the circulation. (d) Differences between the scaled LEV/TEV circulation.

2.2 Effect of the pitching frequency

To examine the effect of the pitching frequency on the vortex dynamics, we plot the vortex trajectories and circulation for $A = 30^\circ$ and four pitching frequencies: $f = 0.25, 0.5, 0.75$ and 1.0 Hz. Fig.3(a) shows that the LEV/TEV trajectories remain almost unchanged for the frequency range tested. In Fig.3(b), we see that the absolute value of the TEV circulation increases with the pitching frequency. The sinusoidal dotted line illustrates the corresponding pitching angle. For all four frequencies, the absolute TEV circulation increases during the downstroke and decreases during the following upstroke, presumably because the downstroke TEV feeding shear layer is cut off by the generation of a new upstroke TEV. If we normalize the TEV circulation with the pitching frequency, we see that the data collapses nicely (Fig.3c), indicating that the circulation of the shed vortex scales linearly with the pitching frequency. The scaled circulation of the LEV and the TEV are plotted in Fig.3(d). The solid curves indicate a quadratic fit to the corresponding data. We see that the TEV has a higher absolute circulation as compared to the LEV, which echoes the observations in [2] that the fluid damping associated with a sharp trailing edge is higher than that resulting from a rounded leading edge.

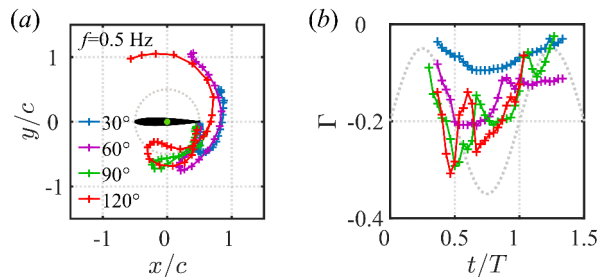


Figure 4: (a) TEV trajectories for $f = 0.5$ Hz, $A = 30^\circ, 60^\circ, 90^\circ$ and 120° . (b) The corresponding TEV circulation.

2.3 Effect of the pitching amplitude

In Fig.4, we plot the TEV trajectories and circulations at $f = 0.5$ Hz for $A = 30^\circ, 60^\circ, 90^\circ$ and 120° . Fig.4(a) shows that for all the pitching amplitudes, the vortex initially follows a circular trajectory (i.e. the gray dashed circle). For small to medium pitching amplitudes (i.e. $A = 30^\circ$ and 60°), the vortex turns outward during the pitch reversal. However, for medium to large pitching amplitudes (i.e. $A = 90^\circ$ and 120°), the vortex turns inward towards to the wing surface during the pitch reversal before moving to the other side of the wing. This behavior presumably results in a *negative* drag force on the wing and contributes to the non-monotonic fluid damping observed in [2]. In Fig.4(b), we see that the absolute TEV circulation increases nonlinearly with the pitching amplitude. For $A = 30^\circ$ and 60° , only one reversed peak of the circulation is observed, which roughly aligns with the pitching angle (i.e. the gray dotted curve). However, for $A = 90^\circ$ and 120° , we observe *two* reversed peaks of the circulation, with the primary peak forming during the downstroke rather than at the pitch reversal. The secondary peak forms right after the primary peak, with a smaller absolute circulation value.

3 Conclusions and future work

In this abstract, we have presented preliminary results regarding the vortex dynamics associated with a sinusoidally pitching wing in quiescent water. We are currently working on (a) comparing the instantaneous fluid drag with the corresponding vorticity field, (b) using a potential flow model which incorporates vortex-vortex interactions to predict the vortex trajectories, and (c) dissecting the force contributions from each vortex using the force partition method proposed by Menon and Mittal [3].

References

- [1] Franciscangeli, D. and Mulleners, K. Discrete shedding of secondary vortices along a modified Kaden spiral. *JFM.*, 917, A44, 2021.
- [2] Zhu, Y., Mathai, V. and Breuer, K. Nonlinear fluid damping of elastically mounted pitching wings in quiescent water. *JFM.*, 923, R2, 2021.
- [3] Menon, K. and Mittal, R. Significance of the strain-dominated region around a vortex on induced aerodynamic loads. *JFM*, 918, R3, 2021.

Formation of vortex pairs using a single surging plate

Anushka Goyal^a and Jovan Nedić^{b*}

^a McGill University, Department of Mechanical Engineering, Montréal, Canada

^b McGill University, Department of Mechanical Engineering, Montréal, Canada

*Correspondence: jovan.nedic@mcgill.ca

1 Introduction

It is well established that a flat plate impulsively set into linear motion will result in the formation of a counter-clockwise vortex, also known as the starting vortex. Similarly, once the plate is stopped, an equal strength vortex with clockwise rotation, or the stopping vortex, will be formed owing to Kelvin's circulation theorem. The resulting starting-stopping vortex pair consists of equal strength, counter rotating vortices that interact with each other. If the plate that forms the starting-stopping vortex is of sufficient length, they can be considered as two vortex lines forming a vortex pair. Thus, such a mechanism of surging a flat plate can be used to study vortex pair dynamics.

In previous studies [1–3], equal strength, counter rotating vortex pairs were generated by flapping two plates from a vertical position to some angle (θ) inwards in a water tank, as shown in Figure 1a. The rotation of the plates results in the formation of a shear layer, which in turn rolls up to form the vortex pair. To ensure that the vortices are nearly equal strength, the plates have to be rotated simultaneously. Such a design has practical challenges. One is the formation of either a single stopping vortex or multiple secondary vortices shed by each plate. These additional structures contaminate the field of interest, which consists of the primary vortex pair. Another drawback is the lack of control over the vortex characteristics, *i.e.*, the vortex circulation and core size. Therefore, the objective of this study is to address both these drawbacks by using a single surging plate and by devising appropriate scaling relations that can link the vortex characteristics, namely circulation (Γ), core size (a) and pair spacing (b) to the initial conditions such as angle of attack (α), surge speed (U) and surge distance (Δx). A schematic of the setup is shown in Figure 1b.

2 Experimental Setup and Limits of Initial Conditions

The experiment is designed for a 30 inches long, 12.5 inches wide and 19 inches deep water tank. The vortex generating flat plate is 26 inches long, 1.5 inches wide and 0.25 inches thick, with a rounded leading edge and a wedge shaped trailing edge. It is attached with end plates to ensure that 2D line vortices are generated. The angle of attack of the plate can be altered from 1° to 10° in 1° increments. The velocity field is obtained by using time resolved planar particle image velocimetry.

As the primary objective of the apparatus is to create isolated vortex pairs of equal strength, it is important to first define the various limiting values of the initial conditions that ensure this is the case. It was found that very low angles of attack (below 5°) and low surge speeds (below 1 c/s) produce weak vortex pairs that dissipate due to viscosity before the pairs interact with each other and undergo instabilities. Therefore the corresponding lower limit for the circulation based Reynolds number, defined as $Re_\Gamma = \Gamma/\nu$ was $Re_\Gamma = 300$. Large angles of attack (above 8°) and surge speeds (above 1.75 c/s) result in a strong leading edge vortex, which has a clockwise rotation. The rotation of the leading edge vortex is in the same direction as the stopping vortex, which means that the strength of the stopping vortex is different to that of the starting vortex. Hence at large angles of attack and speeds, we have a starting-stopping vortex pair of unequal strengths. Large surge speeds also result in the formation of secondary vortices that have the same rotations as the starting vortex. These secondary vortices may or may not merge in the very near field, and the limiting value on the surge speed was determined as the speed at which the train of secondary vortices did not merge. This value was found to be at speeds greater than 1.75c/s. Low surge distances (below 1c) lead to a strong interaction between the starting-stopping vortices and are characterised by elliptical streamlines, as shown in Figure 2. While these small surge distances can be useful in studying elliptical instabilities, they make it hard to characterise the primary vortex pair characteristics, particularly the core size; hence surge distances smaller than 1c are ignored for this part of the study. The various limits of the initial conditions is shown, schematically, in Figure 2; note, however, that the values shown here are specific for the flat plate considered here. Future work will look at ways in which such a plot can be simplified into non-dimensional variables that would allow for scaling laws to be developed.

3 Estimating the Circulation

When a wing is impulsively accelerated from rest, the generated circulation increases over time and eventually settles to its steady state value, which is characteristic of a dynamic response to a system. This dynamic response was first solved analytically by Wagner, who modelled the system as a line of vortex centers shed from the trailing edge of an impulsively accelerated wing, with the last vortex center being



Figure 1: a) Schematic of the vortex generator designed by Leweke and Williamson [1] b) Schematic of the starting/stopping vortex pair generator used in the present study

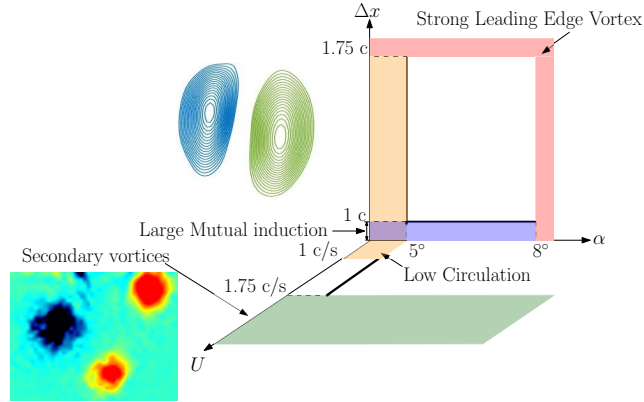


Figure 2: Limits of the angle of attack (α), surge speed (U) and surge distance (Δx)

the starting vortex [4]. The wake, due to its close proximity to the bound vortex space, induces a velocity field to counteract the circulation around the wing. As the starting vortex convects further downstream, its effect on the bound vortex circulation gradually decreases. Consequently, the circulation of the bound vortex also increases asymptotically with surge distance. Since the net circulation in the field must be zero, once the wing is impulsively started from rest, the starting vortex follows the same changes in circulation as the bound vortex. From Figure 3, it is seen that the circulation increases with surge speed and distance. The ratio of the circulation of the starting vortex to the steady state circulation as a function of surge distance can be obtained using Wagner's theory. The steady state circulation ($\pi\alpha cU$) can then be calculated to obtain the theoretical circulation of the starting vortex for various surge speeds and distances, and is shown in Figure 3 as solid symbols. The theoretical values of circulation agree with the experimental results. Deviations at higher surge speeds could be attributed to the presence of secondary vortices which merge with the starting vortex in the near field. Similar results were observed for the stopping vortex, thus, allowing us to predict the vortex pair circulation.

4 Conclusion

Based on preliminary results, it can be asserted that using a single surging plate is an effective way of producing equal strength, counter rotating vortex pairs to study their dynam-

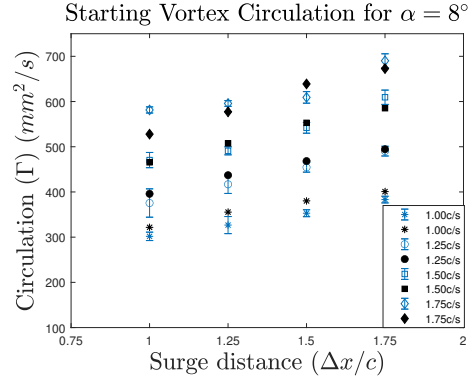


Figure 3: Circulation of the starting vortex at various surge distances and speeds. Solid markers show the theoretical values from Wagner's theory.

ics. In the past, instabilities of vortex pairs were studied using two plates that rotate simultaneously, however, to the best of our knowledge, no scaling laws, or ability to accurately predict the expected strength and size of the vortex pairs exist. This gives us little control over vortex characteristics to study their dynamic motion. In this study, it was shown that changing the initial conditions of surge speed and distance allows one to predict the circulation of the vortex pairs. Our future work will focus on developing scaling relations that can predict the core size and spacing between the vortex pairs using the initial conditions and the size of the plate. It is believed that the use of a thin flat plate has introduced additional complexities in the formation of the vortex pairs, namely the formation of instabilities of the leading edge vortex, that ultimately affect the strength of the stopping vortex. To address these concerns, and allow for larger surge speeds to be studied, we shall consider a NACA 0010 airfoil with different chord lengths.

References

- [1] Leweke, T. and Williamson, C. H. K. Cooperative elliptic instability of a vortex pair. *Journal of Fluid Mechanics*, 360, 85–119, 1998.
- [2] Leweke, T. and Williamson, C. H. K. Experiments on long-wavelength instability and reconnection of a vortex pair. *Physics of Fluids*, 23 (2), 024101, 2011.
- [3] Heyes, A. L. and Taylor, N. P. and Chen, J. Characterising short-wave instabilities on a vortex dipole. *Experiments in Fluids*, 51 (1), 237–245, 2011.
- [4] Wagner, Herbert Über die Entstehung des dynamischen Auftriebes von Tragflügeln *ZAMM - Journal of Applied Mathematics and Mechanics*, 5 (1), 17–35, 1925.

Scaling of drag forces of an accelerated flat plate

Jesse Reijtenbagh^{a*}, Mark Tummers^a and Jerry Westerweel^a

^a Laboratory for Aero- and Hydrodynamics, Delft University of Technology, The Netherlands¹

* Correspondence: j.reijtenbagh@tudelft.nl

1 Introduction

We present results on the instantaneous drag force on a rectangular plate that accelerates in a direction normal to the plate surface. The flow field was measured simultaneously to the drag force to determine relevant flow phenomena that contribute to the drag force. This work is a continuation of the investigation of [1] on the drag force on an accelerating submerged plate as a function of the distance from the free surface. The present study considers a larger range of accelerations, final velocities, and distances over which the plate is accelerated, as well as the role of the vortices generated by the plate edge.

2 Experimental setup

The experiments focus on the drag force that acts on a normal flat plate when it accelerates from rest through a water filled glass tank with dimensions $2.0 \text{ m} \times 2.0 \text{ m} \times 0.6 \text{ m}$. The plate dimensions are $\ell_a \times \ell_b \times \ell_c = 0.2 \text{ m} \times 0.1 \text{ m} \times 0.004 \text{ m}$. The height of the plate (ℓ_b) is used as the characteristic length scale. An industrial gantry robot (Reis RL50) is used to move the plate through the water. The top of the plate is 0.15 m below the free surface, which is sufficient for the free surface to not affect the drag force on the plate [1]. Between the robot and the plate a force/torque transducer (ATI Gamma SI 32-2.5) is installed that samples the drag force at 10 kHz. The experiments are done for a range of accelerations, a , and final velocities, V , which resulted in a Reynolds number, based on the final velocity V and the plate height ℓ_b , between $Re = 15000$ and $Re = 135000$, which is well into the turbulent regime. The results shown in this abstract focus on accelerations between $a = 0.10 \text{ m/s}^2$ and $a = 1.64 \text{ m/s}^2$ towards a final velocity of $V = 0.45 \text{ m/s}$, which is equivalent to a Reynolds number of $Re = 45000$. Instantaneous velocity fields are measured using a PIV system that is based on a dual cavity Nd:YLF laser (Litron 150W LDY303 HE-PIV) and a 4 megapixel high-speed camera (Phantom VEO 640L). Neutrally buoyant fluorescent spheres (Cospheric UVPMS-BR-0.995) with approximately $60 \mu\text{m}$ diameter are used as tracer particles. The high-speed camera was equipped with a long-pass filter (Schott OG570) to remove environmental light. Images were recorded from a field-of-view of $900 \text{ mm} \times 472 \text{ mm}$. The images were processed in DaVis-10 using a sliding sum-of-correlation method starting with a first pass with a 48×48 pixel interrogation window, followed by three 24×24 -px passes with a 50% overlap, which resulted in a time-resolved velocity field of 219×115 velocity vectors taken at 1000 Hz.

¹This work was supported by ERC-AdG Grant 884778 ‘Impulsive Flows’

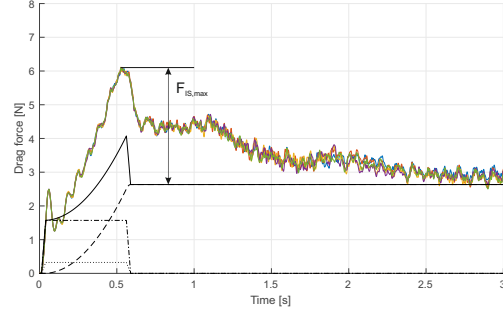


Figure 1: Five repetitions of the force signal $F_x(t)$. Each colored line indicates one repetition of the same experiment with $a = 0.82 \text{ m/s}^2$ and $V = 0.45 \text{ m/s}$. The black lines indicate theoretical values: ... : $m_p a$, plate mass acceleration force; - - : $m_p a + m_h a$, plate mass + added mass acceleration force, m_h according to [2]; - - - : $\frac{1}{2} C_D \rho A V^2$, steady state drag force; - · : $(\frac{1}{2} C_D \rho A V^2 + m_p a + m_h a)$

3 Results

Figure 1 shows five repetitions of the drag force signal $F_x(t)$ for the same experimental parameters ($a = 0.82 \text{ m/s}^2$ and $V = 0.45 \text{ m/s}$). It is seen that the drag force signal reproduces very well over multiple repetitions. The force signal increases during the acceleration phase and reaches a peak value at the end of this phase when the plate assumes its final velocity. The drag force then enters a transition phase towards the steady state phase where the drag force F_{CD} is given by $F_{CD} = \frac{1}{2} C_D \rho A V^2$, where ρ is the fluid density, A ($= \ell_a \times \ell_b$) the frontal area of the plate, V the final velocity of the plate, and C_D the steady state drag coefficient, which was found to be equal to 1.3 in our experiments. The transition from peak drag force to steady state is described in detail by [1]. In their research, the peak force is modelled as the sum of this steady state drag force F_{CD} , the force due to the acceleration of the plate mass F_{mp} ($= m_p a$) and the force due to the acceleration of the hydrodynamic mass F_{mh} ($= m_h a$). The hydrodynamic mass m_h can be modelled as the sum of the time independent added mass term and a time dependent term that accounts for the mass entrainment; see [1] for details. Figure 1 shows the theoretical time independent acceleration forces and the steady state force with respect to the measured force signals.

In this research we divert from this theory of hydrodynamic mass and focus on the instationary force F_{IS} acting on the plate as given by:

$$F_{IS}(t) = F_x(t) - \underbrace{m_p a}_{F_{mp}} - \underbrace{\frac{1}{2} C_D \rho A V(t)^2}_{F_{CD}}. \quad (1)$$

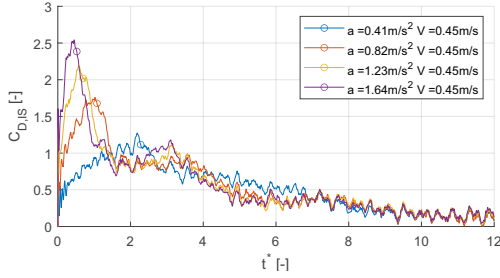


Figure 2: Instationary drag coefficient $C_{D,IS}$ as a function of the formation time t^* for four different accelerations. The moment the plate reaches its final velocity is marked with a circle. Different signals coincide shortly after the end of acceleration, with all them coinciding after $t^* = 7$

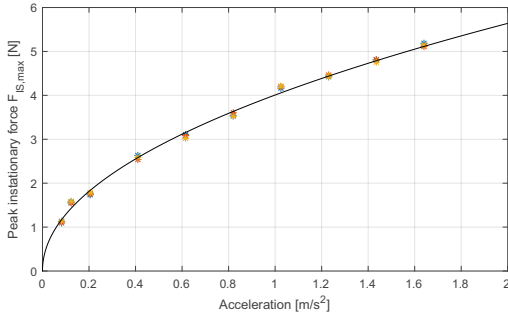


Figure 3: The value of the peak instationary force $F_{IS,max}$ as a function of the acceleration. Stars represent multiple realisations of the experiment at different accelerations towards a final velocity of 0.45 m/s. This peak force shows an increasing trend with increasing acceleration, following the fitted function $F_{IS,max} = 4.0a^{0.5}$, indicated by the black line.

Figure 2 shows the evolution of this instationary force for multiple accelerations ($a = 0.41, 0.82, 1.23, 1.64 \text{ m/s}^2$) towards a final velocity of $V = 0.45 \text{ m/s}$. The dimensionless instationary force is given by the drag coefficient, given by: $C_{D,IS} = F_{IS} / \frac{1}{2} \rho A V^2$. Time is made dimensionless by using the formation time [3], which is given by:

$$t^* = \frac{\int_0^t V(\tau) d\tau}{\ell_b}. \quad (2)$$

The calculation of this instationary force from the experimental data for the entire range of accelerations towards a final velocity of 0.45 m/s leads to Figure 3, which shows the value of the peak instationary force $F_{IS,max}$ across the whole range of accelerations. The least-squares fitted function through the data points in Figure 3 is given by $F_{IS,max} = C \cdot a^{0.5}$, with: $C = 4.0$. This scaling compares very well to similar experiments [4]. We also found this scaling, i.e. $F_{IS,max} = C \cdot a^{0.5}$ in experiments where the plate accelerates towards different final velocities. This scaling proves that the drag force for prolonged acceleration goes against classical added mass theories, which state that the drag force due to acceleration should be linear in the magnitude of the acceleration; see for instance [2]. The value of the prefactor C depends on the final velocity, size and other characteristics of the plate.

For each time step the dimensionless vorticity ω^* was determined from the instantaneous velocity fields as in: $\omega^* = \omega \ell_b / V$. Then, the non-dimensional circulation Γ^* is calcu-

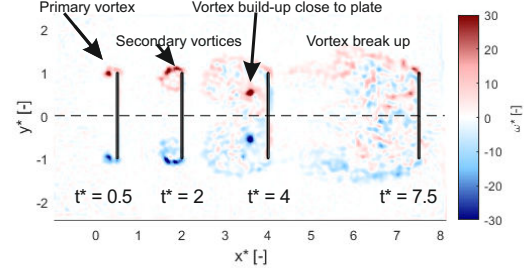


Figure 4: Dimensionless vorticity fields at different formation times t^* for $a = 1.64 \text{ m/s}^2$ towards the final velocity $V = 0.45 \text{ m/s}$. Integration of vorticity over the top half of these pictures for each time step for all accelerations results in Figure 5. The creation of the primary and secondary vortices is visualized in more detail by [1], and is in line with the framework for start-up vortices proposed by [5]. At $t^* = 4$, there is significant vortex growth near the mid plane of the plate. At $t^* = 7$, vortex break-up has occurred and the vorticity field shows more chaotic, turbulent behaviour. Note: x^* is equivalent to t^* in this figure.

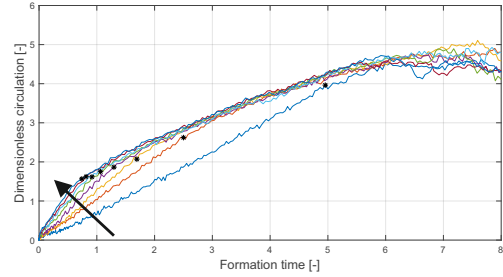


Figure 5: Dimensionless circulation over the top half of the field-of-view (formation) time towards a final velocity of 0.45 m/s. Different colored lines indicate accelerations between $a = 0.21 \text{ m/s}^2$ and $a = 1.64 \text{ m/s}^2$ with increasing acceleration following the arrow. Black stars indicate the end of the acceleration phase. Shortly after the end of the acceleration phase the lines coincide onto the same line. Vortex breakup occurs around $t^* = 7$.

lated from: $\Gamma^* = \int_{S^*} \omega^* dS^*$, where S^* is the area over which the integration takes place. Since the flow field shown in Figure 4 is symmetric in the line $y^* = 0$ over the field-of-view during the experiment, the net circulation should be zero. Therefore the circulation is calculated over the top half of the field-of-view. The circulation for different accelerations ($a = 0.21 \text{ m/s}^2$ to $a = 1.64 \text{ m/s}^2$) is shown in Figure 5. Here, we see similar results as in Figure 2, that is with increasing acceleration the circulation increases faster with the formation time. Shortly after the acceleration period ends and the plate reached its final velocity, the different lines coincide and circulation does not depend on the acceleration history.

References

- [1] E. J. Grift, N. B. Vijayaragavan, M. J. Tummers, and J. Westerweel. Drag force on an accelerating submerged plate. *J. Fluid Mech.*, 866:369–398, 2019.
- [2] P. R. Payne. The virtual mass of a rectangular flat-plate of finite aspect ratio. *Ocean Eng.*, 8(5):541–545, 1981.
- [3] M. Gharib, E. Rambod, and K. Shariff. A universal time scale for vortex ring formation. *J. Fluid Mech.*, 360:121–140, 1998.
- [4] J.N. Fernando, G.D. Weymouth, and D.E. Rival. On the limits of added-mass theory in separated flows and with varying initial conditions. *Journal of Fluids and Structures*, 93:102835, 2020.
- [5] P. Luchini and R. Tognaccini. The start-up vortex issuing from a semi-infinite flat plate. *J. Fluid Mech.*, 455:175–193, 2002.

Rip Entry Investigation: Divers Manipulate The Air Cavity

Elizabeth A. Gregorio^{a*}, Elias Balaras^a, and Megan C. Leftwich^a

^a The George Washington University, Washington, DC, USA

*Correspondence: egregorio@gwu.edu

1 Introduction

Competitive divers achieve higher scores when they perform a dive that appears splash-less. Such a dive was performed inadvertently in competition until the rip entry was popularized by Olympic gold medalist Klaus DiBiasi. Fifty years later, the scoring advantage of this entry motivates all competitive divers to rip every dive.

Judges identify a “ripped” dive by the sound of paper tearing at impact accompanied by characteristic groupings of bubbles that rise to the surface after the dive is completed. A detailed description of the bio-mechanics required to perform this skill is found in [1]. This study will focus on the pike save technique, when divers roll at their hips immediately after entering the water, as illustrated in Figure 1.



Figure 1: Underwater image of a diver performing a pike save, Photo Credit: Jed Jacobsohn for The New York Times

To contextualize this research, consider an Olympic diver performing a dive from the 10m platform. From this height she will impact the water at approximately 16 m/s. With this high velocity and her height as the characteristic length, she will achieve a Reynolds number on the order of 10^7 , Weber number on the order of 10^5 , and Froude number of approximately 3.6. This places us firmly in an inertial regime where surface tension will play a very small role.

This research builds on an extensive background of entry body research including the impact of geometry, water repellancy, biological morphology, and air cavity dynamics after pinch off [2–4]. Studying the rip entry adds the complexity of a body performing a morphological change after impact to deform the air cavity and limit splash. Although this technique is established in the diving community, this is a new branch of entry body research.

We will describe simplified experiments designed to identify the most important aspects of the rip entry, and present results with the goal of understanding how the divers movements change the air cavity and splash. We will consider how these experiments will be coupled with computational simulations. This research will open up further study of deformable entry bodies.

2 Methods

Experiments are performed with a simplified model of an Olympic diver. The model is composed of two sides of a hinge secured at the “hips” with a spring pin. The model has a flat top to mimic the way that divers hold their hands flat when impacting the water, symmetric cuts on two sides for the way the arms slope in from the shoulders to the hands, and an asymmetric cut for the head tucked under the arms.

This model is attached to a driving rod and released into a guided free fall on a dropping cage. It impacts the water at approximately 4 m/s, a high enough velocity to be in the inertial regime. An accelerometer is attached to obtain force information during the model’s impact.

The model’s entry is recorded at 5000 frames per second with a IDT NX3S3 high speed camera. A time series of images from one trial taken as the diver model approaches and then impacts the water surface can be seen in Figure 2.

Upon entering the water, the arms of the model bend to the side, matching the way a diver rolls at their hips during a pike save. This passive roll is initiated by the uneven force on the arms of the model due to the asymmetric cut. The movement is controlled by the torque required to turn the hinge. Therefore, to understand how the air cavity dynamics are affected by divers timing when initiating the pike save, we vary the stiffness of the hinge and the asymmetric angle.

3 Results

The diver model is marked in three places to track the kinematics of the passive roll. The torque required to turn the hinge is measured before and after every trial to account for hinge degradation resulting from the force of impact. These measurements are used to classify each of the experimental trials. Representative plots showing the movement of the models arm marker in along the X and Y axis after impact can be seen in Figure 3.

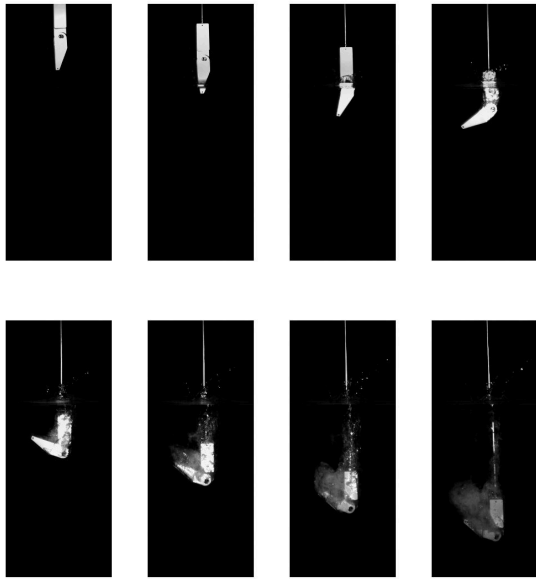


Figure 2: Time sequence of Olympic diver model impacting the water and the evolution of the entrained air cavity. Each image is advanced by 100 frames or 0.017 s.

We see a significant change in the kinematic plots when changing the angle of the asymmetric wedge. Increasing the wedge by seven degrees causes the turn to be initiated 30% sooner than the results shown here. We see similar trends for decreasing the size of this wedge. This work studying the movement of the model after impact has informed our investigation into the development of the air cavity.

We group similar trials by their kinematic chart and the torque to turn the hinge to consider air entrainment and splash production. The underwater portion of the videos are tracked for the percentage change of the air cavity over time. The movement of the air cavity consistently follows the bend of the model's arms. The splash production is measured by the amount of visible splash is generated above the surface of the water. The angle of the initial splash generally follows that of the asymmetric wedge. The three dimensional shape of the air cavity is considered for several trials with the model turned 90 degrees to the camera. This shape is approximately symmetric on both sides of the wedges for the slope between the "shoulder" and "hands" of the model.

4 Conclusion

A simplified geometric model is designed to experimentally investigate an Olympic diver performing a pike save. The kinematic movement, air entrainment, and splash of the model are measured in experiments to understand the air-water interface is manipulated. This research will illuminate how a changing entry body affects air cavity development and splash formation.

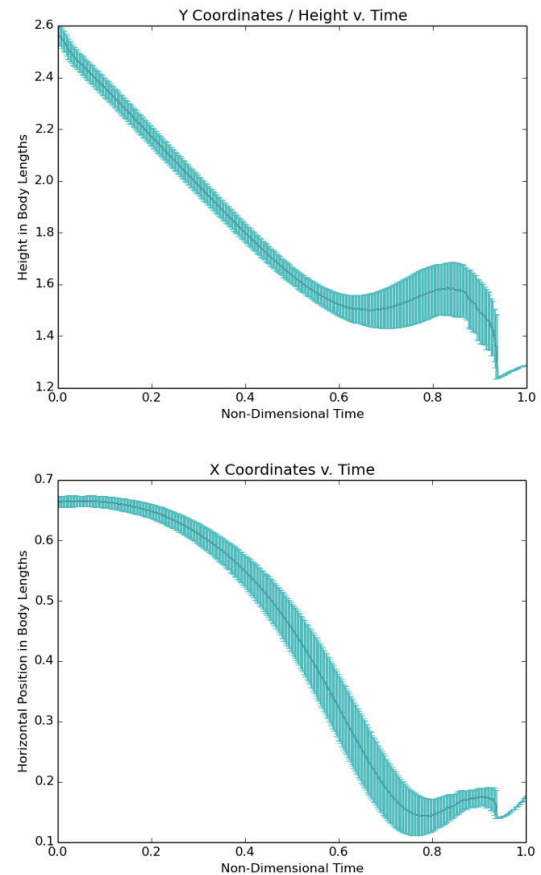


Figure 3: Plots of the arm kinematics over thirty trials using a model with a 67 degree asymmetric wedge that required an average torque of 0.03 Nm to turn.

These results will be used to develop and validate a computational model for a deformable immersed boundary in a multiphase flow. Computational validation work to extend the immersed boundary force formulation developed in [5] to multiphase flows for simple geometric entry bodies will be presented. These simulations are performed using the in-house Navier-Stokes solver deployed on parallel computing platforms.

References

- [1] Brown, J.G., et al. Descriptive analysis of the rip entry in competitive diving. *Research Quarterly for Exercise and Sport*. 55(2):93–102, 1984.
- [2] Chang, Brian, et al. How seabirds plunge-dive without injuries. *Proceedings of the National Academy of Sciences* 113.43 (2016): 12006–12011.
- [3] Louf, Jean-François, et al. Cavity ripple dynamics after pinch-off. *Journal of Fluid Mechanics* 850 (2018): 611–623.
- [4] Truscott, Tadd T., et al. Water entry of projectiles. *Annual review of fluid mechanics*. 46 (2014): 355–378.
- [5] Wang, Shizhao, et al. A hydrodynamic stress model for simulating turbulence/particle interactions with immersed boundary methods. *Journal of computational Physics*. 382 (2019): 240–263.

Session F

Gust encounters



Effect of large amplitude streamwise gust on laminar separation bubbles

V. Ferrand^a, T. Jardin^{a*}, N. Doué^a and E. Gowree^a

^a ISAE-Supaero, Université de Toulouse, France

*Correspondence: t.jardin@isae.fr

1 Introduction

In transitional regimes, the flow past a NACA0012 airfoil may be characterized by laminar separation, laminar-to-turbulent transition and reattachment. In the time-average sense, the resulting flow topology is usually referred to as a laminar separation bubble (LSB). The properties of this LSB is highly dependent on laminar-to-turbulent transition (which drives flow reattachment) and is hence highly dependent on the properties of the freestream. In particular, freestream turbulence intensity is known to be a key ingredient in LSB formation. This is the reason why experiments from different facilities (i.e. wind- and water-tunnels) may exhibit very large discrepancies regarding both flow topology and resulting aerodynamic forces [1]. In addition to freestream turbulence, airfoils may encounter flow perturbations at lower-frequency and/or larger-amplitudes. This is typically the case for small size unmanned air vehicles (UAVs) which have typical dimensions and flight speeds that may be on the order of those found in the atmospheric boundary layer, as generated in urban canyons, for example. In a two-dimensional framework, these perturbations are usually modeled as pure streamwise and transverse velocity variations, referred to as streamwise and transverse gusts respectively. The combination of both streamwise and transverse variations can lead to more complex perturbations such as vortex gusts [2]. In this paper, we focus on the influence of low-frequency, large-amplitude streamwise gust on the aerodynamics of a NACA0012 airfoil in transitional regimes. While streamwise gusts have a quasi-steady effect resulting from time-variations in the airfoil characteristic Reynolds number, they may also influence the overall flow dynamics through unsteady effects on the trailing wake and boundary layer. Our goal is to evaluate the relative importance of quasi-steady and unsteady effects in this specific situation using both experiments and numerical simulations.

2 Methodology

2.1 Problem setup

We consider a two-dimensional NACA0012 airfoil subjected to a varying freestream velocity. The Reynolds number based on the freestream velocity $U_\infty(t)$ and the wing chord c varies between approximately 60,000 and 130,000 as shown in figure 1. The characteristic reduced frequency k based on the time-average freestream velocity $\overline{U_\infty(t)}$ and c

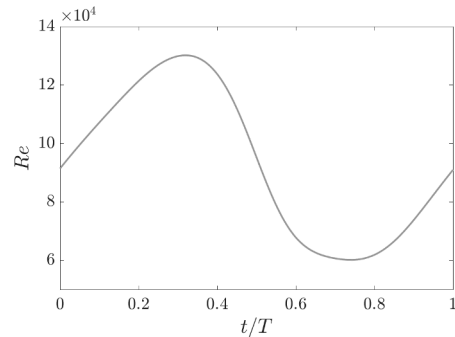


Figure 1: Time-history of the Reynolds number.



Figure 2: Photography of the wind-tunnel test section.

is set to 0.0667. The airfoil angle-of-attack α is set to 2.5° .

2.2 Experiments

Experiments are conducted in an open wind tunnel with test section dimensions $465 \times 465 \text{ mm}^2$ (in the transverse directions). The wing spans the full height of the test section and has a 15 mm chord length. Variations in freestream velocity are generated using oscillating vanes placed at the exit of the test section (figure 2, shown with 3D wing not reported here). Instantaneous loads are measured using a DeltaLab 3 balance placed below the wind tunnel section.

2.3 Numerical simulations

Numerical simulations are performed using StarCCM+ v16.06 code. The latter directly solves the Navier-Stokes equations using a finite volume method on an unstructured mesh (trimmed hexahedral cells). Both 2D and 3D cases are addressed. The airfoil chord length is discretized using

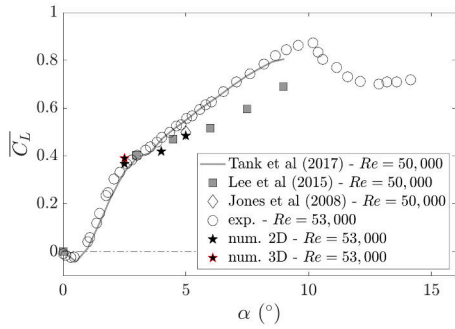


Figure 3: $\overline{C_L}$ vs. α obtained using present experiments and simulations. Comparison with data from the literature.

512 cells with a first cell height at the wall set to ensure that $y^+ < 1$ at $Re = 140,000$. For 3D cases the wing span is $0.2c$ and is discretized using 102 cells. The non-dimensional time step $\Delta t \times \overline{U_\infty(t)}/c$ is equal to $1/200$.

3 Results

3.1 Static cases

We first show the results obtained for the static case at Reynolds number 53,000. Figure 3 plots the time-averaged lift coefficient as a function of angle-of-attack obtained at $Re = 53,000$. Results from present experiments and numerical simulations are compared with data from the literature. Reasonable agreement is observed between the present experimental data and those from [1]. In particular, the $\overline{C_L}$ vs. α curve is characterized by negative lift at small α , followed by a large increase in lift (i.e. with slope larger than 2π) up to approximately 2.5° . Lift continues to grow at a slower rate above 2.5° until stall occurs around 10° . In addition, the lift at 2.5° is reasonably well predicted by both 2D and 3D computations. The former however underpredicts lift at large angles of attack, in agreement with previous simulations from [3] and [4]. Figure 4 displays the flow field obtained at $\alpha = 2.5^\circ$ and $Re = 53,000$ using present 3D numerical simulations. Time-average streamlines and contours of root-mean-square streamwise velocity are shown in a longitudinal section together with instantaneous isosurfaces of Q-criterion. Black lines on the wing surface depicts zero wall-shear stress iso-lines. Overall it can be shown that the flow separates and rolls up into prominently two-dimensional structures which progressively destabilize into three-dimensional structures that eventually shed into the wake. In the time-average sense, the separated shear layer reattaches after it has transitioned to a prominently three-dimensional flow leading to a LSB that covers a large portion of the wing chord.

3.2 Streamwise gust

We now focus on the case with varying freestream velocity. Figure 5 shows the instantaneous lift obtained using present experiments and simulations. These are compared with the quasi-steady lift obtained from experiments as well

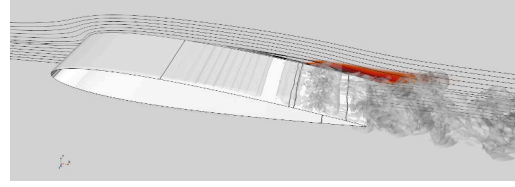


Figure 4: Time-average streamlines, zero wall shear stress isolines, streamwise velocity RMS and Q-criterion isosurfaces.

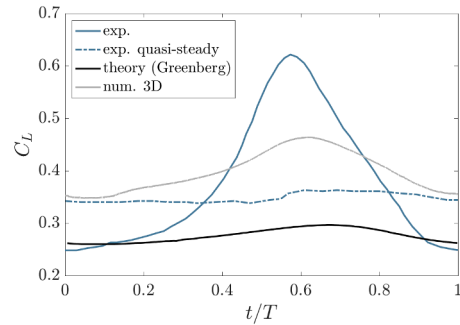


Figure 5: Time history of C_L over a gust period. Comparison between experiments, numerical simulations and theory.

as the solution obtained from Greenberg theory. It is observed from experiments that a large lift increment occurs when the flow decelerates. Although its occurrence is predicted by numerical simulations, the amplitude of this increment is largely underpredicted. Our data suggest that such trend results from unsteady non-linear effects since it is not predicted by the quasi-steady approach and Greenberg theory.

4 Conclusion

The flow past transitional airfoils can be significantly affected by low frequency, large amplitude streamwise gusts due to the presence of unsteady non-linear effects associated with the formation of a laminar separation bubble. In this paper, we conduct both experiments and numerical simulations to evaluate the role of these effects on the lift response to the gust. The final presentation will include additional data for static cases at $Re = 140,000$ and a detailed analysis of the flow physics during streamwise gust encounter.

References

- [1] Tank, J., Smith, L. & Spedding, G. R. On the possibility (or lack thereof) of agreement between experiment and computation of flows over wings at moderate Reynolds number. *Interface focus*, 7(1):20160076, 2017
- [2] Jones, A. R., Cetiner, O. & Smith, M. J. Physics and Modeling of Large Flow Disturbances: Discrete Gust Encounters for Modern Air Vehicles. *Annual Review of Fluid Mechanics*, 54: 469-493, 2022.
- [3] Jones, L. E., Sandberg, R. D. & Sandham, N. D. Direct numerical simulations of forced and unforced separation bubbles on an airfoil at incidence. *Journal of Fluid Mechanics*, 602: 175-207, 2008.
- [4] Lee, D., Nonomura, T., Oyama, A. & Fujii, K. (2015). Comparison of numerical methods evaluating airfoil aerodynamic characteristics at low Reynolds number. *Journal of Aircraft*, 52(1): 296-306, 2015.

Mitigation of transverse gusts using open- and closed-loop pitch maneuvers

Girguis Sedky* and Anya Jones

Department of Aerospace Engineering, University of Maryland, College Park, MD, USA

*Correspondence: gshedky@umd.edu

1 Introduction

Unsteady flow conditions present a challenge to stable flight [1], and gust rejection remains a concern for flight control [2]. Large-amplitude transverse gust encounters represent a canonical unsteady flow condition that has been the focus of many studies dating back to the 1930s. Recent developments in experimental measurement techniques, such as time-resolved particle image velocimetry (TR-PIV), have enabled more comprehensive gust-encounter studies. Some of the recent findings made possible by TR-PIV include the correlation between the lift peaks experienced by a wing in a transverse gust and the formation of strong leading-edge and trailing-edge vortices [3], the deformation of the gust under the influence of the wing [4], and the strong dependence of the aerodynamic response of the wing on the gust's profile and shear layer distribution [5].

Recent studies have introduced pitching for the purposes of gust mitigation. In prior work [6], the authors demonstrated successful transverse gust mitigation without *a priori* knowledge of the gust in an unsteady discrete vortex simulation. Furthermore, Andreu-Angulo and Babinsky [7] demonstrated gust mitigation under the effect of an open-loop maneuver informed by the unsteady aerodynamic theories of Küssner and Wagner. Although this method required knowledge of the gust *a priori*, it was effective at gust mitigation, thereby providing further evidence for the usefulness of classical aerodynamic theory in control design for gust mitigation.

This work expands on these studies by experimentally implementing and analyzing the physics of three different open-loop control (i.e., prescribed prior to the run) maneuvers for gust mitigation. The first maneuver is designed such that the pitching angle of attack opposes the effective angle of attack induced by a non-deforming model of the gust (Eff.-D). The effective angle of attack induced by the gust is obtained using quasi-steady thin airfoil theory and takes into account the non-uniform velocity distribution along the wing's chord. The second maneuver is designed such that the analytical lift result from Wagner and Küssner unsteady aerodynamic models cancel out (WK-D). The third maneuver is obtained from closed-loop control simulations in an

unsteady discrete vortex model (DVM-D). Moreover, we will present preliminary results from closed-loop control experiments based on real-time force measurements. To our knowledge, this will be the first experimental demonstration of closed-loop transverse gust response mitigation on a wing.

2 Results

Figure 1 presents the coefficient of lift C_L time histories normalized by the gust ratio $GR = v_g/U_\infty$, where v_g is the transverse velocity of the gust and U_∞ is the freestream velocity, for all cases. The gray region in the plot highlights the portion where the wing is at least partially within the gust. Force and pitching moment results collapse when normalized by the gust ratio value. The collapse in the forces across gust ratios is shown in Fig. 1. The performance difference across different maneuvers is found to be dominated by the added-mass force. Thus, accurate modeling of added-mass is critical for successful gust mitigation. In addition, the pitching maneuvers are found to partially attenuate the circulatory force contribution experienced by the wing during the gust encounter and counter-balance the remainder through the added-mass force contribution. The utilization of pitching to mitigate lift doubles the fluctuation of the pitching moment experienced by the wing relative to nominal wing-gust encounters. However, they are within the same order of magnitude which may be sufficient with respect to vehicle control focused mainly on lift mitigation. The source of the pitching moment fluctuations differed between the pitch and no-pitch maneuvers. When a wing encounters a gust without pitching, the moment fluctuations are a result of lift fluctuations. On the other hand, for the pitch maneuvers, the pitching moment fluctuations are due to the reaction of the fluid to the pitching of the wing.

The main flow features of the wing-gust encounters were identified using PIV measurements. Figure 1 presents an example of these flowfield measurements. As the wing enters the gust without pitching, it experiences a large upwash, creating a strong leading-edge shear layer which leads to the development of a suction-side leading-edge vortex (LEV). The LEV grows until it sheds towards the latter part of the gust. The transverse gust flow stagnates on the pressure side of the wing, resulting in a large disturbance to the gust structure. This disturbance leads to a large transfer of momentum

¹This work was supported by the Air Force Office of Scientific Research under grant FA9550-16-1-0508 and the National Science Foundation under award numbers 2003951 and 2003999

between the gust and the passing wing, increasing the lift transient experienced by the wing. As the wing with pitching enters the gust, it starts to pitch down, and an LEV develops. The LEV detaches earlier and convects away for the maneuvering wing. As the wing exits the gust, it pitches up and a pressure-side LEV forms. In contrast to the case without pitching, the flow on the pressure side does not experience stagnation, thus minimizing the disturbance to the gust's flowfield. Quantification of the total momentum of the measured flowfield revealed a larger variation for the non-pitching wing compared to the pitching wing.

The unsteady streamlines are computed from the PIV vector fields. In the lab frame, the vertical gust flow stagnates on the pressure side of the wing for the no-pitch case. For the pitching case, the flow does not experience stagnation on the pressure side of the wing. Without pitching, the flow encounters the wing at an angle in the wing's body frame. Thus, streamlines presented in the body frame show a stagnation point of the flow lying on the pressure side of the wing. The wing undergoing the pitching maneuver aligns itself with the flow leading to the stagnation point moving towards the front of the leading edge. This observation reveals the possibility of mitigating gusts through controlling the position of the pressure-side stagnation point throughout the gust encounter.

The circulation strength time histories of the LEVs for the pitching and non-pitching maneuvers are found to be initially similar. Furthermore, the magnitude of the circulation strengths of the suction-side and pressure-side LEVs initially increase linearly for all cases, plateauing near vortex detachment. This suggests that vortex growth during a wing-gust encounter is linear when the vortex is attached which is an important consideration for modeling efforts.

3 Conclusion

This work experimentally implements three open-loop mid-chord pitch maneuvers with the objective of mitigating the lift transient during large-amplitude transverse wing-gust encounters. Force, pitching moment, and flowfield measurements were collected to study the encounters. The performance difference across different maneuvers is found to be dominated by the added-mass force. Additionally, the pitch maneuvers were found to mitigate a significant portion of the circulatory force contribution and counter-balance the remainder using the added-mass force. Pitch control input was found to double the fluctuations in the pitching moment coefficients during the gust encounters. Quantification of the total momentum variation in the measured flowfield showed that pitch maneuvers minimized the disturbance to the gust's flowfield, and thereby minimized the momentum transfer between the gust and the passing wing. Leading-edge vortices shed from the wing during the encounters were found to have an initial linear growth region, followed by a plateau corresponding to vortex detachment.

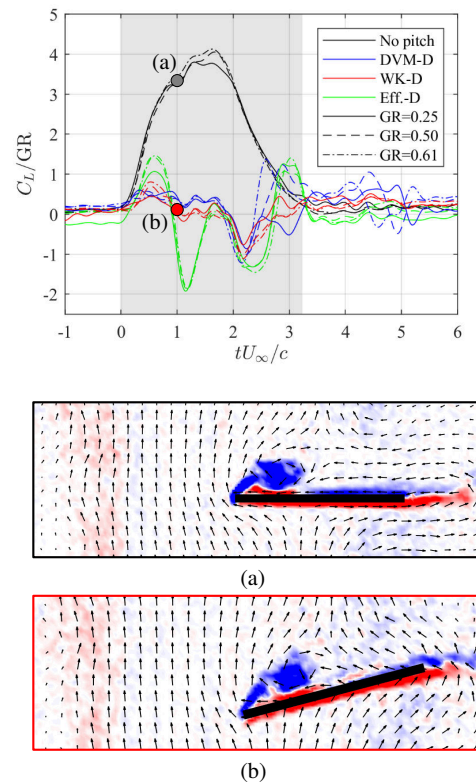


Figure 1: The coefficient of lift normalized by the gust ratio C_L/GR without pitching (black) and with pitching according to various models (colored) as well as corresponding velocity and vorticity fields for $GR = 0.50$ without pitching (a) and with Wagner Küssner pitching (b)

References

- [1] Darryll J Pines and Felipe Bohorquez. Challenges facing future micro-air-vehicle development. *Journal of Aircraft*, 43(2):290–305, 2006.
- [2] Anya R Jones. Gust encounters of rigid wings: Taming the parameter space. *Physical Review Fluids*, 5(11):110513, 2020.
- [3] Gino Perrotta and Anya R Jones. Unsteady forcing on a flat-plate wing in large transverse gusts. *Experiments in Fluids*, 58(8):1–11, 2017.
- [4] S. J. Corkery, H. Babinsky, and J. K. Harvey. On the development and early observations from a towing tank-based transverse wing-gust encounter test rig. *Experiments in Fluids*, 59(9):135, Aug 2018.
- [5] Ignacio Andreu-Angulo, Holger Babinsky, Hülya Biler, Girguis Sedky, and Anya R Jones. Effect of transverse gust velocity profiles. *AIAA Journal*, 58(12):5123–5133, 2020.
- [6] Girguis Sedky, Francis D Lagor, and Anya Jones. Unsteady aerodynamics of lift regulation during a transverse gust encounter. *Physical Review Fluids*, 5(7):074701, 2020.
- [7] Ignacio Andreu Angulo and Holger Babinsky. Unsteady modelling of pitching wings for gust mitigation. In *AIAA Scitech 2021 Forum*, 2021.

Unsteady Flow and Force Response - A General Overview

Pascal Gehlert^a, Ignacio Andreu-Angulo^a and Holger Babinsky^a

^a University of Cambridge, Engineering, Cambridge, U.K.¹

*Correspondence: pg469@cam.ac.uk

1 Introduction

Unsteady flows are ubiquitous in the world around us. They can be observed during the curved flight path of a cricket ball or the wing flapping motion of birds and insects. Furthermore, the time varying nature of atmospheric turbulence has a significant impact on any aerodynamic body it interacts with. This can be especially detrimental to small micro aerial vehicles (MAVs), due to their small size and slow flight speed but the effects also extend to larger objects such as wind and marine turbines.

To expand the aerodynamic envelope of MAVs or to improve the durability and efficiency of turbines situated in unsteady environments, an improved understanding of the aerodynamics as well as associated transient force response can open the door for real-time gust mitigation or fast design iterations. In respect to this, time expensive computational fluid simulations are understandably not viable approaches. Instead low order models (LOMs) that reduce the governing equations to the minimal required form, thereby focusing only on the most dominant flow physics, provide a suitable alternative for such real time computations. Here, a common approach is to split the force into multiple components which are independently solved and superposed thereafter to arrive at the total force. For a successful implementation of this, a detailed understanding of the aerodynamic principles involved is crucial, as mistakes can render the final result inconclusive.

In light of this, the aim of this presentation will be to use a flat plate, circular cylinder as well as a surging and pitching wing, at two different pitch rates, in a water towing tank to demonstrate some of the key concepts that have been explored in Cambridge over the last couple of years by a number of PhD students. This will provide a holistic overview of some of the lessons learned as well as discuss some of the latest findings. The focus will be particularly on how the vorticity field can be interrogated to elucidate the force response and vortex shedding. This allows for an alternative understanding of how the observed flow field is formed as well as to isolate individual force contributions. The latter can be used to comprehend why the total force response evolves the way it does and also provides clues about how to predict the force history. The finite volume of the wing

and circular cylinder allows the discussion to include bodies of volume and to investigate separations that are not *fixed* to sharp edges.

2 Results

2.1 Towing Tank

The experiments are performed in the University of Cambridge Towing Tank facilities. The tank is 9 m long, 1 m wide and filled to a height of 0.8 m and a servo-motor controlled carriage moves the length of the tank. A force balance measuring the lift and drag response with a resolution of ± 0.01 N is situated on the carriage to which a NACA-0021 rapid prototyped wing and circular cylinder are vertically mounted. The Reynolds number is of the order of 10000. The flow response is obtained using planar particle image velocimetry by illuminating a horizontal plane at the midspan using an Nd:YLF laser with a dual-light sheet set-up to remove any shadow regions. Two high-speed Phantom M310 cameras are positioned below the tank and are located upstream and downstream of the wing to allow for complete optical access without any blockage.

2.2 Topics of Discussion

The main lessons learned that we want to discuss are:

- Analysing free and bound vorticity.
Every unsteady flow around an object can be interpreted as the addition of two sets of vorticity: free vorticity residing in the field away from the body as well as boundary layer vorticity; an example of the vorticity field around a pitching and surging wing is shown in figure 1. Free vorticity can be subdivided into vorticity shed by the body as well as into vorticity that was created by an external mechanism separate to the object, such as a gust. In addition, the boundary layer vortex sheet has also been categorized into a number of individual components:

$$\gamma^b = \gamma_{am}^{nc} + \gamma_{ext}^{nc} + \gamma^{shed}. \quad (1)$$

The first contribution is related to a change in kinematic motion, the second is due to free vorticity created by external means and the last is due to free vorticity shed from the body [1]. Moreover, the vortex sheets created by free vorticity can be split into *near* and *far-field* components brought about by vorticity either in close proximity to the body or from vorticity

¹This work was supported by funding from the Engineering and Physical Sciences Research Council under grant numbers EP/M508007/1 and EP/N509620/1 and from the 'la Caixa' Foundation (ID 100010434 and fellowship code LCF/BQ/EU21/11890135)

located far away [2]. Using this grouping it can be observed that vorticity accumulating far away from the body is the responsible entity for the rate of change at which vorticity sheds and thereby brings about the alternate vortex shedding pattern observed behind bluff bodies. In addition the division of the flow field into separate components allows for a systematic approach to mitigate the transient loading during gust encounters [3].

- For simple objects that can be mapped into a circle, the added mass force can be found analytically. This expression can be derived from a momentum / pressure argument or alternatively from a vortex sheet perspective, where the approach remains equally valid for objects of volume. In the general case of fast wing pitch and / or surge motions, the added mass contribution can be significant and dominate the initial force response, as schematically indicated in figure 2 for a translating and pitching wing. With time, the circulatory force develops and becomes the predominant force contribution. Moreover, invoking a small angle approximation, the added mass force is initially a linear function of pitch rate $\dot{\alpha}$. However, as the angle of attack α increases, the relationship becomes more complex, which we will further discuss in the presentation.
- Further to this, we aim to discuss how shed vorticity within the flow field contributes to forces. Using the impulse method, we can write the total force as the variation of the boundary layer vortex sheet, the advection of free vorticity by the boundary layer and the creation of new vorticity shed by the body [4].
 - This can provide insight into the effect that specific regions of vorticity have on the force. For example, the leading edge vortex (LEV) which forms when vorticity leaves the boundary layer and accumulates in a vortical structure just downstream of the leading edge of a wing or flat plate, is normally assumed to *positively contribute to lift*. However, we want to show that this is only true in some instances where the LEV is very close to the wing, whereas otherwise the transfer of vorticity from the boundary layer to the LEV reduces lift.
 - When an object accelerates or experiences a change in angle of attack, the related force can be estimated from the effective angle of attack by employing a quasi-steady assumption (where shed vorticity is assumed to immediately reside infinitely far away from wing). However, unsteady cases require one to account for the effect of the trailing edge vorticity progressively moving away from the wing. The typical effect is a delay to reach the quasi-steady result.

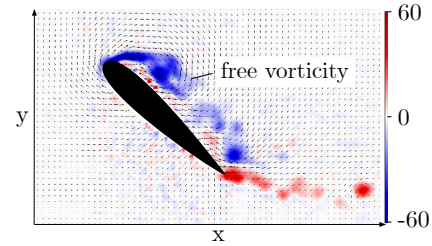


Figure 1: Flow around a pitching and translating wing.

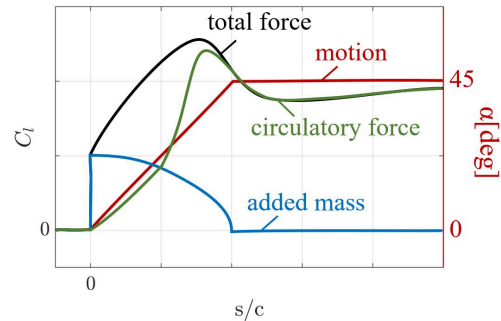


Figure 2: Schematic illustration of the total force and its contributions as a surging wing pitches.

- By assessing the force contributions due to added mass and free vorticity, we can make sense of the changing force history observed for fast and slow kinematic motions. The factors affecting whether the force leads or lags the motion profile will be analysed in the presentation.

3 Conclusion

Observing the flow field in terms of vorticity can provide insight into the individual force contributions. Consistently applying this method allows for a holistic understanding of the flow and force response, however, one needs to be careful to be consistent when grouping vorticity, especially when superposing other analytical force contributions. From a practical perspective an improved understanding can be particularly useful when developing gust mitigation techniques, as the unsteady flow field and its force response no longer appear arbitrary. This allows for a systematic approach to remove the transient force peak and to determine which parts of the gust encounter are worth modelling.

References

- [1] Corkery, S. J., Babinsky, H., Graham, W. R., Quantification of Added-Mass Effects Using Particle Image Velocimetry Data for a Translating and Rotating Flat Plate. *Journal of Fluid Mechanics*, 2019.
- [2] Gehlert, P., Babinsky, H. Boundary Layer Vortex Sheet Evolution Around an Accelerating and Rotating Cylinder. *Journal of Fluid Mechanics*, 2021.
- [3] Andreu-Angulo, I., Babinsky, H., Unsteady Modelling of Pitching Wings for Gust Mitigation. *AIAA Scitech 2021 Forum*, 2021.
- [4] Gehlert, P., Andreu-Angulo, I., Babinsky, H., Unsteady Vorticity Force Decomposition - Evaluating Gust Distortion. *AIAA Scitech 2021 Forum*, 2021.

Data-driven aerodynamic load estimation in gusty environments from sparse pressure data

Frieder Kaiser^{a*}, Giovanni Iacobello^b and David E. Rival^a

^a Department of Mechanical and Materials Engineering, Queen's University, Kingston, ON, Canada¹

^b Department of Mechanical Engineering Sciences, University of Surrey, Guildford, UK

*Correspondence: f.kaiser@queensu.ca

1 Introduction

A series of recent works proposed algorithms for real-time aerodynamic load estimation from sparse pressure measurements [1–3]. In the present study, we suggest an approach for data-driven aerodynamic load estimation from experimentally obtained surface-pressure data. Experimental data captured in highly unsteady and non-linear real-world system is typically sparse, limited, and noisy. The present study suggests a purely data-driven approach tailored to the challenges related to experimental data. In particular, a prediction-correction approach with Bayesian inference (similar to a Kalman filter) is coupled with a pre-trained transition network that models the system's dynamics.

2 Experimental Methods

High Reynolds-number measurements were conducted in a fully-enclosed, water-filled, 15-m-long towing tank facility with $1\text{ m} \times 1\text{ m}$ cross-section (see fig. 1a). Two aerodynamic bodies were considered in consecutive campaigns: (i) an elliptical plate with the dimensions $b = 0.3\text{ m}$ and $w = 0.15\text{ m}$ (see fig. 1b) and (ii) a NACA0012 delta-wing model with a sweep angle $\Lambda = 45^\circ$ and chord length $c = 0.3\text{ m}$ (see fig. 1e). The respective models were connected to the traverse above the towing tank via two vertical actuators. The setup enables the simulation of complex kinematics combining pitch, plunge, and axial accelerations. For the sake of brevity, in this abstract, only the results of the elliptical plate are discussed. The plate was mounted at various angles of attack α and then accelerated from rest ($U_p = 0$) until reaching its final velocity $U_\infty = 1\text{ m/s}$. The plate velocity ($U_p = U_\infty$) is then kept constant over a distance of $\sim 40D_h$ before being decelerated to rest, where D_h is the (characteristic) hydraulic diameter.

Two Omega differential pressure transducers were mounted so as to capture the instantaneous differential pressure Δp between the two sides of the plate. Furthermore, the aerodynamic forces on the plate were measured with an ATI six-axis force-torque sensor, which was mounted between the plate and the horizontal sting (see Fig. 1b). The temporal evolution of the normalized pressures $C_p^i = 2\Delta p_i / (\rho U_\infty^2)$,

¹This work was supported by the Air Force Office of Scientific Research (AFOSR) under grant number FA9550-20-1-0086.

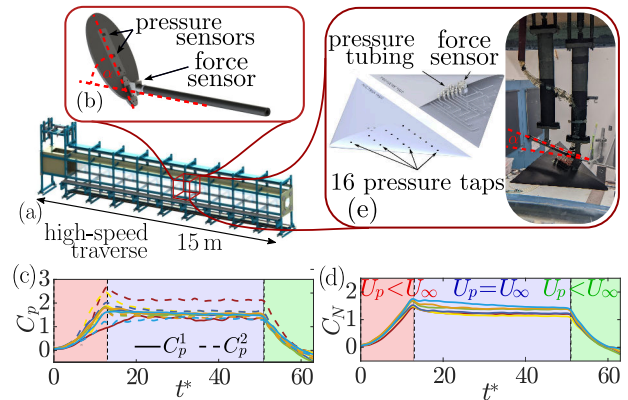


Figure 1: (a) Experimental setup in 15m-long towing-tank facility; (b) elliptical plate with force-torque sensor and two differential pressure sensors; (c) measured differential pressures; (d) measured plate-normal forces; for various angles of attack (α , legend see Fig. 2a).

and the plate-normal load $C_N = 2F_N / (\rho A U_\infty^2)$, are shown in Fig. 1c,d. Note that superscripts, $i = 1, 2$, refer here to sensor position at $y/b = 0.5$ and $y/b = 0.75$, respectively (where y is the direction of the longer principal axis of the plate). Fig. 2a shows the forces and pressures as trajectories in the state space.

3 Transition-network based load estimation

3.1 Training Stage

To create a model of the system dynamics, the state-space trajectories (fig. 2a) of the training data are clustered using the k -means++ algorithm [4], leading to N_{cl} discrete states $S_i = \{C_p^1, C_p^2, C_N\}$ (black dots in fig. 2b). Thereafter, the transition probability matrix \mathcal{P} between pairs of states is extracted from the training data. Hereby, each entry of the transition matrix (\mathcal{P}_{ij}) acts as a directed edge of the network and provides the probability to transition from state S_i to S_j ; see fig. 2b. The detailed algorithm of the training stage is discussed in [5]. The combination of states (S) and edges (\mathcal{P}) represents a low-order model of the system that can predict the state of the system in the consecutive time instance.

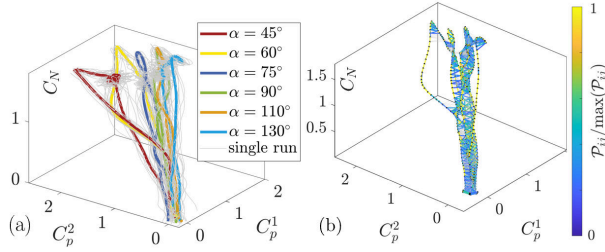


Figure 2: (a) Collected force and pressure data in the state-space representation. (b) Example of a transition network with states (S) as black nodes and color coded transition probabilities (\mathcal{P}) as edges. The cases $60^\circ \leq \alpha \leq 130^\circ$ were used to obtain this network.

3.2 Load estimation

To estimate the unknown variable (here C_N), the low-order model described in section 3 is combined with the real-time input of N sparse sensors (here C_p^1 and C_p^2). In particular, the probability, $Pr_{I,i}$, that a state, S_i , describes the present aerodynamic condition of the system is determined for all states, and updated for each time step t_k . Fig. 3 outlines the procedure. Hereby, the prediction step (fig. 3a) uses the transition matrix (\mathcal{P}) to update Pr_I and predict the state's probabilities in the next time instance

$$Pr_{\mathcal{P},i} = \mathcal{P}_{i,j} Pr_{I,j}. \quad (1)$$

In fig. 3a the resulting probability distribution is visualized as green circles of different size, while the shift of probabilities due to transition step is emphasized by blue arrows. Simultaneously, the real-time pressure measurements provide *evidence* (fig. 3b). Here, we estimate the probability of a measurement $m(t_k) = \{\tilde{C}_p^1, \tilde{C}_p^2\}$ to belong to a particular state S_i , by assuming a multivariate normal distribution of the measurement noise:

$$E_i = \frac{\exp[-0.5(m - S_i)^\top \Gamma^{-1}(m - S_i)]}{\sqrt{(2\pi)^d |\Gamma|}}. \quad (2)$$

Here, Γ is the covariance matrix of the measurements, $^\top$ indicates the transpose, $|\bullet|$ is the matrix determinant, and d is the dimension of the measurement data (here $d = 2$). After normalization the *evidence probability vector* is obtained

$$Pr_{E,i} = \frac{E_i}{\sum_{j=1}^{N_{cl}} E_j}. \quad (3)$$

Note that Pr_E only relies on the instantaneous measurement data and not on the system dynamics. Bayes theorem is then applied to correct the predicted probability distribution ($Pr_{\mathcal{P}}$) by the information obtained from the real-time pressure measurements (Pr_E); see fig. 3c.

$$Pr_{I,i} = \frac{Pr_{\mathcal{P},i} Pr_{E,i}}{Pr_{\mathcal{P},i} Pr_{E,i} + (1 - Pr_{\mathcal{P},i})(1 - Pr_{E,i})}. \quad (4)$$

Finally, the corrected probability distribution $Pr_{\mathcal{P}}$ can be used to estimate the unknown variable \hat{C}_N . Fig. 3(d)

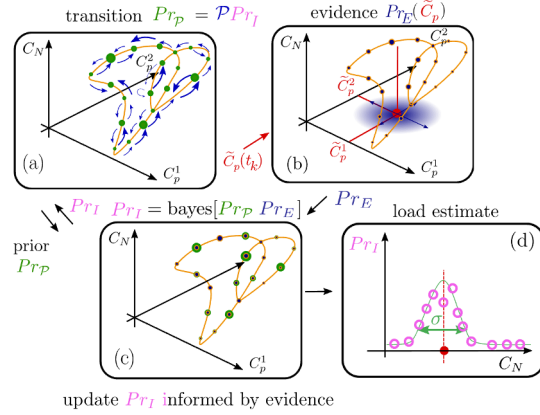


Figure 3: Stages of the algorithm: (a) prediction; (b) evidence; (c) Bayesian inference; and (d) load estimation.

presents this last step of the procedure, where the probabilities, $Pr_{\mathcal{P}}$, are plotted as a function of C_N . A Gaussian distribution is then used to fit Pr_I . The most likely load is assigned as \hat{C}_N and, in addition, the standard deviation σ is obtained that provides a measure for the accuracy of the load estimate. The same procedure can be performed to estimate the pressures \hat{C}_p^i . Doing so, the error magnitude of the estimated pressures relative to the measured pressures $\epsilon_p = \|\hat{C}_p^{1,2} - \tilde{C}_p^{1,2}\|$ can be evaluated. The pressure estimation error ϵ_p can then be used as to assess the accuracy of the load estimate \hat{C}_N .

In the presentation, we discuss the performance of the suggested algorithm concerning sparse sensors, limited training, and noisy data. Finally, the dataset collected with the delta wing shown in fig. 1e is explored, and the load estimation algorithm is applied to extreme delta-wing maneuvers combining streamwise acceleration with rapid pitching.

References

- [1] M. Le Provost, X. He, and D. R. Williams. Real-time roll and pitching moment identification with distributed surface pressure sensors on a ucas wing. In *2018 AIAA Aero. Sci. Meeting*, number 0326, 2018.
- [2] K. Fukami, K. Fukagata, and K. Taira. Assessment of supervised machine learning for fluid flows. *Theor. Comput. Fluid Dyn.*, 34(4):497–519, 2020.
- [3] G. Iacobello, F. Kaiser, and D. E. Rival. Load estimation in unsteady flows from sparse pressure measurements: Application of transition networks to experimental data. *Phys. Fluids*, 34(2):025105, 2022.
- [4] D. Fernex, B. R. Noack, and R. Semaan. Cluster-based network modeling—from snapshots to complex dynamical systems. *Sci. Adv.*, 7(25):eabf5006, 2021.
- [5] F. Kaiser, G. Iacobello, and D. E. Rival. Aerodynamic state estimation from sparse sensor data by pairing Bayesian statistics with transition networks. In *2022 AIAA Aero. Sci. Meeting*, number 1669, 2022.

Detection of coherent structures in a surge propagating in a channel.

L. Thomas^a and L. David^{a*}

^a Institut Pprime, département FTC, Poitiers, France¹

*Correspondence: lionel.thomas@univ-poitiers.fr

1 Introduction

Surges has been studied numerically and experimentally, but most of the time, the coherent structures generation was not considered from an instantaneous point of view. Many studies concentrated on the free surface evolution. For example, Zheng *et al.* (2018) are studying the free surface shape as a function of the Froude number. Chanson (2009) have also shown that the wave characteristics depends on the Froude number, the width of the channel and the flow rate. The studies in Leng & Chanson (2017b) and Leng & Chanson (2017a) used 25 runs to perform ensemble statistics. They have shown that the flow is an-isotropic and unsteady. Already, Yeh & Mok (1990) have observed turbulent patches appearing behind surge fronts. Chanson (2009) have observed large Reynolds stresses near the developing shear layer. Anyway, in most experimental studies, the flow is investigated using one-point measurements, in particular Acoustic Doppler Velocimetry. Some studies were conducted with visualizations, like in Yeh & Mok (1990) or Martin *et al.* (1993)). The use of optical method to study this kind of flow is rather new. Lennon & Hill (2006) have used traditional 2D Particle Image Velocimetry (PIV), but only statistics and shear stresses have been considered, in a stationary hydraulic jump, which is an easier case. Hornung *et al.* (1995) have used PIV to study a dam break. They have shown the presence of a shear layer at the toe, and presented a scenario of vorticity generation mechanism by surface reconnection. More recently, David *et al.* (2014) have investigated the influence of the initial conditions (turbulence intensity, boundary layer thickness) on the free-surface evolution of the surge and the turbulence in the flow. Here, a new point of view on the flow is presented, using time-resolved 2D3C measurements, giving access to the spatial and temporal dynamics of the flow. In particular, the coherence of the flow is studied using Eulerian or Lagrangian representations.

The experimental setup is presented in figure 1. The channel is 8 m long and 40 cm wide. The water level is controlled with a weir at the channel end. The jump is generated using a gate, falling with a controlled velocity. At the channel entrance, on the left of the figure, a 3D convergent and several grids ensures a clean flow. The free surface level

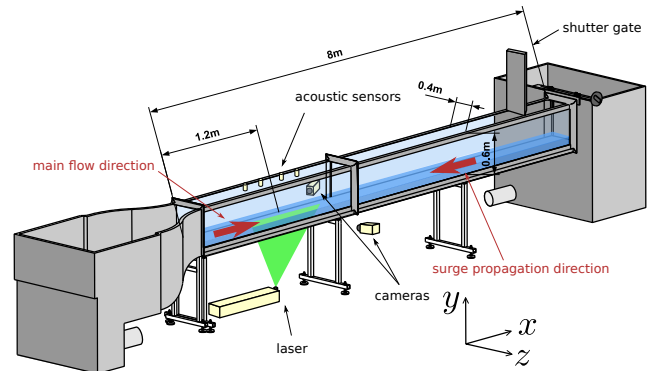


Figure 1: Experimental setup of the open-channel used to generate the flow.

is measured with four acoustic sensors. It is used to provide a mask to PIV processing, using an average of the two central sensors, weighted by the distance from the sensors. Outside the valid measurement region, the velocity is fixed to zero. In this case, not so many bubbles are present as the front roll is of weak intensity. Also, fluorescent particles have been used as PIV tracers. These 20 μm diameter particles are made with polyamid (density 1.04) doped with rhodamine 6G. Only the fluorescent pink signal is measured by the cameras equipped with a high pass filter, avoiding the green light reflections on the free surface. Nevertheless, it is difficult to seed the flow just below the free surface. The stereoPIV spatial resolution is 2,3 mm in X and 2,0 mm in Y , leading to a 123×123 data grid. The chosen configuration corresponds to a 16,66 L/s flow rate, assured by a worm pump. The initial water height (direction y) was $d_1=7,0$ cm, for a mean longitudinal (direction x) velocity $U_1=0,609$ m/s. The jump, generated by a shutter gate, visible on the right part of the figure, was moving upstream with a velocity $U_b=-0,644$ m/s.

2 Results

The coherent structures are studied using in particular Finite Time Lyapunov Exponents (FTLE) and Lagrangian descriptors. The FTLE are calculated as $\frac{1}{2T} \ln \lambda$ where λ is the largest eigenvalue of the Cauchy-Green tensor and T is the observation time. They can be calculated using forward time (Λ_t^{t+T}). The high values corresponds to positions where the trajectories diverge. When using backward time (Λ_t^{t+T}), high values highlight converging trajec-

¹This work was supported by the french research agency under grant number ANR-10-BLAN-0911

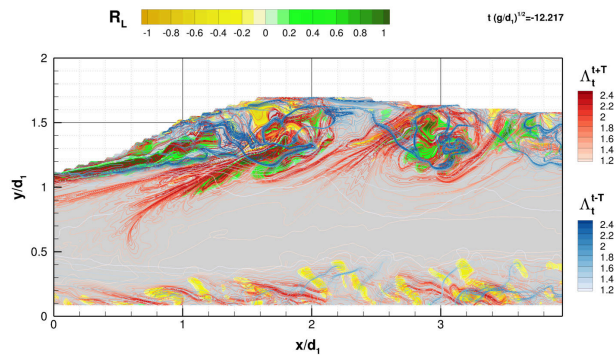


Figure 2: Lagrangian Coherent Structures below a surge. In red, iso-contours of forward FTLE, in blue, iso-contours of backward FTLE, in yellow, clockwise rotating structures, in green, anti-clockwise rotating structures.

tories. The Lagrangian descriptor R_L used here is a mean minimal rotation of a filament transported by the flow during a finite observation time. It is computed by averaging the minimum angular velocity of a filament, given by $\text{sgn}(\omega)(\frac{|\omega|}{2} - |\gamma|)$. ω is the vorticity ($\omega = \frac{\partial v}{\partial x} - \frac{\partial u}{\partial y}$), and γ is the stretching ($\gamma = \sqrt{(\frac{\partial v}{\partial x} + \frac{\partial u}{\partial y})^2 + (\frac{\partial u}{\partial x} - \frac{\partial v}{\partial y})^2}$). These Lagrangian quantities are computed on a self-adaptive grid and using the RK45 integration scheme (Runge-Kutta with self-adaptive time step) in order to have high quality results. The flow map gradient F_1 (necessary here to get the Cauchy-Green tensor $C_1 = F_1^* F_1$), is calculated using the differential equation $\dot{F}_1 = L_1 F_1$ where L_1 is the velocity gradient tensor. The spatial derivatives of the velocity are calculated with schemes reducing the experimental measurement noise. The choice of the observation times will be discussed. The effect of measurement noise is also investigated. An example is presented in figure 2.

Other approaches will be presented, such as spatio-temporal representation of the Lagrangian rotation descriptor (see figure 3). In this figure, the time coherence of the rotating structures generated by the surge are clearly shown, and the change of the boundary layer is also visible.

3 Conclusion

The birth of the shear instability behind the surge will be shown and the evolution of the coherent structures will be described. It will be shown how the coherent structures invade all the flow and that the boundary layer is largely affected by the surge presence. It will be shown how the Lagrangian approach can give more insight in vortex dominated flows understanding.

References

Chanson H (2009) Current knowledge in hydraulic jumps and related phenomena. a survey of experimental results. *European Journal of*

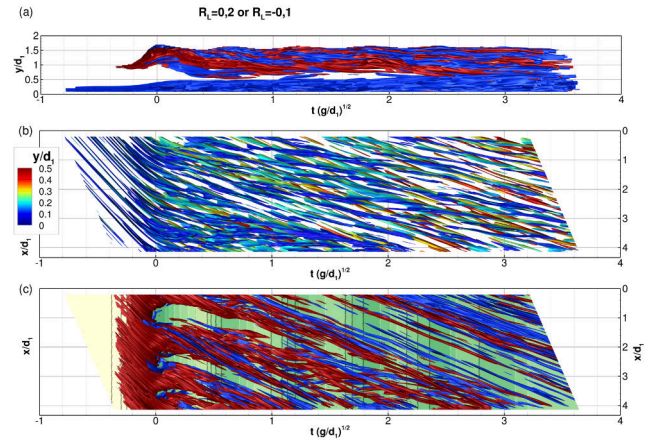


Figure 3: Lagrangian rotation descriptor iso-surfaces below a surge, in a spatio-temporal frame. (a) is a side view. (b) is a top view from $y/d_1 = 0,5$ and (c) is a view from below the free surface, strating also from $y/d_1 = 0,5$

Mechanics - B/Fluids 28(2):191 – 210. doi:<https://doi.org/10.1016/j.euromechflu.2008.06.004>

David L, Chatellier L, Calluau D, Jeon Y, Rousseaux G, Thomas L (2014) Tr-piv measurements in open channel flow for the analysis of undular tidal bores. In 17th International Symposium on Applications of Laser Techniques to Fluid Mechanics, Lisbon, Portugal

Hornung HG, Willert C, Turner S (1995) The flow field downstream of a hydraulic jump. *Journal of Fluid Mechanics* 287:299–316. doi:10.1017/S0022112095000966

Leng X, Chanson H (2017a) Integral turbulent scales in unsteady rapidly varied open channel flows. *Experimental Thermal and Fluid Science* 81:382 – 395. doi:10.1016/j.exthermflusci.2016.09.017

Leng X, Chanson H (2017b) Unsteady turbulence, dynamic similarity and scale effects in bores and positive surges. *European Journal of Mechanics - B/Fluids* 61:125 – 134. doi:<https://doi.org/10.1016/j.euromechflu.2016.09.017>

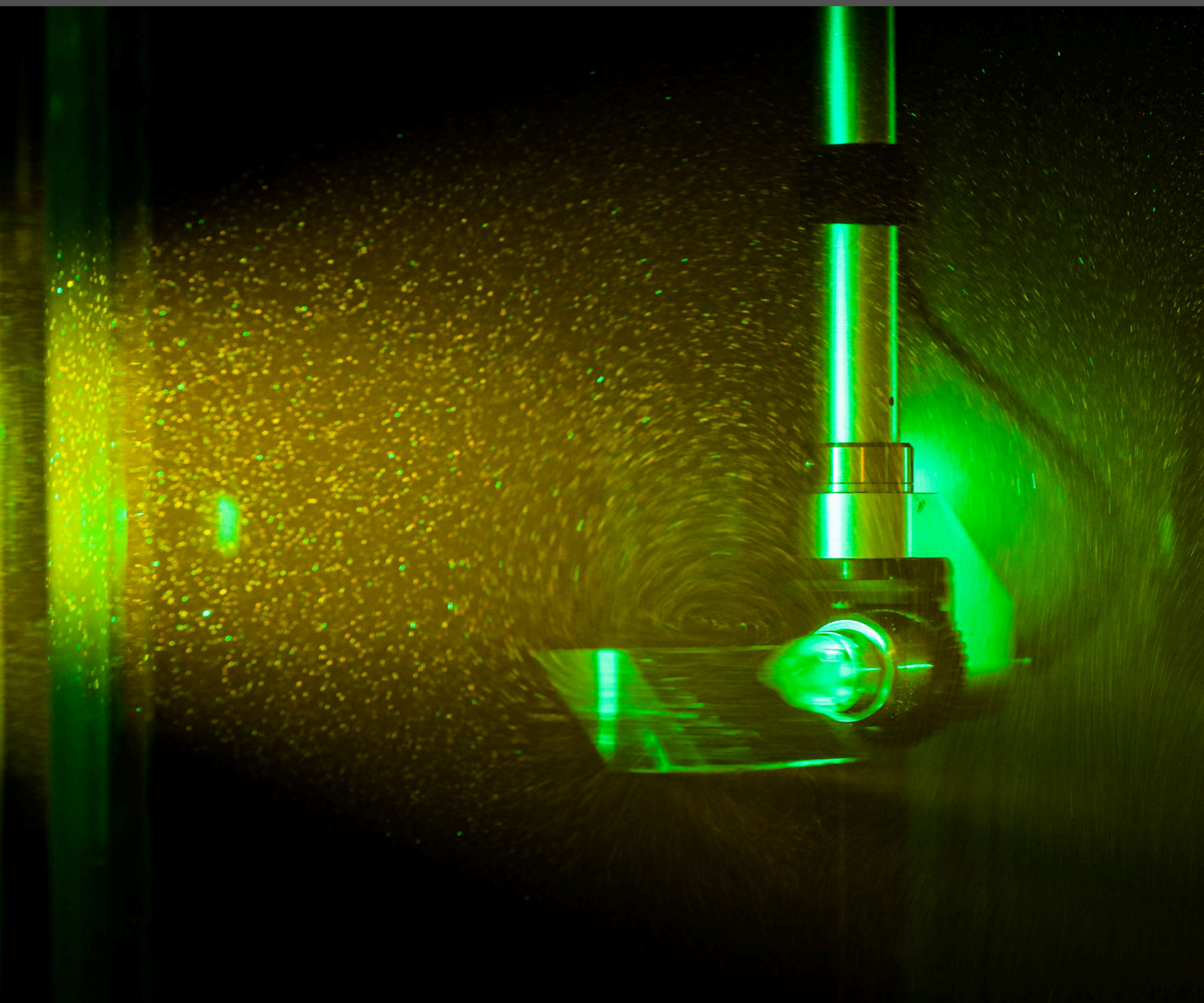
Lennon JM, Hill DF (2006) Particle image velocity measurements of undular and hydraulic jumps. *Journal of Hydraulic Engineering* 132(12):1283–1294. doi:10.1061/(ASCE)0733-9429(2006)132:12(1283)

Martin JPV, Dolz J, Del Estal J (1993) Kinematics of the moving hydraulic jump. *Journal of Hydraulic Research* 31(2):171–186. doi:10.1080/00221689309498843

Yeh HH, Mok K (1990) On turbulence in bores. *Physics of Fluids A: Fluid Dynamics* 2(5):821–828. doi:10.1063/1.857630

Zheng F, Li Y, Xuan G, Li Z, Zhu L (2018) Characteristics of positive surges in a rectangular channel. *Water* 10:1473. doi:10.3390/w10101473

Poster session 2



Separated vortex ring and vortex dipole past inclined porous discs and plates

Chandan Bose, Callum Bruce and Ignazio Maria Viola*

School of Engineering, Institute for Energy Systems, University of Edinburgh, Edinburgh, UK¹

*Correspondence: *i.m.viola@ed.ac.uk*

1 Introduction

The Separated Vortex Ring (SVR) was first observed by Cummins *et al.* [1] in the wake of dandelion diaspores. It was argued that this flow feature is correlated with the high drag per projected area of the dandelion, that is an order of magnitude higher than that of an impervious disk with an equal area. This enhanced drag allows one of the most successful long-distance dispersal in the plant kingdom [2].

The SVR is a stable toroidal vortex, whose closed streamlines are separated from the solid body. An SVR with similar topology to that observed past dandelion diaspores is also observed behind porous disks with uniform permeability and porosity [3]. Its existence is, however, limited within a specific range of the Reynolds number, $Re = \mathcal{O}(10^1 - 10^2)$, and the Darcy number, $Da = \mathcal{O}(10^{-5} - 10^{-4})$. Furthermore, during its flight, a dandelion diaspore experiences different flow incidences. Yet, how the SVR topology varies with different angles of attack (α) is not known.

Castro [4] showed numerically that a vortex dipole, with a topology akin to that of a meridian section of the SVR, is formed in the wake of two-dimensional porous plates. A direct comparison between these topologies have never been undertaken. Furthermore, also for the vortex dipole, it is not clearly understood how its topology varies with α . Hence, in this study, we investigate similarities and differences between the SVR and the vortex dipole topologies, formed behind porous disks and 2D plates, respectively, for a range of Re , Da and α .

2 Computational Methodology

We consider a 2D porous plate and a 3D porous disk, each with an aspect-ratio of 10, immersed in a uniform and steady stream of an incompressible fluid. We solve both the flow and the porous domain with the Darcy-Brinkmann equation (Eq. 1):

$$\frac{1}{\phi^2} \frac{\partial \mathbf{u}}{\partial t} + \frac{1}{\phi^2} (\mathbf{u} \cdot \nabla) \mathbf{u} = -\nabla p + \frac{1}{\phi Re} \nabla^2 \mathbf{u} - \frac{1}{Re Da} \mathbf{u}, \quad (1)$$

where ϕ is the porosity, t is the nondimensional time, \mathbf{u} is the nondimensional velocity vector and p is the nondimensional pressure. The second term on the right hand side of

¹This work was supported by the European Research Council through the Consolidator Grant 2020 ‘‘Dandidrone: a Dandelion-Inspired Drone for Swarm Sensing’’ [H2020 ERC-2020-COG 101001499].

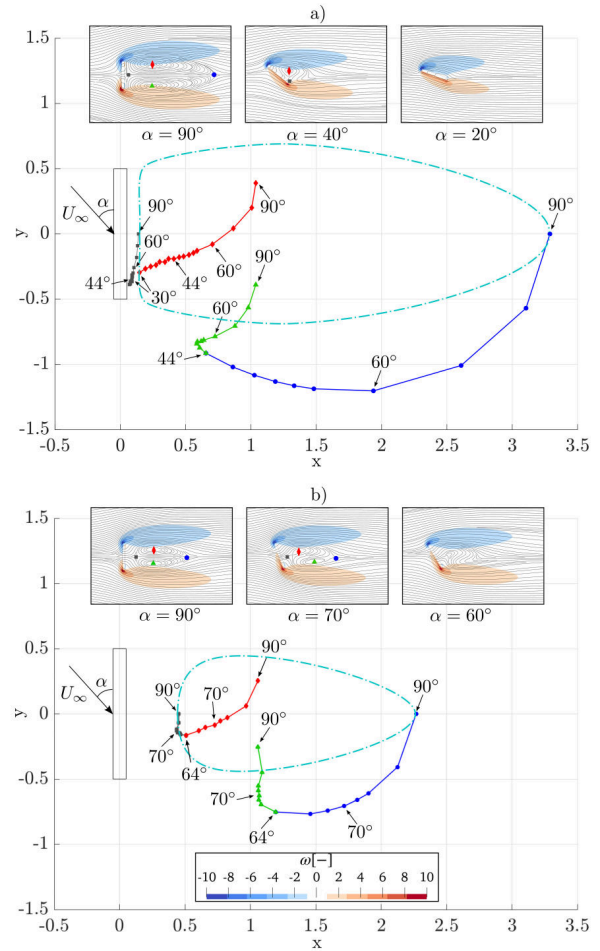


Figure 1: Position of the nodes (red diamond and green triangle) and saddles (grey square and blue circle) of a two-dimensional porous plate at $Re = 30$, $\phi = 0.95$, for $Da = 5 \times 10^{-5}$ (a), and $Da = 5 \times 10^{-4}$ (b). In (a), $\alpha = 90^\circ, 80^\circ, 74^\circ, 72^\circ, 70^\circ, 68^\circ, 66^\circ$ and 64° . In (b), $\alpha = 90^\circ, 80^\circ, 70^\circ, 60^\circ, 54^\circ, 52^\circ, 50^\circ, 48^\circ, 46^\circ, 44^\circ, 42^\circ, 40^\circ, 38^\circ, 36^\circ, 34^\circ, 32^\circ$ and 30° . Light blue dotted lines denote the closed streamline of the vortex dipole at $\alpha = 90^\circ$. Top insets show streamlines and nondimensional vorticity contours for three α values. Bottom inset shows the nondimensional vorticity legend for top insets.

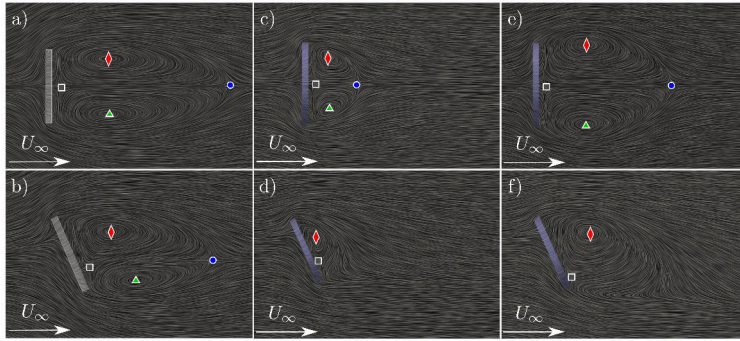


Figure 2: Comparison between a vortex dipole and a meridian section of the SVR through line integral convolution visualization. (a) and (b) show the vortex dipole past a 2D porous plate with $Re = 30$, $Da = 10^{-4}$, $\phi = 1$ at $\alpha = 90^\circ$ and $\alpha = 60^\circ$, respectively; (c) to (f) show a meridian section of the SVR past a 3D porous disc with $Da = 10^{-4}$, $\phi = 1$ at $Re = 30$ (c, d), $Re = 130$ (e, f), $\alpha = 90^\circ$ (c, e), and $\alpha = 60^\circ$ (d, f). The symbols denoting the saddle points and nodes follow the same convention as in Fig. 1

Eq. 1 is the *Brinkman* term [5], and the third term is the *Darcy* linear drag term, originating from Darcy’s law [6]. In the porous body we set $Da \in \mathbb{R} \mid Da > 0$ and $\phi \in (0, 1)$, while in the clear flow region we set $Da \rightarrow \infty$ and $\phi = 1$. We solve Eq. 1 together with the continuity equation within the open-source library *OpenFOAM* using a modified incompressible Navier-Stokes solver, *porousIcoFoam*, with an arbitrary Lagrangian Eulerian framework. The PISO pressure-velocity coupling algorithm is used to iterate forward in time. Simulations were validated against existing literature and the uncertainty on the position of the topological points is found to be $\pm 0.7\%$ of the chord length.

3 Results

First, we show that high permeability suppresses an intermediate topological configuration that exist only for low-permeable plates. Figure 1a and 1b show the coordinates of the nodes and saddles at various α for low and high permeability plates, respectively. The topological points are plotted sequentially in a body-fixed frame of reference.

For the low-permeability plate (Fig. 1a), at $\alpha = 90^\circ$, we identify two saddles (blue circle and grey square) at the stagnation points, and two nodes (red diamond and green triangle). For decreasing α , all points move first downstream parallel to the chord and then turn towards the plate. At $\alpha = 44^\circ$, the downstream node (green triangle) merges with the downstream saddle (blue circle), forming a different topological field with only one clockwise recirculation region (see middle insert in Fig. 1a). This topology exists for α as low as 30° , when the remaining saddle (black) and node (red) merge annihilating the vortex.

In contrast, for the high-permeability plate (Fig. 1b), the intermediate topology with only one recirculation region does not exist. In fact, both node-saddle pairs meet at $\alpha = 64^\circ$. At lower α values, the wake is characterised by tortuous streamlines without a closed re-circulation region. As the permeability increases, the vortex dipole decreases in size and is annihilated at higher α values.

We now compare the flow topology of a 2D vortex dipole with that of a meridian section of the SVR. Figure 2a and 2b present the separated vortex dipole past a 2D porous plate at $\alpha = 90^\circ$ and 60° , respectively. The permeability is in-

termediate to that of the plates in Fig. 1. The two nodes and saddle points are distinctly present at both $\alpha = 90^\circ$ and 60° for the plate. On the other hand, the corresponding 3D cases, presented in Figs. 2(c) and 2(d), shows a significantly shorter SVR, and the annihilation of the two downstream node-saddle pair at $\alpha = 60^\circ$ case. We conclude that these two changes due to the threedimensionality cannot be mimicked by a change in the permeability.

The effect of changing Re from 30 to 130 is revealed by the comparison of Figs. 2c and 2d, with Figs. 2e and 2f. The topology remains similar at the two α values, but the length of the SVR increases with Re . This is consistent with the findings of Cummins et al. [3]. Importantly, at $Re = 130$, the wake behind the 2D plate is unsteady (not showed), demonstrating the increased stability of the SVR compared to the 2D vortex dipole.

4 Conclusion

We showed that the path to transition from a symmetrical vortex dipole at $\alpha = 90^\circ$ to dipole annihilation depends on permeability. The dipole is annihilated in two steps for the low-permeability plate and at significantly lower α than the high-permeability plate.

At $\alpha = 90^\circ$, the 2D topology of the vortex dipole is similar to that of a meridian section of the SVR of porous disks. However, the SVR topology results in a longer bubble, more stable with Re and more subjected to topological changes with Da .

References

- [1] C. Cummins, M. Seale, A. Macente, D. Certini, E. Mastropalo, I. M. Viola, & N. Nakayama (2018) A separated vortex ring underlies the flight of the dandelion *Nature*. **562** (7727), 414-418.
- [2] H. N. Ridley (1905) On the dispersal of seeds by wind *Annals of Botany*.
- [3] C. Cummins, I. M. Viola, E. Mastropalo, & N. Nakayama (2017) The effect of permeability on the flow past permeable disks at low Reynolds numbers *Physics of Fluids*. **29** (9), 097103.
- [4] I. P. Castro (1971) Wake characteristics of two-dimensional perforated plates normal to an air-stream. *Journal of Fluid Mechanics.*, **46** (3), 599-609.
- [5] H. C. Brinkman (1949) A calculation of the viscous force exerted by a flowing fluid on a denseswarm of particles. *Flow, Turbulence and Combustion*. **2** (1), 155–161.
- [6] H. Darcy (1856) *Les fontaines publiques de la ville de Dijon*. Paris.

Two-dimensional airfoil dynamics and Kelvin's circulation theorem : the Couchet framework

Ludovic Chatellier

Institut PPRIME, UPR 3346 CNRS - Université de Poitiers - ISAE-ENSMA, France

Correspondence: ludovic.chatellier@univ-poitiers.fr

1 Introduction

In idealized flow conditions, Kelvin's circulation theorem ensures that the circulation around a closed contour is kept constant at all times. Considering the in-plane motion of an airfoil, the combination of the unsteady Kutta condition and Kelvin's theorem predicts that variations of the lift force due to a change of circulation around the airfoil is balanced by a circulation adjustment away from the airfoil. Situation hosting such effects are extremely common, as in accelerating or decelerating flows or motions, pitching and plunging motions, etc. in which shed vortices or vorticity sheets can be observed or modeled.

Within the classic formulation of two-dimensional unsteady potential flows, Couchet [1] derived a family of motion laws which do not theoretically alter the circulation around the moving airfoil, hence preventing any vorticity release. A first experimental verification of these findings was then provided by Werlé [2]. In a subsequent contribution Couchet [3] extended his formulation to arbitrarily pitching and plunging airfoils by separating the constant and unsteady circulation contribution, and introducing vorticity releases.

Applications of the Couchet laws are rare. Using introductory and applied examples, we will illustrate how circulation can be efficiently used as a kinematic parameter for a variety of in-plane motions of airfoil-type bodies. We will then present and discuss what contributions and limitations can be expected from the Couchet framework for viscous and turbulent flows.

2 Results

Considering the conformal transformation from a circle to an airfoil and the unsteady potential flow around a moving cylinder, Couchet [1, 3] derived a complete analytical framework in which the fluid forces acting on the moving body are explicitly formulated through circulatory and non-circulatory terms.

For a two-dimensional in-plane motion in a fluid at rest, the combination of translation and rotation of the airfoil of Figure 1 in its own reference frame, combined with the unsteady Kutta condition at the trailing edge, imposes a circulation value:

$$\Gamma = 4\pi a(\dot{y} + \dot{\delta}\Omega)$$

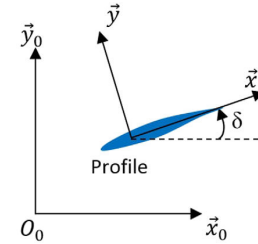


Figure 1: Airfoil with attached reference frame.

in which a is the cylinder diameter and Ω a specific control point along the airfoil chord. Therefore, Kelvin's circulation theorem indicates that no additional vorticity shall be introduced in the flow provided that this quantity remains constant in time. Inversely, any arbitrary modification of the airfoil motion would have to be compensated by additional circulatory terms. From this simple expression, it is for example straightforward to link the normal velocity of a non-pitching airfoil to its steady angle of attack α when immersed in a flow of uniform velocity V : $\Gamma = 4\pi a V \sin\alpha$. More generally, the constant circulation constraint defines a two-dimensional parametric space of in-plane motions from which the fluid forces acting on the airfoil can be analytically derived.

Among the variety of kinematics of interest, one can consider arbitrary pitching laws to analytically derive circulation-preserving trajectories. In this space of parameters, each value of the circulation will result in a different motion of the airfoil along a given path. Though this approach opens the possibility of exploring complex airfoil trajectories, it offers little control on the actual airfoil location. In view of applying Couchet laws to energy harvesting devices, we instead chose to use parametric paths that explicitly drive the airfoil pitching rate. The actual airfoil pitch angle is therefore obtained from time-integration. The chosen paths are circular trajectories with either constant or unknown angular velocities. Depending on the prescribed circulation value and the airfoil to free-stream velocity ratio (or tip speed ratio for a turbine), the airfoil shall lightly oscillate around its mean incidence in the moving frame, or dynamically orient itself with respect to the fixed frame.

This approach is first exploited to prevent the occurrence of dynamic stall for a 4-bladed Darrieus turbine. Using an anal-

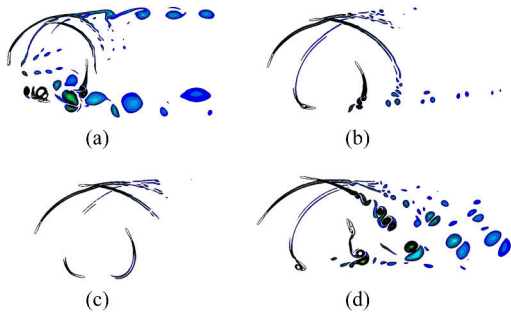


Figure 2: Simulated operation of a Darrieus turbine with (a) fixed blades, (b-c-d) 5°, 10°, -5° equivalent angles of attack [4]. Flow from left to right.



Figure 3: Simulated operation of a Darrieus turbine with a dual (+10°/-5°) circulation constraint [7].

ogy between the static angle of attack of a steady airfoil and the corresponding circulation, the concept of a generalized angle of attack is introduced, which shall be kept constant during the operating cycle of the turbine. While this constraint can be unambiguously ensured in the idealized framework of potential flows, viscous and turbulent flows are likely to limit its applicability. As a result of a series of U-RANS simulations, Figure 2a shows that for a generalized AoA of 5°, the flow remains fully attached to each blade, including when blade-wake interactions occur. This behaviour has been experimentally confirmed in [5]. However, sub-figures b and d indicate that despite efficiently preventing the dynamic stall, the rapid dynamics of the blades generate parasite vortex shedding in the downstream part of the rotor as soon as the generalized angle of attack is set out of a certain operating range.

Furthermore, it is analytically verifiable that the constant circulation constraint results in a theoretical zero power-take-off. We then applied a dual-circulation strategy, in which two generalized angles of attack were chosen along with two transition zones and profiles within the turbine cycle. An exemplary result of this strategy is presented in Figure 3. The change of circulation imposed between the up- and downstream parts of the Darrieus rotor bring control in releasing the compensating vortices outside of the turbine rotor while maximizing the power take-off. The experimental results of [5] have quantified that the shed vortices actually tend to restore the circulation budget.

Continuing with the developpement of an energy harvester based on the flutter phenomena, we have pre-dimensioned a concept making use the unsteady circulation approach of

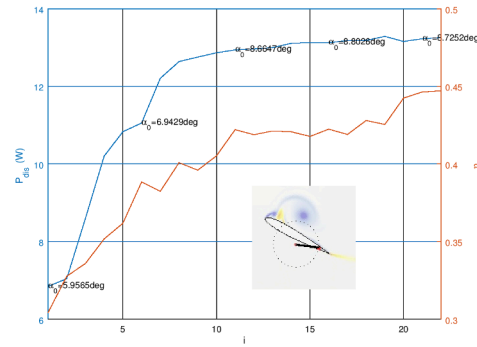


Figure 4: Iterative optimisation of an ascillating harvester [6]. Flow from left to right.

Couchet [6]. A stability analysis of the dynamics of an airfoil elastically mounted on a swing arm evidenced the theoretical operating points leading to actual power take-off. An iterative CFD approach was then conducted to refine the conceptual parameters of the device, as shown in Figure 4. A laboratory demonstrator has been designed from these results, and is currently investigated.

3 Conclusion

From an unsteady potential formulation of the in-plane flow around a moving airfoil, a framework of applications has been build upon circulatory and non-circulatory contributions. This approach allows to consider canonical flows as well as complex wing kinematics with respect to a generalized angle of attack theoretically governing the release of vorticity. While successful applications to energy harvesting devices have first been carried out, further fundamental and applied studies may be be envisioned, based on desired flow kinematics or dynamics.

References

- [1] Gérard Couchet, Sur les mouvements plans, non stationnaires, à circulation constante. *Comptes rendus hebdomadaires des séances de l'Académie des Sciences*, June 11th, 1945
- [2] Henri Werlé, Les mouvements plans, non stationnaires, à circulation constante - Comparaison des résultats théoriques et expérimentaux. *La Recherche Aéronautique* 26, 1952
- [3] Gérard Couchet, Efforts d'un fluide incompressible sur un profil oscillant autour d'une incidence non nulle. *ONERA Publication*, 1959
- [4] Jagan M. R. Gorle, Ludovic Chatellier, Frederic Pons and Malick Ba, Operation of Darrieus turbines in constant circulation framework. *Physics of Fluids* 29:075103, 2017
- [5] Ludovic Chatellier, Jagan M. R. Gorle, Frederic Pons and Malick Ba, Experimental investigations of a controlled-circulation Darrieus turbine. *RENEW2018 - 3rd International Conference on Renewable Energies Offshore*, 2018
- [6] Sylvain Costa, Ludovic Chatellier, Frederic Pons and Malick Ba, Parametric Design of a Hydro-Elastic Energy Harvester. *RENEW2018 - 3rd International Conference on Renewable Energies Offshore*, 2018
- [7] Jagan M. R. Gorle, Ludovic Chatellier, Frederic Pons and Malick Ba, Modulated circulation control around the blades of a vertical axis hydrokinetic turbine for flow control and improved performance. *Renewable and Sustainable Energy Reviews* 105:363–377, 2019

Compressibility Effects on Pitch-Plunge Equivalence of Airfoils Under Dynamic Stall Induced by Ramp Motions

Renato Fuzaro Miotto* and William Wolf

School of Mechanical Engineering, University of Campinas, Campinas, SP, 13083-860, Brazil¹

*Correspondence: *miotto@fem.unicamp.br*

1 Introduction

Historically, the lack of experimental results for plunging airfoils entailed the usage of pitching data to predict plunging responses. The validity of the assumptions made to sustain such motion interchange was legitimately questioned by Carta [1] after noticing occasional discrepancies between them, particularly at high-load conditions. It was postulated that the pitch-plunge mismatch upon departure from small-amplitude linearizations was caused by the distinct dynamic stall breakdown process.

Constant rate pitching motion has been widely used to investigate the dynamic stall inception since it is known to suppress the additional complexity of periodic motion history effects [2, 3]. Under periodic motion, vortices that are being advected downstream with the flow interact with the trailing edge, leading to a change in the airfoil circulation and affecting the following stages of the flow dynamics. Moreover, from the perspective of high-fidelity numerical simulations of dynamic stall, computations are expensive due to the large computational grids and small time steps required to accurately capture the viscous processes developing near the airfoil surface. In this sense, ramp motions also reduce the computational costs associated with these simulations, when compared to periodical motions. Despite its advantages, as far as we know, constant ramp motions have never been used to investigate pitch-plunge equivalence. This is due to the fact that most studies in this context are devoted to predict plunging response based on tables of existing pitching data, which is predominantly dominated by periodically oscillating airfoils.

The purpose of this work is to address this issue, also bringing out the differences in phenomenology due to airfoil kinematics and Mach number variations that lie beyond the assumptions of previous work that considered incompressible potential flows [4, 5]. A natural step to facilitate progress in the understanding of pitch-plunge equivalence in this case is to simplify the airfoil kinematics into a constant-ramp configuration, where the motion-induced angle of attack of the equivalent plunging matches the geometric angle of attack of the pitching case. This equivalence allows the onset and

evolution of the DSV to be compared between pitch and plunge maneuvers starting from the exact same flow conditions in the perspective of numerical simulations.

2 Results

In this section, results from large eddy simulations are presented for an SD7003 airfoil under deep dynamic stall for both pitch and plunge ramp motions. Two freestream Mach numbers are employed to assess compressibility effects, being $M_\infty = 0.1$ and 0.4 , at a $Re = 6 \times 10^4$ chord-based Reynolds number flow. The O-type grid used in the simulations contains $480 \times 351 \times 32$ points and the spanwise length is set as $0.1c$, where c is the airfoil chord. Such computational domain setup is based on studies reported in the literature [6, 7], and is sufficient to properly capture the flow features associated with the onset of DSV.

The term *ramp* used throughout the text refers to the fact that the effective angle of attack α_{eff} is continually increasing, for example, as in a pitch-up movement with a fixed angular velocity. In the pitching ramp motion, the angular rotation rate is prescribed by the following equation

$$\dot{\alpha}_{eff}(t) = \Omega^+ [1 - \exp(-at)].$$

In a plunging airfoil, however, the motion requires the descent velocity to continuously increase following a tangent-like curve to match the geometric angle of attack of the pitching maneuver. For that, the descent velocity must be specified as

$$\dot{h}(t) = -\tan(\Omega^+ t) [1 - \exp(-at)],$$

where Ω^+ is the rate at which the effective angle of attack increases (say $\dot{\alpha}_{eff} = \Omega^+$), and a is a constant used for exponential smoothing set as $a = 9.2$ in the present calculations. The value of Ω^+ analyzed in this work is $\Omega^+ = 0.05$ and the parameters \dot{h} , Ω^+ and a are presented here nondimensionalized by the freestream velocity to follow other studies available in the literature. The airfoil static angle of attack is kept as $\alpha_0 = 8^\circ$.

Results are shown in Figs. 1 and 2 in terms of the aerodynamic loads and contours of pressure coefficient, respectively. The immediate observation from Fig. 1 is the similarity of the pitching and plunging aerodynamic coefficients

¹This work was supported by Fundação de Amparo à Pesquisa do Estado de São Paulo, FAPESP, under grants No. 2013/08293-7, 2017/10795-1, 2019/02335-6 and 2021/06448-0.

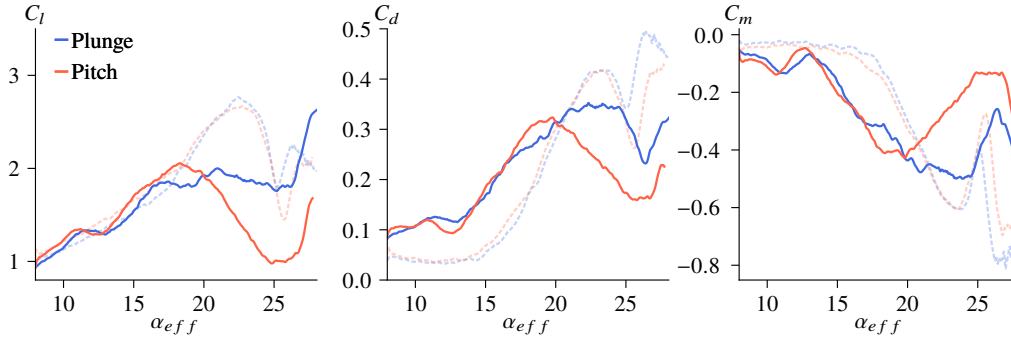


Figure 1: Pitch/plunge effects on lift, drag and moment coefficients for $M_\infty = 0.4$ (solid lines). Results for $M_\infty = 0.1$ are represented by the dashed semi-transparent lines.

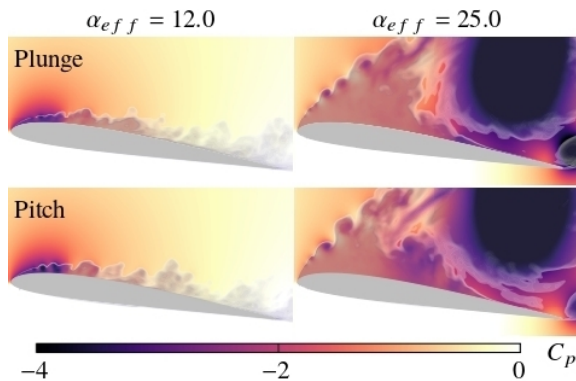


Figure 2: Pressure coefficient contours shaded by an entropy measure (superposed in gray scale) at different time instants for $M_\infty = 0.1$.

within the analyzed time window. For $M_\infty = 0.1$, both lift and drag continue to increase until reaching $\alpha_{eff} \approx 22.5^\circ$. At this point, a sudden drop occurs, indicating the detachment of the DSV. This drop is more pronounced for the pitch motion (red curve) while the trend is reversed for the moment coefficient. Soon after, a rapid recovery in lift and drag coefficients occurs around $\alpha_{eff} \approx 25^\circ$, which coincides with the formation of a low-pressure vortex at the trailing edge.

For $M_\infty = 0.4$, the pitch-plunge equivalence holds up to $\alpha_{eff} \approx 17^\circ$, beyond which the curves vary drastically between pitch and plunge. When compared to the $M_\infty = 0.1$ cases, it corresponds to a drop of 5° of effective angle of attack over which the equivalence remains valid. From Fig. 1, one can also see that the lift coefficients display a similar behavior for both $M_\infty = 0.1$ and 0.4 up to $\alpha_{eff} \approx 17^\circ$. However, the higher compressibility results in an increased drag and magnitude of pitching moment coefficients that starts from the beginning of the motion.

In the last column of Fig. 2, we observe the presence of the trailing-edge vortex growing further downstream the airfoil for the pitching case compared to the plunging one. As a consequence, in the plunging motion, the low pressure of the trailing-edge vortex encompasses a larger area over the airfoil suction side and its interaction with the DSV holds the

former closer to the airfoil surface. These facts explain the higher lift and drag coefficients observed at high effective angles of attack for the plunging motion compared to the pitching case.

3 Conclusion

Results show that the pitch-plunge equivalence holds until the formation of the trailing-edge vortex for all rates of motion and Mach numbers analyzed. In this sense, the way the trailing-edge vortex interacts with the DSV differs between pitch and plunge, causing the aerodynamic coefficients to mismatch. The birth and development of the DSV, in turn, is remarkably similar for the two types of motion, especially for low Mach numbers. Considerable topological changes occur in the flow fields when compressibility is varied, even before the airfoil initiates its motion. During the airfoil motion, the higher compressibility results in an overall increase of drag due to the more evenly distributed pressure forces over the airfoil chord. In addition, the residence time and strength of the DSV decrease with an increasing Mach number, the former being responsible for the earlier breakdown of pitch-plunge equivalence since the trailing-edge vortex begins to form at lower incidence angles.

References

- [1] F.O. Carta. *A Comparison of the Pitching and Plunging Response of an Oscillating Airfoil*. NASA contractor report. National Aeronautics and Space Administration, Scientific and Technical Information Branch, 1979.
- [2] Peter F. Lorber and Franklin O. Carta. Airfoil dynamic stall at constant pitch rate and high Reynolds number. *Journal of Aircraft*, 25(6):548–556, 1988.
- [3] S. I. Benton and M. R. Visbal. Understanding abrupt leading edge separation as a mechanism for the onset of dynamic stall. In *2018 AIAA Aerospace Sciences Meeting*, 2018.
- [4] G. Z. McGowan, K. Granlund, M. V. Ol, A. Gopalathnam, and J. R. Edwards. Investigations of lift-based pitch-plunge equivalence for airfoils at low Reynolds numbers. *AIAA Journal*, 49(7):1511–1524, 2011.
- [5] Yeon Sik Baik, Luis P. Bernal, Kenneth Granlund, and Michael V. Ol. Unsteady force generation and vortex dynamics of pitching and plunging aerofoils. *Journal of Fluid Mechanics*, 709:37–68, 2012.
- [6] M. R. Visbal. Numerical investigation of deep dynamic stall of a plunging airfoil. *AIAA Journal*, 49(10):2152–2170, 2011.
- [7] M. R. Visbal and D. J. Garmann. Analysis of dynamic stall on a pitching airfoil using high-fidelity large-eddy simulations. *AIAA Journal*, 56(1):46–63, 2018.

Do we need structural approaches to LES wall-models?

J. Leetch^{a,b,*}, A. Zurman-Nasution^{a,1}, G. Weymouth^{a,c} and B. Ganapathisubramani^a

^a Faculty of Engineering and Physical Sciences, University of Southampton, Southampton, UK

^b Institute of High Performance Computing, A*STAR, Singapore

^c Data-Centric Engineering, The Alan Turing Institute, London, UK

*Correspondence: jallg17@soton.ac.uk

1 Introduction

Successful implementations of wall modelled large eddy simulation (WMLES) for vortex-dominated flows involving complex or unsteady geometry and/or separating and turbulent flow are currently very limited. However, this prospective capability is identified as an important technological goal by [1], and would facilitate impactful changes in CFD-dependent industries such as transportation, marine/offshore and energy production by allowing truly general and therefore predictive CFD tools.

The limitations of current WMLES techniques are found in the use of specific empirical assumptions which do not necessarily extend well to general flow scenarios. Mainstream approaches [2] can be seen to use ideas based strongly upon the mean picture of a statistically steady flow whether by using the so-called log law or by employing solution of the steady RANS or boundary layer equation on the near-wall region. Schemes are also seen to provide boundary conditions to the external LES using velocity or derivative conditions along an interface, following from the presumption that the two zones should be essentially decoupled.

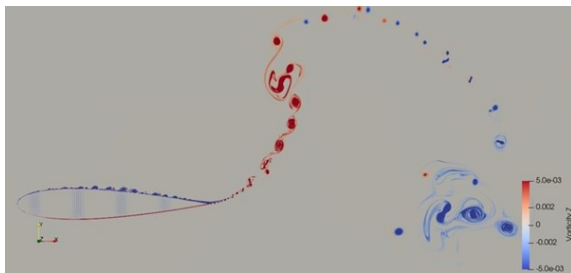


Figure 1: Instantaneous spanwise vorticity on a 2D flapping foil at Reynolds number of 1 million.

Through these approaches, the important correspondence between structure and statistics in turbulence is lost. In contrast, it is well known that turbulent vortices and instantaneous structures present in the boundary layer hold great significance for the behaviour of complex flows [3]. From recent results shown in Figure 1, it seems that this is yet

more important in complex, dynamic cases where vortex effects become more dominant and where unsteady separation is present. When solving mean wall-model equations, structural features of the inner layer are ignored, whilst in reality the physical behaviour is controlled by them in many flows such as that shown by Figure 1. This can explain, for example, why detached eddy simulation can struggle with basic separating flows even when compared to RANS models and is mainly seen to perform well on bluff body flows [4], where the wake inherits less of its structure from the preceding boundary layer turbulence, making the accurate modelling of this turbulence unimportant.

Because of this, there is strong motivation to be found for the development of WMLES techniques which feature:

- structural aspects of turbulence theory;
- strong coupling between inner and outer regions.

Furthermore, it is in keeping with the spirit of LES to faithfully consider the large, dominating structures of boundary layer turbulence. However, resolution of fine scales must be avoided for the wall model to fulfil its primary goal of reducing computational cost compared to a wall-resolved LES. Therefore, the exploitable phenomenon present in near-wall turbulence is the extreme intermittency of the statistics, which correspond to the existence of coherent structures/vortices. Since this is not capitalised on by static grid geometries and these structures are generally advected with the flow, it can be proposed that the appropriate perspective for a structural wall model is one which also incorporates an adaptive Lagrangian viewpoint. In fact, it has been shown that Lagrangian statistics are yet more intermittent [5], offering further potential for compression of the important spatio-temporal near-wall data.

However, it can be suggested that this path of approach is difficult to achieve for two reasons. Firstly, it is difficult to imagine that a simple mathematical model can be written down for this more complex conceptual standpoint. On the other extreme, it has been demonstrated that predicting correct, instantaneous near-wall modelling terms for turbulence using machine learning (ML) methods directly is not trivial

¹ Portions of this work were supported by the Defence Science and Technology Laboratory, UK

due to challenges faced in generalisation between different geometries [6].

Overall, it is suggested that an additional physical perspective embodied by a focus on the near-wall vortices is required in order to provide the ML algorithms with a set of inputs they can efficiently handle to provide accurate and general near-wall LES modelling. Work towards implementation of a new, dynamic wall modelling technique which considers the instantaneous, structural nature of turbulent flow and involves the use of ML techniques is the subject of the principal author's new PhD research project.

2 Results and future work

Recent DNS results obtained by members of this group can be used to confirm that current wall modelling approaches are practically unusable in complex flow cases. 2D simulation of a thrust-generating flapping foil at high Reynolds number shows phase-averaged, wall-normal velocity profiles (Figure 2) which are not at all in agreement with the log-law and show complex statistics and dynamic effects. Figure 1 shows a procession of strong vortices which are bound near the foil surface by the thrust generating motions before they are shed directly into the wake structure. It is clear that the body and vortex dynamics are responsible for the highly non-standard boundary layer development and phase-averaged velocity profiles presented in Figure 2 as well as the useful thrust production. These profiles do not fit with classic approaches based on empirical evidence, instead showing an extended laminar sublayer and flattened velocity profiles in regions typically expected to follow a log-law. These results demonstrate that there is certainly significant progress to be made before such complex flow cases may be handled routinely by LES methods.

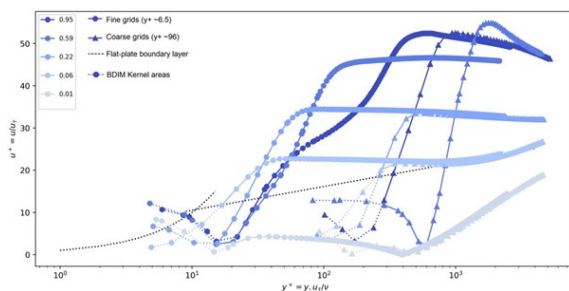


Figure 2: Phase-averaged velocity profiles at different chord locations on a 2D flapping foil at Reynolds number of 1 million.

Because coherent flow structures are known to be crucial in governing general near-wall turbulence physics [3], it is logical to attempt to introduce them to wall models by modelling their locations and characteristics, their dynamics, and their instantaneous effects on the resolved flow. Since direct and generalisable ML modelling of wake turbulence was clearly shown to be possible by [6], it can be observed that the ML model must struggle to differentiate between different flow

scenarios specifically in the presence of the wall.

It is hypothesised that this failure is due to an increased range of possibilities for the form of the unresolved flow in these situations, related to the diversity and irregularity of near-wall structures. [7] shows that low-order Eulerian statistics such as those used in [6] are in some contexts not sufficient to differentiate between extremely different flow cases. It is proposed that a similar principle is in effect here, where the cited theoretical observation gives weight to the proposal that mixed Eulerian-Lagrangian coordinates are of significance in efficiently capturing near-wall turbulence effects necessary for more advanced, future wall modelling.

The overall approach aims to place the emphasis on data efficiency by attempting to formulate an effective representation of the essential near-wall structural features. This will allow important non-equilibrium effects to be captured at the desired resolution so that models can be endowed with sufficient flexibility in their actions to deal with the vast array of possible states which the unresolved flow-field might take at any given instant. It is intended for numerical experiments to be carried out alongside theoretical work which will build on the efforts in [6], with particular focus on their near-wall modelling which was less successful. The aim is to provide novel models which are able to generalise between geometries even in the near-wall region; this would represent a significant advance in wall models for LES.

3 Conclusion

This project aims to argue that vortices are still dominant in a subject area which has traditionally neglected them in favour of Eulerian statistics. Methods which aim to use the physical structure of wall turbulence to their advantage for modelling the wall boundaries of a large eddy simulation are an exciting and novel area of research. It is hypothesised that a structural and Lagrangian perspective on the near-wall turbulence will be helpful for wall modelling by allowing ML models to properly identify the unknown flow behaviour and therefore to model its effects in a physical way. Having just begun, ongoing investigation is being made into this area, with strong potential for interesting preliminary results to be presented at DisCoVor.

References

- [1] J.P. Slotnick, et al. CFD Vision 2030 Study: A Path to Revolutionary Computational Aerodynamics. *Tech. Rep. NASA/CR-2014-218178*, pp. 1–51, The Boeing Company, 2014.
- [2] S.T. Bose, G.I. Park. Wall-Modeled Large-Eddy Simulation for Complex Turbulent Flows. *Annu. Rev. Fluid Mech.*, 50:535–561, 2018.
- [3] J. Jimenez. Near-wall turbulence. *Phys. Fluids*, 101302, 2013.
- [4] P.R. Spalart. Detached-eddy simulation. *Annu. Rev. Fluid Mech.*, 41(1):181–202, 2009.
- [5] R. Benzi, et al. Inertial range Eulerian and Lagrangian statistics from numerical simulations of isotropic turbulence. *J. Fluid Mech.*, 653:221–244, 2010.
- [6] B.Font, et al. Deep learning of the spanwise-averaged Navier–Stokes equations. *J. Comput. Phys.*, 434:110199, 2021.
- [7] R.H. Kraichnan. Kolmogorov's Hypotheses and Eulerian Turbulence Theory. *Phys. Fluids*, 7:1723–1734, 1964.

Vortex-Dominated Flows around Morphing Bodies

Alfonso Martínez^a and Kiran Ramesh^{a*}

^a Aerospace Sciences Division, University of Glasgow, G12 8QQ, Glasgow, United Kingdom¹

*Correspondence: *Kiran.Ramesh@glasgow.ac.uk*

1 Introduction

Unsteady production of vorticity is a unifying principle in biological locomotion. Natural fliers and swimmers continuously produce vorticity through the motion and shape-tailoring of their aerodynamic/hydrodynamic surfaces. Millions of years of evolution have endowed them with extraordinary capabilities to switch between regimes of attached and separated flow while holding excellent control authority. Modern engineering bio-inspired concepts, like micro aerial vehicles (MAVs) and autonomous underwater vehicles (AUVs), are designed to operate at similar high dimensionless rates of motion and low Reynolds numbers, and are prone to encounter external flow disturbances. Man-made small-scale devices aim to exploit fluid dynamics phenomena dominant in these regimes, dynamic stall for example, by mimicking the shape control ability of their natural counterparts.

Active and passive surface deformations can play a significant role in aero-/hydrodynamic performance. Trailing-edge flexion has been observed to affect leading-edge vortex characteristics on unsteady aerofoils. Despite the potential of this technique in modulating vortex-shedding behaviour, a more thorough understanding of the correlation between trailing-edge deformation and vortex dynamics could be gained through theoretical analysis. The acquired knowledge could then be utilised to devise flow control strategies based on camber variation to enhance biologically-inspired locomotion.

Current low-order models (LOMs) for unsteady flows are capable of accurately capturing the formation of vortical structures [1], providing valuable analytical insight on the post-stall flowfield. However, these simplified representations of a fluid problem rarely consider time-varying surface deformations. The dearth of such models motivates the development of a low-order model to simulate the flow response to bodies undergoing arbitrary camber variations in time. This is the main goal of the work here presented.

2 Results

Unsteady thin-aerofoil theory is extended to include the effect of temporal variations in camber. And it is combined with a discrete-vortex method empirically augmented for

viscous events, such as leading-edge vorticity shedding. The result is a low-computational cost, physics-based tool, capable of modelling unsteady flows past deforming bodies in the order of seconds in a personal laptop.

Computational fluid dynamics (CFD) simulations are performed to validate the low-order model under different flow regimes: fully attached flow, and deep dynamic stall. Examples of both scenarios are depicted in figure 1, where the spatial distribution of vortex particles from the LOM overlaps the vorticity contour extracted from CFD. Critical unsteady flow features, like large vortical structures shed into the wake from both edges, are captured with accuracy by this numerical model.

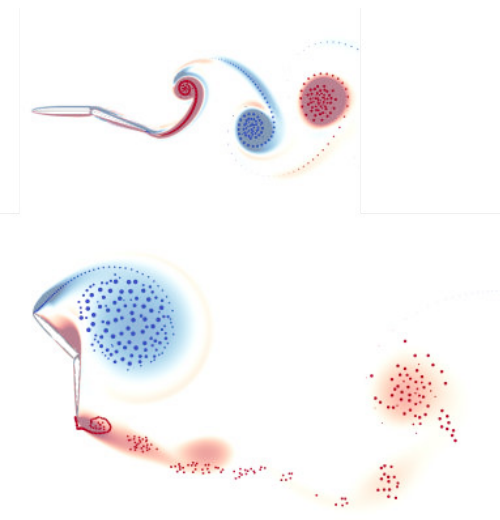


Figure 1: Flowfield comparison between LOM and CFD. Reverse Kármán vortex street (upper) and dynamic-stall vortex (lower) as representative examples of aquatic locomotion and flapping-wing flight.

The most basic representation of chordwise deformation is the flapped flat plate, this is, a rigid plate (the control surface) hinged at a specific point to another rigid plate (the main body). This mechanism, despite its simplicity, serves to set the basis of morphing modelling with discrete-vortex methods. And the extension to more complex deforming patterns is an ongoing research within this project. The very nature of the low-order model allows for a broad spectrum of shape-varying parameters to be analysed, including the length of the control surface, the amplitude, and the reduced

¹This work was supported by EPSRC through a DTA scholarship, grant EP/R513222/1

rate of deformation. This study can help us to better understand the connection between prescribed flexion at the trailing edge and alteration of leading-edge properties from a theoretical perspective.

Large amplitude deformations are observed in the performance of many natural species, in both water and air, with the associated benefits this can pose in flow control. Since thin-aerofoil theory was originally conceived for small flow disturbances, a new variant is presented here to extend its range of applicability. Contrary to a classical approach of transferring the zero normal flow boundary condition from the camberline to a fixed chordline, a time-varying chordline is considered in this work. Results from both approaches are compared against each other, and improvements in terms of aerodynamic loads are evinced with the new formulation, specially for cases where large deflections of the control surface are performed.

3 Conclusion

The long term goal of this project is to characterise vortex dynamics in response to shape-varying foils, and to exploit unsteady flow control capabilities based on this concept:

1. Mathematical relations between morphing-defining parameters (maximum camber and its chordwise position) and resultant flow behaviour are derived.
2. A low-order model to simulate unsteady flows past deforming foils is developed and used to explore the capacity of chordwise deformation in altering vortical structures characteristics (strength, convection speed).

References

- [1] Martínez, et al. Modulation of the Leading-Edge Vortex Shedding Rate in Discrete-Vortex Methods. *AIAA SciTech forum*, 2022.

Classifying Kinematics and Vortex Wake Structures of Oscillating Foils using Machine Learning

Bernardo Luiz R. Ribeiro* and Jennifer A. Franck

University of Wisconsin—Madison, Department of Engineering Physics, Madison, USA ¹

*Correspondence: rocharibeiro@wisc.edu

1 Introduction

This research develops a machine learning algorithm to classify vortex wake structures behind an oscillating foil. Although commonly used in propulsive applications, oscillating foils can also extract energy from the flow in a similar manner as a rotational turbine [1, 2]. Due to the coherent alternating signed vortex wake generated from oscillating foils there is a strong potential for cooperative motion within tightly packed array configurations. In order to design the control laws for foil-array performance optimization, it is important to fully understand and model the vortex wake structure as a function of flow conditions and foil kinematics. A sample oscillating foil wake is illustrated in Figure 1 for a given foil's reduced frequency (fc/U_∞), heave amplitude (h_o) and pitch amplitude (θ_o).

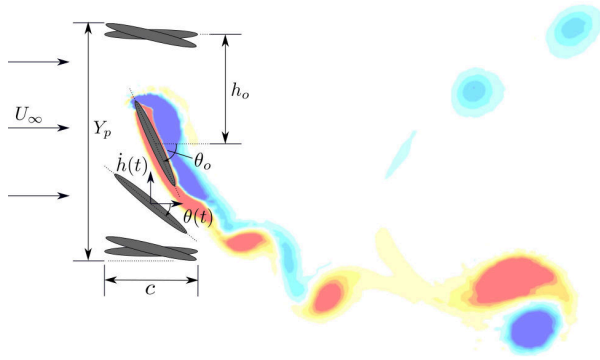


Figure 1: Foil kinematics: pitch amplitude (θ_o), heave amplitude (h_o) and foil's swept area (Y_p) shown. Spanwise vorticity for the kinematics $fc/U_\infty = 0.10$; $h_o = 1.00$; $\theta_o = 75^\circ$ is displayed as an example of the oscillating foil wake.

To assist in the wake modeling of oscillating foils, various machine learning techniques can be utilized. Particularly, convolutional neural networks (CNN) are commonly used on extracting patterns and predicting flow fields from images [3]. When analyzing unsteady flows like what is found in the wake of oscillating foils, the time evolution of structures can be captured with recurrent neural networks or the long short-term memory (LSTM) method [4], which can predict flow quantities by holding information from an input sequence,

¹This work was supported by the National Science Foundation under Grant No. 1921594.

and not simply from the current input to the neural network [5].

Through the combination of neural networks and LSTM, a machine learning model is developed towards classification of the bluff body wake structures behind oscillating foils. Classification models have been implemented for wakes of propulsive foils [6], which have extracted data from point-measurements or from the foil's kinematics. In contrast, this research classifies vortex wake structures through the use of convolutional layers and LSTM units solely based on images of vorticity flow fields, and correlates the resulting classes with oscillating foil kinematics and energy harvesting efficiency. Thus, by understanding how the kinematics are associated with wake structure, foil performance predictive models can be constructed.

2 Methods

2.1 Supervised Classification

The classification or supervised model is comprised by 2D spanwise vorticity fields extracted from a frame in the wake and interpolated onto a cartesian grid as displayed in Figure 2. The wake window is chosen such that it contains all vortices shed from the foil in all simulated kinematics.

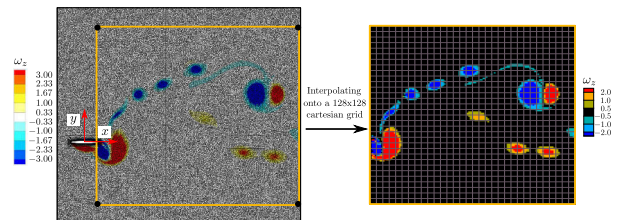


Figure 2: Data pre-processing for the classification model. A subset of the mesh and the wake window selected for the input data are displayed in the left figure. The interpolated spanwise vorticity field onto a 128×128 cartesian grid is displayed in the right figure.

The model is built from a combination of five convolutional layers, 90 LSTM units and two dense layers. The input data contains 23,692 samples arranged in blocks of five consecutive time steps and the output is designated to each class of images.

To validate the model and prepare the training and test data,

a five-fold stratified cross-validation is utilized since this technique is also commonly used to avoid overfitting [7].

2.2 CFD

A total of 46 unique kinematics are prescribed to an elliptical foil through numerical simulations, with each foil parameter, namely, reduced frequency, fc/U_∞ , heave amplitude, h_o , pitch amplitude, θ_o , having values within the energy harvesting regime. A sinusoidal foil motion in pitch and heave is utilized for each kinematics.

During foil motion, heave and pitch are changing simultaneously, which creates a time-varying relative angle of attack with respect to the freestream flow (U_∞) given by

$$\alpha_{rel}(t) = \tan^{-1}(-\dot{h}(t)/U_\infty) + \theta(t), \quad (1)$$

where $\dot{h}(t)$ is the heave velocity. A characteristic relative angle of attack is evaluated when the foil reaches the mid-stroke, which is equivalent to the foil's position of maximum pitch and maximum heave velocity, and occurs at one quarter of the cycle period T , or

$$\alpha_{T/4} = \alpha_{rel}(t = 0.25T). \quad (2)$$

3 Results

The $\alpha_{T/4}$ parameter collapses the kinematics into one characteristic parameter. The classification model discerns four classes, based on $\alpha_{T/4}$, which reveal the vortex wake patterns outlined in Figure 3.

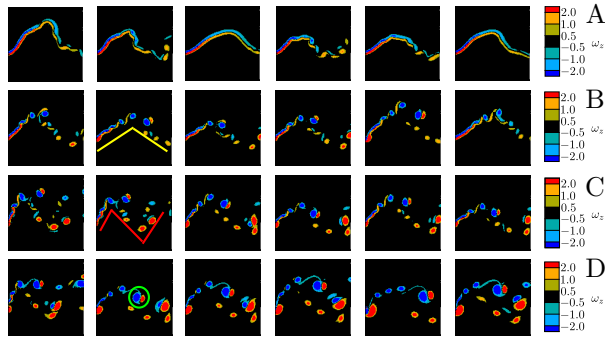


Figure 3: Wake structures colored by spanwise vorticity (ω_z) for each class obtained through the algorithm. Each square image represents a different foil kinematics and the yellow, red lines and green circle correspond to each wake pattern.

Each row in Figure 3 highlights different wake images colored by spanwise vorticity fields from a sample of kinematics within each class. Class ‘A’ contains foil kinematics represented by an $\alpha_{T/4}$ range of $0.09 \leq \alpha_{T/4} \leq 0.20$. Within this class, the foil generates a shear layer wake pattern as noticed by the absence of coherent vortices in the wake. This wake pattern is found when the foil has a high

reduced frequency ($fc/U_\infty = 0.15$) and low pitch amplitudes ($\theta_o < 55^\circ$), which often translates to poor foil performance for energy harvesting. Classes ‘B’ ($0.20 < \alpha_{T/4} < 0.40$) and ‘C’ ($0.40 \leq \alpha_{T/4} \leq 0.51$) contain stronger and more coherent vortices, that are obtained when foils are oscillating at higher pitch amplitudes and low reduced frequencies. However, the wake path is considerably different between the classes, with ‘B’ showing a longer wavelength within the selected wake window compared to ‘C’ (see yellow and red lines). In contrast, class ‘D’ ($0.51 < \alpha_{T/4} \leq 0.88$) holds the kinematics in which the foil generates the largest number and strongest coherent vortices compared with the other classes as highlighted by the presence of a strong leading edge vortex in the majority of wake images (the green circle). In addition, the wake path is significantly different to those from classes ‘B’ and ‘C’ due to the unsteadiness induced by the vortices and the interaction with one another.

4 Conclusion

A machine learning model is developed to classify wake structures behind an oscillating foil in the energy harvesting regime of kinematics using only the vorticity fields downstream of the oscillating foil. This model gives insight on wake similarity among various foil kinematics, which is important to build predictive models of oscillating foil arrays for energy harvesting.

References

- [1] Young, J., et al. A review of progress and challenges in flapping foil power generation. *Progress in Aerospace Sciences*, 67:2–28, 2014.
- [2] Xiao, Q. and Zhu, Q. A review on flow energy harvesters based on flapping foils. *Journal of Fluids and Structures*, 46:174–191, 2014.
- [3] Brunton, S. L., et al. Machine Learning for Fluid Mechanics. *Annual Review of Fluid Mechanics*, 52(1):477-508, 2020.
- [4] Hochreiter, S. and Schmidhuber, J. Long Short-Term Memory. *Neural Computation*, 9(8):1735–1780, 1997.
- [5] Han, R., et al. A novel spatial-temporal prediction method for unsteady wake flows based on hybrid deep neural network. *Physics of Fluids*, 31(12):127101, 2019.
- [6] Colvert, B., et al. Classifying vortex wakes using neural networks. *Bioinspiration & Biomimetics*, 13(2):025003, 2018.
- [7] Brunton, S. L. and Kutz, J. N. Data-Driven Science and Engineering: Machine Learning, Dynamical Systems, and Control. *Cambridge University Press*, 2019.

Topological data analysis of pitching and heaving wakes

William Roslansky, Justin T. King,^a Marko Budišić,^{b*} and Melissa A. Green^a

^a University of Minnesota, Aerospace Engineering and Mechanics, Minneapolis, MN, USA¹

^b Clarkson University, Mathematics, Potsdam, NY, USA

*Correspondence: *magreen@umn.edu*

1 Introduction

There are very few, if any, products of human design that effectively replicate the fast movement, large thrust, and highly efficient swimming associated with fish and aquatic mammals. Despite this, many engineers still seek to incorporate bio-inspired designs into their vehicles. Animal swimming modes can be placed along a spectrum ranging from purely undulatory modes to purely oscillatory modes. Two of these modes are of primary importance, the carangiform and the thunniform modes, which are associated with fast and efficient swimming [1]. In carangiform and thunniform swimmers, the anterior region is typically held rigid while the posterior region moves with significant heave, or lateral oscillations, in combination with pitching oscillations. Prior work within our research group has focused on the wake dynamics and propulsive performance of an isolated, purely pitching propulsor with bio-inspired platform. The current work aims to build upon prior results and explore how the introduction of heave to a pitching propulsor impacts the behaviors of wake vortices.

This work will incorporate topological data analysis (TDA) to identify and track important features and patterns of the vortex patterns created by the combined propulsor motion. Vortex wakes and coherent vortex interactions have been well studied since the vortex behavior are highly relevant with the flow dynamics such as lift, drag or propulsion [2]. In order to identify the vortical structure and investigate the dynamics of turbulent flow, various techniques including both experimental and numerical methods have been introduced to this field. For instance, the Q-criterion, developed by Hunt [3], is a commonly used Eulerian method to identify vortices. It evaluates the balance between shear strain rate and vorticity magnitude based on the Eulerian velocity field, and defines vortices as regions where vorticity is dominated over the rate of strain. The Finite-time Lyapunov exponent (FTLE), proposed and developed by Haller [4] and Shadden [5], is a commonly used Lagrangian technique that reveal the vortices boundaries by calculating quantities based on the behavior of fluid particle trajectories.

Topological data analysis (TDA) as a collection of statistical data analysis methods [6], has been widely applied to different fields considering its high capacity for detecting connections and illuminating structure in high-dimensional data sets. TDA analyzes complex high-dimensional data

by converting local information about data, e.g., pairwise distances between data points, into characterization of the global structure, in a multi-scale fashion. Since TDA relies only on an abstract definition of *distance* between points in the data set, it can efficaciously handle high-dimensional data sets, including phase space trajectories of dynamical systems, without the need for the dimension reduction as a preprocessing step, therefore avoiding the potential loss of valuable information from original data [7]. In this work, we will apply methods of TDA to the vortex wakes generated by pitching and heaving flat plates as models of bio-inspired (fish and cetacean swimming) propulsion.

2 Methods

2.1 Discrete Vortex Method

The two-dimensional discrete vortex method (DVM) was applied to an infinitely thin plate [8] as a model of the hydrodynamics of an unsteady flapping foil. This model is based on potential flow theory, and therefore assumes the flow to be inviscid, irrotational, and incompressible. We evaluated the forces experienced by the thin plate by using the vortex impulse method [9], which provides a comprehensive framework to analyze vortex-dominated flows.

2.2 Experimental apparatus

Eulerian vorticity fields were also calculated from velocity vector fields acquired using stereoscopic particle image velocimetry (SPIV) in the flow around a pitching and heaving trapezoidal and rectangular plates at a Strouhal number $St = fA/U = 0.3$, where f is the oscillation frequency, A is the length scale of the oscillation amplitude, and U is the outer flow freestream velocity. It has been documented in the literature that most animals swimming and flying occurs when the relevant appendages (wings, fins) oscillate with a frequency that corresponds to a Strouhal number range of $0.2 < St < 0.4$ [10, 11].

A rack and pinion based apparatus that was previously constructed at Syracuse University is used in a recirculating water tunnel at the University of Minnesota. Two DC motors are mounted on a rack assembly that is free to move laterally on a guide rail. The output shaft of the heaving motor directly engages with the pinion allowing for linear heaving of the entire assembly. A pitching shaft with attached panel is controlled by a pitching motor, allowing for independent

actuation of pitching and heaving motions.

3 Results

Previous DVM results, shown in Figure 1, showed that the point vortex distribution and organization are similar for a purely pitching plate vs. a purely heaving plate with the same Strouhal number (St), when synchronized by the trailing edge excursion. Despite that, the time-resolved thrust signals are different. DVM thrust calculation is necessarily decomposed into circulatory and non-circulatory (added mass) contributions, and it is clear that the pitching plate total thrust (black line) is dominated by non-circulatory contributions (red dashed line), while heaving plate total thrust (black line) is dominated by circulatory contributions (particularly the bound circulation, pink dotted line). These observations are not novel and have been part of the basis for time-averaged thrust scaling arguments [12].

FTLE analysis of these DVM results shows, in a time-resolved sense, how the timing of thrust production via circulatory or non-circulatory force is related to the acceleration of fluid around the panel trailing edge. When this accelerating fluid is fed into the growth of the trailing edge vortex (TEV), the heaving thrust increases but the pitching thrust decreases. When fluid is accelerated between two TEVs, pitching thrust increases but heaving thrust decreases. In Figure 1, a snapshot is shown at maximum pitching thrust and near-minimum heaving thrust. It is clear near the trailing edge that before the roll-up of a new TEV, the fluid had been accelerating between the previous TEV and the new one about to form. This is consistent with the result that pitching thrust had been increasing until this moment, and will now start to decrease. It is also consistent with heaving thrust starting to increase from this moment on.

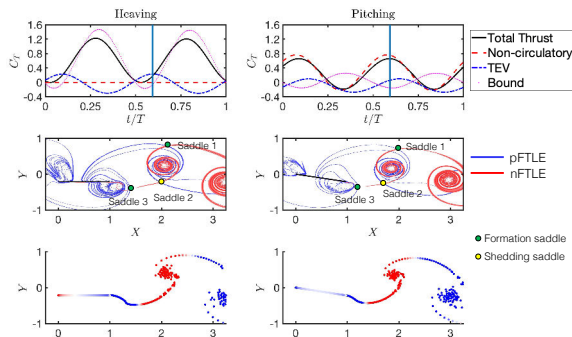


Figure 1: Thrust, FTLE, and point vortex distribution of flat plate DVM simulation pitching and heaving with $St = 0.3$.

Figure 2 (top) shows a representative snapshot of the the pitching plate DVM wake with an overlay of topological features detected via persistent homology. Analyzing the persistent homology of sublevel and superlevel sets of the stream function, represented using the persistence on a cubical complex, the algorithm identifies the vortex core centers (black dots), and the vortex boundaries (green lines) as representatives of the zeroth and first homology groups. The

topological loops are sensitive to complex cut-off, similar to Eulerian vortex identification criteria.

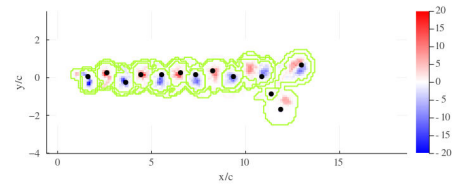


Figure 2: DVM snapshot of a purely pitching plate with $St = 0.3$ with representatives of the zeroth and first homology groups of the stream function approximating vortex core centers (black dots), and vortex boundaries (green lines).

Experimental data collection is ongoing, and will include purely pitching, purely heaving, and a combined heave-and-pitch motion of a series of rigid panel with rectangular and trapezoidal geometries. We will compare the vortex wake organization of each to determine if the same wake distributions develop at the midspan in the viscous 3D experiments, and use the cubical complex algorithm to identify the features of the vortex wakes.

These results will form the foundation for future work to model and predict the vortex generation (and correlated forces) for a range of bio-inspired panels for which we know thrust contribution may be the result of different physical mechanisms (circulatory vs. non-circulatory).

References

- [1] Michael Sfakiotakis, David M. Lane, and J. Bruce C. Davies. Review of fish swimming modes for aquatic locomotion. *IEEE Journal of oceanic engineering*, 24(2):237–252, 1999.
- [2] Firas F. Siala and James A. Liburdy. Leading-edge vortex dynamics and impulse-based lift force analysis of oscillating airfoils. *Experiments in Fluids*, 60(10):157, September 2019.
- [3] J.C.R. Hunt, A.A. Wray, and P. Moin. Eddies, streams, and convergence zones in turbulent flows. *Studying Turbulence Using Numerical Simulation Databases*, (N89-24555):193–208, 1988.
- [4] George Haller. Lagrangian coherent structures from approximate velocity data. *Physics of Fluids*, 14(6):1851–1861, 2002.
- [5] Shawn C Shadden, Francois Lekien, and Jerrold E Marsden. Definition and properties of Lagrangian coherent structures from finite-time Lyapunov exponents in two-dimensional aperiodic flows. *Physica D. Non-linear Phenomena*, 212(3-4):271–304, 2005.
- [6] Larry Wasserman. Topological Data Analysis. *Annual Review of Statistics and Its Application*, 5(1):501–532, March 2018.
- [7] Václav Snášel, Jana Nowaková, Fatos Xhafa, and Leonard Barolli. Geometrical and topological approaches to Big Data. *Future Generation Computer Systems*, 67:286–296, February 2017.
- [8] Joseph Katz and Allen Plotkin. *Low-Speed Aerodynamics*, volume 13. Cambridge university press, 2001.
- [9] Philip G Saffman. *Vortex Dynamics*. Cambridge university press, 1992.
- [10] Graham K. Taylor, Robert L. Nudds, and Adrian L. R. Thomas. Flying and swimming animals cruise at a strouhal number tuned for high power efficiency. *Nature*, 425:707–711, October 2003.
- [11] G.S. Triantafyllou, M.S. Triantafyllou, and M.A. Grosenbaugh. Optimal thrust development in oscillating foils with application to fish propulsion. *Journal of Fluids and Structures*, 7:205–224, 1993.
- [12] Fatma Ayancik, Qiang Zhong, Daniel B Quinn, Aaron Brandes, Hilary Bart-Smith, and Keith W Moored. Scaling laws for the propulsive performance of three-dimensional pitching propulsors. *Journal of Fluid Mechanics*, 871:1117–1138, 2019.

Vortex interactions in the wake of the axisymmetric elongated body at high angle of attack

Kourosh Shoele^{a*} and Al Shahriar^a

^a FAMU-FSU College of Engineering, Mechanical Engineering, Tallahassee, USA¹

*Correspondence: *kshoele@eng.famu.fsu.edu*

1 Introduction

At high angles of attack, axisymmetric bodies frequently exhibit asymmetric flow responses. The flow asymmetry around slender bodies is well-documented, discovered in the early 1950s. The asymmetric vortices frequently switch positions, causing unpredictable side forces and yawing moments on the body, a common maneuvering scenario for any slender body. Minor defects in the forebody can trigger flow instabilities at much smaller angles of attack, potentially leading to the development of vortex asymmetry [1–3]. The extent of the asymmetry in the vortices is determined by the size of the imperfection [3–5]. Still, limited information is available about the unsteady vortex dynamics behind a cone at different angles of attack. Moreover, there is no physical explanation of why the cone at higher angles of attack forms asymmetric vortex fields. The cone is a special self-similar canonical geometry with no unique geometrical feature that can be used as a definite length scale. The thickness of the boundary layer is influenced by geometrical changes and the intrinsic length scale of the cone cross-section perpendicular to the flow direction. Using a fully resolved CFD model, we extend our prior work [6] to investigate the effect of angle of attack on flow asymmetry and the coherent flow structures over elongated models. In addition, we plan to investigate the aerodynamics of the asymmetric vortex field by partitioning the pressure force on the surface [7]. The primary goal is to identify potential characteristic parameters incorporating geometrical effects and flow dynamics. Potential metrics can be used to predict the transition location and aerodynamics of the post-transition coherent flow structures.

2 Results

The unsteady incompressible Navier-Stokes equations are solved using a curvilinear staggered grid flow solver [8] where a second-order fractional step method and central difference method are employed for the discretization. The momentum equations are solved by a matrix-free Newton–Krylov solver, and the Poisson equation is solved using an iterative solver with a multigrid preconditioner. The surface of an axisymmetric body is represented with triangular

¹This work was jointly supported by Defense Advanced Research Projects Agency under grant number of D19AP00035 and Army Research Office under grant number of W911NF1810462.

meshes and a sharp interface immersed boundary method is used to impose wall boundary conditions in the flow simulation. The values are interpolated on immersed boundary nodes in the fluid-domain at the local normal to the boundary [9]. Numerical simulations were conducted for the cross-flow over a cone at the angle of attack of 0°, 15°, 30°, 45°, 60°, 75° and 90°. At AoA = 0°, the flow is completely steady at this Reynolds number. Again, at AoA = 90°, the flow features are very chaotic, not showing any gradual development of the flow, as shown in Fig. 1(f). Hence, these two cases are outside the scope of this study.

The wake behind a cone at higher angles of attack can be divided into three main regions in terms of their behaviors over a long time, as shown in Fig. 1: steady (primary and secondary vorticity only), intermediate (which includes primary, secondary, and helical vortices), and an unsteady region (small-scale irregular vortical structures and the secondary vorticity). The primary vortex, shear layer and secondary vorticity (fish-hook shape) can be easily identified in the contour slices of Fig. 1. Another relatively small-scale vortices in the shape of a helix appear around the primary vortex. These vortices can be identified in the isosurface of the Q-criterion in the intermediate region. For flow over a cylinder, the three-dimensional reconfiguration of these small vortices accounts for the irregular shape of the primary vortex and the laminar to turbulence transition in the wake [10]. This connection is weakened for the flow over a cone due to the geometrical change of the cone along the axis. At a farther distance from the tip, the flow becomes unsteady and the large coherent structure of the primary vortex breaks into small-scale rotational elements. Even though the primary vortex loses its strength along the cone’s axis, the secondary vortex remains strong but is gradually pushed toward the surface as the primary vortex intensifies.

At higher angles of attack, the core vortex structure breaks earlier due to the higher adverse pressure gradient in the wake as the flow develops more in the circumferential direction. At a low angle of attack of 15° and 30°, the wake is only associated with a primary vortex and a secondary vortex. No helical vortices were observed for these cases. While AoA = 45.0° and 60.0° have similar flow features, the case of AoA = 75°, shows a faster breakup of the primary vortex. The AoA = 90.0° case, on the other hand, shows entirely different behavior, and the wake is now mimicking

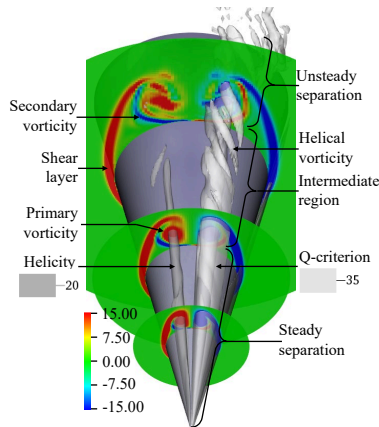


Figure 1: Iso-surface of the helicity (gray) and Q-criterion (silver) of the instantaneous flow field for $\text{AoA} = 45^\circ$. Contour slices showing the z -component of instantaneous vorticity at $z/D = 0.5, 1.25, 2.0$.

the flow behind a bluff body. At such a high angle of attack, there is no coherent steady primary vortex anymore and the flow becomes turbulent almost at the place where the Reynolds number based on the projected shape exceeds the transition limit Fig. 2.

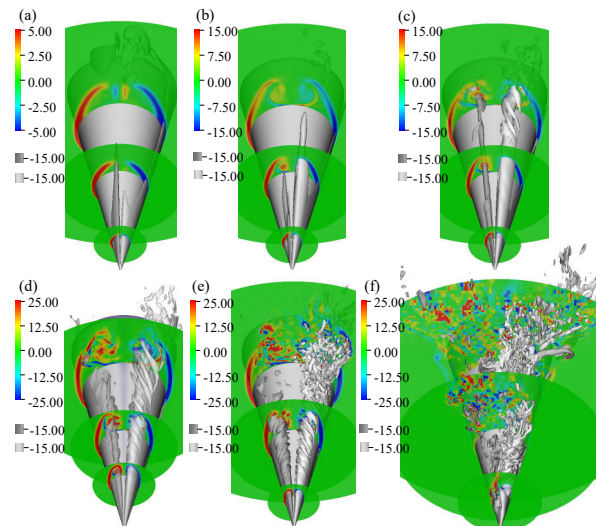


Figure 2: Iso-surface of the helicity (gray) and q -criterion (silver) of the instantaneous flow field for $\text{AoA} =$ (a) 15° , (b) 30° , (c) 45° , (d) 60° , (e) 75° and (f) 90° . Contour slices of the z -component of the vorticity at $z/D = 0.5, 1.25, 2.0$.

As expected, the total drag acting on the body increases as the angle of attack increases. Nevertheless, the lift drops after a certain angle of attack. The side force is almost zero for the low angle of attack but starts to appear as the angle of attack increases.

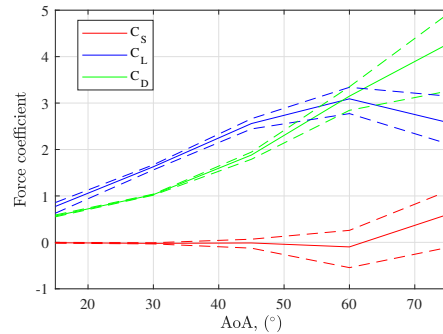


Figure 3: Time average side force, drag and lift for different angle of attack. Dotted line shows the limit in which the coefficient fluctuate over the time.

3 Conclusion

The wake of axisymmetric objects like the cone consists of two main vorticity fields: primary and secondary. Helical vortices occasionally appear, encircling the primary vortex. The secondary vorticity undergoes a substantial three-dimensional transformation along the cone axis, playing a critical role in determining the changes of the primary vortex along the cone axis. The angle of attack has a significant impact on the cross-flow characteristics. The core of the primary vortex breaks into small-scale vortical structures at a very high angle of attack, and the flow becomes asymmetric similar to the flow over a bluff body. The pick lift force is observed at $\text{AoA} \approx 60^\circ$ asymmetric forces result from an asymmetric vortex structure in the lee of the body.

References

- [1] B Hunt. Asymmetric vortex forces and wakes on slender bodies. In *9th atmospheric flight mechanics conference*, page 1336.
- [2] Rajan Kumar, PR Viswanath, and ON Ramesh. Nose bluntness for side-force control on circular cones at high incidence. *Journal of aircraft*, 42(5):1133–1141, 2005.
- [3] David Degani and Murray Tobak. Experimental study of controlled tip disturbance effect on flow asymmetry. *Physics of Fluids A: Fluid Dynamics*, 4(12):2825–2832, 1992.
- [4] Cary Moskovitz, Fred Dejarnette, and Robert Hall. Effects of surface perturbations on the asymmetric vortex flow over a slender body. In *26th Aerospace Sciences Meeting*, page 483.
- [5] Bao-Feng Ma, Yu Huang, and Xue-Ying Deng. Dynamic responses of asymmetric vortices over slender bodies to a rotating tip perturbation. *Experiments in Fluids*, 57(4):54, 2016.
- [6] Al Shahriar and Kourosh Shoele. Vortex interactions in the wake of the axisymmetric body in uniform cross-stream. In *AIAA Scitech 2021 Forum*, page 0026, 2021.
- [7] Vahid Tavanashad and Kourosh Shoele. Analysis of shock-wave boundary layer interaction in compressible flows over rigid and flexible surfaces. In *AIAA AVIATION 2021 FORUM*, page 2807, 2021.
- [8] Liang Ge and Fotis Sotiropoulos. A numerical method for solving the 3d unsteady incompressible navier–stokes equations in curvilinear domains with complex immersed boundaries. *Journal of computational physics*, 225(2):1782–1809, 2007.
- [9] Anvar Gilmanov and Fotis Sotiropoulos. A hybrid cartesian/immersed boundary method for simulating flows with 3d, geometrically complex, moving bodies. *Journal of computational physics*, 207(2):457–492, 2005.
- [10] Tao Wei and CR Smith. Secondary vortices in the wake of circular cylinders. *Journal of Fluid Mechanics*, 169:513–533, 1986.

Bistable Response of Inverted Flags with Moderate Aspect Ratios

Oluwafemi Ojo^a and Kourosh Shoele^a

^a FAMU-FSU College of Engineering, Mechanical Engineering, Tallahassee, USA¹

*Correspondence: kshoele@eng.famu.fsu.edu

1 Introduction

The flow structure interaction of flexible bodies is a naturally occurring phenomenon; some common examples are flapping leaves in the wind and animals swimming or flying using their wings. The flapping motion of a flexible structure has many applications, such as heat transfer and energy harvesting. Recently the inverted flag with the free leading edge and the fixed trailing edge has drawn much attention due to its lower critical flapping velocity. The inverted flag problem was first studied experimentally by [1]. They identified three dominant response modes of the structure due to its interaction with the flow: namely a stationary mode- at low flow velocities, a two-sided flapping mode at intermediate flow velocities, and the deflected mode at high flow velocities [1]. Later other modes were identified at the transition point between these three response modes. These modes emerge from the balance between vortex-generated forces and the elastic restoring force in the flag, resulting in self-sustained vibrations at relatively low flow speeds. The inverted flag has better wind energy harvesting due to its lower critical flow velocity and large amplitude vibration compared to the regular flag configuration [2]. It is known now that the maximum energy can be achieved at flow velocities near the transition point from the stationary to flapping modes. However, the dynamic response of the flag at this condition is affected by the flag's bistability behavior. Therefore, it is important to quantify their bistable response to reach a better energy production from the inverted flags.

Both regular and inverted flag configurations can undergo different bifurcation paths during the increase and decrease of the flow velocity, hereafter called upsweep and downsweep conditions, respectively. This mismatch in the critical velocities results in the appearance of the hysteresis loop. In regular flags [3], it is shown that during the downsweep, below the critical flapping velocity, the hysteresis loop decreases from wide to narrow flags to the extent that no hysteresis occurs for $AR < 1$. Instead, the inverted flag exhibits hysteresis over a wide range of parameters. It is still unknown why the hysteresis loop always exists in inverted flags across different AR s and what is the role of leading and side edges vortices on the flag bistability. This study explores the numerical investigation of a inverted flag's bistable vibration for a wide range of AR s ($AR = 0.25 - 2$), and the interconnection between the hysteresis behavior and the flow field.

The structural dynamics of the inverted flag is governed by the force-balanced momentum equation while the governing equation for the fluid flow is the Navier-Stokes momentum and continuity equations for incompressible fluids.

$U^* = UL\sqrt{\frac{\rho L}{\kappa_b}}$ and $M^* = \frac{\rho L}{m_s} = 0.2$ are nondimensional parameters which quantify the importance of flexibility and inertia of the inverted flag, respectively, where ρ is the density of the fluid, U is the flow velocity, L is the length of the flag, m_s is excessive mass of the flag per unit area, and κ_b is the flexural rigidity.

The role of vortical structures are identified using the modal force partitioning approach. In this approach the aerodynamic pressure force are projected on the dominant rotational mode shapes of the flag defined as, $\Theta(s_1, s_2, t) = \sum_{i=1}^M \Psi_i(s_1, s_2) q_i(t)$, where $q_i(t)$ is the time-dependent generalized coordinate of mode i , $\Psi_i(s)$ is the corresponding angular mode shape and Θ is the steamwise angle of the flag. The dynamic of the flag can be written using modal approximation as a nonlinear modal angular equation of motion [4],

$$\ddot{q}(t) + \int_S \Psi(s) \frac{\sin(\Theta(s, t))}{\cos(\Theta(s, t))} I(s, t) ds \quad (1)$$

$$- \left(\int_S \Psi(s) \Psi''^T(s) ds \right) q(t) + f_F = 0,$$

where $I(s, t)$ is the nonlinear inertia force presented in and f_F is the modal external force from the aerodynamic pressure. An auxiliary time-varying function ϕ^i is then formed for mode i . To enforce the solenoidal condition of the flow velocity, the auxiliary function should satisfy $\nabla^2 \phi^i = 0$ in the body of the fluid and it is equipped with a proper modal boundary condition of the thin flag. The calculated ϕ^i in the domain is employed to calculate the kinematic force (KF), the force due to viscous effect ($FDVE$), and the vortex-induced force (VIF) [5].

2 Results

Three distinct response modes were observed during the increase and decrease of velocity for the heavy inverted flag with $AR = 1$. For low non-dimensional velocity values of $U^* \leq 1.8$ during upsweep (when velocity increases), the flag remains stationary. As U^* increases, a two-sided, self-sustained fluttering mode is obtained; this is the second response mode and is observed at intermediate velocity values of $1.82 \leq U^* \leq 3$. The final response mode is the one-sided

¹This work was supported by NSF under grant number CBET-1943810

fluttering mode, which is observed at high-velocity values around $U^* > 3$. These modes are consistent with previous numerical observations [1]. When U^* is reduced (downsweep), during the transition from the one-sided mode to the fluttering mode, no hysteresis is observed. As U^* is reduced further, the flag continues to flutter at a lower U^* than the upsweep result, thereby extending the fluttering region and creating a sustained subcritical bifurcation loop at $1.3 \leq U^* \leq 1.8$. After that, the flag reverts to its stationary mode when U^* further reduces.

We also observed three different response behaviours depending on the flag's AR. For narrow flags ($AR = 0.25 - 0.5$), the fluttering dynamics is mainly controlled by the appearance and strengthening of the side-edge vortices (SEV) as $SEV > LEV$. Also, the upsweep critical velocity remains constant. When $AR = 0.75 - 1.25$, the critical fluttering velocity exhibits a monotonic change. Also, the flag experiences the largest hysteresis region/loop at $AR = 0.75$. Here, the LEV becomes larger and its influence is now similar to the action from side edge vortices. This competing and almost equal effect of the two vortices strongly modifies the critical fluttering velocity. For wide flags, at $AR = 1.5 - 2$, the LEV is clearly more dominant than the SEV , and is responsible for its fluttering dynamics. The upsweep critical velocity shows a linear reduction with AR with a slope of $s = -2.85$. It was also observed that the downsweep critical velocity linearly reduces as aspect ratio reduces with a slope of $s = -6.06$.

Since the hysteresis behavior of the flag in the bistable region is highly dependent on the vortical structures. The roles of different vortical structures are therefore quantified using the modal force partitioning. It is found that the vortex-induced force (VIF) is always the most dominant fluid force. VIF can be split up into its leading-edge VIF_{LEV} , and side-edge VIF_{SEV} and trailing-edge vortices contributions; the first two are the dominant effects. The total VIF contribution is expressed as VIF_{Total} . We then normalize the force with the flag width to compare VIF between flags of different AR . Figure 1 illustrates the modal force created from the vortical structure for $AR = 0.25, 0.75$, and 1.5 . The integrand of VIF_{LEV} and VIF_{SEV} are shown when they are projected on Q-criterion iso-surfaces. For all AR , a very small strip of VIF_{LEV} and no VIF_{SEV} keeps the flag at the zero deflection state ($t/T = 0$). As the flag deflects ($t/T = 1/8$), VIF_{SEV} starts to grow and its contribution to the modal force increases as the flag deflects from its stable position. The VIF_{LEV} remains attached to the flag during most of the deflection cycle. The side vortices remain attached and gradually shifts toward the leading edge as the side angle of attack increase. Figure 1 also shows that $VIF_{SEV} > VIF_{LEV}$ for narrow flags while $VIF_{LEV} > VIF_{SEV}$ for wider flags. This suggests that at low AR , the fluttering is governed by the VIF_{SEV} while the effect of VIF_{LEV} increases for larger flag aspect ratios and VIF_{LEV} governs the fluttering dynamics in these cases.

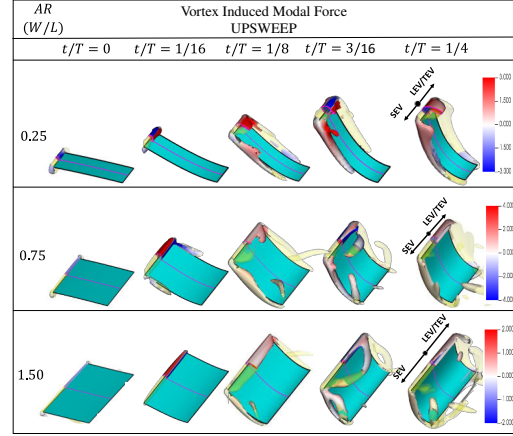


Figure 1: Integrand of vortex-induced modal force from the leading/trailing edges vortices ($VIF_{LEV/TEV}$) and side-edge vortices (VIF_{SEV}) for $AR = 0.25, 0.75$, and 1.5 ($U^* = 2, 2.09, 1.83$ respectively) at $t/T = 0, 1/16, 1/8, 3/16$, and $1/4$. The right halves of the figures show the contribution from $VIF_{LEV/TEV}$ and the left halves show the contribution from VIF_{SEV} .

3 Conclusion

A subcritical bifurcation is observed for all AR s, which is different from the regular flag where the hysteresis disappears at the lower AR limit. The consistent side edge vortices in narrow inverted flags ensure its continued hysteresis. The modal force partitioning method is used to study the roles of dominant vortical structures on the bistable response of the flag. For slender flags, the fluttering behavior is primarily governed by the VIF_{SEV} . For intermediate AR s, a relatively equal contribution of VIF_{SEV} and VIF_{LEV} is observed, which enables the flag to flutter in the bistable range. For wider flags, the VIF_{LEV} governs its fluttering dynamics. These observations suggest that an energy harvesting flag can maintain a sustained fluttering response even with significant fluctuations in wind velocity. A reduction in the wind velocity could bring the inverted flag to the bistable region, and if the bistable range is sufficiently large, the flag does not lose its energetic fluttering response and continues its large amplitude fluttering motion.

References

- [1] Daegyoum Kim, Julia Cossé, Cecilia Huertas Cerdeira, and Morteza Gharib. Flapping dynamics of an inverted flag. *Journal of Fluid Mechanics*, 736, 2013.
- [2] Kourosh Shoele and Rajat Mittal. Energy harvesting by flow-induced flutter in a simple model of an inverted piezoelectric flag. *Journal of Fluid Mechanics*, 790:582–606, 2016.
- [3] Christophe Eloy, Nicolas Kofman, and Lionel Schouveiler. The origin of hysteresis in the flag instability. *Journal of Fluid Mechanics*, 691:583–593, 2012.
- [4] Mohammad Tavallaeinejad, Mathias Legrand, and Michael P Paidoussis. Nonlinear dynamics of slender inverted flags in uniform steady flows. *Journal of Sound and Vibration*, 467:115048, 2020.
- [5] Karthik Menon and Rajat Mittal. On the initiation and sustenance of flow-induced vibration of cylinders: insights from force partitioning. *Journal of Fluid Mechanics*, 907, 2021.

Gust response of free-falling bodies

Chandan Bose, Callum Bruce and Ignazio Maria Viola*

School of Engineering, Institute for Energy Systems, University of Edinburgh, Edinburgh, UK¹

*Correspondence: *i.m.viola@ed.ac.uk*

1 Introduction

In the next decade, distributed sensor network systems made of small flying sensors, from dust-scale to insect-scale, will enable a step change in monitoring natural disasters and remote areas [1]. They will contribute to protecting the environment by providing data on the contamination of physical and biological systems and on the impact of human activities. To date, a key barrier to the development of these small flyers is that insect-scale flapping devices are energy inefficient and can remain airborne only for a few minutes [2].

Nature offers ingenious solutions to this challenge. In fact, plant seeds maximise their endurance and dispersal to ensure the proliferation of the plant. Some natural flyers, such as the dandelion diaspores, travel unpowered for days and hundreds of kilometers [3]. The arrangement of the dandelion filaments form a shape resembling a porous disk. This results in a separated vortex ring and an up to a ten-fold increase in the upward force per projected area [4].

The kinematics of bodies settling in gravity is well characterised [5]: the steady or unsteady nature of the kinematics depends primarily on the Reynolds number, Re and, when unsteady, the falling style depends mostly on the ratio between the inertia of the body and that of the fluid, I^* . However, how the porosity and non-homogeneous mass distributions modify the kinematics is not yet understood and has only recently been explored [6, 7].

Most importantly, existing wind dispersal models for plant seeds are typically based on the terminal velocity measured in quiescent flow [8]. However, large particles compared to the Kolmogorov scale could present strong interactions with turbulent eddies of comparable size, resulting in a very different terminal velocity than in quiescent flow [9]. Hence, understanding the kinematics of passive flyers in unsteady flow conditions is critical to underpin the design of future flying sensors.

To demonstrate the strong vortex-body interaction, we focus on the kinematics of a two-dimensional impervious plate experiencing a transverse gust. The two-dimensionality of the problem simplifies the interpretation of the results. Within the talk, however, we aim to discuss how the phenomenon demonstrated in this abstract extends to

porous three-dimensional disks with non-coinciding centers of mass and buoyancy.

2 Computational Methodology

To simulate a free-falling plate under gravity, we solve the incompressible Navier-Stokes equations for Newtonian fluids using an overset mesh-based flow solver `overPimpleDyMFoam`, available within the open-source library `OpenFOAM`. The *inverse distance* overset interpolation technique is used to facilitate interpolation between the *donor* and *acceptor* cells. The cells inside the impervious body are considered to be *holes*, which do not take part in the calculations. To simulate the two-way coupled motion of the body, a partitioned weak coupling strategy-based 6-DoF solver is used, where the fluid and solid solvers interact in a staggered manner. The structural solver uses a Newmark-beta time integration scheme.

A plate with chord D , thickness $h = D/10$, and $I^* = 0.6$ is initially kept stationary with the chord on the $z = 0$ plane. When released, the plate falls due to the gravitational acceleration in the negative z direction. First, we consider the plate as free-falling in quiescent flow. After the initial transient, the plate falls fluttering with terminal velocity $-V_t$. The Reynolds number $V_t D/\nu$ is 250, where ν is the kinematic viscosity of the fluid.

Thereafter, we repeat the simulation with a transverse gust along the x -direction. The gust speed is initially zero. For time t between $t_0 = V_t/D$ and $t_1 = 2V_t/D$, it increases as follow: $u = \frac{1}{2} \left[1 - \cos \left(\frac{\pi(t-t_0)}{t_1-t_0} \right) \right] G_R V_t$, where $G_R = 0.4$ is the gust ratio. The gust speed $u(t)$ is plotted in Fig. 1a.

3 Results

To show that the transverse gust slows down the fall of the plate, we present the results in a reference system $O(X, Z)$ centred on the plate at instant $t = 0$, and that moves at the terminal velocity $-V_t$. Hence, in this reference system the disk appears stationary when it falls at the terminal velocity.

First, we present the displacement envelop and the flight trajectory in Fig. 1b, and the trajectory of the center of mass (C.M.) in Fig. 1c. Since released, the plate falls slower than the terminal velocity, and thus it appears to move upwards in the $O(X, Z)$ reference system. Specifically, the plate initially goes up steadily without any angular displacement for up to half of the gust period ($tV_t/D = 3.75$). Over this initial stage, a vortex dipole is formed in the wake of the plate (Fig. 2a). Because the gust is from left to right in Fig. 2a,

¹This work was supported by the European Research Council through the Consolidator Grant 2020 ‘‘Dandidrone: a Dandelion-Inspired Drone for Swarm Sensing’’ [H2020 ERC-2020-COG 101001499].

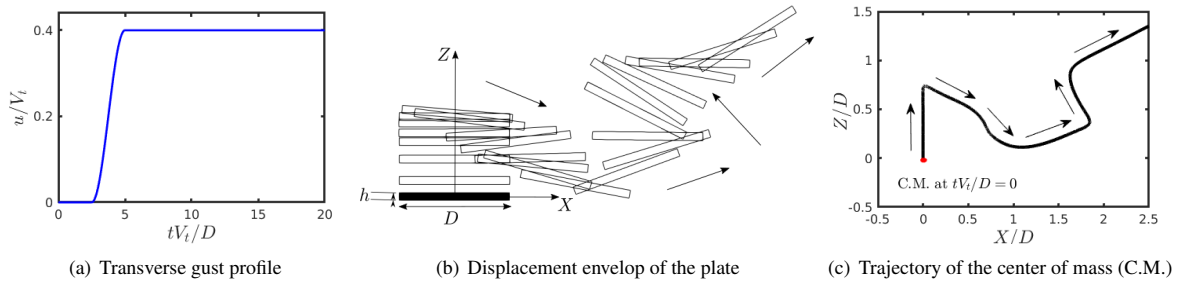


Figure 1: Gust response of a free-falling plate at $Re = 250$ and $I^* = 0.6$.

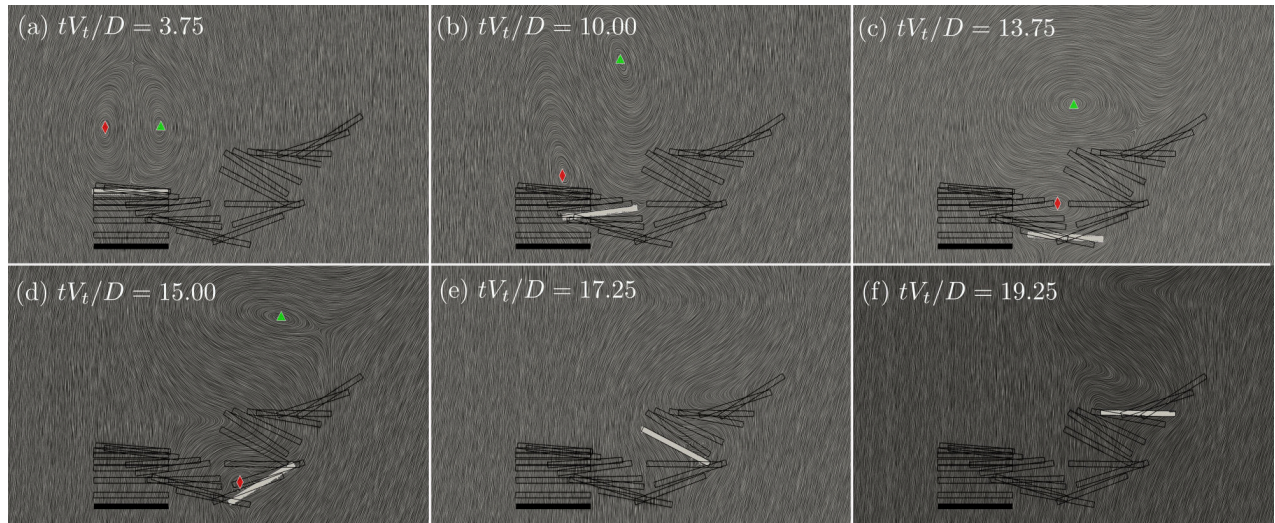


Figure 2: Instantaneous line convolution integral visualisation of a free-falling plate subjected to a transverse gust. The plate initial position is showed in black, and the position at each instant is showed in white. The nodes of the vortex dipole are marked with the red diamond and the green triangle.

we call the left and right vortices of the dipole the leading edge vortex (LEV) and the trailing edge vortex (TEV), respectively. The corresponding nodes are showed in Fig. 2a by the red diamond and the green triangle, respectively.

As typical of the flutter regime, when the plate tilts, it begins to fall faster than the terminal velocity (Fig. 2b). However, because of the gust, the vortex dipole grows and rotates, as the TEV advects away from the plate and the LEV grows to the size of the plate. The low pressure associated with the LEV results in an upward force. In fact, in the following instants (Figs. 2d-f.), the plate appears to move upwards with respect to $O(X, Z)$.

4 Conclusions

We demonstrated with numerical simulations that a horizontal gust can decrease the terminal velocity of a settling plate, and we explained the upward force through the vortex dynamics. This mechanism, which was here depicted for the transient phase of a free-falling impervious plate released from rest, will be further elucidated in the presentation, where we will also discuss the role of permeability and of the position of the centre of mass with respect of the centre of buoyancy.

References

- [1] Dario Floreano and Robert J. Wood. Science, technology and the future of small autonomous drones. *Nature*, 521(7553):460–466, 2015.
- [2] Noah T. Jafferis, E. Farrell Helbling, Michael Karpelson, and Robert J. Wood. Untethered flight of an insect-sized flapping-wing microscale aerial vehicle. *Nature*, 570(7762):491–495, 2019.
- [3] James Small. The origin and development of the Compositae. *New Phytologist*, 17(8-9):200–230, 1918.
- [4] Cathal Cummins, Madeleine Seale, Alice Macente, Daniele Certini, Enrico Mastropaolo, Ignazio Maria Viola, and Naomi Nakayama. A separated vortex ring underlies the flight of the dandelion. *Nature*, 562:414–418, 2018.
- [5] Stuart B. Field, M. Klaus, M. G. Moore, and Franco Nori. Chaotic dynamics of falling disks. *Nature*, 388(6639):252–254, 1997.
- [6] Wentao Huang, Hong Liu, Fuxin Wang, Junqi Wu, and H. P. Zhang. Experimental study of a freely falling plate with an inhomogeneous mass distribution. *Physical Review E - Statistical, Nonlinear, and Soft Matter Physics*, 88(5):1–7, 2013.
- [7] Minhyeong Lee, Seung Hun Lee, and Daegyoum Kim. Stabilized motion of a freely falling bristled disk. *Physics of Fluids*, 113604(August), 2020.
- [8] Ran Nathan, Gabriel G. Katul, Gil Bohrer, Anna Kuparinen, Merel B. Soons, Sally E. Thompson, Ana Trakhtenbrot, and Henry S. Horn. Mechanistic models of seed dispersal by wind. *Theoretical Ecology*, 4(2):113–132, 2011.
- [9] L. B. Esteban, J. S. Shrimpton, and B. Ganapathisubramani. Disks settling in turbulence. *J. Fluid Mech.*, 883, 2019.

Session G

Wakes



Interaction of a cylinder wake with a turbulent boundary layer

E. Torres-De Jesus^a and T. Saxton-Fox^{a*}

^a University of Illinois at Urbana-Champaign, Aerospace Engineering department, Urbana, United States¹

*Correspondence: tsaxtonf@illinois.edu

1 Introduction

The interaction of bluff body wakes with turbulent boundary layers is relevant to many practical applications. The atmospheric turbulent boundary layer interacts with the wakes of bridges, buildings, islands. A canonical example of a wake - boundary layer interaction is the interaction of a cylinder wake with a turbulent boundary layer. Previous laboratory work has studied cylinder wake - turbulent boundary layer interactions with cylinders mounted with their axes normal to the wall and to the flow as well as with their axes parallel to the wall and normal to the flow (1; 2). The geometry with a wall-normal axis perturbs the boundary layer throughout the boundary layer height simultaneously and generates primarily wall-normal vorticity, while the geometry with a wall-parallel axis perturbs the boundary layer at one height at a time and generates primarily spanwise vorticity. Each geometry is relevant to real world applications, with the wall-normal geometry having relevance to buildings and the wall-parallel geometry having relevance to bridges. The focus of previous work has often been on the wake's effect on the boundary layer. For example, a cylinder in the wall-parallel geometry has been shown to lead to changes in the skin friction and heat transfer at the wall within the boundary layer (3). An array of cylinders in the wall-normal geometry has been shown to disrupt boundary layer hairpin packets (4).

The focus of this work is on the effect of the boundary layer on the wake, rather than the effect of the wake on the boundary layer. A wall-parallel cylinder was embedded in a turbulent boundary layer at multiple wall-normal heights. The cylinder wake was studied in the wall-normal - streamwise plane using particle image velocimetry. The work focuses on the effect of incoming turbulent structures on the propagation of the cylinder wake, treating the turbulent boundary layer as an unsteady "free stream." The data are analyzed using conditional averaging paired with a vortex identification method (5) and using conditional projection averaging (6).

2 Results

A cylinder was placed in the turbulent boundary layer with its axis normal to the flow direction and parallel to the wall.

¹This work was supported by the United States National Science Foundation under grant number 2118209 and with a United States National Science Foundation Graduate Research Fellowship.

The cylinder had a diameter of 0.05δ , where δ was the 99% boundary layer thickness. The cylinder was placed at three wall-normal positions, $y_c = 0.38\delta$, 0.64δ , and 0.9δ . The Reynolds number for the cylinder was $Re_D = \frac{U_\infty D}{\nu} \approx 1160$, where U_∞ is the free-stream velocity, D is the cylinder diameter, and ν is the kinematic viscosity. The friction Reynolds number for the boundary layer was $Re_\tau = \frac{U_\tau \delta}{\nu} \approx 1090$, where U_τ is the friction velocity. A schematic of the experimental setup is shown in Fig. 1. A black cylinder passes through the flow just upstream of the particle image velocimetry field of view, shown in green.

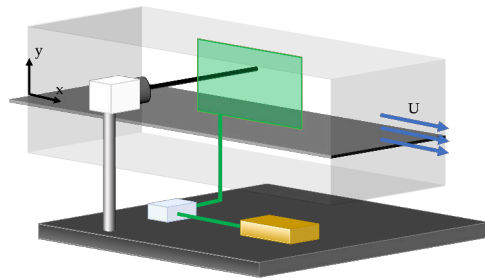


Figure 1: Experimental setup

Particle image velocimetry was performed at two frequencies, 100 Hz and 3750 Hz. The velocity fields were calculated using DaVis software. The mean streamwise velocity field is shown in Fig 2 for the case where the cylinder is positioned at $y_c/\delta = 0.9$, with the x and y axes normalized by the boundary layer thickness and the mean streamwise velocity field normalized by the freestream velocity.

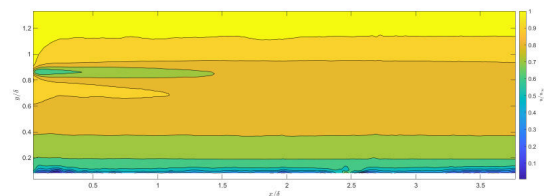


Figure 2: Mean Velocity Flow Field

The cylinder wake was observed to be distorted by the turbulent boundary layer, with larger distortions when embedded deeper in the boundary layer ($y_c/\delta = 0.38, 0.64$) than when sitting at its edge ($y_c/\delta = 0.9$). This distortion can be observed in Figure 3 as a waviness or variability in the instantaneous height at which the wake is strongest downstream of the cylinder. The wall-normal height oscillations

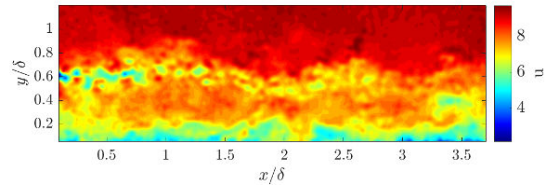


Figure 3: Instantaneous streamwise velocity field of the case with a cylinder at $y_c = 0.64\delta$.

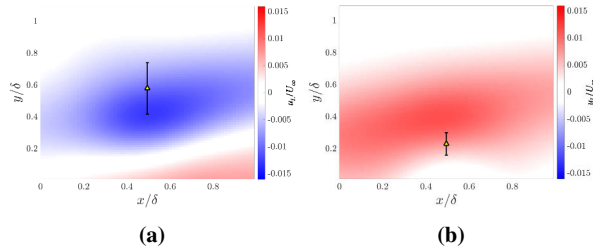


Figure 4: Conditional averaging results showing the variation of vortex heights in the presence of large-scale structures (5).

of the cylinder wake were not observed when the cylinder was positioned outside of the turbulent boundary layer, and are hypothesized to be a result of the large-scale turbulent structures advecting the wake vortices. To test this hypothesis, the height of the cylinder wake vortices will be analyzed using conditional averaging (5) and the wake vortex intensity will be analyzed using conditional projection averaging (6).

Previously, our research group has used conditional averaging to analyze the height of vortices within a turbulent boundary layer, based on the local behavior of large scale structures. An example result from this work is shown in Figure 4: the contours show the conditionally-averaged large-scale streamwise velocity field while the triangle and error bar show the average and standard deviation range of vortices identified with the Triple Decomposition Method (5). We have also previously used a method called conditional projection (CP) averaging to analyze the intensity of small-scale velocity fluctuations in a turbulent boundary layer. An example result from this work is shown in Figure 5. In Figure 5(a), the CP-averaged streamwise velocity field is shown, while in Figure 5(b), the corresponding CP-averaged streamwise small-scale intensity is shown. The height of maximum streamwise intensity varies depending on the large-scale structure phase. We will apply both methods to the cylinder wake - boundary layer interaction problem to study the amplitude and height variation of the wake as large-scale turbulent structures convect past the cylinder.

3 Conclusion

The interaction of a cylinder wake with a turbulent boundary layer is studied using particle image velocimetry and multi-

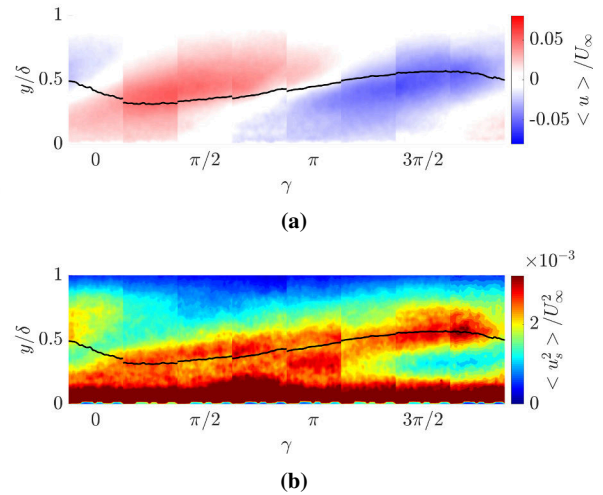


Figure 5: The streamwise fluctuating velocity field (a) and the corresponding streamwise small-scale intensity (b) from conditional projection averaging (6).

ple conditional averaging techniques. Data are presented for three heights of the cylinder, aligned parallel to the wall and normal to the flow direction. The cylinder wake's instantaneous shape is observed to be modified by the presence of turbulent structures. Vortex identification and conditional averaging will be used to identify the variation in height where the cylinder wake vortices are observed depending on the local large-scale turbulent dynamics. Conditional projection averaging will be used to identify the height and amplitude variation of the wake intensity as a function of the passing large-scale turbulent structures.

References

- [1] Eisuke Marumo, Kenjiro Suzuki, and Takashi Sato. A turbulent boundary layer disturbed by a cylinder. *Journal of Fluid Mechanics*, 87(1):121–141, 1978.
- [2] Shaokai Zheng and Ellen K Longmire. Perturbing vortex packets in a turbulent boundary layer. *Journal of fluid mechanics*, 748:368–398, 2014.
- [3] E Marumo, K Suzuki, and T Sato. Turbulent heat transfer in a flat plate boundary layer disturbed by a cylinder. *International Journal of Heat and Fluid Flow*, 6(4):241–248, 1985.
- [4] Yan Ming Tan and Ellen K Longmire. Recovery of vortex packet organization in perturbed turbulent boundary layers. *Physical Review Fluids*, 2(10):104602, 2017.
- [5] Shaurya Shrivastava and Theresa Saxton-Fox. Correlation between large-scale streamwise velocity features and the height of coherent vortices in a turbulent boundary layer. *Fluids*, 6(8):286, 2021.
- [6] Theresa Saxton-Fox, Adrián Lozano-Durán, and Beverley J McKeon. Amplitude and wall-normal distance variation of small scales in turbulent boundary layers. *Physical Review Fluids*, 7(1):014606, 2022.

When turbulence matters in vortex dominated flows

G. Winckelmans^{a*}, D.-G. Caprace^b, M. Duponcheel^a, L. Bricteux^c, I. De Visscher^d, F. Trigaux^a
and P. Chatelain^a

^a University of Louvain (UCLouvain), iMMC, Louvain-la-Neuve, Belgium

^b Brigham Young University (BYU), FLOWlab, Provo, Utah, USA; UCLouvain

^c University of Mons (UMONS), Mons, Belgium

^d Wake Prediction Technologies (WAPT), Louvain-la-Neuve, Belgium

*Correspondence: gregoire.winckelmans@uclouvain.be

1 Introduction

This contribution reflects on the role that turbulence plays in various flows that contain coherent and dominating vortical structures. We hence don't consider flows where turbulence is everywhere and has continuous spectrum of scales, such as decaying homogeneous isotropic turbulence, or the canonical channel and pipe flows, and the boundary layers without separation (canonical ZPG and others). We also don't consider the far wake of non-lifting bodies: their wake is solely due to drag and it too has a continuous spectrum of scales; it is also found to be self-similar with self-similar profiles of the mean velocity components \bar{u}_x and \bar{u}_r and for the turbulent fluctuations.

The focus is here on flows at high Reynolds numbers and where large scale coherent vortices are present and dominating. For that to happen, one needs to consider bodies with significant lift. The intensity of the coherent vortical structures is then associated with that lift. It is then of interest to consider the wake of bodies where the lift is much higher than the drag, such as aircraft and rotorcraft. The Reynolds number associated with real scale aircraft and rotorcraft is very high; hence it is not possible to use scale-resolved simulations to compute both the details of the flow near the wing/blade surfaces and the wake development (from the very near wake to the mid wake and then to the far wake). Even when using the unsteady version of the Reynolds-averaged Navier-Stokes equations (URANS) to compute the details of the flow past the wing or blades, it is not possible (or extremely expensive) to combine that with a long domain simulation of the wake itself (say up to 30 wingspans downstream) and for long time simulations (as required to gather the proper statistics of the flow).

Concerning the simulation of the wake itself, use of the URANS formulation is inadequate as this formulation assumes time-averaging of the physics over a large time window and hence it does not allow to capture the relevant turbulent scales that develop in the wake; nor they dissipation. The proper way to proceed is to use the large-eddy simulation (LES) formulation of the Navier-Stokes equations; a truncation of the physics is then done in physical space (the scales smaller than the grid size are not captured

by the simulation; yet their effect of the captured scales is modelled, using a subgrid-scale (SGS) model) but no time-averaging of the physics is done. LES simulation are thus scale-resolving simulations, down to scales limited by the grid size.

The quality of the numerical code used for the LES also matters. We use in-house developed codes that have good conservation properties (using centred stencils so as to have negligible numerical dissipation and high order for low dispersion errors): either our Eulerian code in the velocity-pressure formulation and using a fourth order method on a staggered grid; or our mixed Eulerian-Lagrangian code in the vorticity-velocity formulation that uses particles for the convection step and a grid for all the rest; also for a spectral Poisson solver that can handle unbounded, bounded or periodic direction(s) [8]: the so-called Vortex Particle-Mesh (VPM) code. The codes having negligible numerical dissipation, the dissipation of the turbulent kinetic energy is handled by the SGS model. Hence, we also developed multi-scale SGS models that mostly act at on the high wavenumbers of the function captured by the LES grid (velocity or vorticity, depending on the code) and leave the small to medium wavenumbers unaffected [1]. Those codes have both been developed for HPC.

In this work, we use various types of actuator models to impose the presence of the wing or blade elements within the flow computational grid. In the VPM code, we use an immersed lifting line (and also dragging [4]) method that sheds into the wake the proper wake vorticity field emanating from each wing/blade element, and also allows for a time-step larger than that from the classical CFL limitation. In the Eulerian code, we use an improved actuator line model that avoids the smearing of the forces in the wing/blade span direction [6]; it is limited by the CFL; it also handles flexible curves and is coupled to various beam models so as to also perform aeroelastic studies [9].

2 Results

We will present various examples of wake flows where the turbulence that develops within the wake plays an important role in what is obtained as a net result in the far wake and

how it decays. For the case of a simple wing, the addition of parasitic drag (= friction and form drag from each wing section) is mandatory to obtain a wake that becomes turbulent, with obtention of a turbulent two-vortex system (T-2VS) at statistical equilibrium in the far wake [5]. Alternatively, a wing without parasitic drag flying in some atmospheric turbulence (e.g., fed as inflow using a box of Mann synthetic turbulence or using a box of turbulence co-computed in LES) will have its developing wake “resonate” with the various scales of the inflow turbulence (from scales larger than the wingspan to scales of the order of the wing chord); also leading, in fine, to a T-2VS. One can also consider the combination of both: effects of parasitic drag together with atmospheric turbulence.

The T-2VS in itself constitutes an interesting and important canonical flow, and is characterised: distribution of the circulation $\Gamma(r)$ as measured from the center of each vortex, turbulent kinetic energy in the Rankine oval and dissipation rate of that turbulent kinetic energy; decay rate for the total circulation Γ_{tot} of each vortex; those quantities being of importance for support to air traffic safety studies.

It is then also important to consider the interaction of such T-2VS with a ground; also because the safety studies in landing consider aircraft wakes near the runway, after they have interacted with the ground and gone back up, potentially encountering a follower aircraft. A wall-resolved LES was performed at $\Gamma_{\text{tot}}/v = 2 \cdot 10^5$ and the various important diagnostics were collected: trajectories of the vortices, decay of their circulation in time, etc. The fact that there is turbulence in the vortex system is seen to be very important, with large differences when compared to LES using a vortex system without turbulence: smoother interaction of the wake vortices with the ground, lower rebound and enhanced decay. Cases with addition of a turbulent cross-wind were also investigated, hence with a different behaviour for the port and starboard vortices [3].

The wake of a four-blade rotor with the typical advance ratio of a rotorcraft is considered next [7]. The formation of the wake is then far more complex than behind a wing, and much turbulence is generated by the complex interactions of the vorticity field shed by the various blades (even without considering any parasitic drag that here plays no significant role). The far wake is also obtained as a T-2VS which is characterised and found to be much different from that of a wing of same size, flying at the same speed and with same lift. The wake development is also quite different when considering low advance ratios, as in Fig. 1. A vehicle made of four rotors (a quad-rotor) is considered next. The wake development is also investigated and is compared to that of the single rotor.

Finally, we illustrate how wake turbulence strongly interacting with the ground can also be beneficial for wind farms (here a small farm made of two rows, each with with five wind turbines in tandem) in an atmospheric boundary layer (itself obtained using a co-simulation that is fed at inflow).

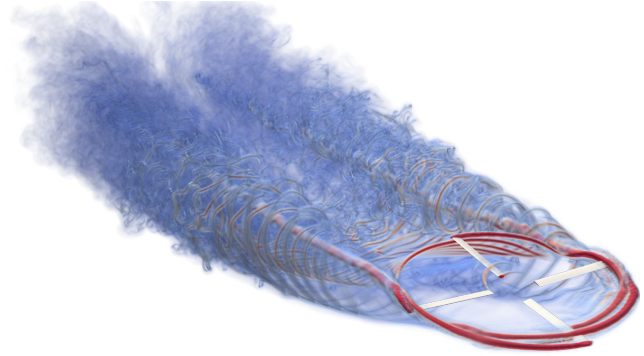


Figure 1: View of the norm of the vorticity field for the case of a rotor at a low advance ratio.

We compare the baseline configuration with a configuration where the turbines are tilted by 25° so as to deviate their wake towards to ground [6]. The stronger turbulent interaction of the deviated wakes with the ground, together with the entrainment downward of fast air from above the wind turbines, increase significantly the recovery rate of each wake; here resulting in a 14 % increase of the produced total power.

3 Conclusion

We presented wake flows with dominating coherent vortices and where turbulence plays a major role in the way the wake develops towards the far wake, where a turbulent two-vortex system is obtained. The fate of that system further downstream will depend on its interaction with the turbulence and/or stratification of the atmosphere (as investigated in [2]); or the interaction with a ground. The case of tilted wind turbines, although not with strong coherent vortices, further illustrated how the increased interaction of a turbulent wake with a ground can be beneficial.

References

- [1] Laurent Bricteux, et al. A multiscale subgrid model for both free vortex flows and wall-bounded flows. *Phys. Fluids* **21**, 105102, 2009.
- [2] Ivan De Visscher, et al. Aircraft vortices in stably stratified and weakly turbulent atmospheres: simulation and modeling. *AIAA Journal*, Vol. 51, No. 3, 2013.
- [3] Laurent Bricteux, et al. LES investigation of the transport and decay of various strengths wake vortices in ground effect and subjected to a turbulent cross-wind. *Phys. Fluids* **28**, 065105, 2016.
- [4] Denis-Gabriel Caprace, et al. Lifting line with various mollifications: theory and application to an elliptical wing. *AIAA Journal*, Vol. 7, No. 1, 2019.
- [5] Denis-Gabriel Caprace, et al. An immersed lifting and dragging line model for the vortex particle-mesh method. *Theor. Comput. Fluid Dyn.*, 2020.
- [6] François Trigaux, et al. Tilted wind turbines in farm configuration for improved global efficiency. *J. Phys.: Conf. Ser.* **1618** 062035, 2020.
- [7] Denis-Gabriel Caprace, et al. Wakes of rotorcraft in advancing flight: A large-eddy simulation study. *Phys. Fluids* **32**, 087107, 2020.
- [8] Denis-Gabriel Caprace, et al. FLUPS: a Fourier-based library of unbounded Poisson solvers. *SIAM J. Sci. Comput.*, Vol. 43, No. 1, C3-C60, 2021.
- [9] François Trigaux, et al. A flexible actuator curve model for aerelastic simulations of wind turbines in atmospheric boundary layers. *J. Phys.: Conf. Ser.* Submitted Jan. 2022 for TORQUE 2022.

Simplified model for capturing helical vortex interactions with applications to asymmetric rotor wakes

Aliza Abraham^{a*}, Andrés Castillo-Castellanos^a, and Thomas Leweke^a

^a Aix-Marseille Université, CNRS, Centrale Marseille, IRPHE, Marseille, France¹

*Correspondence: aliza.abraham@univ-amu.fr

1 Introduction

The wakes of rotors, such as those found on helicopters, wind turbines, and propellers, are characterized by helical vortices. The interaction between these vortices can lead to various types of instabilities, including displacement instabilities, the focus of the current study. Displacement instabilities occur when the vortex core is shifted from its baseline position, causing adjacent vortices to group together (pairing). When the entire helix is shifted, global pairing occurs. This type of instability can be caused by asymmetry in the rotor generating the helical vortex system, as demonstrated for a two-vortex system by Quaranta et al. [1]. Most rotors in industrial applications (and their laboratory-scale counterparts) have three or more blades, substantially increasing the complexity of the interlaced helical vortex system. Furthermore, global pairing occurs frequently in laboratory experiments (e.g., [2]), likely due to small asymmetries that are unavoidable in scaled-down experiments. This phenomenon has not been thoroughly investigated due to this increased complexity.

The current study proposes a simplified model to develop a more complete understanding of the effect of rotor asymmetry on the development of the helical vortices in the wake. The model is based on the behavior of an infinitely repeating periodic strip of point vortices, which represents a cross-section of an infinite helical vortex system. Though highly simplified, a previous study by Delbende et al. [3] for a two-vortex system shows that point vortices can be used to represent helical vortices for low values of helical pitch, as is usually the case for rotor wakes. In addition, comparisons with experiments show that the point vortex model captures rotor wake behavior remarkably well. With this simplified model, the broad parameter space required to fully characterize rotor asymmetry (i.e., variations in length, axial position, and pitch of all blades) can be explored in detail.

2 Methods

2.1 Point vortex model

The representation of helical vortices as point vortices is based on the assumption that, for small values of helical pitch relative to the radius of the helices, the effects of

curvature and torsion are small [3]. Under these conditions, the interlaced helices can be “unrolled” and represented as an array of straight parallel vortices subject to periodic boundary conditions dictated by the helical geometry. These straight vortices can in turn be represented by periodically-repeating point vortices in two dimensions, whose non-linear dynamics can be calculated easily using the induced velocity of neighboring vortices. For a strip of N point vortices repeated periodically along the x -axis, where N represents the number of helices in the original system, the following formula governs the displacement of the basic strip [4]:

$$\frac{dz_{\alpha}^*}{dt} = \frac{1}{2Li} \sum_{\substack{\beta=1 \\ \beta \neq \alpha}}^N \Gamma_{\beta} \cot \left\{ \frac{\pi}{L} (z_{\alpha} - z_{\beta}) \right\}$$

where $z_{\alpha} = x_{\alpha} + iy_{\alpha}$ is the complex position of the point vortex α , $*$ represents the complex conjugate, and L is the length of the basic strip. If the point vortices are identical and evenly spaced, there will be no displacement. However, the system is unstable, so any asymmetry will perturb the vortices along intertwining trajectories determined by the equation above. Once the trajectories of the point vortices within the $x - y$ plane are determined, the helical wake can be reconstructed. To transform from the temporal evolution of the helical system to the spatial evolution representing a rotor wake, the point vortices advance along a helical path determined by the advection speed and rotational speed of the rotor. The perturbation deforms the helices, with point vortex displacements in the y -direction corresponding to radial displacements in the helical system, and x -direction point vortex displacements having components in the axial and azimuthal directions of the helix.

2.2 Experimental set-up

To investigate the accuracy of the point vortex model, water channel experiments visualizing the wake of asymmetric rotors are conducted. The water channel test section is 150 cm \times 38 cm \times 50 cm (length \times width \times height). Two- and three-bladed rotors with radii of 8 cm and 9 cm, respectively, are used to generate helical vortex wakes. The vortices are visualized by painting the rotor blade tips with fluorescent dye and illuminating the test section with a laser or LED panel. These visualizations are captured on video for further analysis. The rotation rate and flow speed of the channel are

¹This work was supported by technology transfer company SATT Sud-Est (Marseille).

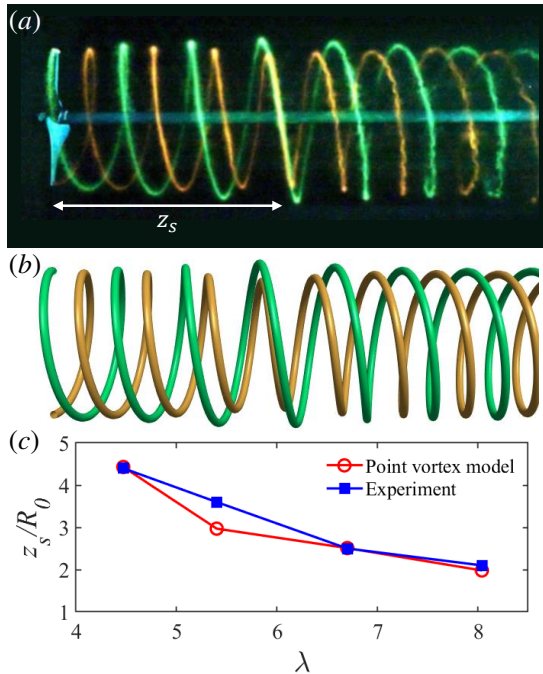


Figure 1: (a) Dye visualization of the wake of the asymmetric two-bladed rotor with tip speed ratio $\lambda = 5.4$, reproduced from [1]. The white arrow indicates z_s , the distance to leapfrogging. (b) Helical vortices reconstructed from the point vortex model using the same parameters as the experiment shown in (a). (c) Comparison between z_s normalized by the rotor radius R_0 obtained from the experiments in [1] and the point vortex model for a range of tip speed ratios.

varied to achieve different values of helical pitch. For the two-bladed rotor, asymmetry is introduced via radial offset relative to the shaft, as described in detail by Quaranta et al. [1]. For the three-bladed rotor, all blades are 3D printed and can be removed and replaced individually.

3 Results

Comparisons between predictions from the point vortex model and the experimental results show good agreement. Qualitatively, the key feature of the asymmetric two-bladed rotor wake is the occurrence of leapfrogging, where loops of the two helices swap positions, observed for the experimental case in figure 1(a). When using the values of vortex circulation, helical pitch, and blade asymmetry from the experiment as inputs, the point vortex model reproduces this leapfrogging phenomenon (figure 1b). To quantitatively compare the model to the experiments, the distance z_s is defined as in [1], i.e., the downstream distance where leapfrogging occurs (figure 1a). Quaranta et al. [1] showed that z_s depends on tip speed ratio (λ), the ratio between the speed of the blade tips and the speed of the axial flow approaching the rotor, as λ affects the strength and geometry of vortices in the wake. Figure 1(c) compares z_s values from the experiments to those obtained from the point vortex model

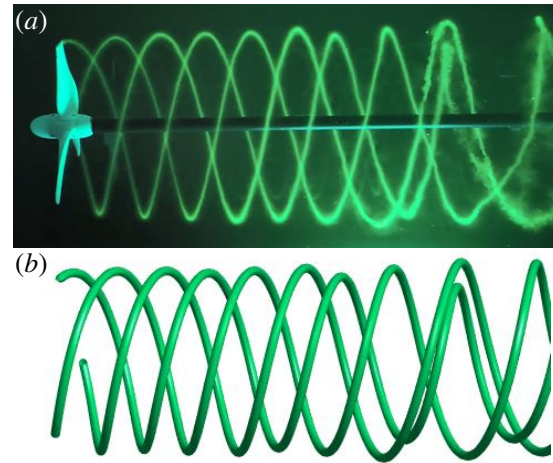


Figure 2: (a) Dye visualization of the wake of the asymmetric three-bladed rotor. (b) Helical vortices reconstructed from the point vortex model.

for a range of values of λ . The results agree well considering the uncertainty in the experimental measurements and the simplicity of the point vortex model. Similar qualitative agreement can be observed in the three-vortex case (figure 2), though a quantitative validation campaign is still underway. A vortex filament model of interlaced helices will also be used for further validation of the point vortex model.

4 Conclusion and outlook

The point vortex model for the helical vortex system provides a simple way to predict the behavior of asymmetric rotor wakes. Though it neglects many of the components influencing helical vortices (e.g., curvature, torsion, viscosity, spatial evolution), it is shown to accurately capture key features of rotor wake vortex interaction. As different configurations can be tested quickly, this model has a range of applications. For an experiment investigating undeformed helical vortices, a level of acceptable asymmetry for a given region of interest can be determined. To explore the acceleration of coherent structure breakdown and wake recovery, different rotor asymmetries can be tested to determine the combination of perturbations that most effectively achieves this goal. Furthermore, the agreement between the experimental wake visualizations and the point vortex model suggests that, under the conditions of low helical pitch frequently observed in rotor wakes, helical vortex dynamics are dominated by the interactions between a few neighboring vortex loops.

References

- [1] H.U. Quaranta, et al. Local and global pairing instabilities of two interlaced helical vortices. *Journal of Fluid Mechanics*, 863:927–955, 2019.
- [2] M. Felli, et al. Mechanisms of evolution of the propeller wake in the transition and far fields. *Journal of Fluid Mechanics*, 682:5–53, 2011.
- [3] I. Delbende, et al. Nonlinear dynamics of two helical vortices: A dynamical system approach. *Physical Review Fluids*, 6(8):084701, 2021.
- [4] H. Aref. On the equilibrium and stability of a row of point vortices. *Journal of Fluid Mechanics*, 290:167–181, 1995.

Vortex sensing and uncertainty propagation for aircraft formation flight

Ignace Ransquin^a, Denis-Gabriel Caprace^{a,b}, Matthieu Duponcheel^a and Philippe Chatelain^{a*}

^a Université catholique de Louvain, Institute of Mechanics, Materials and Civil Engineering, Louvain-la-Neuve, Belgium¹

^b Brigham Young University, Provo, Utah

*Correspondence: philippe.chatelain@uclouvain.be

1 Introduction

Formation flight is known to improve the efficiency of a two-aircraft formation (leader+follower). Indeed, the follower benefits from substantial apparent drag reduction when flying in the upwash region of the leader wake. This bio-inspired technique can therefore lead to significant fuel savings as recently showed in commercial aviation [1, 2]. For civilian applications, the concept of extended formation flight is favored due to evident safety concerns: the follower then flies several tens of wingspans downstream of the leader and nevertheless benefits from the wake. This requires, however, an accurate tracking of the wake position to preserve the efficiency gains: 50% of the benefit is lost if the follower cannot ensure a wake tracking accuracy within 10% of the span of the leader.

A corollary lies in the hazard posed by such formation scenarios to downstream air traffic. Indeed, as the follower flies close to the leader's wake vortices, the inboard vortices of the resulting wake are very close to each other and undergo drastically faster dynamics. Furthermore, the uncertainty on the relative position between the follower and the wake of the leader that is inherent to any tracking strategy, further increases the complexity and uncertainty of the resulting vortex dynamics over large distances, making the prediction of the wake hazard extremely challenging.

In this work, we design and assess a wake sensing method based solely on the assimilation of the aircraft dynamics [3]. The wake dynamics of the two-aircraft formation are then simulated over large distances using a combination of space- and time-developing Large Eddy Simulations, enabling the quantification of the uncertainty of the wake haz-

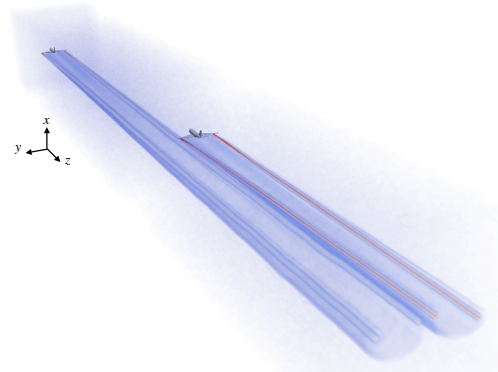


Figure 1: Large Eddy Simulation of an aircraft Formation within a turbulent flow field

ard far downstream. This also allows us to assess the feasibility of commercial formation flight with more than two aircraft.

2 High fidelity simulation of formation flights

We use a state-of-the-art Vortex-Particle Mesh (VPM) method [4] to simulate the vortex-dominated flow within the formation. It combines the advantages of a particle method and of a mesh-based approach, which makes it a hybrid approach among the many variants of vortex methods [5]. The method is based on the vorticity-velocity formulation ($\omega - u$) of the Navier-Stokes equations for incompressible flows.

The generation of vorticity along the lifting surfaces of an aircraft is accounted for through an Immersed Lifting Lines (ILL) method [6]. Ambient turbulence is added to the simulation to reproduce as closely as possible actual flight and wake conditions. Synthetic turbulence, reproducing the spectrum of Homogenous Isotropic Turbulence (HIT), and generated using the Mann algorithm [7], is smoothly injected at the inlet of the computational domain. The 6 degrees-of-freedom dynamics of the aircraft are handled by a Multi-body system integrator, Robotran [8].

¹This project has received funding from the European Research Council (ERC) under the European Union's Horizon 2020 research and innovation program (grant agreement no. 725627).

The development work benefited from the computational resources provided by the supercomputing facilities of the Université catholique de Louvain (CISM/UCL) and the Consortium des Équipements de Calcul Intensif (CÉCI) en Fédération Wallonie Bruxelles (FWB) funded by the Fond de la Recherche Scientifique de Belgique. The production simulations were performed on the Tier-1 supercomputer of the Fédération Wallonie-Bruxelles, infrastructure funded by the Walloon Region under the grant agreement n°1117545.

3 Data assimilation of aircraft wake parameters

Following the methodologies pursued in [9] and [10], the proposed approach relies on an Ensemble Kalman Filter that propagates a surrogate model of the formation. The model output is here corrected within the estimator through a comparison with measurements of the full 6 degrees-of-freedom dynamics of the follower, as well as geometric characteristics of the leader. This essentially waives the need for dedicated hardware devices and only requires episodic communication between the leader and the follower. The chosen combination of estimator and dynamics measurements are found to be able to detect the position of the impacting wake as long as the dynamics are accurately reproduced by the surrogate model. Additionally, it is shown that a lack of observability hinders the concurrent estimation of the wake position and strength in the presence of uncertainty.

One final observation concerns the energy gains. In a perturbed environment, the follower endowed with the wake sensing capability is able to track the wake and therefore the energy-optimal position, ensuring a 10% gain whereas a straight-flying follower loses most of the benefit.

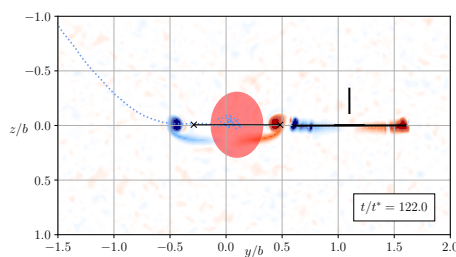


Figure 2: Cross section of the streamwise vorticity behind the follower (—). The dotted line (····) is the history of the estimated position of the leader’s wake, with the current estimation (×——×). The shaded area (●) represents the $1 - \sigma$ confidence interval of the estimate.

4 Uncertainty propagation of wake trajectories

The uncertainty on the relative position between the follower and the leader’s wake leads to an uncertainty on the dynamics of the wake vortices from their emission to the far-wake. The propagation of this uncertainty is performed through a sampling of the relative positions and the simulation by means of LES up to the far-wake conditions. Every single simulation presents a markedly multi-scale spatio-temporal problem as one has to capture the wake development from its generation to its development one minute later or, equivalently, 10km downstream.

For that purpose, we have developed a numerical methodology that combines 3D Space Developing (SD) and 3D Time Developing (TD) VPM simulations in order to capture the roll-up of the vortex sheets originating from the leader and follower, their mutual interactions, and their evolution

within ambient turbulence.

The probabilistic analysis led us to observe the impact of a formation wake in an operational context, and to compare it to the wake of an isolated aircraft. By computing a Rolling Moment Coefficient in the wake of both the formations and the isolated aircraft, we observed that the wake of a formation was less constraining in terms of Rolling Moment Coefficient intensity. However, it did not decrease as fast as the one computed in the wake of an isolated aircraft. We also defined a Vertical Force Coefficient that characterized the increase in vertical force experienced by an aircraft flying in a wake because of upwash winds. That Vertical Force Coefficient was shown more intense in the wake of a formation, compared to the wake of an isolated aircraft. This observation would justify the deployment of larger aircraft formations, as a third aircraft would enjoy even greater savings.

5 Conclusions

The present wake sensing and uncertainty quantification frameworks bring concrete contributions to the operational feasibility of formation flight.

While limited to a two-aircraft scenario, our work clearly hints at the potential and the challenges of multi-aircraft formations. The string stability of such formations for instance will require specific precautions for the flight controllers that result from sensing and tracking tasks.

Finally, the used assimilation techniques can be exploited to provide observability estimations of the assumed flow structures and should then enable the optimization of wake tracking trajectories that maintain the system observable.

References

- [1] T. C. Flanzer, S. R. Bieniawski, and J. A. Brown. “Advances in Cooperative Trajectories for Commercial Applications”. In: *AIAA Scitech 2020 Forum*. 2020.
- [2] Airbus. *Airbus and its partners demonstrate how sharing the skies can save airlines fuel and reduce CO2 emissions*. Nov. 2021.
- [3] I. Ransquin and P. Chatelain. “Bio-inspired Wake Tracking for Aircraft Formation Flight Based on Reinforcement Learning”. In: *AIAA Scitech 2021 Forum*. Ed. by AIAA. 2021.
- [4] P. Chatelain, A. Curioni, M. Bergdorf, D. Rossinelli, W. Andreoni, and P. Koumoutsakos. “Billion vortex particle Direct Numerical Simulations of aircraft wakes”. In: *Computer Methods in Applied Mechanics and Engineering* 197.13 (Feb. 2008), pp. 1296–1304.
- [5] C. Mimeau and I. Mortazavi. “A Review of Vortex Methods and Their Applications: From Creation to Recent Advances”. In: *Fluids* 6.2 (2021).
- [6] D.-G. Caprace, G. Winckelmans, and P. Chatelain. “An immersed lifting and dragging line model for the vortex particle-mesh method”. In: *Theoretical and Computational Fluid Dynamics* 34 (2020), pp. 21–48.
- [7] J. Mann. “Wind field simulation”. In: *Probabilistic Engineering Mechanics* 13.4 (Oct. 1998), pp. 269–282.
- [8] N. Docquier, A. Poncelet, and P. Fiset. “ROBOTRAN: a powerful symbolic generator of multibody models”. In: *Mechanical Sciences* 4.1 (2013), pp. 199–219.
- [9] D.-G. Caprace, G. Winckelmans, P. Chatelain, and J. Eldredge. “Wake Vortex Detection and Tracking for Aircraft Formation Flight”. In: *AIAA Aviation 2019 Forum*. Ed. by AIAA. June 2019.
- [10] M. S. Hemati, J. D. Eldredge, and J. L. Speyer. “Wake Sensing for Aircraft Formation Flight”. In: *Journal of Guidance, Control, and Dynamics* 37.2 (2016/01/25 2014), pp. 513–524.

Vortex pairs in the wake of fixed and rotating split-tip wings

D. Schröder^{a*}, T. Leweke^b, R. Hörschemeyer^a and E. Stumpf^a

^a RWTH Aachen University, Institute of Aerospace Systems, Aachen, Germany¹

^b CNRS / Aix-Marseille Université / Centrale Marseille, IRPHE, Marseille, France¹

*Correspondence: schroeder@ilr.rwth-aachen.de

1 Introduction

The flow around lifting surfaces of finite span is associated with the generation of concentrated vortices at their tips. In the case of a fixed wing, a rectilinear trailing vortex is found, whereas a rotating wing (rotor blade) creates a helical tip vortex in its wake. Lift-generated vortex systems have been studied extensively in the context of aircraft and helicopter wakes. For fixed-wing aircraft, the trailing vortex pair can represent a danger to following aircraft, due to the downwash and rolling moment it induces. For helicopters, the interaction between a rotor blade and the tip vortex of the preceding blade can lead to unwanted noise and structural vibrations (Blade-Vortex Interactions – BVI) [1]. Various strategies have been devised to mitigate these negative effects associated with wing tip vortices. One of them aims at modifying the vortex structure, and in particular increasing the vortex core size. This reduces the rotation rate of the core fluid and decreases the velocity gradients, which is beneficial for the induced rolling moment behind a fixed wing and for BVI-related noise generation by rotors. We here present a method which achieves this goal by splitting the concentrated tip vortex into a pair of co-rotating vortices of similar strength, with the help of a tip device in the form of a perpendicular fin (see Fig. 1). Numerical simulations and water channel experiments are used to characterise the evolution of the vortex pair and the resulting final vortex for configurations involving both a fixed and a rotating wing.

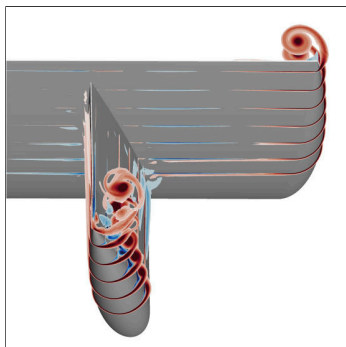


Figure 1: Schematic of the wing tip geometry and vortex formation for the fixed wing, from a RANS simulation [2].

¹This work was supported by the Deutsche Forschungsgemeinschaft under grant no. 391677260, and by the French Agence Nationale de la Recherche under grant no. ANR-17-CE06-0018.

2 Methods

We consider simple generic wing geometries based on a NACA 0012 profile, constant chord, and rounded tips. The fixed wing has semi-span 290 mm and chord 100 mm, whereas the rotating wing has chord 80 mm and is part of a one-bladed rotor of radius 240 mm, with a twist distribution suitable for operation close to hover conditions. The fin is mounted perpendicularly to the wing near the tip. It has the same NACA 0012 profile, and its geometric parameters (position, height, angle of attack) are varied by exchanging the entire tip geometry. The tip chord-based Reynolds number is of order 10^5 . Numerical simulations using a RANS method with an SSG/LRR- ω Reynolds stress turbulence model, combined with stereoscopic PIV measurements in a water channel, were used to characterise the initial tip vortex system generated for a fixed wing equipped with a fin. The results were then used for the design of the rotating blade, which aimed at producing a similar circulation distribution in the tip region. The downstream evolution of the helical tip vortex pair generated by the rotating wing was investigated experimentally using stereoscopic and volumetric PIV, as well as dye visualizations (Fig. 2).

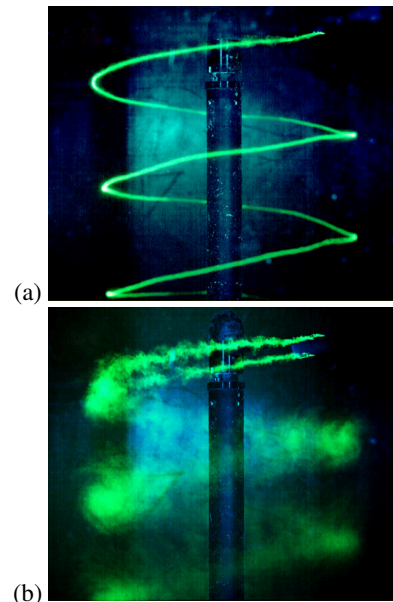


Figure 2: Dye visualization of the tip vortices for the rotating blade, (a) without and (b) with fin [3].

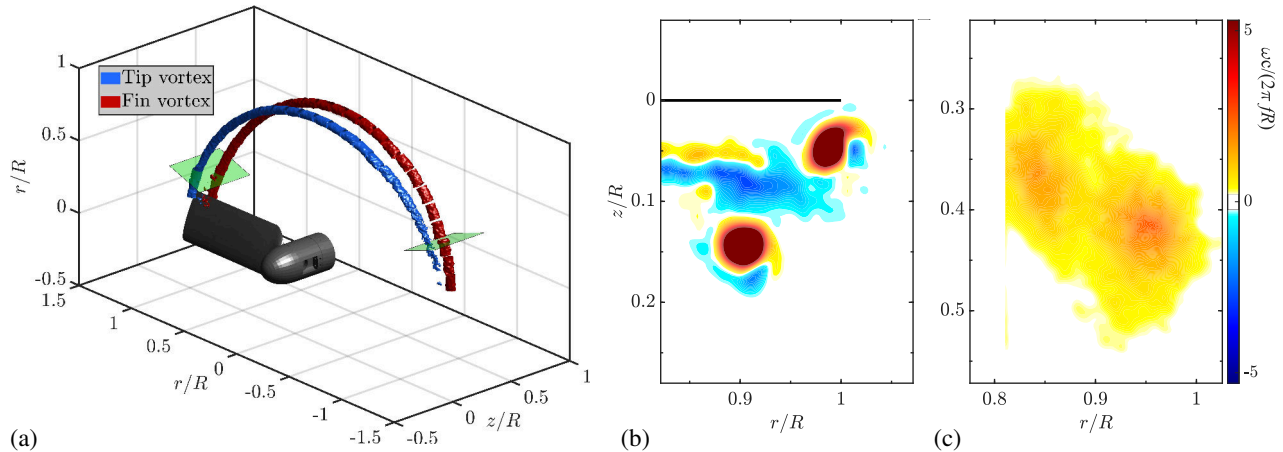


Figure 3: Vorticity from tomographic PIV for the rotating split-tip wing. (a) Volumetric isocontours of vorticity magnitude; (b,c) azimuthal vorticity fields for the two wake ages highlighted in (a). R, f : rotor radius and frequency, c : blade chord.

3 Results

The numerical RANS simulations with the fixed-wing geometry have revealed a tendency for flow separation at the fin root when it is placed on the suction side of the wing [2]. Consequently, all further investigations were carried out with the fin located on the pressure side. Both the numerical and experimental investigations showed that the desired objective of splitting the concentrated tip vortex can be achieved with the presented modification. An experimental parameter study for the fixed wing demonstrated how the characteristics of the resulting tip vortex pair (distance between wing and fin vortices, circulation ratio) are influenced by the parameters of the fin geometry and position. Pairs of co-rotating vortices with similar circulation could be achieved, which are prone to develop interactions which accelerate the core growth and eventually lead to merging into a widened final vortex. The fixed-wing study was limited to the near wake of the wing, where no such interactions and merging were observed.

The experiments with a rotating wing showed that the method of tip vortex splitting also works in this configuration. Two separate vortices are created, whose initial parameters are again influenced by the fin geometry [4]. However, the evolution of the vortex pair strongly differs from the fixed-wing results. For certain configurations, the core radii of both vortices rapidly increase immediately after emerging from the trailing edges, suggesting the presence of an instability phenomenon (see Fig. 2) [3]. PIV results confirm the qualitative observations from the visualizations: an example of a volumetric reconstruction of the wake, as well as two field cuts showing azimuthal vorticity are given in Fig. 3. Comparing the two fields, the rapid core growth and the onset of vortex merging are clearly visible. The merging results in a less concentrated single vortex with strongly decreased peak tangential velocities. A closer analysis of the initial velocity fields reveal that both vortices are subject to centrifugal instability, which arises in vortices whose radial vortic-

ity profile changes sign [5]. The vorticity field in Fig. 3(b) shows that the initial vortex pair is indeed surrounded by regions of opposite-signed vorticity. Its origin can partly be traced back to the interaction between the secondary fin vortex and the blade surface [6]. In addition, contrary to the fixed wing case, the spanwise circulation distribution of the rotating blade leads to a trailing vortex sheet of opposite sign in the inner part of the blade span. Due to the three-dimensional character of the perturbations leading to rapid core growth and merging, the current study uses volumetric measurement techniques to allow a more detailed investigation of the instability and its effects. Further time-resolved measurements, combined with supporting numerical calculations of the rotating system, are planned to obtain a deeper understanding of the underlying physics.

4 Conclusion

A wing tip modification using a perpendicular fin on the pressure side was investigated combining numerical simulations and experiments. For both fixed and rotating wings, a splitting of the tip vortex into a vortex pair was observed, whose characteristics depend on the fin parameters. In the rotating case, a rapid merging occurs into a final vortex with a considerably larger core, a promising result concerning the problem of BVI noise reduction.

References

- [1] Y. H. Yu. Rotor blade–vortex interaction noise. *Progress in Aerospace Sciences*, 36(2):97–115, 2000.
- [2] D. Schröder, et al. Generation of a wingtip vortex pair using a pressure-side fin. *Aerospace Science and Technology*, submitted, 2022.
- [3] D. Schröder, et al. Experiments on helical vortex pairs in the wake of a rotor. *AIAA Paper 2021-1088*, 2021.
- [4] D. Schröder, et al. Experimental investigation of a rotor blade tip vortex pair. *CEAS Aeronautical Journal*, doi:10.1007/s13272-021-00555-1, 2021.
- [5] B. J. Bayly. Three–dimensional centrifugal–type instabilities in inviscid two–dimensional flows. *Physics of Fluids*, 31(1):54–64, 1988.
- [6] D. Schröder, et al. Instability and merging of a helical vortex pair in the wake of a rotor. *Journal of Physics: Conference Series*, 1934:012007, 2021.

Numerical analysis of helical vortex pairs

A. Castillo-Castellanos^{a*} and S. Le Dizès^{a*}

^a Aix Marseille Université, CNRS, Centrale Marseille, IRPHE, Marseille, France¹

*Correspondence: *andres-alonso.castillo-castellanos@univ-amu.fr*

1 Introduction

We are interested in the dynamics and instability of concentrated vortices, which are relevant to industrial applications. For instance, rotating blades generate concentrated vortices at their tips, which are advected to form a characteristic helical pattern. From a theoretical perspective, the stability properties of uniform helices have been the subject of numerous works. Experimental measurements under typical operating conditions show a good agreement between the measured growth rates with theoretical predictions based on the vortex filament framework (see, for instance refs. [1, 2]). However, such predictions are specific to a prescribed geometry and their complexity increases dramatically as we include the radial expansion/contraction observed near the rotor plane [3], or the interaction with a hub vortex or additional tip vortices [4].

Our work is motivated by a novel approach to noise reduction which uses a modified air-foil to split and spread the vorticity in two tip vortices [5]. The tip vortices are expected to generate a helical vortex pair like the ones displayed in figure 1a. We present a general approach based on the free vortex method to study the stability of such a vortical wake where helical symmetry is not present. We consider vortices in the form of thin vortex filaments of finite but small core size, and compute the induced velocity using a cut-off method. In this simplified framework, we first search for ‘steady’ solutions in the rotor frame, in the sense that vortices are moving along the steady filament vortex structure. The linear stability with respect to long-wave displacements and the transition towards the non-linear regime are also analysed.

2 Results

A typical steady solution of the wake produced by a two-bladed tip-splitting rotor is illustrated in figure 1a. In the far-field, these solutions are spatially periodic [6]. Their properties are governed by purely geometrical parameters identified in figure 1b: separation distance d , radius R , vortex core size a , and two axial pitches, H and h . A temporal frequency analysis is used to identify the different unstable modes. To do so, first we linearise the equations of motion around the steady solution and evaluate the linear op-

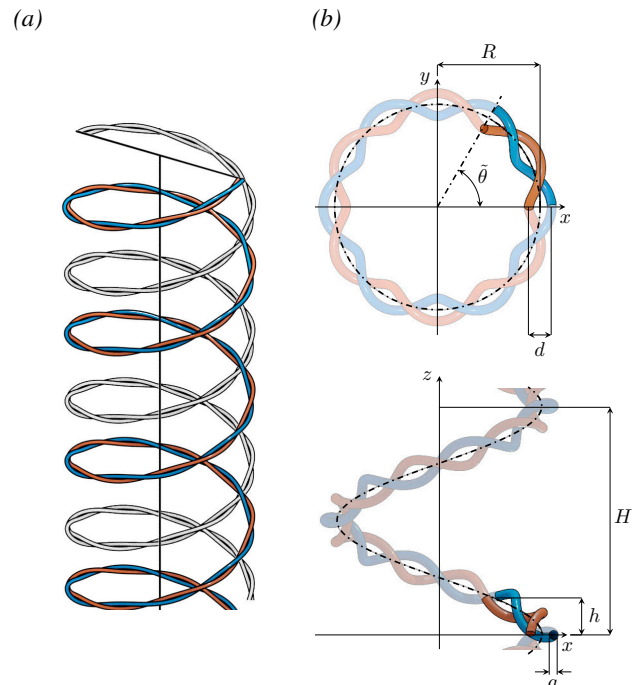


Figure 1: (a) Schematic representation of the wake structure detached from a two-bladed tip-splitting rotor in ascending flight regime. (b) Geometric parameters of closely spaced vortices: separation distance d , radius R , vortex core size a , axial pitches H and h .

¹This work was supported by the Agence Nationale de la Recherche (grant no. ANR-17-CE06-0018) and the Deutsche Forschungsgemeinschaft (grant no. 391677260).

erator using only the discretised vortex filaments. Then, we perform a global stability analysis by solving an eigenvalue problem in standard fashion [7]. Two kinds of instability modes are obtained [8, 9]. Symmetric modes are characterized by a block displacement of the vortex pair, analogous to the local pairing modes in helical geometries (figure 2a). Anti-symmetric modes are characterized by a mirrored displacement with respect to the vorticity centre of the pair, with the most unstable mode corresponding to a local pairing between one member of a pair with the other member of a pair in the neighbouring turn (figure 2b). The dependency of the stability properties with respect to different parameters is provided (figure 2c). The transition associated with the instability is also considered by looking at the temporal evolution of the most unstable mode in the non-linear regime. Finally, the results are applied to a spatially evolving wake and discussed in the context of wake transition and noise reduction.

References

- [1] Hugo Umberto Quaranta, Hadrien Bolnot, and Thomas Leweke. Long-wave instability of a helical vortex. *Journal of Fluid Mechanics*, 780:687–716, 2015.
- [2] Hugo Umberto Quaranta, Mattias Brynjell-Rahkola, Thomas Leweke, and Dan S Henningson. Local and global pairing instabilities of two interlaced helical vortices. *Journal of Fluid Mechanics*, 863:927–955, 2019.
- [3] E Durán Venegas, P Rieu, and Stéphane Le Dizès. Structure and stability of joukowski’s rotor wake model. *Journal of Fluid Mechanics*, 911, 2021.
- [4] E Durán Venegas and Stéphane Le Dizès. Generalized helical vortex pairs. *Journal of Fluid Mechanics*, 865:523–545, 2019.
- [5] Dominic Schröder, Thomas Leweke, Ralf Hörschemeyer, and Eike Stumpf. Instability and merging of a helical vortex pair in the wake of a rotor. In *Journal of Physics: Conference Series*, volume 1934, page 012007. IOP Publishing, 2021.
- [6] Andrés Castillo-Castellanos, Stéphane Le Dizès, and E Durán Venegas. Closely spaced corotating helical vortices: General solutions. *Physical Review Fluids*, 6(11):114701, 2021.
- [7] Vassilios Theofilis. Global linear instability. *Annual Review of Fluid Mechanics*, 43:319–352, 2011.
- [8] A Castillo-Castellanos, E Durán Venegas, and S Le Dizès. Joukowski’s wake model for tip-splitting rotors. *Journal of Physics: Conference Series*, 1934(1):012005, may 2021.
- [9] Andrés Castillo-Castellanos and Stéphane Le Dizès. Closely spaced co-rotating helical vortices: Long-wave instability, 2021.

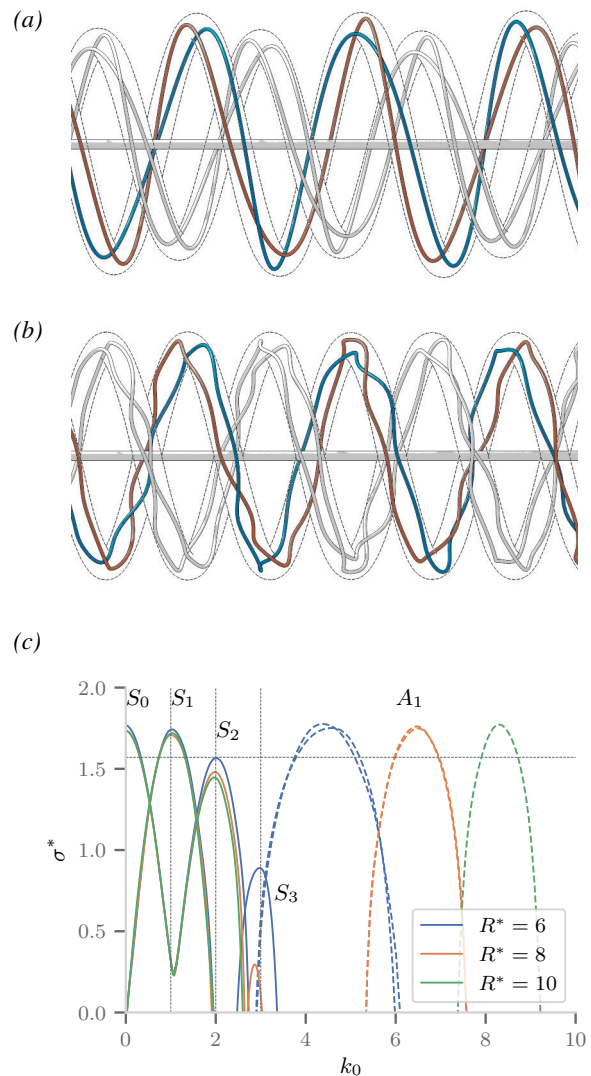


Figure 2: Three dimensional view of the base state perturbed by modes (a) S_0 and (b) A_1 for $R^* = 7$. (b) Growth rate σ^* as function of the wavenumber k_0 for $a/d = 0.1$, $H/R = 10.5$, $\beta \equiv H/h = 3/4$, and three values of $R^* \equiv R/d$.

Invited speakers



William Wolf is an Associate Professor at the School of Mechanical Engineering at the University of Campinas, in Brazil, where he coordinates the Laboratory of Aeronautical Sciences. He obtained his BSc in Mechanical Engineering from the University of São Paulo, in 2003, and his PhD in Aeronautics & Astronautics from Stanford University, in 2011. His areas of expertise include high-fidelity numerical simulations and reduced-order modeling of unsteady aerodynamics and aeroacoustics.

Andres Goza is an Assistant Professor in the Aerospace Engineering Department at the University of Illinois at Urbana-Champaign. He received his PhD from Caltech in 2017 and was a postdoctoral researcher at Princeton University from 2017-2018. His research focuses on the use of computational fluid dynamics and modeling techniques to gain fundamental physical insights into fluid-structure interaction (FSI) systems. Andres's interest in these systems ranges from harnessing flow-induced vibrations for robust energy harvesting to utilizing FSI for passive control and/or estimation of unsteady aerodynamic flows. He was awarded an NSF Graduate Research Fellowship to perform his doctoral work, and his thesis work led to his selection as a Caltech Everhart Lecturer. He was also a "Teacher Ranked As Excellent" at UIUC in 2020-2021, and was awarded the 2021 "AIAA Teacher of the Year" award by the Aerospace Engineering Department at UIUC.



Daniel Quinn received his PhD from the Hydrodynamics Lab at Princeton University, where he studied the role of flexibility in fish-inspired robots. While a graduate student, Quinn was also a Visiting Fellow at the Museum of Comparative Zoology at Harvard University. For his doctoral work, Professor Quinn was awarded the American Physical Society's Andreas Acrivos Dissertation Award in Fluid Dynamics. He went on to become a Postdoctoral Fellow in the Bio-Inspired Research and Design group at Stanford University, studying the stability characteristics of birds flying in turbulent gusts. Professor Quinn joined the faculty at the University of Virginia in 2017. He is a member of the Link Lab, a group of UVA researchers studying Cyber-Physical Systems—particularly autonomous vehicles, body sensor networks, and smart homes. His most recent work is funded by a NSF CAREER Award, which he received in the fall of 2020.

Kiran Ramesh is a Senior Lecturer in Aerospace Sciences at the University of Glasgow. His research interests are in unsteady external flows past moving surfaces and bio-inspired locomotion. He works on analytical and numerical fluid dynamics, with a focus on low-order numerical methods for fast simulation and design.



Jennifer Franck is an Assistant Professor in the Department of Engineering Physics at the University of Wisconsin-Madison. She leads the Computational Flow Physics and Modeling Lab, using computational fluid dynamics (CFD) techniques to explore the flow physics of unsteady and turbulent flows. Ongoing research projects are in the areas of bio-inspired flows and the fluid dynamics of renewable energy systems with current projects funded by NSF and ARPA-E. Prior to joining the UW-Madison faculty in 2018, she was faculty at Brown University. She received her undergraduate degree in Aerospace Engineering from University of Virginia, followed by a M.S. and Ph.D. from California Institute of Technology. Following her PhD, she was awarded an NSF Postdoctoral Fellowship hosted at Brown University to computationally explore fluid dynamics mechanics of flapping flight.



Thierry Jardin is director of research at ISAE-SUPAERO in Toulouse, France. He obtained his Master degree from INSA (Toulouse, France) before joining Institut Pprime (Poitiers, France) as a PhD student. He then moved to ISAE-SUPAERO, first as a post-doc and then as a research scientist and director of research in 2020. During this period he also moved to Caltech as a visiting researcher in 2015-2016. His research interests are unsteady aerodynamics, rotor aerodynamics and bluff body wakes, with a focus on massively separated flows.



Theresa Saxton-Fox is an Assistant Professor of Aerospace Engineering at the University of Illinois at Urbana-Champaign. She received her Masters and PhD from Caltech and did her post-doctoral research at Princeton University, prior to starting at the University of Illinois in January 2019. Her work focuses on wall-bounded turbulent flows with particular interests in nonlinear interactions, global unsteadiness, and curvature effects. She was awarded the Centennial prize for best thesis in the Mechanical and Civil Engineering department at Caltech in 2018 and the Young Investigator Program award from the Office of Naval Research in 2021.



Organisation

Organising committee



Karen Mulleners
École polytechnique fédérale
de Lausanne (EPFL)
karen.mulleners@epfl.ch



Rajat Mittal
Johns Hopkins University
mittal@jhu.edu

Advisory committee



Jeff Eldredge
University of California, Los Angeles
jdeldre@g.ucla.edu



Anya Jones
University of Maryland
arjones@umd.edu



Bharathram Ganapathisubramani
University of Southampton
G.Bharath@soton.ac.uk

List of participants

Abraham, Aliza	Aix-Marseille Université/IRPHE
Andreu Angulo, Ignacio	University of Cambridge
Balla, Ashok	Indian Institute of Science
Breuer, Kenny	Brown University
Brunner, Claudia	Princeton University
Castillo, Andres	IRPHE
Chatelain, Philippe	UC Louvain
Costa Ormonde, Pedro	Lehigh University
Dave, Mukul	University of Wisconsin-Madison
David, Laurent	Institut Pprime
Eldredge, Jeff	University of California Los Angeles
Farnsworth, John	University of Colorado Boulder
Franck, Jennifer	University of Wisconsin-Madison
Fuzaro Miotto, Renato	University of Campinas
Ganapathisubramani, Bharathram	University of Southampton
Gehlert, Pascal	University of Cambridge
Gehrke, Alexander	École polytechnique fédérale de Lausanne
Gloutak, Dasha	University of Colorado Boulder
Gopalarathnam, Ashok	North Carolina State University
Goyal, Anushka	McGill University
Goza, Andres	University of Illinois Urbana-Champaign
Green, Melissa	University of Minnesota
Gregorio, Elizabeth	George Washington University
Gursul, Ismet	University of Bath
Hultmark, Marcus	Princeton University
Jardin, Thierry	ISAE-SUPAERO
Jones, Anya	University of Maryland
Kaiser, Frieder	Queen's University
King, Justin	University of Minnesota
Lauber, Marin	University of Southampton
Le Fouest, Sebastien	École polytechnique fédérale de Lausanne
Leetch, James	University of Southampton
Leftwich, Megan	The George Washington University

Leweke, Thomas	CNRS-IRPHE
Manohar, Kevin	University of Calgary
Martinez, Alfonso	University of Glasgow
Massey, Jonathan	University of Southampton
Menon, Karthik	Stanford University
Mittal, Rajat	Johns Hopkins University
Mivehchi, Amin	Lehigh University
Moored, Keith	Lehigh University
Mulleners, Karen	École polytechnique fédérale de Lausanne
Nedic, Jovan	McGill University
Otomo, Shuji	University of Edinburgh
Quinn, Daniel	University of Virginia
Ramesh, Kiran	University of Glasgow
Reijtenbagh, Jesse	Delft University of Technology
Rocha Ribeiro, Bernardo Luiz	University of Wisconsin-Madison
Roslansky, William	University of Minnesota
Saxton-Fox, Theresa	University of Illinois Urbana-Champaign
Shoele, Kourosh	Florida State University
Stin, Vincent	Sorbonne Université / PMMH ESPCI PSL
Thomas, Lionel	Institut pprime
Toppings, Connor	University of Waterloo
Vadher, Paras	The University of Cambridge
Vilumbrales Garcia, Rodrigo	University of Southampton
Viola, Ignazio Maria	University of Edinburgh
Westerweel, Jerry	Delft University of Technology
Weymouth, Gabriel	University of Southampton
Winckelmans, Gregoire	UC Louvain
Wolf, William	University of Campinas
Yaghoobian, Neda	Florida State University
Yarusevych, Serhiy	University of Waterloo